REPORT DOCUMENTATION PAGE

1. REPORT DATE (DD-MM-YYYY)	2. REPORT TYPE	3. DATES COVERED (From - To)
1-2-2012	Final Performance Report (Revised)	From 15-08-2008 to 31-08-2011

4. TITLE AND SUBTITLE
Hybrid Materials for Thermal Management in Thin Films and Bulk Composites

5a. CONTRACT NUMBER

5b. GRANT NUMBER
FA9550-08-1-0431

5c. PROGRAM ELEMENT NUMBER

6. AUTHOR(S)
Texter, John; Baghdachi, Jamil

5d. PROJECT NUMBER

5e. TASK NUMBER

5f. WORK UNIT NUMBER

7. PERFORMING ORGANIZATION NAME(S) AND ADDRESS(ES)
Eastern Michigan University
Office of Research and Development
Starkweather Hall
Ypsilanti, MI 48197, USA

8. PERFORMING ORGANIZATION REPORT NUMBER

9. SPONSORING/MONITORING AGENCY NAME(S) AND ADDRESS(ES)
USAF, AFRL
AF Office of Scientific Research
875 Randolph Street, Room 3112
Arlington, VA 22203

10. SPONSOR/MONITOR'S ACRONYM(S)
AFOSR

11. SPONSOR/MONITOR'S REPORT NUMBER(S)

12. DISTRIBUTION/AVAILABILITY STATEMENT

13. SUPPLEMENTARY NOTES

14. ABSTRACT

We developed and applied nanolatexes and triblock copolymers and processes that stabilize waterborne dispersions of nanocarbon at concentrations 10 to1000-fold greater than previously reported. By nanocarbon we mean SWCNT, MWCNT, graphene, and hydrothermal carbon (HTC). We developed waterborne coating of MWCNT dispersions to produce the most highly thermally conducting man-made materials prepared outside of a vacuum chamber. We were successful in synthesizing triblock copolymers of poly(propylene oxide) centerblocks having endblocks of an ionic liquid monomer with about 2 to 15 units on either side by controlled ATRP with PDI in the range of 1.20 to 1.7. This new class of stimuli responsive triblocks also was found to exhibit thermoreversibility by forming a lyotropic liquid crystalline gel phase by warming above its LSCT (lower solution concentrations temperatures). We showed that hydrothermal carbon can be formulated to easily be dispersed at the nanoscale and that it shares interesting optical absorption limits with graphene and carbon nanotubes. HTC is a sustainable resource that can be used for nanotechnology development in several areas, including indirect carbon fuel cells.

15. SUBJECT TERMS
SWCNT, MWCNT, hydrothermal carbon, graphene, thermal conductivity, electrical conductivity, templated coatings, nanolatexes, triblock copolymers, waterborne dispersions, waterborne coating

16. SECURITY CLASSIFICATION OF:			17. LIMITATION OF ABSTRACT	18. NUMBER OF PAGES	19a. NAME OF RESPONSIBLE PERSON
a. REPORT	b. ABSTRACT	c. THIS PAGE			John Texter
U	U	U	UU		19b. TELEPHONE NUMBER (Include area code) 585-413-8278

Standard Form 298 (Rev. 8/98)
Prescribed by ANSI Std. Z39.18
Adobe Professional 7.0

Final Performance Report (Revised)
Activity Report for period August 2008 through August 2011

Hybrid Materials for Thermal Management in Thin Films and Bulk Composites

John Texter, PI, Eastern Michigan University; jtexter@emich.edu

Contents

Archival Publications

17. "Solvent-free nanofluid heat capacity anomalies;" J. Texter, K. Bian, D. Chojnowski, and J. Byrom. *Nature* (submitted) (2012).

16. "Stimuli-responsive nanolatexes – Porating films;" D. England, N. Tambe, and J. Texter. *ACS Macro Lett.* (submitted) (2012).

15. "Triblock copolymer based on poly(propylene oxide) and poly(1-[11-acryloylundecyl]-3-methyl-imidazolium bromide**)**;" J. Texter, V. Arjunan Vasanthat, R. Maniglia, L. Slater, and T. Mourey. *Macromol. Rap. Com.* **xx,** xxx-xxx (2011); doi: 10.1002/marc.201100586.

14. "Nanoparticle dispersions with ionic liquid-based stabilizers;" J. Texter, US Patent Application Publication, US 2011/0233458 A1, 29 September 2011.

13. "Polymer dewetting via stimuli responsive structural relaxation – Contact angle analysis;" X. Ma, R. Crombez, Md. Ashaduzzaman, M. Kunitake, L. Slater, T. Mourey, and J. Texter, *Chem. Commun.* **47**, 10356-10358 (2011); doi:10.1039/C1CC12656C.

12. "Stimuli-responsive triblock copolymers – Synthesis, Characterization, and Application;" J. Texter, V. Arjunan Vasantha, K. Bian, X. Ma, L. Slater, T. Mourey, and G. Slater. Ch. 9 in *Non-Conventional Functional Block Copolymers*, B. Coughlin, P. Theato, and A. Kilbinger, Eds., American Chemical Society, Washington, DC (2011) pp. 117-130; doi: 10.1021/bk-2011-1066; *ACS Symp. Ser.* **2011**, 1066, 117-130 (2011).

11. "Stimuli responsive poly(1-[11-acryloylundecyl]-3-methyl-imidazolium bromide) – dewetting and nanoparticle condensation phenomena;" X. Ma, Md. Ashaduzzaman, M. Kunitake, R. Crombez, J. Texter, L. Slater, and T. Mourey, *Langmuir* **27,** 7148-7157 (2011); doi: 10.1021/la200184c.

10. "Waterborne nanocarbon dispersions for electronic and fuel applications;" J. Texter, R. Crombez, X. Ma, L. Zhao, F. Perez-Caballero, M.-M. Titirici, and M. Antonietti, *Prep. Symp. - ACS Div. Fuel Chem.* 56, 388-389 (2011).

9. "Waterborne WC nanodispersions;" C. Giordano, Wen Yang, A. Lindemann, R. Crombez, and J. Texter, *Colloids Surfaces A* **374,** 84-87 (2011); doi:10.1016/j.colsurfa.2010.11.014.

8. "Sustainable nitrogen-doped carbon latexes with high electrical and thermal conductivity;" L. Zhao, R. Crombez, M. Antonietti, J. Texter, and M.-M. Titirici, *Polymer* 51, 4540-4546 (2010); doi: 10.10.16/j.polymer.2010.07.044.

7. "(IL)m(PO)n(IL)m – Ionic liquid-based triblock copolymers;" J. Texter and K. Bian, *Polymer Preprints* 51(2) 105-106 (2010).

6. "Stimuli responsive coatings of carbon nanotubes an nanoparticles using ionic liquid based nanolatexes;" J. Texter, Nikhil Tambe, R. Crombez, M. Antonietti, and Cristina Giordano, *Polymer Mater. Sci. Eng.* 102, 401-402 (2010).

5. "Sustainable polymerization in recoverable microemulsions;" Z. Z. Chen, L. H. Qiu, J. M. Lu, F. Yan, and J. Texter, *Langmuir* 26, 3803-3806 (2010); doi: 10.1021/la100502x.

4. "Amphiphilic ionic liquid-based block copolymers – Stimuli responsive new materials;" J. Texter, K. Tauer, N. Weber, and A. Masic, *Polymer Preprints* 51(1), 355-356 (2010).

3. "Single-wall carbon nanotube latexes;" M. Antonietti, Y. Shen, T. Nakanishi, M. Manuelian, R. Campbell, L. Gwee, Y. Elabd, N. Tambe, R. Crombez, and J. Texter, *ACS Appl. Mater. Interfaces* 2, 649-653 (2010); doi: 10.1021/am900936j.

2. "Core-shell particle interconversion with di-stimuli-responsive diblock copolymers;" K. Tauer, N. Weber, and J. Texter, *Chem. Comm.* 6065-6067 (2009); doi:10.1039/B912148J.

1. "Advanced applications of ionic liquids in polymer science," F. Yan, J. Lu, and J. Texter, *Prog. Poly. Sci.*, **34**, 431-448 (2009); doi:10.1016/j.progpolymsci.2008.12.001.

Changes in Research Objectives

Research Tasks 3-6, 8, 11, 12, and 14 were abandoned in favor of focusing intensively on Tasks 9 and 10 wherein transformational results were obtained, particularly in scalable thermally conductive coatings (see detailed text below).

Extensions Granted

A no cost extension was granted to extend the term of the award to 31 August 2011 from 15 January 2011.

New Discoveries

Our penultimate discovery in this project has been the development and application of organic dispersing aids (nanolatexes and triblock copolymers) and processes that stabilize waterborne dispersions of nanocarbon at concentrations 10-1000-fold greater than previously reported. By nanocarbon we refer to single wall carbon nanotubes (SWCNT), multiwall carbon nanotubes (MWCNT), graphene, and hydrothermal carbon (HTC). This success will put nanocarbon at the inventor's, formulator's, and manufacturer's fingertips at reasonable costs (limited by the nanocarbon cost). These transformational advances will be enabling for new generations of transparent conducting electrodes, for super capacitors, for battery and fuel cell membranes and electrodes, for printed conductors in printed electronics, and for conducting paints.

Our ultimate discovery was the demonstration of waterborne "paper coating" (we call templated coating) of waterborne MWCNT dispersions to produce the most highly thermally conducting man-made materials ever made outside of a vacuum chamber, with thermal conductivities in the range of 0.5-3 kW/m/K (the low to mid "diamond range"). This accomplishment, while not quite ready for the marketplace, represents a 1,000-fold advance over what is currently used in plastic electronics. Our processes can only be described as mid-20th century, but as such they can be scaled up effortlessly.

We also found that hydrothermal carbon can be formulated to easily be dispersed at the nanoscale and that it shares interesting optical absorption limits with graphene and carbon nanotubes. HTC is a sustainable resource that can be used for nanotechnology development in several areas, including indirect carbon fuel cells.

Although there were technical difficulties, we succeeded in producing ionic liquid-based monomers that gave us polymers that love to adsorb to nanocarbon. We devised a new family of triblock copolymers that exhibits thermoreversible gel formation on warming above a line of LSCTs (lower solution concentration temperatures). In addition to stabilizing nanocarbons in water, these triblocks will lead to new templated zeolites and new hybrid ceramic materials.

The best of these accomplishments would not have been realized if it were not for the kind hospitality and collaboration of Prof. Dr. Markus Antonietti during my 2008-2009 sabbatical in his department at the Max Planck Institute of Colloids and Interfaces, facilitated by Eastern Michigan University and this AFOSR Grant Award.

Patent Application

Archival publication #13 above, "Nanoparticle dispersions with ionic liquid-based stabilizers," is being actively being prosecuted. Here is the abstract:

The disclosure generally relates to a dispersion of nanoparticles in a liquid medium. The liquid medium is suitably water-based and further includes an ionic liquid-based stabilizer in the liquid

medium to stabilize the dispersion of nanoparticles therein. The stabilizer can be polymeric or monomeric and generally includes a moiety with at least one quaternary ammonium cation from a corresponding ionic liquid. The dispersion suitably can be formed by shearing or otherwise mixing a mixture/combination of its components. The dispersions can be used to form nanoparticle composite films upon drying or otherwise removing the liquid medium carrier, with the stabilizer providing a nanoparticle binder in the composite film. The films can be formed on essentially any desired substrate and can impart improved electrical conductivity and/or thermal conductivity properties to the substrate.

Contributing Personnel

John Texter (PI)

Laboratory Assistants: Rene Crombez

Postdoctoral Research Associates: Kejian Bian, Xiumin Ma, and Vivek Arjunan Vasantha

Graduate Students: Hong Gu, Beatrice Benhamida, Ninad Dixit, Nikhil Tambe, Nrupen Patel, Hua Jin, Jigneshbhai Ayar, Krishna Joshi, Manuela Zejnati,

Undergraduate Students: Joseph Byrom, David Ager, Rafael Maniglia

Uncompensated Collaborators: Markus Antonietti, MPI KG; Robert Campbell, Netzsch USA; Yousaf Elabd, Drexel University; Cristina Giordano, MPI KG; Masashi Kunitake, Kumomoto University; Admir Masic, MPI KG; Thomas Mourey, Eastman Kodak; Takashi Nakanishi, NIMS; Fernando Perez-Caballero, TU Berlin; Weidien Shen, EMU; Klaus Tauer, MPI KG; Mary-Magdalena Titirici, MPI KG; Feng Yan, Soochow University

Jamil Baghdachi (co-PI)

Graduate Students: Kirapat Pakjamsai, Chunlai Sun

Development of Porous Templates (Texter)

It is anticipated that porous templates can be infused with various organic and inorganic phases and components to produce films and bulk hybrid materials having diverse properties. In addition it is envisioned that some of such hybrid materials may be pyrolized or chemically treated to remove the organic template to produce an inverse hybrid material having pores in the spaces formerly occupied by the templating polymer.

Research Task 1

This task addresses the use of various chemical components and amounts to modify and control pore size and pore connectivity.

Some solvent effects on poration

A sample film of poly(ILBF4-co-MMA) produced by microemulsion polymerization was soaked in 0.1 M KPF$_6$ for 4 days to produce an opaque film as has been previously

documented. A freeze fracture surface of this film is illustrated in Fig. 1 (a) and (b). The image in Fig. 1(a) shows at low magnification many large pores in the 30-60 µm diameter range. The slightly higher magnification image in Fig. 1(b) shows these pores more clearly, and also a large number of much smaller pores, 3-5 µm in diameter, are seen along the orthogonal surface.

The process of soaking in toluene for 3 days results in the closing of the biggest pores as illustrated in Fig.(c) and (d). The largest pores are of the order of 10 µm or so. The smallest visible pores appear of the order 1 µm. Subsequent soaking in ethanol for 2 days, as illustrated in Fig. 1(e) and 1(f), appears to have closed the larger pores, with the largest visible being about 5 µm. Soaking in water for 2 days then appears in Figs. 1(g) and 1(h) to reopen the 40-50 µm pores as the most prominent with a subpopulation of 1-3 µm pores. The pore sizes here in Figs. 1(g) and 1(h) are essentially the same as seen in Figs. 1(a) and 1(b).

Ability to porate with AOT

Poly(IL-BF$_4$/MMA) transparent gel produced by microemulsion polymerization turned opaque after being subjected to ion-exchange for 4 days in saturated AOT aqueous solution (saturation concentration in water is approximately 1 w/w) and the resulting opaque film was softer than the membrane ion-exchanged in 0.1 M KPF$_6$ aqueous solution. In this experiment, the bis(2-ethylhexyl)sulfosuccinate anion exchanges with the tetrafluorborate anion.
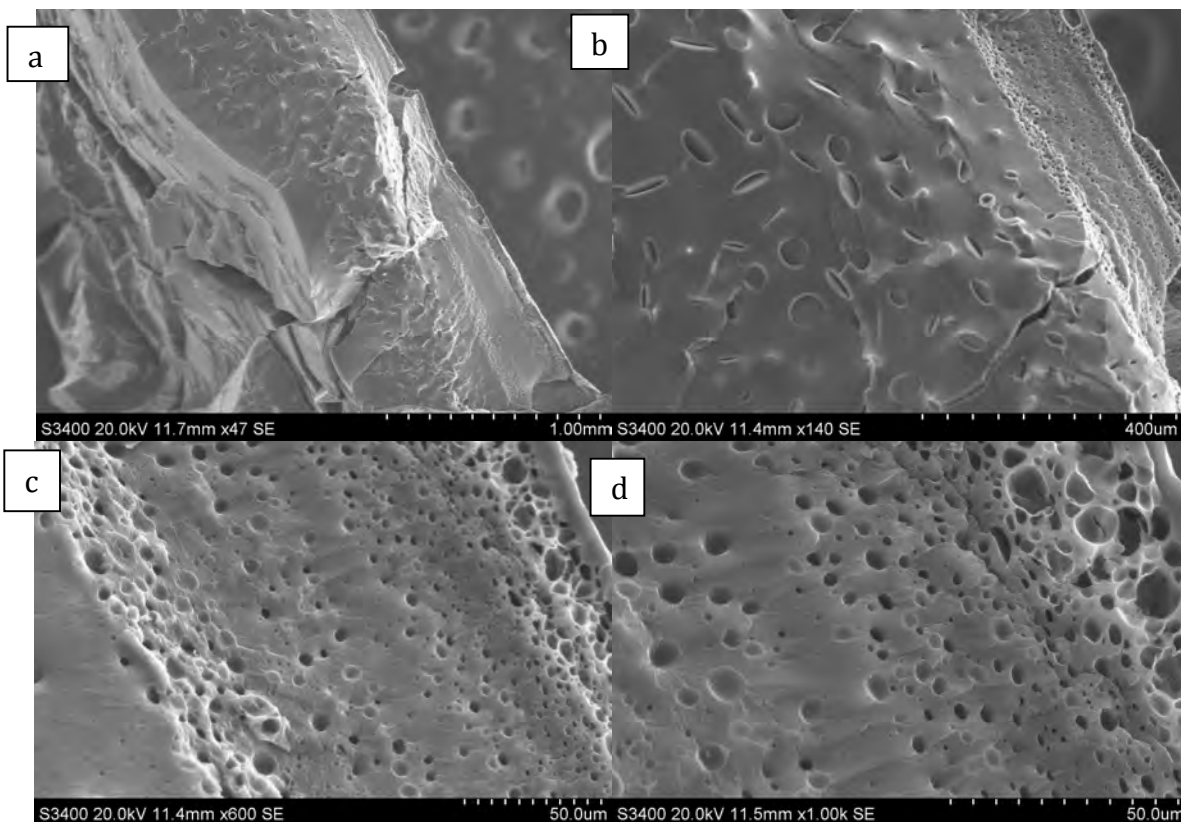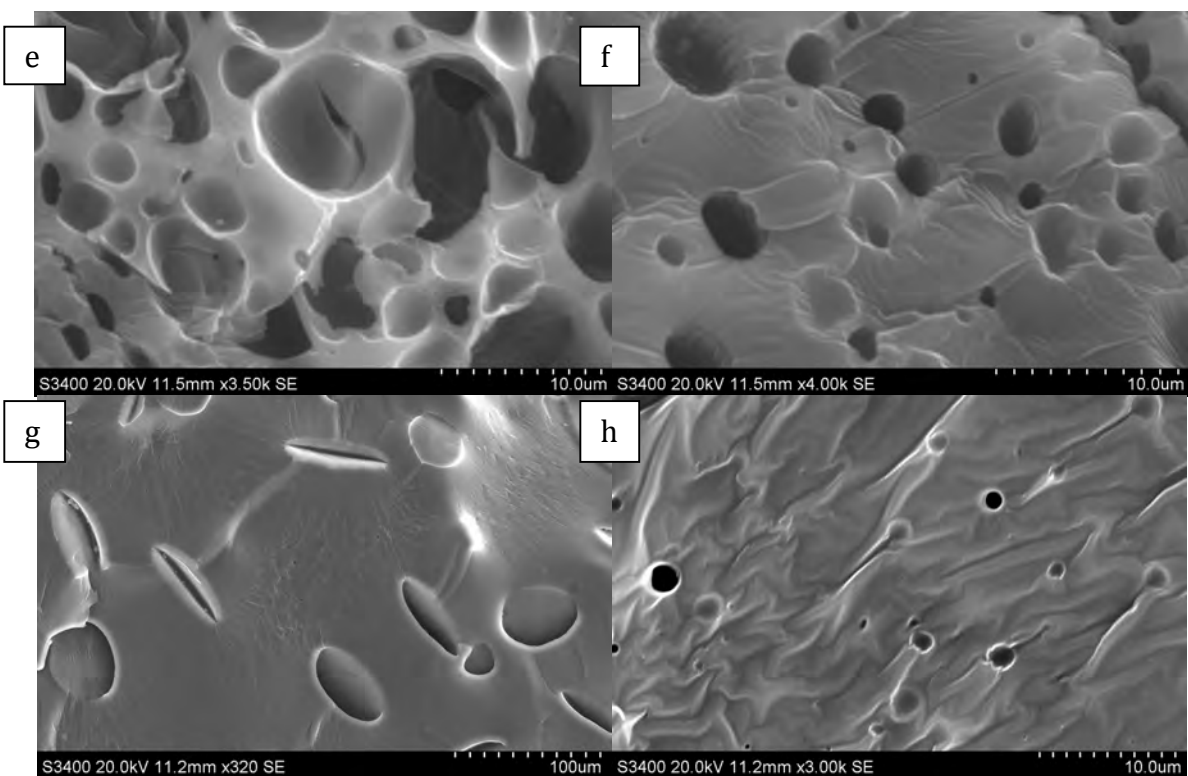
Figure 1. SEM of freeze fracture surfaces of poly(ILBF$_4$-*co*-MMA) gel film sequentially soaked in (a,b) aqueous 0.1M KPF$_6$ for 5 days; (c,d) toluene for 3 days; (e,f) ethanol for 2 days; (g,h) water for 2 days.
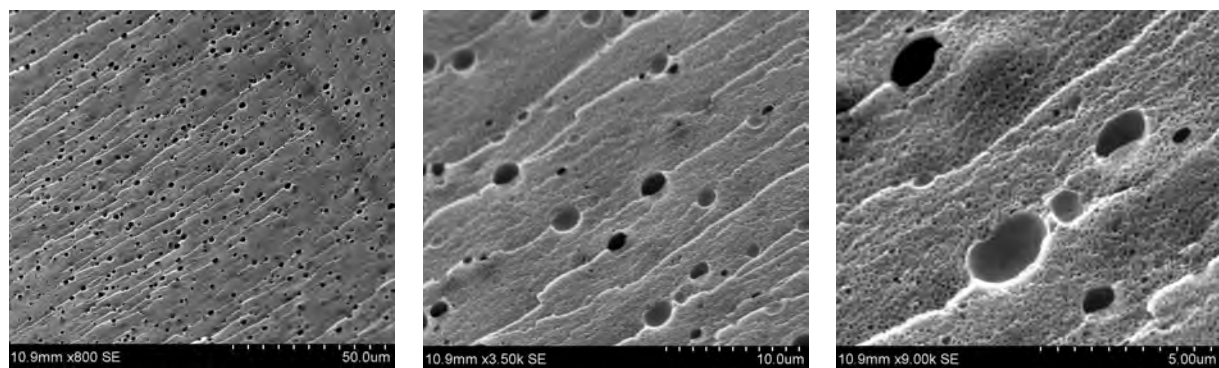
Figure 2. SEM at increasing magnification (left to right) of freeze fracture surface of poly(ILBF$_4$-*co*-MMA) gel film soaked in saturated AOT for about 10 days.

The pore structure revealed at the fracture surface examined in Fig. 2 appears bimodal. At lower magnification there appears to be a uniform number of large pores of approximately 2 µm diameter. At higher magnification a very large number of pores about 100 nm in diameter are evident.

Besides this distinctive bimodal pore structure, it appeared that this AOT exchanged material was appreciably softer than the hexafluorophosphate exchanged materials.

Nanolatex formation of porous coatings

Overview. A new class of ultrastable latexes based on copolymers of reactive ionic liquid surfactants is synthesized and characterized by various methods. These latexes are produced by microemulsion polymerization to yield ultrastable dispersions of nanometer length scale particles. Aqueous coating of these latexes dry to form robust films that exhibit elastic thermomechanical properties typical of rubbers. The nature of the reactive ionic liquid surfactant monomers induces an ion exchange capacity in the resulting copolymers. Transparent films of such latexes can be reversibly transformed into opaque and porous films by simple ion exchange treatments (washes) and by solvent treatments. Taking advantage of these characteristics, superprimers have been prepared which exhibit excellent substrate and top coat adhesion for waterborne as well as solvent borne top coats. High adhesion is obtained from the electrostatic nature of the copolymeric backbone and from the variable porosity that can be induced for particular applications. When used as conventional waterborne binders, these nanolatexes provide enhanced durability.

Introduction

Primer coatings are primarily designed to facilitate adhesion of an overcoat (often a topcoat) onto a given substrate. Design features usually include wetting and interfacial energy considerations that influence the type and properties of added surfactants and solvents, and the type and functionality of the binder used. These interactions usually are fundamentally based on dispersion and van der Waals interactions and have been very thoroughly analyzed and discussed. Electrostatics considerations in coatings have largely been restricted to electrodeposition and to electrospray processing. More recently, layer-by-layer assembly methods based upon electrostatics provide Ångstrom-level thickness control as oppositely charged polyelectrolytes are used to construct coatings, capsules, and free standing films.

The feature and performance driven incorporation of various kinds of pigments and additives in primer coatings is an important secondary design feature. Pigments imparting opacity, corrosion protection, color and electrical conductivity are some of the more important pigment classes often used in primers.

Porosity in coatings has been found useful in diverse applications including anticorrosion treatments [1], antislip coatings [2], perfumed coatings [3], and antireflective coatings [4,5]. Porosity in subcoats is also a well known approach to improving intercoat adhesion, through higher intercoat surface area provided by the overcoat curing after penetrating the subcoat's pores.

In this study we develop a polycationic-based copolymeric nanolatex for binding to a wide variety of substrates, including metals, plastics, and wood, that is also highly adhesive to a wide spectrum of topcoat formulations, both solventborne and waterborne. We show also that pigmented primers derived form these nanolatexes can be treated post coating to

produce poration for light scattering and adhesion modification. Further, we demonstrate an advanced materials application involving a novel carbon nanotube (CNT) waterborne primer.

Latex Synthesis and Characterization

Our nanolatexes are prepared via microemulsion polymerization, a special type of dispersion polymerization, from aqueous acrylate/methacrylate microemulsions stabilized by reactive ionic liquid surfactants. To exemplify our process we use methylmethacrylate (MMA) as a comonomer along with the ionic liquid reactive acrylate surfactant 1-(2-acryloyloxyundecyl)-3-methylimidazolium bromide (IL-Br) to compose the nanolatex dispersion. Ionic liquids are defined as salts, mostly organic, that melt below 100°C; IL-Br melts at about 50°C.

IL-Br
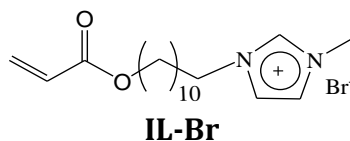
Microemulsion polymerization. A partial ternary phase diagram of this system is illustrated in Fig. 3, where the composition for microemulsion polymerization we utilize is indicated by the "✕". The microemulsion domain is a thermodynamically stable and somewhat exotic single phase solution. In the illustrated domain, MMA swollen micelles of IL-Br are the most prevalent complexes, although irregular bicontinuous microstructure exists at some of the higher surfactant levels.
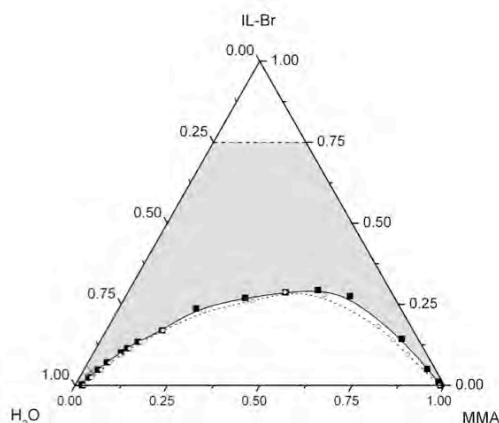
Figure 2. Partial ternary phase diagram of water, MMA, and IL-Br illustrate segments of the single phase microemulsion domain and the multiphase emulsion domain. The boundary between these two domains is essentially the same at 25 and 60°C. The small "✕" marks the 0.040/0.027.0.933 IL-Br-MMA-water composition (very near lower left corner) of the microemulsion prior to polymerization.

Nanolatexes in this system were first reported [6] by Yan and Texter at the 0.07/0.07.0.86 IL-Br-MMA-water composition. These latexes were about 40 nm in diameter and were found to be superstable! By superstable we mean that they appear *immune to coagulation* by indifferent salt (or by elimination of the Debye-Hückel screening layer). In this study we produced latexes at the composition ✕ indicated in Fig. 3. We have observed that such nanolatexes can be coagulated only by specific interaction between various anions (Br⁻, BF₄⁻, PF₆⁻) and the imidazolium moiety in the copolymers produced. Coagulation by Br⁻ occurs only after the [Br⁻] exceeds about 0.2 M!

The nanolatex samples were dialyzed using 12,000 molecular weight cut off dialysis tubing against deionized (DI) water for 3 days in order to remove any unreacted monomer before they were analyzed for stability in aqueous NaBr solutions. First the lowest concentration of NaBr solution which caused the nanolatex to destabilize and agglomerate was determined as 0.21 ± 0.06 M by visually observing the addition of small quantities of nanolatex suspension to solutions of varying NaBr concentration. Then a dilution series of aqueous NaBr was prepared. In each dilution an equal amount of dialyzed nanolatex was added and the resulting solution was observed for turbidity visually and then at 800 nm. These data are presented in Fig. 4. We take the midpoint of the rising curve as the concentration needed to destabilize the dispersion. The maximum is reached and then the curve falls off; this fall off is due to extremely large agglomerates being formed at the higher concentrations, where these agglomerates quickly settle to the bottom of the cell, and no longer contribute to the apparent turbidity.
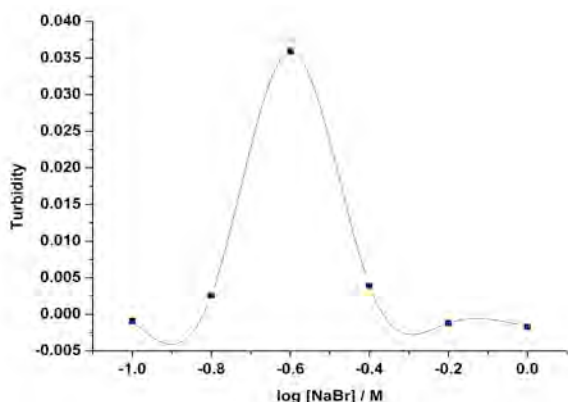

Figure 4. Turbidity of nanolatex dispersions at different aqueous NaBr concentrations as determined by absorbance at 800 nm.

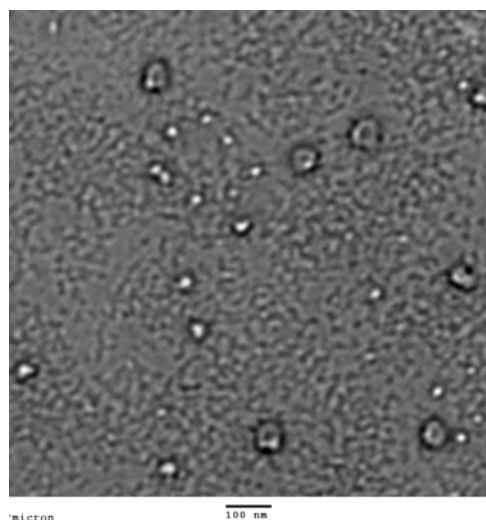**Figure 5. TEM image of 4% IL-Br content nanolatex polymerized at 0.040/0.027.0.933 IL-Br-MMA-water composition; 1,000-fold dilution; scale bar is 100 nm.**

Latexes produced at this more dilute composition are about 25 nm in diameter as measured by photon correlation spectroscopy and about 22-28 nm in diameter as perceived in micrographs obtained by transmission microscopy. An example image is

illustrated in Fig. 5. Most prominent are some larger clusters that have polymerized together, but the largest number fraction are the individual particles. These individual particles appear to be undergoing film formation by the process of coalescence on the TEM grid. These latexes are only 6.67% solids. For most of our work we concentrated these polymerized latexes by ulrafiltration to 15-26% solids (w/w).

Primer Formulation and Coatings

Primer clearcoat. Some 20% (w/w) solids nanolatexes obtained by microemulsion polymerization and subsequent ultrafiltration were used "as is" for applications where clearcoat priming was made. This concentrated nanolatex was applied on microscope slides (draw down applicator) to yield 150 µm wet film thicknesses. These films were allowed to dry and coalesce overnight to yield dry film thicknesses of 30-35 µm (1.2-1.6 mil).

Preparation of pigment dispersion. Titanium dioxide-based pigment dispersions were prepared in water. Appropriate amounts of deionized (DI) water (150 g) and wetting and dispersing agent (BYK 333; 1.5 g) were taken in a metal container. Flash rust inhibitor (BYK 181; 900 mg) was added at about 0.1% of total weight for dispersions used to prime steel, and the mixture was mixed at moderate speed using a high speed disperser (HSD). Priming and anticorrosion results on steel will be presented elsewhere. TiO_2 pigment (DuPont R-902; 300 g) was then added under stirring. After addition of pigment, grinding was done with a HSD for 3-4 h. This processing yielded a fineness of grind of 7 (Hegman gauge).

Preparation of pigmented primer. To 81.1 parts of 20% nanolatex (above) was added 18.9 parts titania dispersion (60% in water). This mixture was stirred for 45 minutes to 1 h using a magnetic stirrer, and resulted in a pigment to binder weight ratio of 0.7 and a pigment to binder volume ratio 0.18. This volume ratio corresponds to a (pigment volume concentration) PVC of ~16%. This pigmented primer was applied to aluminum (3003 h-14; bare mill finish), plastic (ABS), and wood (R 1D birch plywood) panels using an automatic draw down applicator to produce films having a wet thickness of about 150-200 µm. After application the films were allowed to dry and coalesce at room temperature overnight to produce films about 16-35 µm thick see cross-cut adhesion discussion).

Comparison of Elasticity with Commercial Latexes

The elasticity of a polymer film is generally obtained by measuring Young's modulus. This was done by doing isothermal stress-strain analyses using a TA Instruments Q800 Dynamical Mechanical Analyzer with a thin film clamp on dried films of concentrated nanolatex and on similar films of commercial latexes (Dow Chemical, Rohm and Haas) selected for comparison. The films were prepared using a Teflon mold to facilitate film removal. The latex dispersions were placed and leveled in these molds and allowed to coalesce and dry for 5 days. The films were then peeled out of the mold and cut to 20 mm x 5 mm dimension for analysis at 25°C.
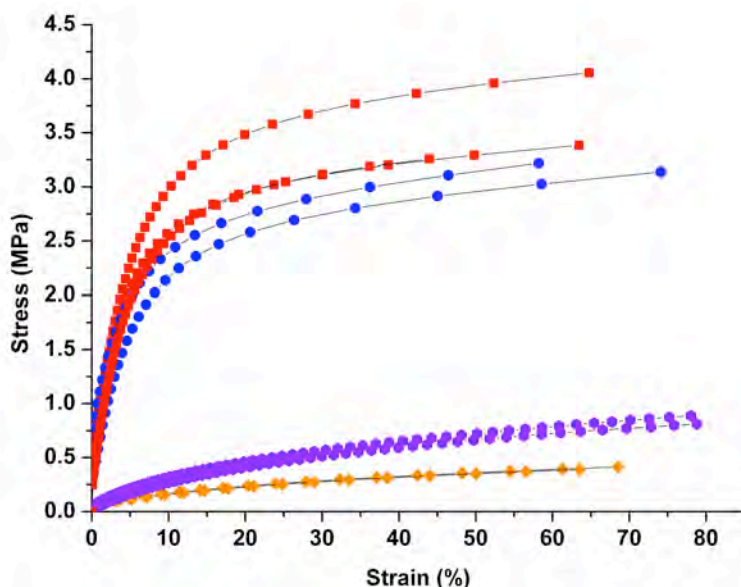
Figure 6. Isothermal (25°C) stress strain curves for p(IL-Br/MMA) films (■,●) and for two comparison films derived from Commercial Latexes 1 (●) and 2 (◆).

Some example curves are illustrated in Fig. 6 for duplicate samples of duplicate nanolatex films and for latex films of Commercial Latexes 1 and 2. It appears all of the films break in the 65-80% strain interval. The films from the nanolatexes of this study appear much more resilient than those from these two commercial latexes. The elasticity of the films is measured by extracting Young's modulus from these data as the initial slope of these curves in the limit of zero strain.

Table 1. Young's modulus measurements and latex properties

Latex type	Young's Modulus (MPa)	Particle Size (nm)	Monomers
Nanolatex	50.5 ± 1.8	25	IL-Br/MMA
Commercial Latex 1	1.41 ± 0.03	297	Vinyl/Acrylic
Commercial Latex 2	4.0 ± 1.8	322	Vinyl/Acrylic
Commercial Latex 3	2.0 ± 0.6	256	Vinyl/Acrylic
Commercial Latex 4	1.4 ± 0.2	237	Styrene, Butyl Acrylate/Acrylonitrile
Commercial Latex 5	140 ± 16	990	Styrene, Butyl Acrylate/Styrenated Polymer/Polyalkylene Glycol

Table 1 lists Young's modulus results for all of the comparison commercial latex films, the size weighted particle size as measured by photon correlation spectroscopy, and the basic monomer/chemical make up of the latex/polymer. We see that the results for our nanolatex films are dramatically more robust than all of the commercial latex films except for Latex 5, wherein the emulsion polymer is just one of three diverse polymers incorporated in the "latex" (see below). A higher Young's modulus means that initial deformations are resisted with a higher "spring constant" and that higher energies are absorbed reversibly during small deformations. The stress strain relationships deviate from linearity in each case, and the integral of these curves out to the strain at break gives the total energy per unit area absorbed at film rupture. Commercial Latex 4 is marketed specifically for aluminum substrate applications. Commercial Latex 5 is marketed for difficult to adhere substrates and is a mixture also comprising a styrenated polymer and a polyalkylene glycol.

Primer Poration

Nanolatex film poration. These dry films were then exposed to aqueous 0.1 M KPF_6 solution for time intervals varying from 1 min, 10 min to 48 h. After exposure the films were washed in DI water and dried. Their turbidity was then measured using a Jasco UV/Vis spectrophotometer at 800 nm by measuring the absorbance, A_{800}, relative to an uncoated microscope slide control in the reference beam. The copolymer has no intrinsic absorbance at 800 nm, so this measure is a good measure of turbidity. The repeat curves illustrated in Fig. 7(left) show that there appears to be an induction period of about 2-4 h where the turbidity increases slowly. After this time the turbidity appears to increase more rapidly over the 40 h test period. Since the turbidity appears not to have saturated, we surmise that maximum poration is achieved only at longer treatment times.
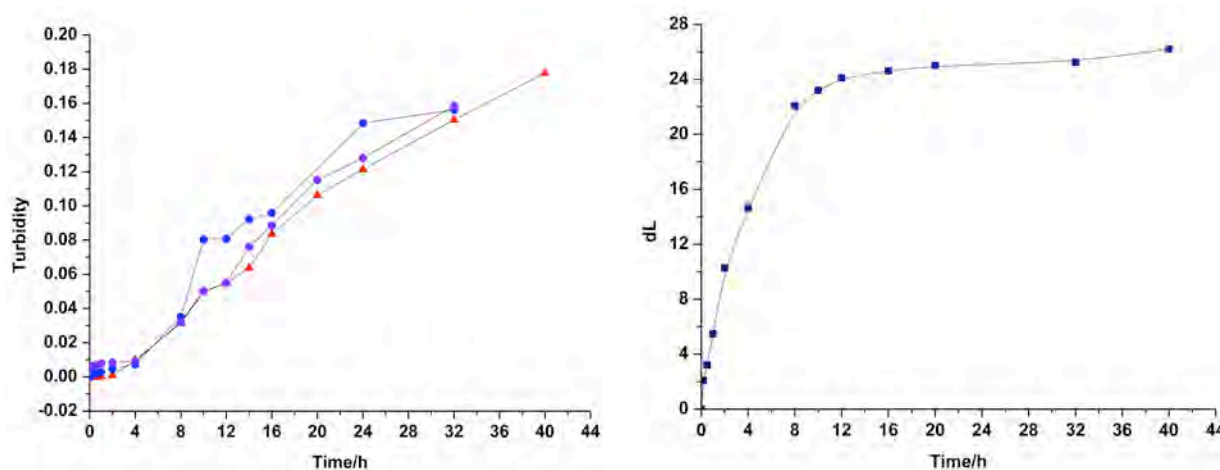

Figure 7. (left) Turbidity @ 800 nm and (right) lightness (dL) as a function of exposure time to aqueous 0.1 M KPF_6 solution for IL-Br latex film on (left) glass and (right) aluminum.

The change in lightness values with increasing PVC is often used as a measure for determining the Critical Pigment Volume Concentration (CPVC) in latex based paints and

other waterborne systems. In order to analyze the effect of poration on dL values, films of IL-Br latex were applied on aluminum panels by an automatic draw down applicator to produce a WFT of 200 μm. The films were then allowed to dry and coalesce overnight and then they were exposed to aqueous 0.1 M KPF$_6$ for various time intervals as indicated in earlier experiments. After exposure, all the films were washed with DI water and allowed to dry overnight. The lightness value for the first film which was exposed to KPF$_6$ for 1 min was considered as a standard and changes in lightness values for all other films was determined against the first film as a standard. The lightness values were measured using a portable BYK Gardner Color-guide (45°/0°). The results are presented in Fig. 7-right where it is seen that qualitatively different behavior is obtained by this *reflectance* technique in comparison to the data of Fig. 5-left.

From the data on each side of Fig. 7 we can conclude that the initial poration is localized on the surface and that the proportion of light scattered and transmitted *forward* (Fig. 7-left) into the detector decreases only slightly over the 0-4 h exposure interval, while the dL values indicate the light scattered backwards increases steadily over this same time interval. This is consistent with the main changes being confined to the top surface of the coatings at early exposure times. As poration increases with further exposure, the transmittance steadily decreases, but the reflectance appears to reach an asymptotic limiting value at about 12-20 h exposure. This result means that the reflectance or incident surface poration is fully porated in this 12-20 h interval, as the back scattering does not increase thereafter, even though the bulk poration appears to be still increasing at 40 h exposure. This lightness limiting value may also be instrumentally limited, as stray light may prevent higher lightness values being registered; this is a common limitation of reflectance measurements made in ambient light.

SEM of similarly treated coated films, where the films have been removed from the slide substrate and freeze fractured (liquid nitrogen) so that the poration could be examined in cross-section. Poration after 8 h is not particularly evident in Fig. 8(a), except there is an indication of surface roughening (not the fracture surface of the cross-section but the top surface visible "below" the cross-section). After 16 h (Fig. 8(b)) the top surface appears to be more rough, but not much is evident in the cross-section. After 24 h, Fig. 8(c), we see distinct pores penetrating normal to the film surface in the cross-section. And finally after 48 h as we see in Fig. 8(d), the poration is extensive.
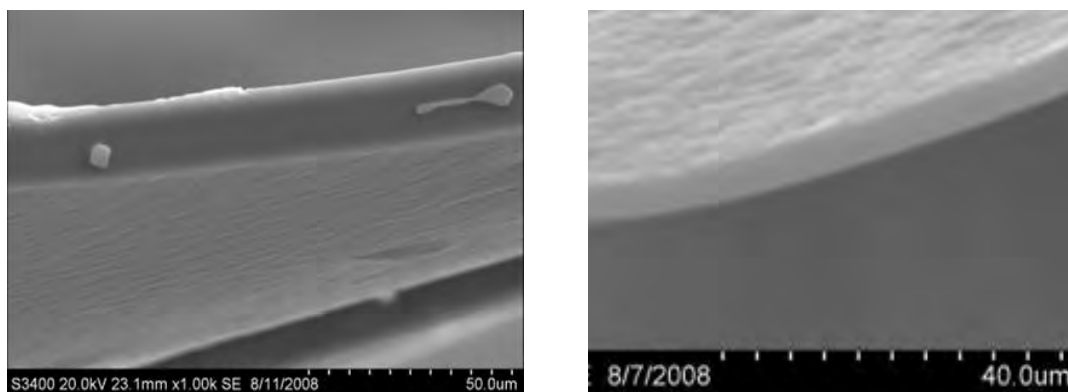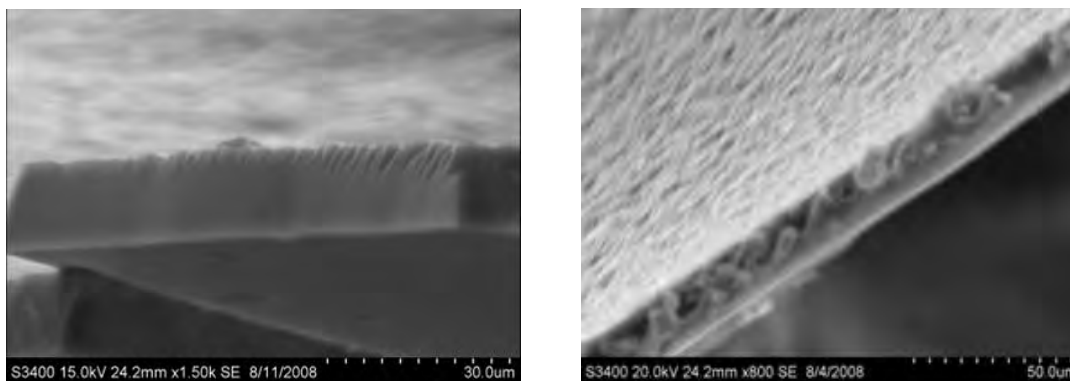
Figure 8. SEM of freeze fractured surfaces of nanolatex membrane coatings after aqueous 0.1 M KPF$_6$ treatment for (a) 8 h; (b) 16 h; (c) 24 h; (d) 48 h. Where pores are evident it must be kept in mind that their connectivity to the "missing halves" of the fracture surfaces is not known.

Adhesion to Various Substrates

Nanolatex film (clearcoat) adhesion to aluminum. Substrate adhesion was investigated by painting a film of each latex on flat mill base aluminum, allowing the film to cure for 5 days, and then administering the tests. Latex film-aluminum cross-cut adhesion, conical mandrel flexibility (1/32" diameter fold), and MEK double rub results are listed in Table 2, where we also list the glass transition temperatures for the different latexes.

We see that none of the standard commercial latexes adhere to aluminum; commercial latex 4 was engineered to bind to aluminum; commercial latex 5 is a mixture of latex and two polymeric binders. All of the latexes passed the conical mandrel test; each has a T$_g$ lower than our nanolatex and is in the rubbery state at room temperature where the test was done. The solids content of each of the commercial latexes was in the range of 50-55%, while that of the nanolatex was not quite 20%, so the DFT obtained were 2-fold or more greater than the nanolatex for each of the commercial latexes. The MEK double rub results for our nanolatex and the first three commercial latexes are essentially the same, while the nanolatex film was only about 35% as thick. The results for commercial latexes 4 and 5 are about 3-fold higher than for the nanolatex films, as also are their DFTs.

Table 2. Comparison of nanolatex clearcoat film properties on aluminum with commercial latexes.

Latex Film	T$_g$ (°C)	Cross Cut Adhesion	Conical Mandrel Flexibility (1/32")	MEK Double Rub
Nanolatex	13-16	5 B	Pass	15-16
Commercial Latex 1	4-5	Fail	Pass	12

Commercial Latex 2	3-4	Fail	Pass	15-14
Commercial Latex3	3-4	Fail	Pass	14
Commercial Latex 4	1-2	5B	Pass	42
Commercial Latex 5	-3	5B	Pass	51

Latex as a sealer. We applied our most concentrated nanolatex (26% solids) on a wood panel to evaluate it as a sealer. We allowed the film to dry overnight and then we lightly sanded it to make the surface smooth. Then we applied nanolatex based primer on the wood panel. A cross-cut adhesion value of 5B was obtained, indicating good adhesion resulted at the sealer-wood and primer-sealer interfaces.

Effects of poration on adhesion. If the porosity of a coated film is very high, as may be the case when the coating is formulated near its PVC or in excess of its CPVC, the mechanical properties will deteriorate when porosity increases beyond certain limits which depend on the CPVC for that coating, or more properly (since poration can be independent of PVC and CPVC) when the porosity exceeds a certain limit.

While these p(IL-Br/MMA) nanolatexes have an inherent capability of forming porous structures, the extent of poration varies with exposure to KPF_6 solution. In order to better understand the mechanical limitations of such nanolatexes when used as porous primers and coatings, we examined how the time of exposure to KPF_6 solution affects the adhesion of (pigment free) nanolatex films without an overcoat and the adhesion of pigmented nanolatex primer with an overcoat. We used a commercial waterborne latex (**Flat-L**) to make the overcoat by brushing. Nanolatex films, clear primer coats, were applied on aluminum substrate using an automatic draw down applicator to produce a WFT of 200 μm and a DFT of about 30-40 μm. The films were exposed to aqueous 0.1 M KPF_6 for various time intervals, rinsed, and dried. The samples primed with pigmented nanolatex were then overcoated with **Flat-L** and dried for an additional day. The coatings were then analyzed for cross-cut adhesion.

Adhesion results are summarized in Fig. 9-left for the nanolatex clearcoat primer without an overcoat and in Fig. 9-right for our pigmented nanolatex primer coating overcoated with **Flat-L**. The porated clearcoat without overcoat exhibits excellent adhesion with up to 4h exposure. At 8h the adhesion decreases somewhat and at 10h it decreases further, where it plateaus through 32h exposure. At 48h exposure the coating fails completely.

An overcoat is expected to of course fill the pores created by the poration treatment, and the resulting adhesion is more or less an open question and must be investigated for each topcoat of interest. In this system with **Flat-L**, we see that the poration created through 10h exposure, causes no degradation after overcoating, where a 5B rating is preserved. Additionally, the 1B ratings obtained in the absence of an overcoat with 12h and 16h

poration, respectively, are improved to ratings of 4B and 2N as a result of pore filling with the **Flat-L** overcoat.

In each and every case of failure or partial failure, delamination at the primer-substrate interface was the type of failure observed, and there was no intercoat adhesion failure observed. Several reasons for failure are possible: extensive poration simply weakens the adhesion to the substrate by decreasing the contact area (pores penetrate to the substrate) with overcoat failing to penetrate and fill all of the pores formed; the overcoat fills all or most of the pores, but in penetrating to the substrate no gain is realized in adhesion of the overcoat itself has poor adhesion to the substrate (the basic reason for using a primer, and a scenario where too much poration is deleterious and destroys the mechanical and cohesive integrity of the bulk primer layer.
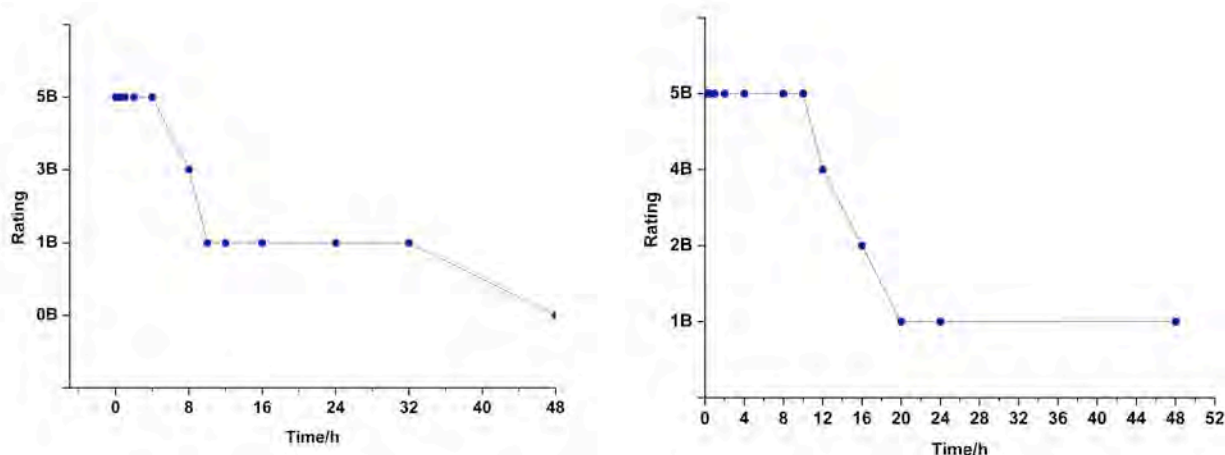
Figure 9. Cross cut adhesion of (left) nanolatex clearcoat primer on aluminum substrate without an overcoat and (right) pigmented nanolatex primer with a waterborne latex (Flat-L) overcoat after pretreatment exposures of the primer layers to aqueous 0.1 M KPF$_6$.

Topcoat adhesion. To evaluate topcoat adhesion to our nanolatex-based primer we chose five diverse types of topcoats manufactured by RustOLeum, Behr Paints, Benjamin Moore Paints, and Sherwin Williams. These products were selected for their diverse formulations and curing chemistries. A solventborne enamel that cures via oxidative polymerization in air (**Enamel**), a waterborne flat latex that cures by coalescing while air drying (**Flat-L**), a 2K waterborne acrylic-epoxy (**A-Epoxy**) that cures by cross-linking (parts A and B combined at equal volume), a solventborne urethane-alkyd that cures by oxidative polymerization (**U-Alkyd**), and a 2K high solids epoxy (**HS-Epoxy**) that cures by cross-linking (parts A and B mixed at 4:1 volume ratio)) were chosen for our tests.

Results for the adhesion of these topcoats on bare substrate, on the substrate coated with our pigmented nanolatex-based primer, and on the same nanolatex-based primer after treatment with aqueous 0.1 M KPF$_6$ are illustrated in Table 3. The thicknesses of the nanolatex primer coats on aluminum, plastic, and wood were, respectively, 35 μm, 25 μm, and 16 μm. The significantly lower thickness obtained on wood, we believe, was due to

Table 3. Topcoat cross-cut adhesion/thickness (µm) results for nanolatex-based pigmented primer on aluminum, plastic, and wood substrates

Topcoat	Aluminum			Plastic			Wood	
	Bare	Primer	Primer + KPF$_6$	Bare	Primer	Primer + KPF$_6$	Bare	Primer
Enamel	5B/45	5B/58	5B/60	5B/13	5B/18	5B/22	5B/15	5B/13
Flat-L	Fail/50	5B/78	5B/65	1B/33	3B/28	5B/32	5B/12	5B/20
A-Epoxy	5B/27	5B/47	5B/63	Fail/17	5B/33	Fail/32	5B/15	5B/14
U-Alkyd	5B/63	5B/60	5B/62	5B/16	5B/26	5B/26	5B/6	5B/16
HS-Epoxy	5B/162	5B/156	5B/152	5B/35	5B/44	5B/41	5B/23	5B/21

sorption of the nanolatex by the unsealed substrate. The purpose of the treatment with aqueous 0.1 M KPF$_6$ was to lightly porate the nanolatex primer and increase the intercoat adhesion. The test panels were dipped in the aqueous KPF$_6$ for 4 h, rinsed with DI water for 30 s, and then dried over night. All of the topcoats were applied by brush and then allowed to cure for 7-8 days before being tested for adhesion. The very low thicknesses measured on wood are a consequence of the wood not being sealed, as was mentioned earlier in the case of the primer application.

The performance of our latex-based primer appears excellent for 23 of the 25 pigmented nanolatex primer-topcoat combinations investigated. The single failure with the **A-Epoxy** on the porated primer is ascribed to dimensional instability induced by the high solvent loading in the **A-Epoxy**. In this failure the coating delaminated at the primer-substrate interface. Less severe was the partial adhesion failure of the **Flat-L** on the untreated latex primer. Improved **Flat-L** adhesion was obtained with the use of our slightly porated nanolatex primer.

Conical mandrel (1/32" radius) test results for these topcoats on aluminum are listed in Table 4. High flexibility is demonstrated for 7 of the 10 primer-topcoat combinations. In the three cases of failure (with primer), failure occurred at the primer-substrate interface rather than at the topcoat-primer interface. We are uncertain about the failure mechanism for the **U-Alkyd** in the porated primer. We believe the **HS-Epoxy** failures are mainly due to its brittleness from its high crosslink density.

Table 4. Topcoat conical mandrel results for pigmented nanolatex primers on aluminum

Topcoat	Substrate Treatment		
	Bare	Primer	Primer + KPF$_6$
Enamel	Pass	Pass	Pass
Flat L	Pass	Pass	Pass
A-Epoxy	Pass	Pass	Pass

U-Alkyd	**Pass**	**Pass**	**Fail**
HS-Epoxy	**Fail**	**Fail**	**Fail**

Advanced Materials Applications

In addition to various conventional and porous primer applications described above, the inclusion of specialty pigments and other materials represent an important new class of applications. Here we illustrate the preparation [7] of a highly stable waterborne single-wall carbon nanotube (SW CNT) dispersion. The CNTs were obtained from Aldrich and cleaned with nitric acid to reduce the metallic catalyst content. The CNTs formed tight bundles and had the consistency of a hard powder. The nanolatex was added to a vial containing the CNTs and subjected to sonication, and this treatment resulted in nearly complete dispersion of the SW CNTs. The stability was tested over a 6 week period, during which partial evaporation occurred but there was no sedimentation or visible phase separation. The lost water was added back, sonicated briefly, and the now low viscosity suspension was poured into a yellow polypropylene centrifuge cap, of the type illustrated in Fig. 10. The suspension filled the annular dish in the bottom of the cap, and overnight the suspension dried forming a shiny black film on the bottom of the dish and leaving a shiny black film on the inside walls of the dish. After two more days of drying at room temperature, the casting had the appearance illustrated in Fig. 10. The plastic surface was not strongly wetted by the suspension, but use of a copper wire to move the sessile drop around the dish resulted in full wetting. It is particularly noteworthy that during the drying and coalescence process, the plastic was not dewetted, and dry shiny films were obtained on all surfaces wetted.
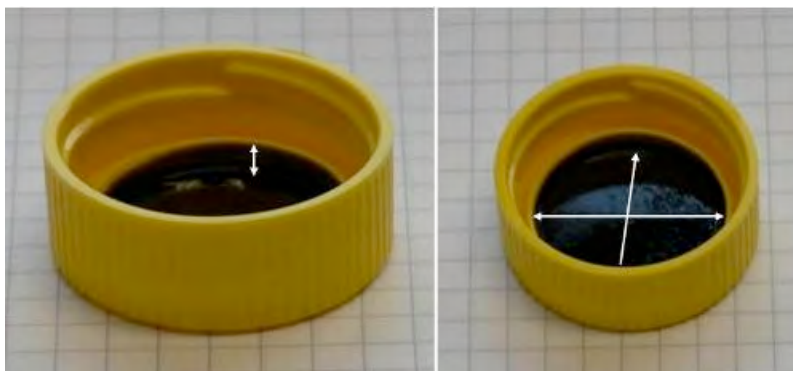
Figure 10. CNT latex film prepared by casting in annular dish in bottom of centrifuge tube cap. The height of the annular ring seen on the left and on the right is 2.6 mm. The diameter was 0.24 cm.

Conclusions

These p(IL-Br/MMA) nanolatexes are ultra stable because of the ionic liquid nature of the surfactant used as a co-monomer and because they show excellent stability in concentrated salt solutions. The surfactant cannot migrate disproportionately to the surface jeopardizing

the film interfacial energy properties which commonly occurs in conventional latexes. This nanolatex also does not need any coalescing agent for film formation. These nanolatexes produce films that have rubber like mechanical properties as shown by the stress-strain analysis and that are much, much tougher than commercially available latex films. These nanolatexes show excellent adhesion on aluminum, wood, and plastic.

We term these nanolatex-based primers, superprimers, because of the very high stability against coagulation they exhibit in high salt, and because of the high adhesion they offer on aluminum, plastic, and wood, and for the adhesion they offer to a diverse array of topcoats. The mechanical elasticity, as expressed by the Young's modulus results, far surpasses all of the regular commercial latexes by over an order of magnitude! The sources for these adhesion and mechanical effects will bear further study. There undoubtedly is an electrostatic effect in certain cases because of the cationic backbone charge of the nanolatex copolymer. However, the excellent results obtained with the CNTs suggest, as was observed by Someya et al. that the imidazolium group or imidazolium-bromide ion-pair exhibit some kind of attractive polarizability effect. We appear to see this also in the demonstrated adhesion to ABS (Table 3) and to the polypropylene centrifuge cap (Fig. 10).

References

1   Lamaka, S.V.; Zheludkevich, M.L.; Yasakau, K.A.; Montemor, M.F.; Cecilio, P.; Ferreira, M.G.S. (2006) *Electrochem. Comm*. **8**, 421-428.
2   Ishikawa, Y. (2002) Japanese Patent document: JP 2002-90838 20020328.
3   Kassner, H.; Siegert, R.; Hathiramani, D.; Vassen, R.; Stoever, D. (2008) *J. Thermal Spray Tech.* **17**, 115.-123.
4   Edwards, M.O.M.; Andersson, M.; Gruszecki, T.; Pettersson, H.; Thunman, R.; Thuraisingham, G.; Vestling, L.; Hagfeldt, A. (2004) *J. Electroanal. Chem*. **565**, 175–184.
5   Biswas, P.K.; Sujatha Devi, P.; Chakraborty, P.K.; Chatterjee, A.; Ganguli, D. (2003) *J. Mater. Sci. Lett.* **22**, 2003, 181– 183
6   Yan, F.; Texter, J. (2006) *Chem. Commun*. 2696-2698.
7   Antionetti, A.; Tambe, N.; Texter, J.; Nakanishi, T. (2009) to be published.
8   Sekitani, T.; Noguchi, Y.; Hata, K.; Fukushima, T.; Aida, T.; Someya, T. (2008) *Science* **321**, 1468-1472.

Di-stimuli responsive diblocks

Core–shell reversible particle precipitation from aqueous di-stimuli-responsive diblocks is demonstrated as also is the interconversion from one core–shell combination to the other. Results are given in Archival publication Nos. 2 and 4. The electronic supplementary information (ESI) for publication No. 2 may be found at the following link:

http://www.rsc.org/suppdata/cc/b9/b912148j/b912148j.pdf
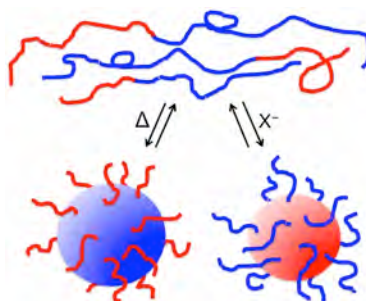
See Fig. 1 below for graphical abstract:

Figure 1. **Cartoon illustrating reversible condensation of particles from di-stimuli responsive diblocks to produce (left) poly(NIPAM) core nanoparticles on heating or (right) poly(ILBr) core nanoparticles on addition of excess bromide.**

Stimuli Responsive Block Copolymers

Poly(ILBr)

Initial attempts to make poly(ILBr) by ATRP resulted in two publications, a Chemical Communication and a longer paper in Langmuir.
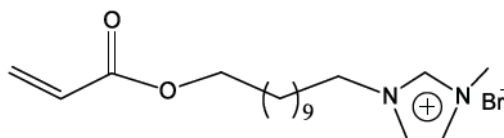
ILBr

The brief abstract for this Chemical Communication, archival publication No. 13, is given here:

Thin films of a stimuli-responsive homopolymer dewet as a stimulus response after anion exchange of the imidazolium's counter anion. Contact angle analysis and interfacial energy considerations indicate dewetting goes counter to increasing spreading coefficient. Intrafilm stress arising from structural relaxation drives the dewetting.

The electronic supplementary information (ESI) for publication No. 13 may be found at the following link:

http://www.rsc.org/suppdata/cc/c1/c1cc12656c/ c1cc12656c.pdf

See Fig. 1 below for graphical abstract:

Figure 1. Anion exchange stimuli induced dewetting via stress relaxation.

The brief abstract for this Langmuir, archival publication No. 11, is given here:

A stimuli-responsive homopolymer poly(ILBr) is fabricated via a "two-phase" atom transfer radical polymerization (ATRP) process, where ILBr stands for the reactive ionic liquid surfactant, 1-[11-acryloylundecyl]-3-methyl-imidazolium bromide. An extraordinarily wide molecular weight distribution (PDI = 6.0) was obtained by introducing the initiator (4-

bromomethyl methyl benzoate) in a heterogeneous two-phase process. The molecular weight distribution of poly(ILBr) was characterized by size-exclusion chromatography (SEC). The resulting homopolymer was found to be surface active and stimuli responsive. Poly(ILBr) films coated on quartz exhibit stimuli-responsive dewetting after ion exchange of Br_ by PF6_. This dewetting phenomenon can be understood in chain segmental terms as a stimuliinduced structural relaxation and appears to be the first such reported stimuli-responsive polymeric dewetting. Titrating aqueous poly(ILBr) with aqueous bis(2-ethylhexyl)sulfosuccinate induces nanophase separation and results in the condensation of nanoparticles 30_60 nm in diameter.

The electronic supplementary information (ESI) for publication No. 11 may be found at the following link:

See Fig. 2 below for graphical abstract:
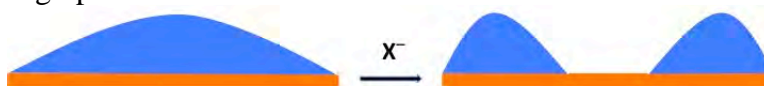
Figure 2

Stimuli-Responsive Triblocks

The initial report[1] of using ILBr as an ionic liquid monomer for making stimuli responsive gels, membranes, and latexes showed that latexes comprising ILBr did not coagulate in high salt, such as in 0.1 M NaBr. Further studies showed that such ultrastable nanolatexes could only be coagulated at relativley high concentrations of various stimuli triggering anions, such as BF_4-, PF_6-, and $S^=$,[2,3] where the condensing anion appeared to bind strongly to the imidazolium ring, turning the hygroscopic imidazolium bromide into a much more hydrophobic ion pair. A more recent report[4] of making distimuli responsive copolymers of ILBr and of *N*-isopropylacrylamide illustrated the thermal condensation of PNIPAM core – polyILBr corona particles that appeared impervious to boiling. These observations suggest that the imidazolium bromide moiety can provide very effective steric stabilization. It therefore seemed desirable to produce triblock copolymers comprising ILBr blocks in a series of stabilizers analogous to the well known Pluronic® series having central blocks composed of polypropylene oxide and endblocks composed of polyethylene oxide.[5]
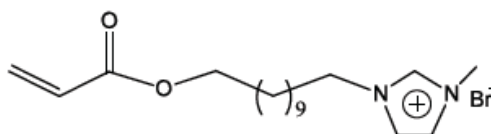
ILBr

Triblock copolymers incorporating the hydrophobic polypropylene oxide (PPO) block with endblocks derived by ATRP of the ionic liquid reactive surfactant, ILBr, were therefore designed. We report converting PPO blocks of about 1,000 and 3,500 Daltons, respectively, into macroinitiators I and II, respectively. A methanol/water CuBr system shown recently[6] to produce ILBr homopolymers by ATRP was used to grow the ILBr blocks. Good control was observed, and the resulting triblocks appear quite surface active. These triblocks are also anion stimuli responsive, and surface activity can be tuned by ion exchange. We expect

that these triblocks represent a new class of steric stabilizers that will prove effective in low and high salt, despite being ionic in nature.

Materials. The following were purchased from Sigma-Aldrich: Acryloyl chloride (96%), 11-bromo-1-undecanol (98%), triethylamine (99.5%), 1-methylimidazole (99%), 2,6-di-tert-butyl-4- methylphenol (99%), neutral aluminum oxide (activated, Brockman I standard grade, ~150 mesh), poly(propylene glycol)s (PPG, Mn 1000 and 3500 respectively), ethyl 2-bromoisobutyrate (EBiB, 98%), 1,1,4,7,10,10-hexamethyltriethylenetetramine (HMTETA, 97%), copper (I)bromide (99.99%), sodium bicarbonate, anhydrous sodium sulfate (≥99%) and anhydrous magnesium sulfate (≥97%) were used without further purification. Tetrahydrofuran (THF, ≥99.9%), dichloromethane (≥99.8%) and toluene (99.8%) were anhydrous. Diethyl ether was obtained from Fisher Scientific. Deionized water was used for all experiments.

Instrumentation. 1H NMR experiments were performed on a JEOL 400 MHz NMR. A 5mm O.D. NMR tube was used and the spectrum was accumulated with scans of 16 for macroinitiators and with 32 for all block copolymer samples. DSC analysis was performed on a TA Instruments DSC Q2000. Tzero Aluminum pans and lids were used. The samples were heated at 10oC/min to 110°C and held isothermally for 5 min to remove their thermal history. They were then cooled at 5°C/min to -180oC and heated again to the desired temperature. All reported transitions were obtained from the second heating portion of the cycle. Surface tension measurement was conducted using a dynamic contact angle (DCA) instrument (FTA200, First Ten Angstroms, Inc.) with a pendant drop method. A 3 mL plastic syringe and a needle with I.D. 0.483 mm and O.D. 0.711 mm were used. The aqueous drops were recorded by video and averages from at least 6 readings were used for reported values.

Synthesis of Macroinitiators I and II, The procedures are similar to those reported in literature with modification.[7,8] Poly(propylene glycol) with a Mn ~ 1000 (17 repeating units) and hydroxyl value of 111 mg KOH/g (8.0 g, 8 mmol) was dissolved in 120 mL anhydrous toluene. After azeotropic distillation of ~20 mL of toluene by rotary evaporator to remove traces of water, triethylamine (2.43 g, 24 mmol) was added, and the mixture was cooled to 0°C in an ice-water bath. In an argon atmosphere, 2-bromoisobutyryl bromide (BiBB) (5.52 g, 24 mmol) in 30 mL toluene was added dropwise over 50 min to the reactor. The reaction mixture was stirred for 24 hours at room temperature. After filtration, the filtrates were evaporated to remove most of solvent (~20 mL left) on a rotary evaporator. The residue was dissolved in 120 mL methylene chloride and extracted with saturated NaHCO$_3$ solution (3°—50 mL). The organic phase was then dried over anhydrous NaSO4 and the solvent was removed using a rotary evaporator. The product was further dried in vacuo at 90°C for 3 hours to give a brown viscous liquid abbreviated as Br-PPG17-Br (macroinitiator I). A yield of 10.4 g (100%) was obtained. 1H NMR indicated that the degree of esterification was complete. Macroinitiator II, Br-PPG60-Br, was prepared following a similar procedure as above from a poly(propylene glycol) with a Mn ~ 3500 (60 repeating unit).
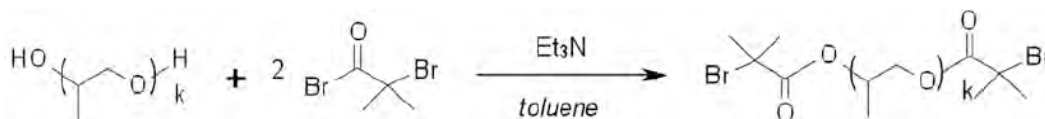
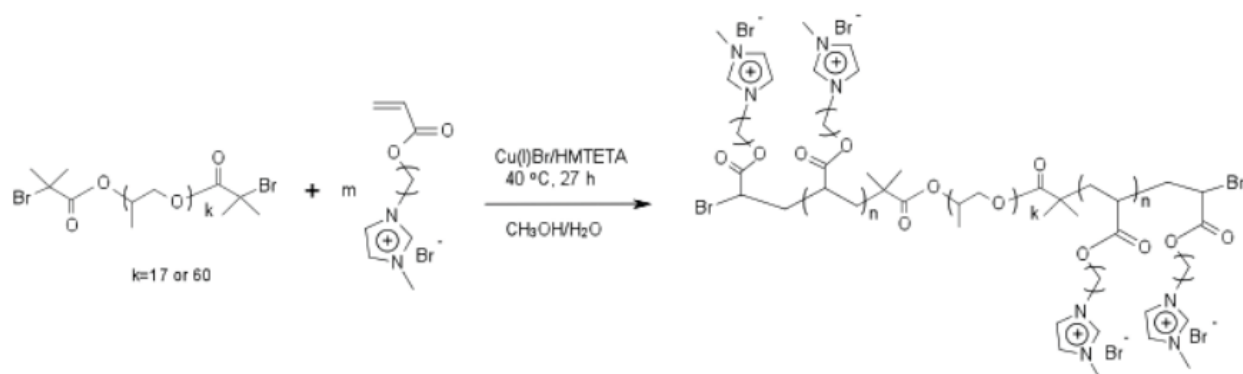**Figure 1. Scheme for preparing bifunctional macroinitiator.**

Figure 2. Scheme for synthesizing triblocks.

Synthesis of Triblocks by ATRP. Macroinitiator was dissolved in a flask with argon presaturated methanol and water, followed by the addition of Cu(I)Br. This solution was bubbled with argon for 5 minutes. ILBr monomer was then added, bubbling was continued for 8 minutes. Ligand (HMTETA) was last added to the flask by micropipette followed by an additional 3 minutes bubbling. The reaction flask was installed with condenser connected with an argon balloon and a vacuum inlet. Vacuum-argon cycling was performed for 10 minutes and the flask was immersed in a preheated oil bath at 40oC. After polymerization,
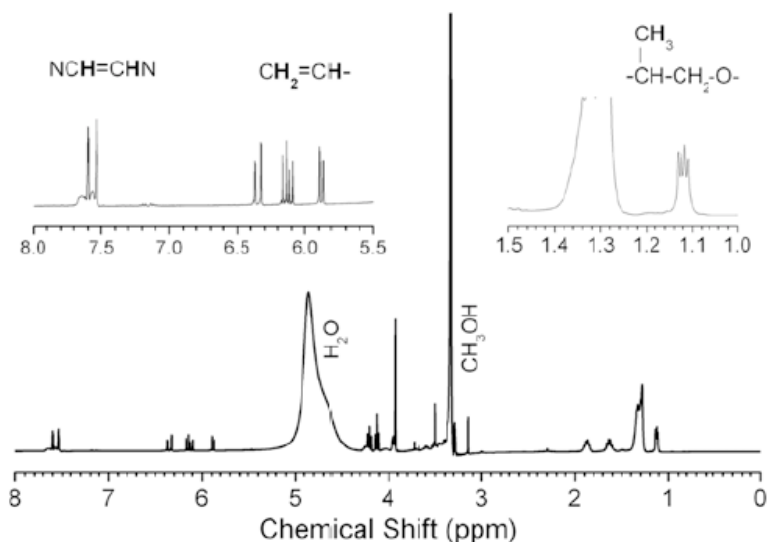
Figure 3. 1H NMR spectrum of ATRP reaction mixture diluted in deuterated methanol. The left upper insert illustrates the detail for two of the imidazolium protons and for the vinyl protons. The right upper insert illustrates the detail for the propylene oxide methyl protons.

the solution was dialyzed against water in SnakeSkin® Pleated Dialysis Tubing (MWCO 3500). Dialysis was done for two days with water changes 3 times a day. Purified polymers were recovered by lyophilization.

Conversion. The conversion of ILBr was estimated from 1H NMR spectra, such as shown in Figure 1. The imidazolium proton resonance relative area for the =N-CH=CH-N= protons

over 7.40-7.80 ppm, divided by two, represents the sum of unreacted and polymerized monomer. The vinyl proton **H**2C=C**H**- area over 5.7-6.5 ppm, divided by three, represents the unreacted ILBr monomer. The quotient of these quantities gives 1 minus the fractional conversion (p) of ILBr,

Differential Scanning Calorimetry. The DSC for the macroinitiators I and II, triblock copolymers I and II, and poly(ILBr)x homopolymer produced6 by ATRP are shown in Figures 3(a) and 3(b), respectively. The distinct Tg evident in macroinitiator I at -65°C appears suppressed in triblock I, while it appears present but shifted to -60°C in triblock II. The double Tg behavior of the poly(ILBr) oligomer appears evident in both triblocks to some extent.
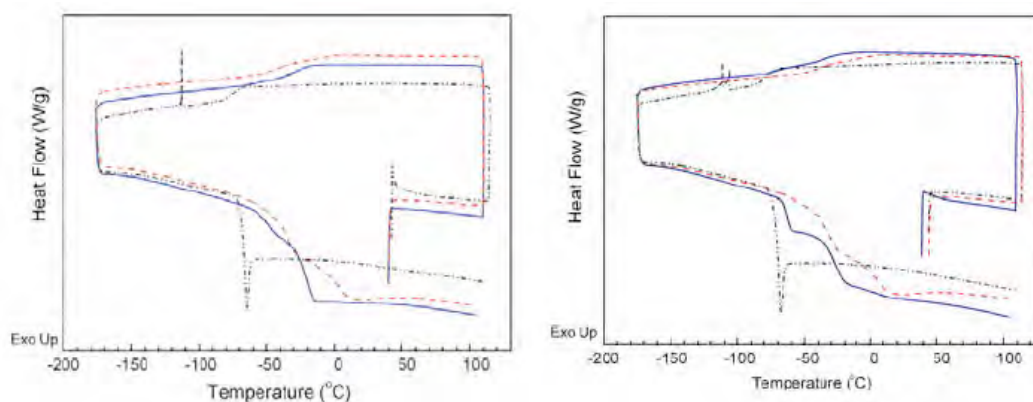
Figure 4. DSC traces: (left) – · · – Br-PO$_{17}$-Br (macroinitiator I), – – – poly(ILBr)$_6$, and ——— (IL)$_{3.6}$-(PO)$_{17}$-(IL)$_{3.6}$ (triblock I; TBP-20); (right) – · · – Br-PO$_{60}$-Br (macroinitiator II), – – – poly(ILBr)$_6$, and ——— (IL)$_8$-(PO)$_{60}$-(IL)$_8$ (triblock II; TBP-28).

Molecular weight distribution. Figs. 5-9 detail our SEC (GPC) analyses of triblocks TBP-20 (09-1049-20) and TBP-28 (09-1049-28). Fig. 5 compares the PMMA equivalent distributions for these two triblocks. Qualitatively, TBP-20 appears broader than does TBP-28. The TBP-20 distribution appears to be trimodal, with modes at 9,260, 39,627, and 102,258 Da. Number average and weight average molecular weights of 14,400 Da and 47,600 Da, respectively. The corresponding PDI = 3.31. The TBP-28 distribution appears to be bimodal, with modes at 19,966 and 41,333 Da. Number average and weight average molecular weights of 25,900 Da and 52,800 Da, respectively. The corresponding PDI = 2.04.
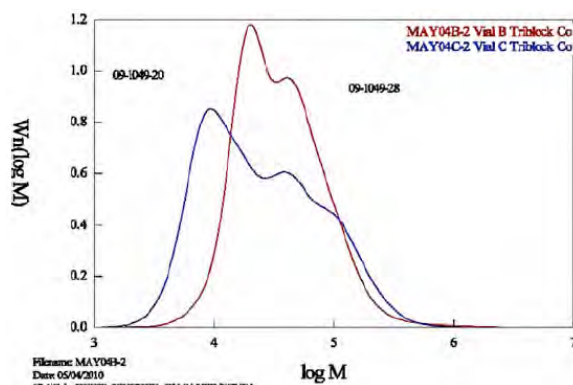
Figure 5. Molecular weight distributions of triblocks 09-1049-20 (blue, trimodal

distribution) and 09-1049-28 (reddish brown, bimodal distribution). These data are obtained using PMMA molecular weight standards and this distribution is a PMMA equivalent molecular weight distribution.
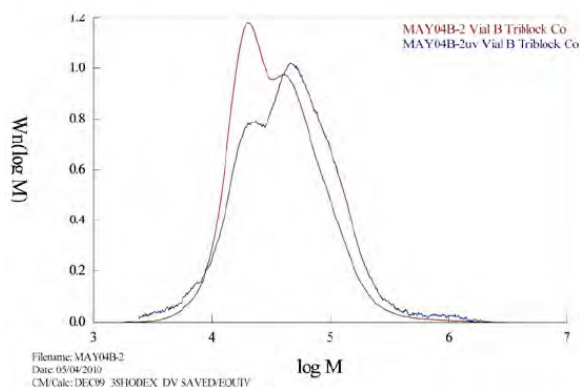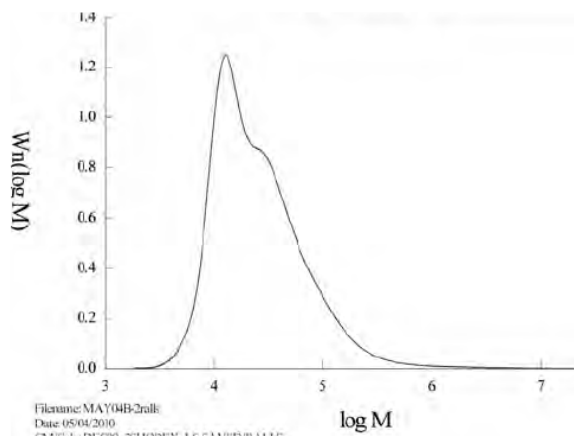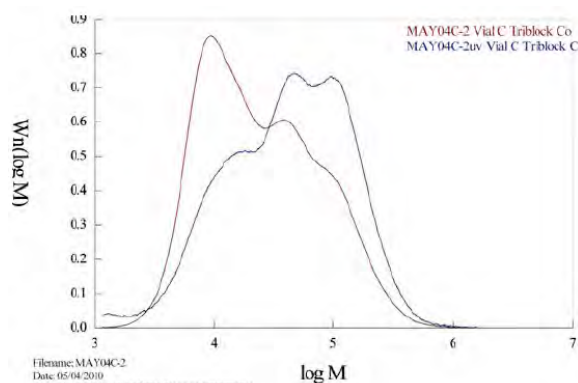

Figure 6. Molecular weight distributions of triblock 09-1049-28 (blue, 270 nm detection; reddish brown, DRI detection).

Figure 6 compares distributions of TBP-28 obtained by RI detection and by UV detection at 270 nm. The differences in these curves illustrate that the higher molecular weight components have a higher weight fraction of UV absorbing component. This is consistent with there being a fixed middle block of PO with variable length end blocks of ILBr, with end block length increasing with overall logM. The UV detection distribution, when multiplied by the weight fraction of UV absorbing monomer, ILBr, provides the fractional content of ILBr relative to total polymer, at each logM value. Figure 7 displays the molecular weight distribution for TBP-28 obtained using light scattering detection. The light scattering and DRI results are self-consistent. The TBP-28 distribution from light scattering detection (Fig. 7) has a number average and weight average molecular weights of 17,800 Da and 56,000 Da, respectively, with a corresponding PDI = 3.15.

Figure 7. Absolute molecular weight distribution determined by light scattering detection of triblock 09-1049-28.

Figure 8. Molecular weight distributions of triblock 09-1049-20 (blue, 270 nm detection; reddish brown, DRI detection).

Figure 8 compares distributions of TBP-20 obtained by RI detection and by UV detection at 270 nm. The higher values of the UV detection data show that the proportion of ILBr monomeric increases with increasing logM. Light scattering detection results in Fig. 9 agree well with the DRI results in Fig. 8. The TBP-20 distribution from light scattering detection
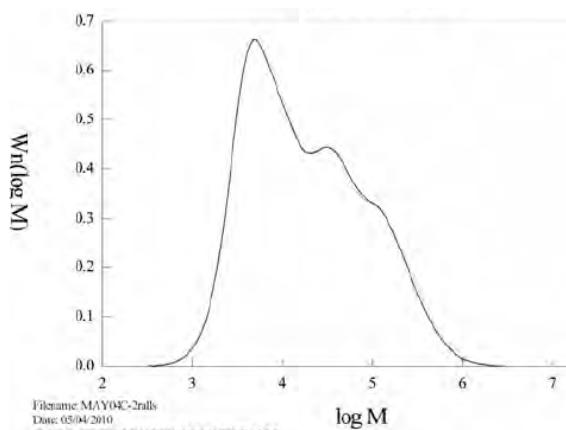

Figure 9. Absolute molecular weight distribution determined by light scattering detection of triblock 09-1049-20.

(Fig. 9) has a number average and weight average molecular weights of 7,560 Da and 58,200 Da, respectively, with a corresponding PDI = 7.70.

Surface activity at the air-water interface. Figure 10 illustrates surface tension as a function of Ln(weight fraction) for triblocks TBP-**20** and TBP-**28**. TBP-**20** actually has a larger molecular weight than TBP-28, and an apparently lower cmc (Ln cmc**28** = -10.5; cmc = 2.8 x 10-5; Ln cmc**20** = -7.6; cmc = 5.0 x 10-4. Both triblocks exhibit further surface tension lowering upon dissolving above the respective cmc and ultimately yield surface tensions at 25°C of 35 dyn/cm.
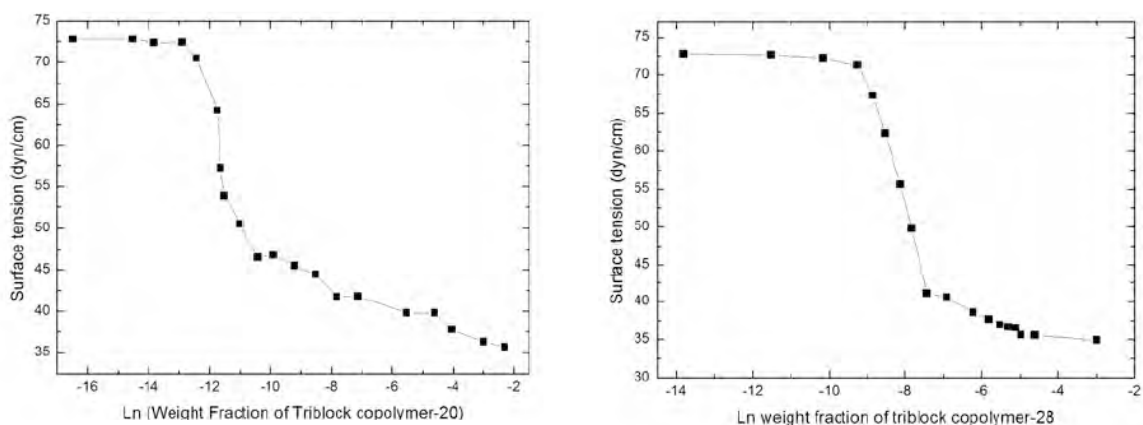
Figure 10. Surface tension at the air-water interface for two triblock copolymers, I (left) and II (right) at 25°C.

Immunization against Debye-Hueckel screening induced coagulation.

The ultrastability observed for nanolatexes derived from ILBr suggests that triblock copolymers having poly(ILBr) blocks may not be sensitive to indifferent electrolytes, but only to specific
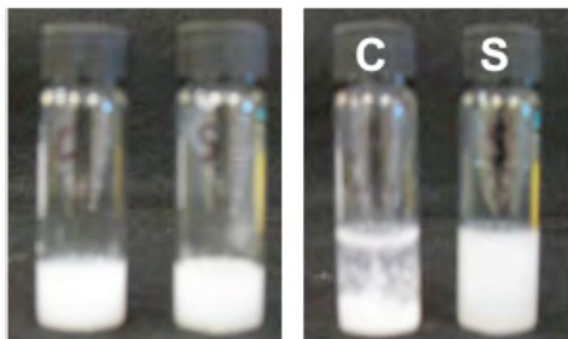

Figure 11. Stabilization of polystyrene-sulfate beads (110 nm) using 0.101% by weight TBP-28 solution. (Left) The vial marked C on the left contains 0.2 mL of DI water and 1.0 mL of 0.15 w/v Invitrogen beads. The vial marked S contains 1.0 mL of 0.15 w/v Invitrogen beads and 0.2 ml of TBP-28 (0.00101 g/ml). (Right) On the right we see the same vials as on the left, except after addition of 1.0 ml of 10 M aqueous KBr. The illustrated sedimentation is after 16 h.
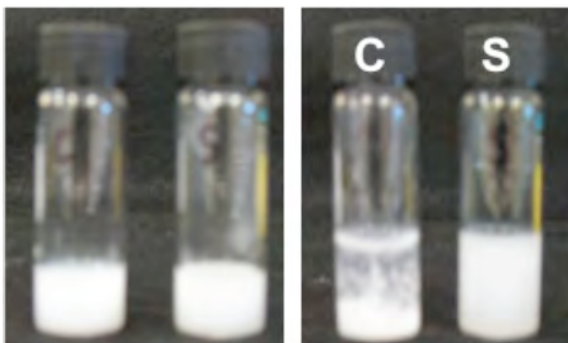
Figure 12. Stabilization of polystyrene-sulfate beads (500 nm) using 1.01% by weight

TBP- 28 solution. (Left) The vial marked C on the left contains 0.2 mL of DI water and 1.0 mL of 0.15 w/v Invitrogen beads. The vial marked S contains 1.0 mL of 0.15 w/v Invitrogen beads and 0.2 ml of TBP-28 (0.0101 g/ml). (Right) On the right we see the same vials as on the left, except after addition of 1.0 ml of 10 M aqueous KBr. The illustrated sedimentation is after 16 h.

stimuli inducing anions. To test this hypothesis we prepared suspensions of highly negatively charged polystyrene beads, 110 and 500 nm in diameter, and restabilized some of them by adsorbing what he estimated as an excess of TBP-28. These preparations are illustrated on the left sides of Figs. 11 and 12, wherein the control (C) is stabilized with surface sulfate groups and the sample (S) is restabilized with adsorbed TBP-28.

When concentrated aqueous KBr is added to each vial, two things happen. In the cases of the sulfate stabilized beads in the "C" vials, the added aqueous KBr causes rapid coagulation due to the electrostatic screening provided b the high concentration of indifferent electrolyte, KBr. In the vials wherein the beads have been restabilized with excess TBP-28, the beads are immunized against this high electrolyte induced coagulation,
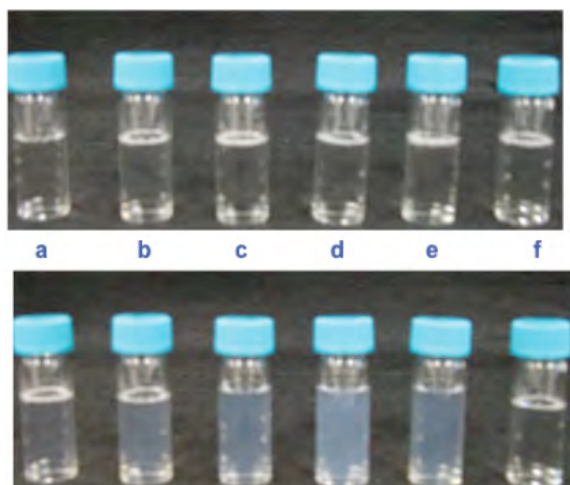
Figure 13. The upper series of vials each contain 2 ml DI water and 100 μl of aqueous 1.5% addition of 0.01 M KPF6 solution in the amounts of 50 μl (a); 100 μl (b); 150 μl (c); 200 μl (d); 250 μl (e); and none (f).

and the bead suspension remains unperturbed and stable. These respective coagulation and continued stable suspension effects are clearly seen for both bead sizes in the righthand photos of Figs. 11 and 12.

Stimuli-responsive behaviors.

Figure 13 illustrates a selective precipitation behavior exhibited by the TBP-28 solution when varying amounts of KPF6 are added. The hexafluorophosphate anion interacts strongly with imidazolium rings and transforms these rings from hygroscopic moieties into hydrophobic centers due to the formation of a strong ion pair. This decrease in water solubility results in the formation of insoluble particles, shown by dynamic light scattering to be of the order of 200-300 nm in diameter.
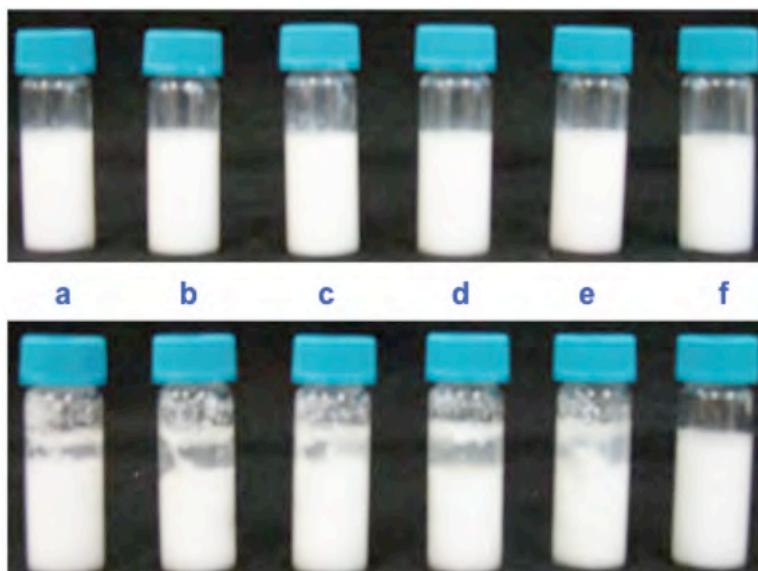
Figure 14. The upper series of vials each contain 2 ml of 4.0% (v/v) UCAR 300. Vials (a) through (e) had 75 μl of 1.5% (w/w) aqueous TBP-28 added. The lower series of vials are the same as above but after addition of 0.01 M aqueous KPF6 in the amount of 100 μl (a); 150 μl (b); 200 μl (c); 250 μl (d); 300 μl (e); 250 μl (f).

Another such interest behavior induced by the addition of hexafluorophosphate anion is illustrated in Fig. 14. Here a commercial latex dispersion normally not sensitive to indifferent or other salt levels was sensitized by adsorbing TBP-28 from solution. The vials (a) through (e) had varying amounts of destabilizing KPF6 added, and the resulting coagulation illustrated the effect, induced by the sequential adsorption of TBP-28 followed by addition of the hexafluorophosphate anion. The vial (f) had no TBP-28 added while it did have an appreciable amount of KPF6 added, and illustrated the basic insensitivity of the latex to the added salt in the absence of the stimuli responsive triblock.

In Fig. 15 we illustrate particle size distributions obtained by jar milling, overnight, some pigment yellow 138 (PY138) using 100 μm ceramic beads and TBP-28 to stabilize the dispersion. The highest resolution data show that the 200-300 nm particles are being reduced further to about 60 nm, and illustrate the high efficacy of the TBP-28 as an aqueous dispersing aid. We then took equal aliquots of this dispersion and added varying amounts of KPF6 to destabilize the dispersion, relying on the stimuli responsiveness of the ILBr blocks in the TBP-28. The photos in Fig. 16 illustrate this destabilization as evidenced by the sedimentation shown as well as by the stickiness of some of the dispersions (third vial from the right in Fig. 16) to the interior vial surface.
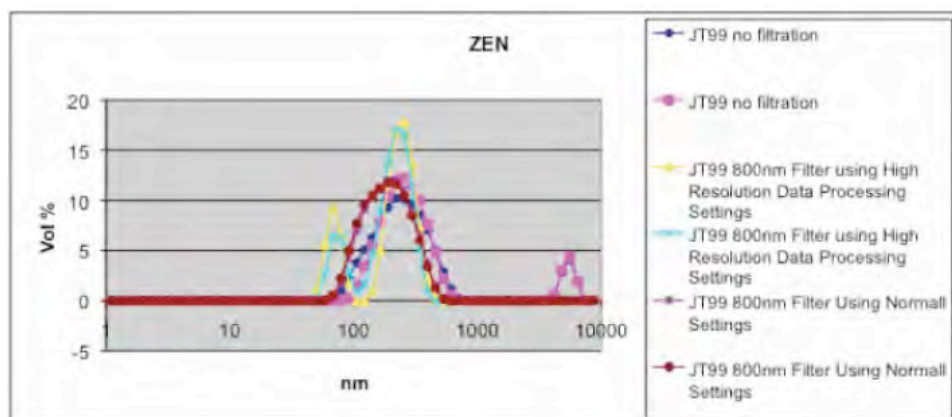
Figure 15. Particles size distributions of PY138/TBP-28 aqueous dispersions determined by dynamic light scattering on an advanced Malvern instrument courtesy of Gary Slater of Eastman Kodak Research Labs, Rochester, NY. The yellow and tourquoise plots show that the 200-300 particle size is gradually being reduced to about 60 nm. The magenta and blue plots show there is a bit of loose aggregate in the multimicron size regime. The reddish-brown curve shows that the distribution is broad, going from about 80 to about 300 nm at peak and further.
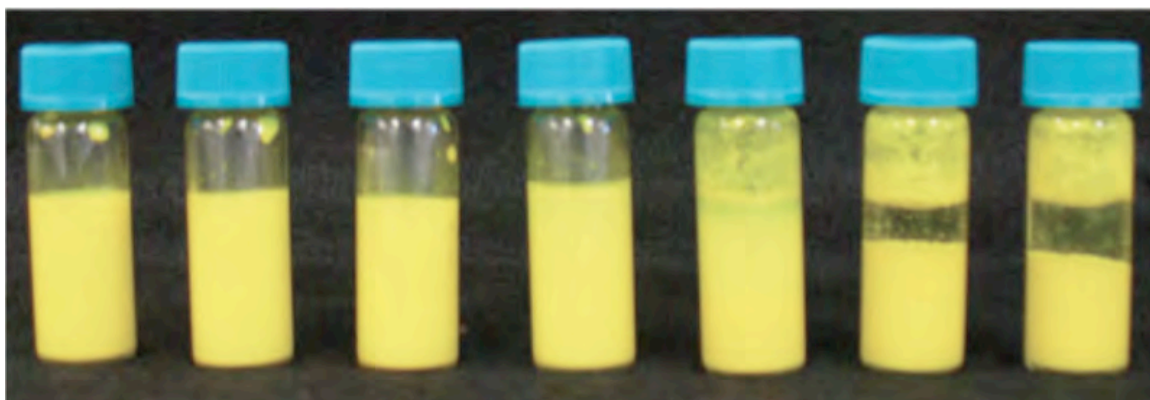
Figure 16. Stimuli responsiveness of the PY138/TBP-28 dispersions after addition of 0.1 M aqueous KPF6 to equal aliquots of the dispersion. The vial at far left had only DI water added as a diluent. Then increasing amounts of KPF6 were added with shaking. The significant sedimentation illustrated in the right most two vials shows that these dispersions were significantly destabilized by the added KPF6. The dispersion at the lower level used in the vial third from right was also partially destabilized, as it is plain to see that some of the dispersion particles therein stick to rather than drain away from the inner glass wall of the vial.

References

1 Yan, F.; Texter, J., *Chem. Comm.*, 2696-2698 (2006).

2 England ,D., MS Thesis. Eastern Michigan University (2008).

3 Tambe, N., MS Independent Study Report, Eastern Michigan University (2009).

4 Tauer K, Weber N, Texter J (2009) Core-shell particle interconversion with di-stimuli

responsive diblock copolymers. *Chem. Comm.* 6065-6067; doi:10.1039/B912148J.

5 Alexandridis, P.; Holzwarth, J. F.; Hatton, T. A., *Macromolecules* **T**, 2414-2425 (1994).

6 Liu, S.; Armes, S. P., *J. Am. Chem. Soc.* **123** (40), 9910–9911 (2001).

7 Li, C. H.; Ge, Z. S.; Jin, F.; Liu, S. Y., *Macromolecules* **42**(8), 2916-2924 (2009).

ESI analysis of PPG and macroinitiators

As described in earlier reports the nominally 1,000 Da PPG available from Aldrich forms the basis for one family of triblocks being synthesized, and a 3,500 Da PPG forms the basis for another family. The smaller example appears amenable to ESI analysis. An example spectrum is illustrated in Fig. 1 below. The spectrum can be interpreted as two overlaying primary spectra from singly charged oligomers. The more intense family has lost an oxygen or methyl group in the ionization process and a less intense family of peaks, displaced 16 mass units relative to the "high" set appears to represent the starting material bearing an additional proton. The family of peaks on the 400-700 mass/z range is likely a multiply ionized series. The 3,500 Da PPG starting material did not yield a satisfactory singly ionized family of peaks, and more experimentation will be needed to learn how to satisfactorily run such larger mass samples.
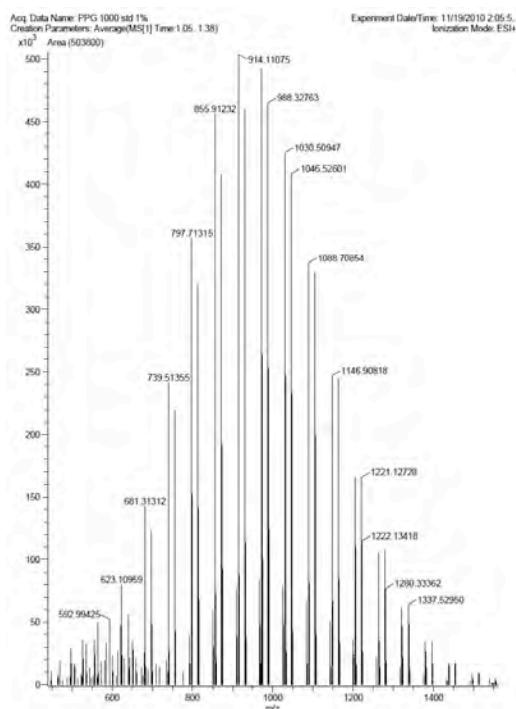
Figure 1. ESI MS-TOF spectrum of 1,000 Da PPG

Aspects of the primary, singly charged spectrum for PPG of 3,500 Da are seen in Fig. 2, along with at least two multiply charged peak series. More work is needed to refine the study of this material, as the primary families of peaks in Fig. 2 over the 3,000 to 4,000 m/z range do not appear symmetrical. However, it appears promising that such large materials can be successfully analyzed on our new instrument (Jeol Dart TOF with ESI accessory).

Macroinitiator produced by the coupling shown in Scheme 1 (of the next section) with the 1,000 Da PPG materials was successfully run using the ESI mode and the mass spectrum is shown in Fig. 3. This spectrum has not yet been analyzed, but the primary and highest family of peaks appears to be in the expected range.
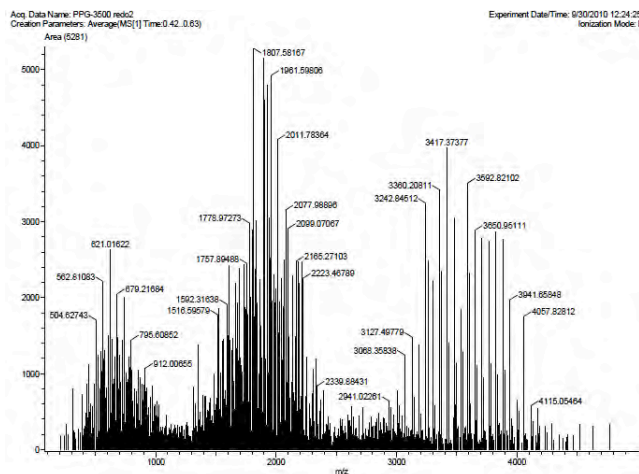

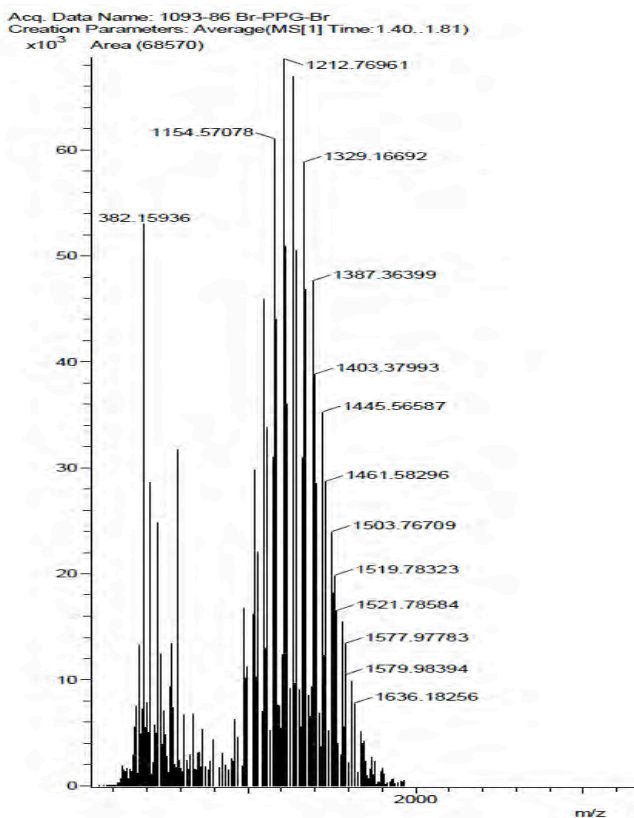Figure 2. ESI MS-TOF spectrum of 3,500 Da PPG.

Figure 3. ESI MS-TOF spectrum of 1,000 Da PPG centered macroinitiator.

Successful ATRP of poly(ILBR-*b*-PO-*b*-ILBr) (3,500 Da PPO)

We achieved useful but uncontrolled ATRP earlier in attempting the ATRP of these triblock copolymers. In the following we detail our success in archiving respectably controlled ATRP syntheses. The following in press manuscript details our success with triblocks having a center block (3,500 Da) of PPO: (DOI: 10.1002/marc.201100586)

Triblock Copolymer Based on Poly(propylene oxide) and Poly(1-[11-acryloylundecyl]-3-methyl-imidazolium bromide)

This paper in Macromolecular Rapid Communications is No. 15 in our list of archival publications.

We report the controlled atom transfer radical polymerization (ATRP) of a stimuli-responsive ionic liquid surfactant acrylate (ILBr), from both ends of a telechelic poly(propylene oxide) (PPO) macroinitiator, (BrX-PPO-XBr), wherein both ends of the PPO center block are esterified with bromoisobutyryloyl (BrX). The resulting highly water soluble triblock copolymer, poly(ILBr-*b*-PO-*b*-ILBr) is multi-stimuli responsive. This new class of triblocks exhibits classical surface activity in lowering surface tension at the air-water interface and in modifying wetting in waterborne coatings. It also immunizes model colloids against coagulation induced by Debye-Hückel (indifferent electrolyte) electrostatic screening. The poly(ILBr) endblocks are stimuli-responsive to certain anions, such as hexafluorophosphate, which induces precipitation by converting the hygroscopic imidazolium bromide groups into hydrophobic imidazolium hexafluorophosphate ion pairs. Further, sol-gel thermoreversibility was unexpectedly found as an additional form of stimuli-responsiveness. The aqueous triblock thermoreversibly forms a gel phase above a line of LSCTs (lower solution concentration temperatures) at weight fractions above 0.33. The structure of this gel phase has not been established, but it most likely is a lyotropic liquid crystalline phase of ILBr micelles. This gel phase will be used to template new zeolites.

The supplementary information (SI) is available at the following link:

http://onlinelibrary.wiley.com/store/10.1002/marc.201100586/asset/supinfo/marc_201100586_sm_suppl.pdf?v=1&s=282eec9b140604021ddee9d90266cce5dfdaf605

The graphical abstract below illustrates how the diblocks equilibrate to form micelles and how the micelles equilibrate to form a gel phase above the LCST.
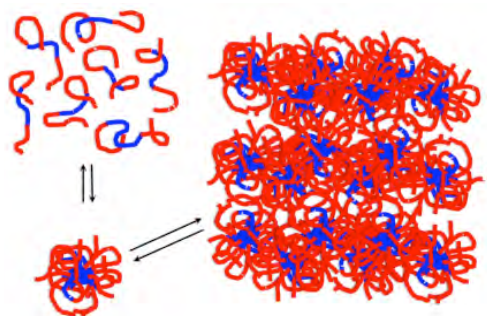
Graphical Abstract

Summary of other poly(ILBr$_{n/2}$-b-PO$_k$-b-ILBr$_{n/2}$) syntheses

The stimuli responsive and reactive surfactant ILBr was made into poly(ILBr)-PPG-poly(ILBr) triblock copolymers (TBP) by controlled ATRP syntheses, dramatically improving on the syntheses last reported. Size exclusion chromatography (SEC) analysis of this surface active TBP is illustrated in Fig. 1(left), and a kinetic analysis of the ATRP synthesis is illustrated in Fig. 1(right). The kinetic analysis shows that the conversion of monomer to polymer was first order over the reaction period of 26 h. The SEC analysis illustrated shows detection by refractive index and detection by UV at 270 nm. The shifted UV curve shows that as the TBP molecular weight increases, the weight fraction of ILBr monomer increases. The center of the molecule is 1,000 Da PPG, and this block is not lengthened during the synthesis. ILBr addition is done via ATRP, subsequent to esterifying each end of the PPG center block with bromoisobutyrylbromide. The SEC analysis also yielded M_n, M_w, and M_w/M_n values of 6,900 Da, 9,510 Da, and 1.38, respectively. This is a controlled polymerization example of a new class of stimuli responsive TBPs, with n = 7-11 in this example and larger in other examples being characterized.
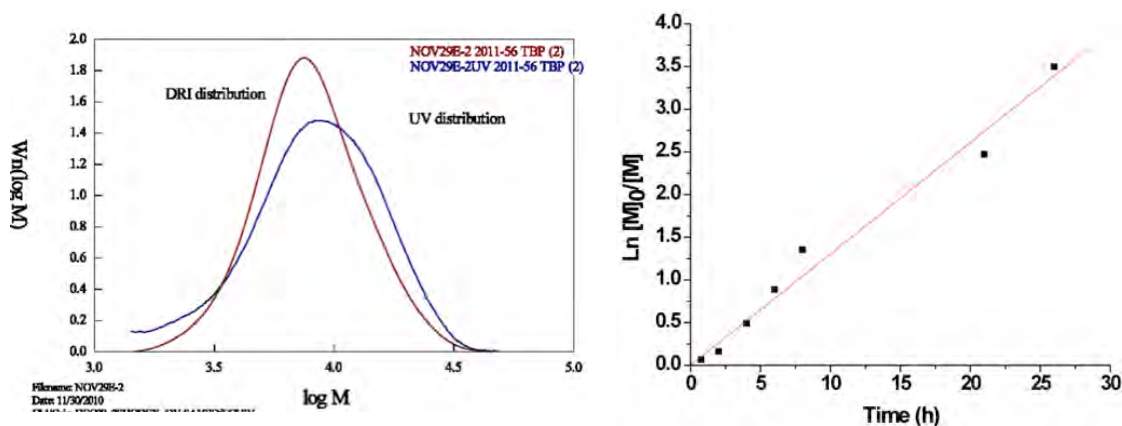
Figure 1. SEC and kinetic analysis of IL$_{n/2}$-PO$_{17}$-IL$_{n/2}$ stimuli responsive triblock copolymer with a polypropylene oxide core (PO) of about 17 units and with highly water soluble end blocks made by ATRP of ILBr, with n = 7-11. The molecular weight distributions picture on the left show how the end blocks vary with overall size. The UV detection curve is weight normalized and senses the amount of ILBr due to the UV absorption of the imidazolium ring at 270 nm. The DRI curve goes from the refractive index detection of the entire polymer.

The above example corresponds to 2011-56-TBP with k=17 and aim n = 10 (see also below). We prepared a series of examples having k=17 and n = 4, 10, and 30, and various properties and synthetic results are listed below:

2021-22-TBP (PPO ~1000 Da; k=17; n=4)

ILBr:CuBr:HMTETA:macroinitiator = 25.8:6.45:8.06:6.45; methanol:water = 2.5:1 = 105 mL

2025-13-TBP (PPO ~1000 Da; k=17; n=4)

ILBr:CuBr:HMTETA:macroinitiator = 25.8:6.45:8.06:6.45; methanol:water = 2.5:1 = 105 mL

Yield ~ 10.9 g; Mn (NMR) ~ 3,000

2011-36-TBP (PPO ~1000 Da; k=17; n=10)

ILBr:CuBr:HMTETA:macroinitiator = 12.1:1.29:2.58:1.29; methanol:water = 2.5:1 = 52.5 mL

Potentiometric Br/g triblock ~ 1.42 mmol/g

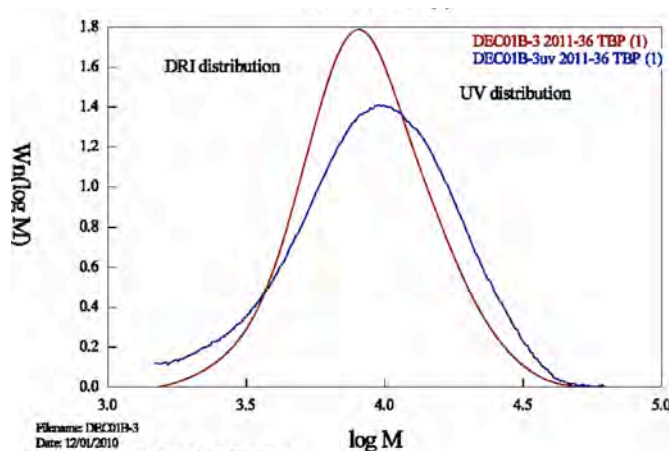Yield ~ 1.37 g; Mn (NMR) ~ 5,100 Da; Mn (GPC) ~ 7,400 Da; PDI ~ 1.32

Figure 2. GPC results for 2011-36-TBP; UV and DRI distributions

2011-56-TBP (PPO ~1000 Da; k=17; n=10)

ILBr:CuBr:HMTETA:macroinitiator = 12.1:1.29:2.58:1.29; methanol:water = 2.5:1 = 52.5 mL

Potentiometric Br/g triblock ~ 1.44 mmol/g

Yield ~ 2.51 g; Mn (NMR) ~ 5,400 Da; Mn (GPC) ~ 6,900 Da; PDI ~ 1.30

See Fig. 1 for kinetics and GPC distributions.

Table 2. Data summary for 2011-36, -56, -74

SEC file	Sample ID	PMMA-equivalents			Absolute by Ucal			Absolute by LS			MW no DRI	dn/dc
		Pn	Pw	Pz	Mn	Mw	Mz	Mn	Mw	Mz		
NOV29C-2	2011-71 BrPPGBr (6)	4850	6380	8640	3680	4640	6020	not calculated				
NOV29E-2	2011-56 TBP (2)	6940	9020	11700	6900	9510	12400	5010	7860	11000	7550	0.191
NOV29F-2	2011-74 TBP (3)	12800	16900	22900	11500	15400	21200	7630	13500	22400	13400	0.193
DEC01A-3	2011-52 BrPPGBr (5)	1100	1290	1550	1120	1270	1580	not calculated				
DEC01B-3	2011-36 TBP (1)	7380	9830	13100	7340	10200	13900	3450	5280	7640	5260	0.195
DEC01C-3	1049-30 TBP (4)	21000	37200	70400	19800	42100	97100	21900	36700	81100	36600	0.194

2013-38-TBP (PPO ~1000 Da; k=17; n=10) See molecular weight distribution below.

ILBr:CuBr:HMTETA:macroinitiator = 25.8:2.58:5.18:2.58; methanol:water = 2.5:1 = 105 mL

Potentiometric Br/g triblock ~ 1.23 mmol/g

Yield ~ 9.04g; Mn (NMR) ~ 5,300 Da; Mn (GPC) ~ 5,800 Da; PDI ~ 1.74

2015-39-TBP (PPO ~1000 Da; k=17; n=10) See below for GPC molecular weight distribution.

ILBr:CuBr:HMTETA:macroinitiator = 25.8:2.58:5.18:2.58; methanol:water = 2.5:1 = 105 mL

Yield ~ 7.87g; Mn (NMR) ~ 5,200 Da; Mn (GPC) ~ 8,100 Da; PDI ~ 1.56
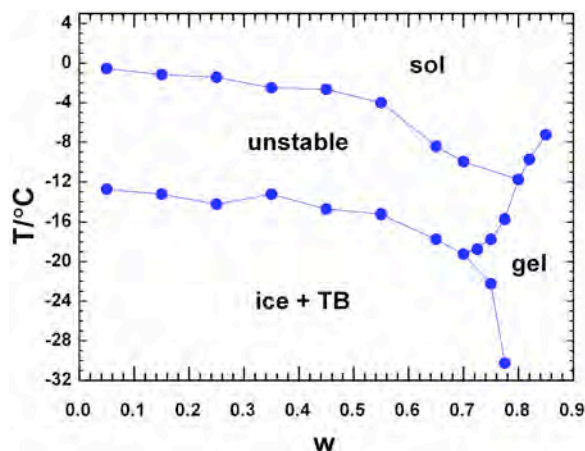
Figure 3. Phase diagram for 2015-39-TB with k=17 and n=10.

2011-95-TBP (PPO ~1000 Da; k=17; n=30)

ILBr:CuBr:HMTETA:macroinitiator = 12.9:0.43:0.86:0.43; methanol:water = 2.5:1 = 52.5 mL

Potentiometric Br/g triblock ~ 1.70 mmol/g

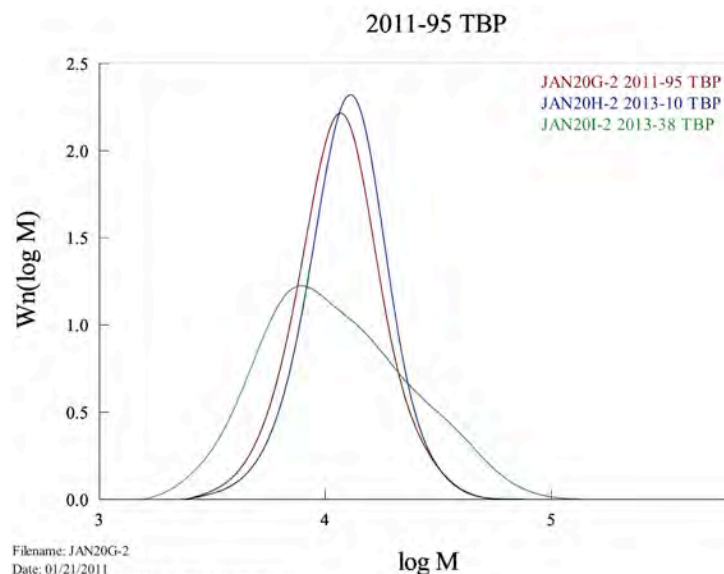Yield ~ 2.78g; Mn (NMR) ~ 12,700 Da; Mn (GPC) ~ 10,400 Da; PDI ~ 1.22

Figure 4. GPC results for 2011-95-TBP, 2013-10-TBP, and 2013-38-TBP.

2013-10-TBP (PPO ~1000 Da; k=17; n=30)

ILBr:CuBr:HMTETA:macroinitiator = 12.9:0.43:0.86:0.43; methanol:water = 2.5:1 = 37 mL

Potentiometric Br/g triblock ~ 1.77 mmol/g

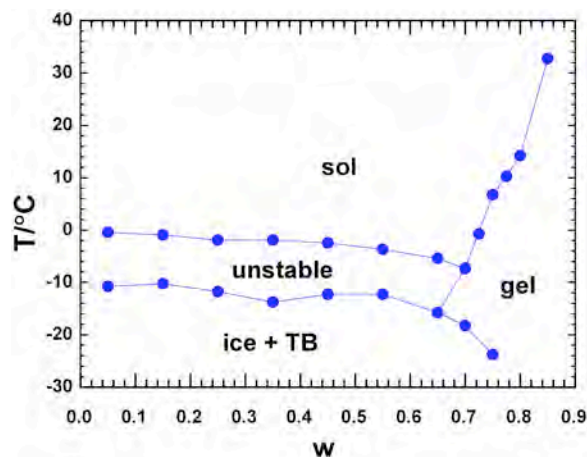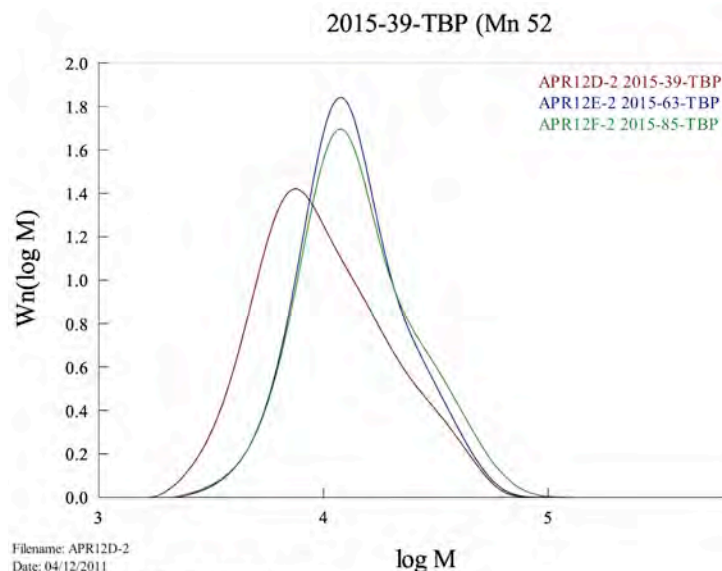Yield ~ 6.80g; Mn (NMR) ~ 14,000 Da; Mn (GPC) ~ 11,300 Da; PDI ~ 1.20

Figure 5. Phase diagram for 2013-10-TB with k=17 and n=30.

2015-63-TBP (PPO ~1000 Da; k=17; n=30)

ILBr:CuBr:HMTETA:macroinitiator = 12.9:0.43:0.86:0.43; methanol:water = 2.5:1 = 105 mL

Yield ~ 5.02g; Mn (NMR) ~ 12,100 Da; Mn (GPC) ~ 11,400 Da; PDI ~ 1.36

Figure 6. GPC results for 2015-39-TBP, 2015-63-TBP, and 2015-85-TBP.

2015-85-TBP (PPO ~1000 Da; k=17; n=30)

ILBr:CuBr:HMTETA:macroinitiator = 12.9:0.43:0.86:0.43; methanol:water = 2.5:1 = 105 mL

Yield ~ 5.53g; Mn (NMR) ~ 12,300 Da; Mn (GPC) ~ 11,800 Da; PDI ~ 1.4

Table 3. Summary for 2015-39, -63, -85

SEC File	Sample ID	PMMA-equivalent			Absolute by LS			Mw no DRI from LS	dn/dc
		Mn	Mw	Mz	Mn	Mw	Mz		
APR12D-1	2015-39-TBP (Mn 5200)	7840	11300	16300					
APR12D-2		8100	12600	20200	4900	7730	13000	7710	0.198
APR12E-1	2015-63-TBP (Mn 12100)	11300	15000	20200					
APR12E-2		11400	15500	21500	7410	10700	16700	10700	0.196
APR12F-1	2015-85-TBP (Mn 12300)	11800	16800	24500					
APR12F-2		11800	17000	25200	8510	12000	18400	12000	0.2

Sample used in above Macromol Rap. Comm. article

2011-74-TBP (PPO ~3500 Da; k=60; n=10)

ILBr:CuBr:HMTETA:macroinitiator = 12.9:1.293:2.58:1.29; methanol:water = 2.5:1 = 52.5 mL

Potentiometric Br/g triblock ~ 0.81 mmol/g

Yield ~ 5.82g; Mn (NMR) ~ 8,400 Da; Mn (GPC) ~ 12,800 Da; PDI ~ 1.32

2021-01-TBP (PPO ~3500 Da; k=60; n=10)

ILBr:CuBr:HMTETA:macroinitiator = 25.8:2.56:5.16:2.56; methanol:water = 2.5:1 = 105 mL

Yield ~ 13.8g; Mn (NMR) ~ 9,900 Da

2025-02-TBP (PPO ~3500 Da; k=60; n=10)

ILBr:CuBr:HMTETA:macroinitiator = 25.8:2.56:5.16:2.56; methanol:water = 2.5:1 = 105 mL

Yield ~ 14.8g; Mn (NMR) ~ 11,000 Da

Research Task 2

The effects of tether length on pore size will be examined by making a series of new imidazolium-based ionic liquid surfactants, wherein the chain length between the acrylate and imidazolium will be varied.

Effect of tether length on pore size

The nonyl analogue (C9Br) of ILBr (3-methyl-1-yl[undecylacrylate] imidazolium bromide) was synthesized and most of the ternary phase diagram was constructed (see below) at 25°C and at 60°C. The weight fraction ternary diagram (Fig. 17) And mole fraction ternary diagram (Fig. 18) are illustrated below:
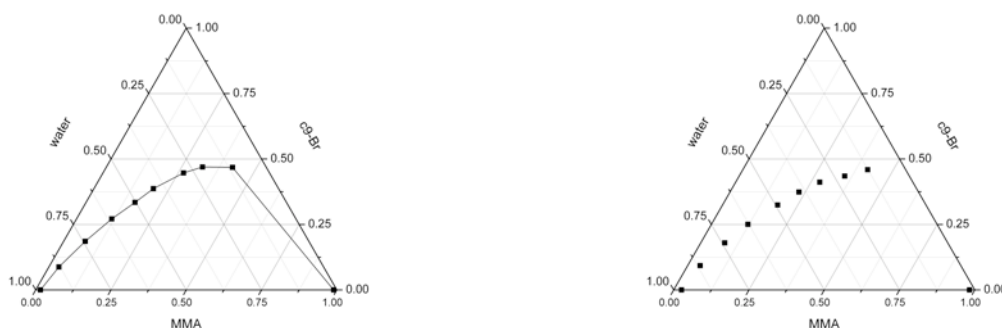
Figure 17. **Weight fraction ternary phase diagram for the water/C9Br/MMA system at (left) 25°C and (right) 60°C.**
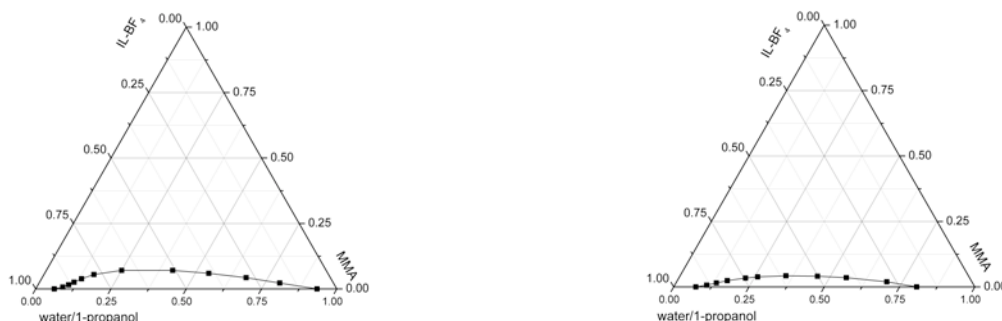
Figure 18. Mole fraction ternary phase diagram for the water/C9Br/MMA system at (left) 25°C and (right) 60°C.

A few more data points need to be generated to complete the phase diagrams. Subsequently, a series of polymerizations at the molar equivalent of 30% (w/w) ILBr will be generated, and the resulting pore structure will be characterized in detail.

Research Tasks 3, 4, 5, & 6

These tasks aimed at formulating fluorinated monomer-based copolymers and polymerized microemulsions, poly(amide-etherimides), 5-(4-trimellitimidophenoxy)-1-trimellitimido naphthalenes (TMTMN) based microemulsion copolymers, and poly(trimellitic anhydride chloride-*co*-4,4′-methylenedianiline) based microemulsion copolymers were abandoned in favor of more extensive development of Tasks 9 and 10.

Composite Metal/Organic and Hybrid/Organic Materials by Templating (Texter)

Research Task 7

Planar open-cell porous sheets derived from the above tasks will be placed upon a suitably porous web, and particulate aluminum will be infused into the sheets from suspensions or by other methods (e.g., electrochemical).

Light weight composites for space vehicle exteriors

Initial attempts to infuse particulate metals into porous wafers of poly(ILBr-*co*-MMA) were disappointing due to apparent lack of fluid flow through the wafers or due to unfavorable wetting phenomena. The biggest poration problem encountered in this work was the difficulty in understanding and controlling the penetration depths of open cell structures during and after membrane poration. Such understanding is needed in order to use such materials in the fabrication of light weight composites. Figure 1 illustrates the problem, wherein poration progresses at a finite rate, and where the pore size decreases on further penetration away from

the film-solution boundary. The poration on either side is distinct and appears much smaller in the central third of the membrane.
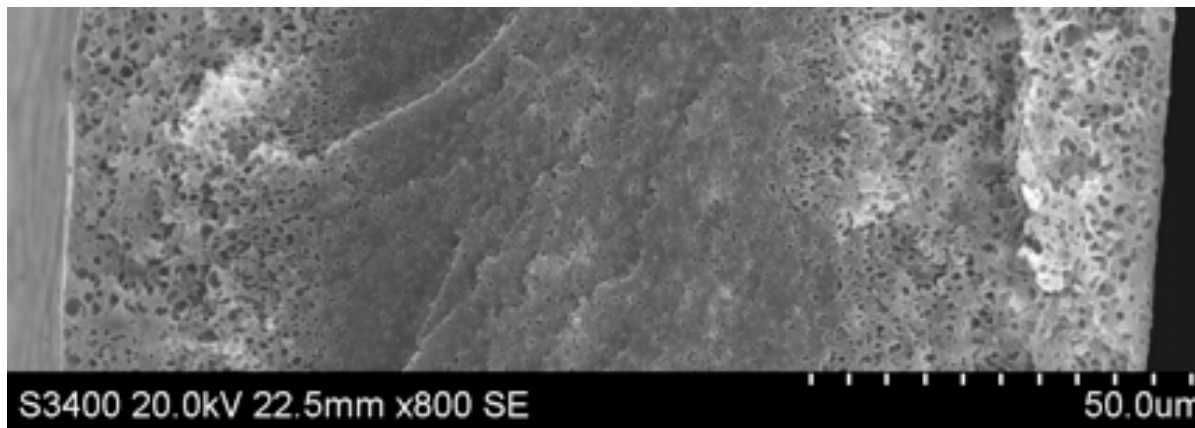

Figure.1. SEM of freeze fracture cross-section of 130 µm thick film for 10 days in 0.1 M KPF$_6$. The largest pores visible to the eye at this magnification are about 1 µm in diameter.
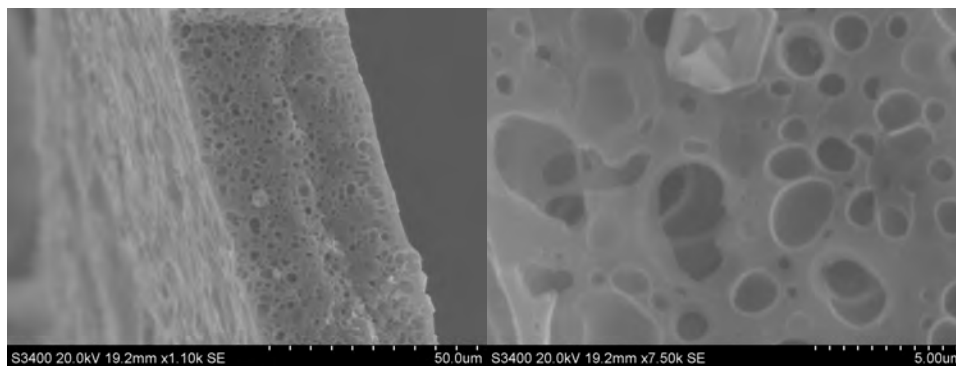

Figure 2. Latex film before being embedded with Cu nanoparticles.

Much thinner nanolatex films (40 µm thick) were extensively porated as shown in Fig. 2. This film appeared to be adequately porous to water infusion, as tested in a syringe-type membrane holder.

A commercial sample of Cu nanoparticles, shown in Fig. 3, was dispersed in water, and it was then attempted to infuse these particles into the same porated thin film. Many of the pores were plugged by Cu nanoparticles blocking exit pores, and the high pressure needed to get perceptible flow resulted in damage to the film wafer.
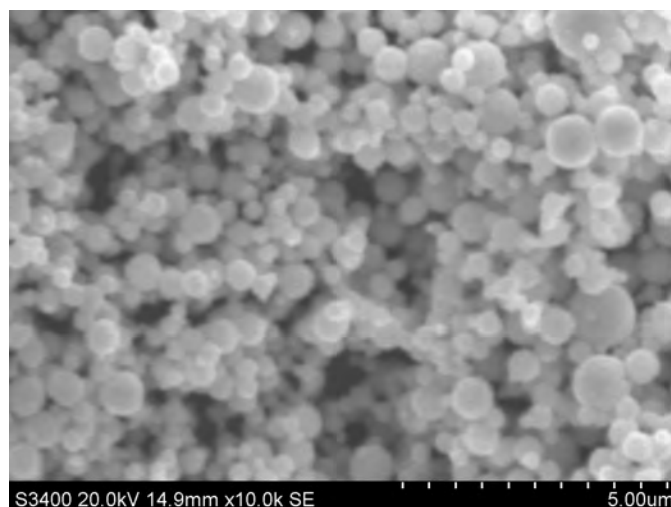
Figure 3. Cu nanoparticles nominally 500 nm in diameter.

Some limited infusion of Cu nanoparticles was achieved as shown in the freeze fracture cross-sections of Fig. 4. In this system the larger Cu nanoparticles made some progress into the film, but were blocked when they reached pores either having too small exit holes or having pores previously blocked by nanoparticles. These difficulties suggest electrochemical pore filling by reducing metals from solution into the pores, from one side to the other is probably a more practical approach to preparing such hybrid films. For these reasons nanoparticle infusion was abandoned in favor of work on tasks 9 and 10.
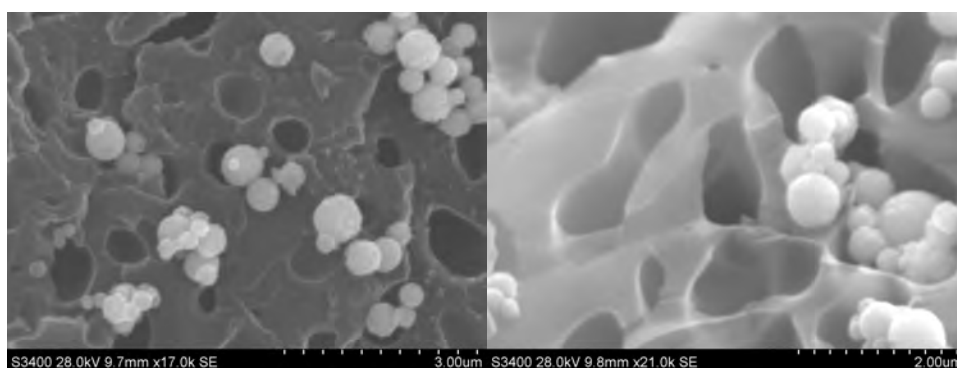
Figure 4. Freeze fracture cross-sections after pumping Cu nanoparticles into film.

Research Task 8

The electrochemical filling of pores by reduction of metal ions from solution was put on hold so as to better address Tasks 9 and 10.

Research Task 9

Thermal transfer materials that can dissipate heat efficiently to the ambient atmosphere will be derived by infusing or electrochemically filling suitably porous polymers or random arrays of polymer beads.

Hybrid thermal transfer materials

Due to difficulties in perusing our porous wafers we have focused on our ability to prepare composites of various materials with our nanolatexes. A variety of promising applications are described in the sequel.

Copper nanoparticle/nanolatex films

Copper nanoparticles about 78 nm in diameter were obtained from Aldrich. As received they were interesting because they appear black in color, undoubtedly due to surface oxidation coating the articles with CuO. These particles were mixed with various nanolatex suspensions, and then metered into the bottoms of cup cake tins to make thin films by casting via drying under ambient conditions. Because of the relatively high density of copper, 8.96 g/cm^3, our dispersions at 0.5 to 16 % w/w in our nanolatexes, 15-20% organic solids w/w, did not have long term stability because of gravitational sedimentation. Much smaller colloidal copper, < 10 nm diameter, would be needed to achieve Brownian motion dominated behavior immune to gravitational sedimentation.
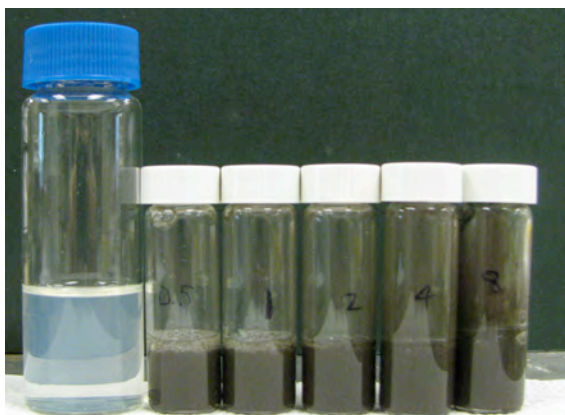
Figure 19. Concentrated nanolatex suspension (far left) followed by 0.5, 1, 2, 4, and 8% (w/w) Cu nanocopper suspensions made in this nanolatex.
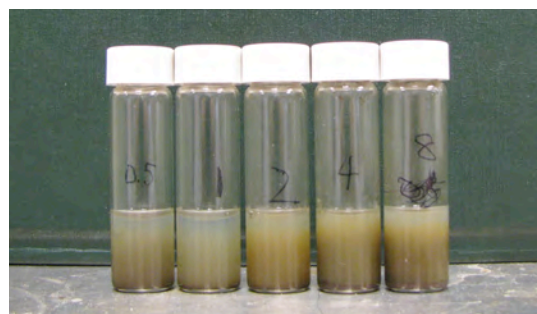

Figure 20. Nanocopper/nanolatex dispersions after one day sedimenting (from left to right, 0.5, 1, 2, 4, and 8% w/w copper).

A photograph of the slightly turbid nanolatex, concentrated to about 18% w/w solids, is shown in Fig. 19 along with a concentration series nanocopper-nanolatex dispersions prepared by sonicating the mixture. Initially the dispersions appear blackish-green due to the high state of dispersity and the blackish green color of the nanocopper (emanating from

oxidation of the nanoparticle surfaces. The long-time dispersion instability due to gravitational sedimentation is shown if Fig. 20. When freshly prepared dispersion are used to immediately cast films for drying, using cupcake tins as molds for the films, blackish green films are obtained on drying, as is shown in Fig. 21.
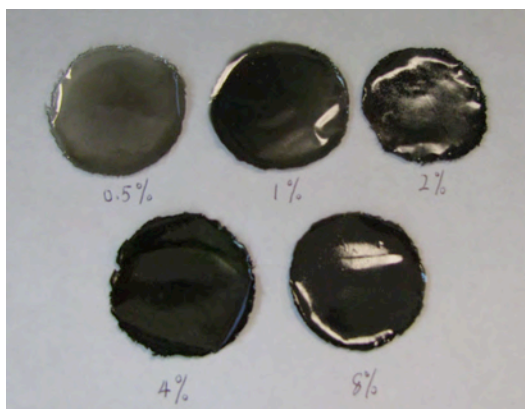

Figure 21. Thin films made from nanocopper/nanolatex dispersions (Fig. 19) by casting and drying. The weight % nanocopper is indicated beneath each film.

The dried nanocomposite films illustrated in Fig. 21 are suitable for various kinds of tests including dielectric spectroscopy, thermal diffusivity, and SEM. Since the first sets of films examined were prepared by ambient drying overnight, we expected to see evidence of nanocopper sedimentation.
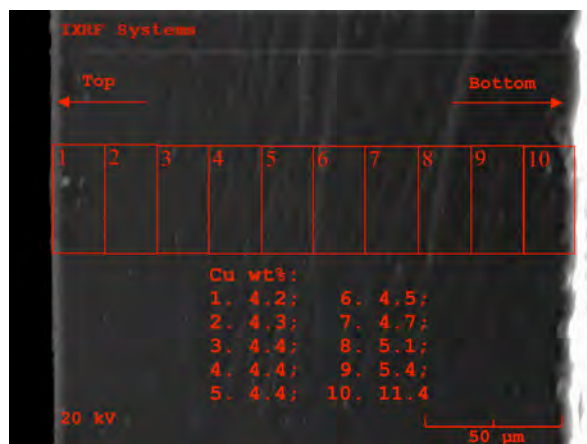
Figure 22. SEM cross-section of nanocopper-nanolatex film derived from 1% w/w copper suspension. The red superimposed grid illustrates how an EDAX analysis was done for measuring Cu concentration across the film. The righthand boundary is the film bottom, and there you can see some evidence of nanoparticle sedimentation.
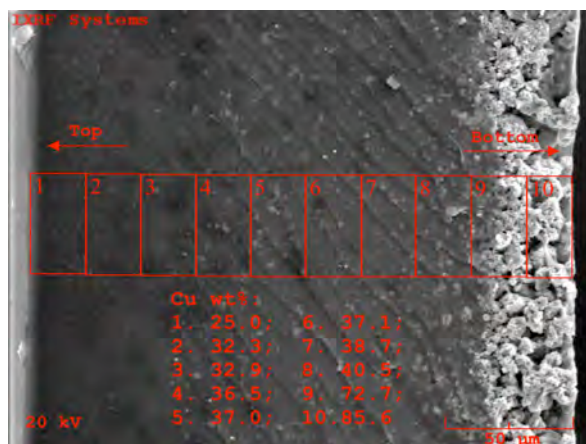
Figure 23. SEM cross-section of nanocopper-nanolatex film derived from 16% w/w copper suspension. The red superimposed grid illustrates how an EDAX analysis was done for measuring Cu concentration across the film. The righthand boundary is the film bottom, and there you can see a thick region of nanoparticle sedimentation.

The SEM in Figs. 22 and 23 illustrate this gravitational sedimentation. At low added nanocopper in Fig. 22 we see some agglomeration of small copper particles into clusters evident along the bottom boundary of the film at the far righthand side of the micrograph. Occasional clusters are evident elsewhere in the image. In the most highly concentrated film in Fig. 23 it is clear that a dense layer of copper has formed in the rightmost 20% of the film, and that copper clusters are distributed at high concentration throughout the film, except at the left boundary surface where only a few clusters are found.
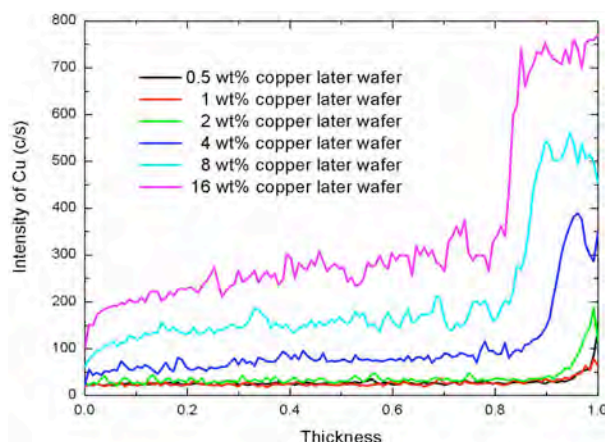
Figure 24. Copper EDAX emission intensity as a function of relative depth (top to bottom: 0-1) for the films made from the 0.5-16% w/w Cu, nanocopper-nanolatex dispersions. These results were derived from EDAX measurements made along a normal traversing the fracture surfaces from top to bottom.
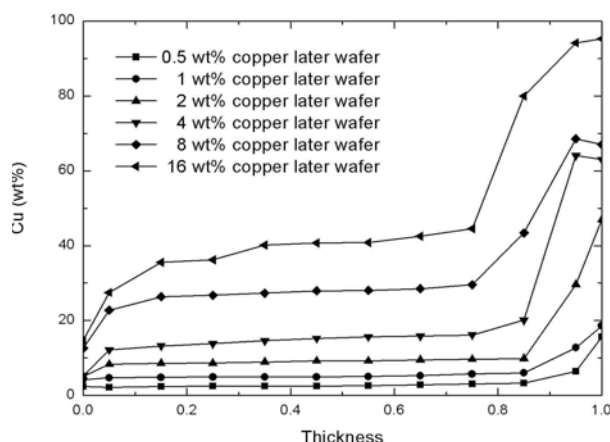
Figure 25. Copper concentration as a function of relative depth (top to bottom: 0-1) for the films made from the 0.5-16% w/w Cu, nanocopper-nanolatex dispersions. These results were derived from EDAX measurements made in the grids illustrated in Figs. 22 and 23.

EDAX analysis was applied to fracture surfaces of all of the film samples in order to try to quantify the sedimentation. Average values of fluorescence emission intensity obtained along a lines normal to the film top and bottom surfaces from freeze-fracture surfaces are illustrated in Fig. 24. The emission intensities for the low levels 0.5, 1, and 2% (w/w) copper are indistinguishable over most of the samples, except close to the bottom surface where they separate in response to the sedimentation at the bottoms of the respective films. No significant depletion at the tops of the respective films is evident until the copper concentration reaches 4, 8, and 16%. The bulk distribution of copper appears to increase steadily on going to 4, 8, and 16%. The thicknesses of the bottom sediment increase from about 8% of the film thickness at 4% loading to 20% of the film thickness at 16% copper (in the dispersion). In these films the actual film thicknesses increased with increasing nanocopper loading. The dispersions were formulated by mixing a fixed amount of nanolatex with increasing amounts of nanocopper powder, prior to the sonication treatment.

More accurate Cu concentration distributions are depicted in Fig. 25 where (1) the grid system illustrated in Figs. 22 and 23 were raster scanned for Cu content (weight %) and averaged over the grid rectangle, (2) the grids rectangles were uniformly spaced over the actual film thickness, and (3) the average values in each raster scanned rectangle were scaled to correspond to the theoretical weight of copper in the sample overall, by summing these average values, dividing by 10, and multiplying by a constant so that the theoretical weight % was obtained. The measured average in each rectangle were then multiplied by this constant to produce the values illustrated in Fig. 25. Here we see that the central or mid-film copper concentration increases in proportion to the dispersion loading. As in Fig. 24, the thickness of the bottom sediment is pronounced.

The blackish green coloration from the CuO layer around the particles may, along with the sedimentation, account for the relatively low conductivity values found in dielectric spectroscopy measurements of these films (discussed later). However, the dark coloration should suffice to impart a high affinity for light absorption with concomitant heating. Thermal diffusivity measurements obtained at the Netzsch applications laboratory in Selb, Germany with the collaboration of Dr. Andre Lindemann there are illustrated in Figs. 26 and 27.
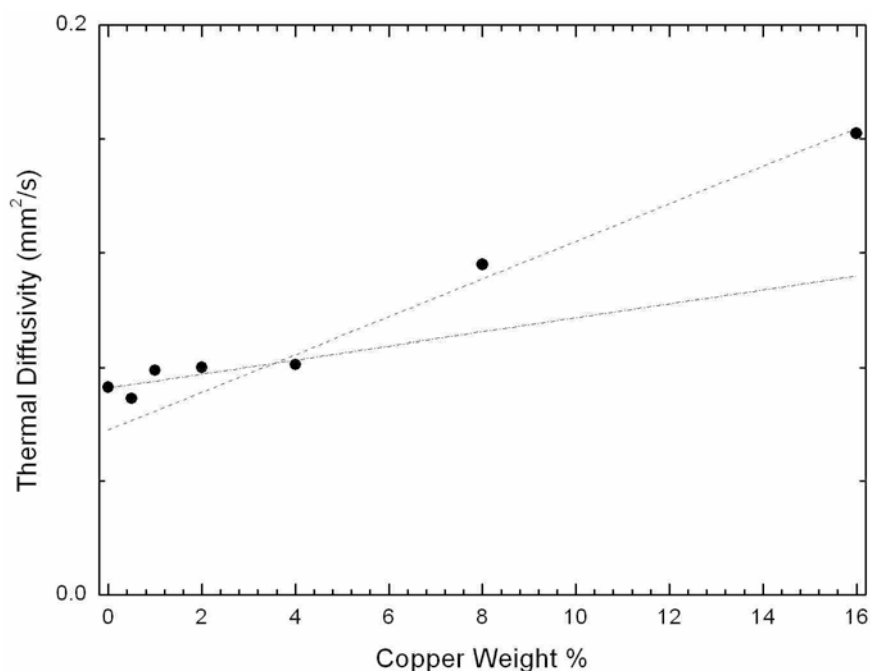

Figure 26. Thermal diffusivity of nanocopper/nanolatex films at room temperature versus weight % copper in the respective nanolatex dispersions after film drying.

The thermal diffusivity of this nanocopper/nanolatex film samples with increasing copper loading is illustrated in Fig. 26. The low copper values are essentially the same as the no copper control of about 0.07 mm^2/s. The 0-4% copper loading data were fitted to a straight

line by linear regression, and the 4, 8, and 16% loading data points were also fitted by linear regression. The intersection of these two lines indicates a break point close to 4% loading. This point corresponds to a percolation threshold in thermal diffusivity.

The temperature dependence of the thermal diffusivity for 0, 4, 8, and 16% loading thin films is illustrated in Fig. 27. There we see that the thermal diffusivity for the nanocomposite decreases very slightly on going from 25 to 100°C, and this trend is often seen in polymers. However, the control film of only the nanolatex stays rather constant at about 07 mm²/s. The high value of 0.162 ± 0.002 mm²/s clearly shows enhancement due to the dispersed (and aggregated) nanocopper. The data in Fig. 27 suggest that the percolation threshold is not significantly affected by temperature.
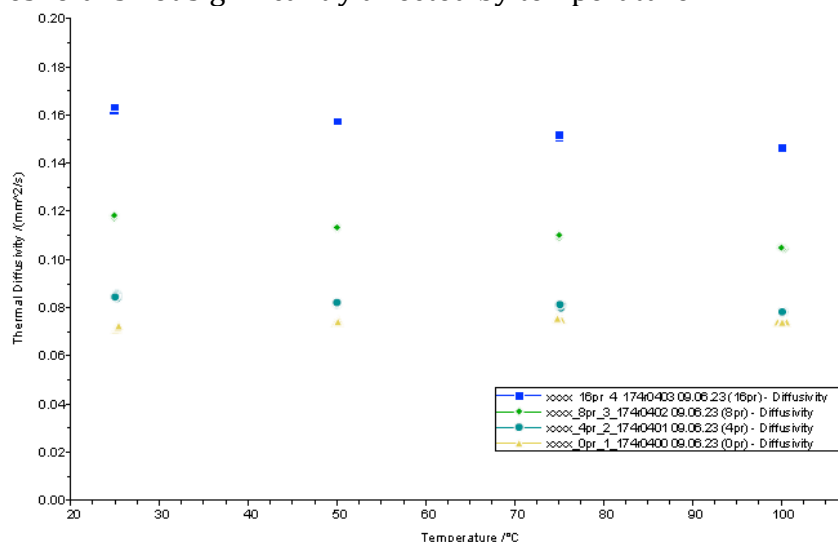
Figure 27. Thermal diffusivity versus temperature for nanocopper/nanolatex films at 0, 4, 8, and 16% (w/w) nanocopper in the nanolatex dispersions.
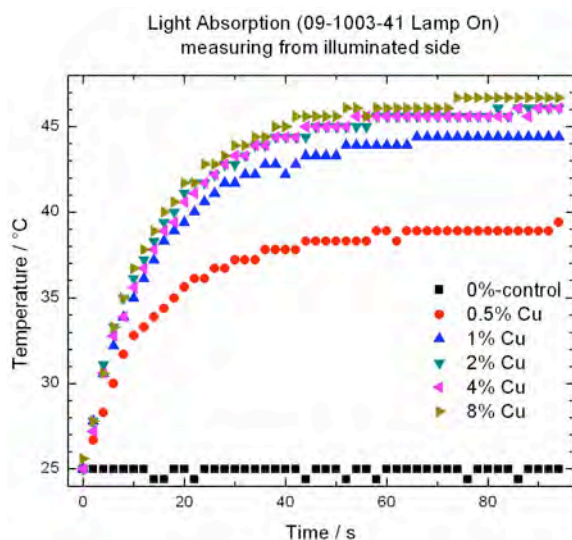
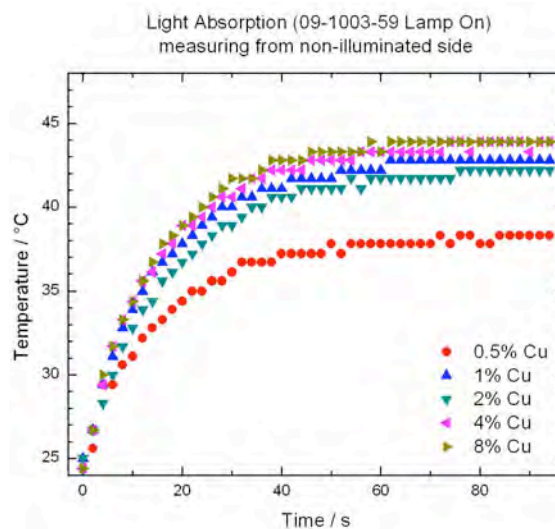**Figure 28. Photoheating of nanocopper-nanolatex films on illuminated side.**

Figure 29. Photothermal heating of nanocopper-nanolatex films on non-illuminated sides.

These experimental values can be compared with values of 0.05 mm²/s for poly(sec-butyl methacrylate), 0.11 mm²/s linear polyethylene, 0.09 mm²/s for nylon, 0.08 mm²/s for wood, 0.13 mm²/s for rubber, 1.2 mm²/s for aluminum oxide, 22 mm²/s for air, 84 mm²/s for aluminum, 112 mm²/s for copper, 166 mm²/s for silver, and 1220 mm²/s for pyrolytic graphite. Since the 16% film has about a 13% volume fraction, it is clear that thermal diffusivity is not an additive property. It is likely that this is due in part to the insulating matrix and insulating CuO coating on the nanoparticles.

As a practical matter we investigated the photothermal heating of these films using an overhead projector light source and an infrared reflective sensor for measuring surface temperatures. In these experiments the filament was diffusely focused on a circular area of the film, and the temperature was monitored using an infrared sensitive non-contact thermometer. Figure 28 shows the effect of copper loading on the temperature rise on the illuminated surface and Fig. 29 shows the backside temperature increase of the non-illuminated sides. A plate of glass was used to insulate the samples from convective heating effects. In rom ambient conditions it took about a minute to achieve maximal temperature rise, and the temperature on the illuminated side rose to about 46°C and that on the reverse side to about 44°C.

Photothermal bonding

Nanolatex films stabilizing and binding single wall carbon nanotubes (SWCNT) discussed in a later section were used to examine the photothermal bonding of nanolatex films together. Since the blackness of high quality coating and dispersions of carbon nanotubes assures a
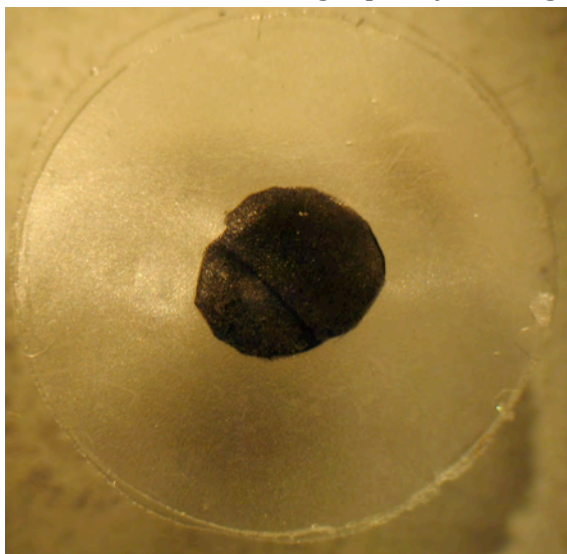

Figure 30. Photograph of two nanolatex films loosely sandwiched around a patch of SWCNT/nanolatex film.

Figure 31. Figure showing separation of nanolatex films photothermally bonded together by intervening patch of SWCNT/nanolatex film after photoirradiation.

broad spectrum of absorption of visible light, and most of this absorbed light energy is converted to heat, it would seem that light may be a convenient way to bond together plastic sheets and materials for various consume and industrial purposes.

To test this hypothesis some clear nanolatex films produced form the nanolatexes described earlier were sandwiched around an approximately circular patch of SWCNT nanolatex film (described later). A photo of this sandwich is shown in Fig. 30. This sandwich was then exposed with a focused tungsten filament lamp housed in an overhead projector, where the sample was thermally insulated from the source by a sheet of glass. After photothermally heating this sandwich the sandwich was subjected to compressive pressure, and after cooling the sample was tightly bonded together. This photothermally bonded sandwich is illustrated in Fig. 31, where some forceps are being used to separate the outer portions of the sandwich.

We envision that such waterborne SWCNT nanolatex dispersions described earlier will be useful for various kinds of photothermal bonding applications including the sealing of plastic containers for consumer use and advanced materials adhesion applications.

Solvent-free Nanofluids

Nanofluids are solvent-free viscous liquids composed of suitably surface functionalized nanoparticles [a]. Some few examples are uncharged [b], but the majority of examples reported to date may be viewed as supramolecular ionic liquids [c]. The preparation of such nanofluids is in an induction stage, but applications in producing new materials include magnetic fluids [d], [e], and novel resins [f], Previously reported nanofluids have been derived by surface modifying core nanoparticles to produce a shell or corona that induces viscous liquid behavior with apparently classical glass transition and melting transitions. Here we show that direct autocondensation of suitable alkoxysilanes produce core-free nanoparticle nanofuids that exhibit apparent lambda transitions in heat capacity centered around a glass transition (T_g) and just below the melting transition (T_m). Nanofluid nanoparticles may be synthesized as bulk condensation products. The Tg-proximal lambda transition appears to be the first experimental support for the long argued existence of a second order transition associated with a glass transition. This anomalous heat capacity spanning the glass transition shows that some glass transitions may have a thermodynamic basis in addition to a kinetic basis. The second anomaly just below the melting point shows that a solid-liquid transition of an amorphous solid may be second-order. This new class of nanofluid focuses attention on the alkoxysilane building blocks for designing functional materials. It appears that the polydispersity of these nanofluids nanoparticles may provide further insight into the role of free volume in molecular liquids.

This synthesis was motivated by analytical ultracentrifugation measurements by Volker and Coelfen (Max Planck Institute for Colloids and Interfaces, Golm) of some of our "conventional" nanosilica core nanofluids decorated by the trimethoxysilane illustrated in Fig. 1. Those measurements showed that in addition to the desired silica-core nanoparticles, a high molecular weight impurity of lower density was also present. We

therefore hypothesized that autocondensation of this same silane may also lead to nanofluids. The two step scheme of our synthesis is illustrated in Fig. 1. We first condensed the didecylmethylpropyl trimethoxyilane in methanol with a small amount of water over a two day period. After harvesting the chloride salt by centrifugation and drying, we anion exchanged the chloride by preparative potentiometric titration to produce the desired product. After suitable dialysis and drying, a nanofluid of moderate viscosity was obtained.

The resulting nanofluid is thermally robust. Although an organic-inorganic hybrid material, little decomposition can be perceived below 200°C as shown by thermal gravimetric analysis (TGA; see Supplementary Information, SI). This same TGA shows that it is straightforward to dry the nanofluid *in vacuo*, although the nanofluid is miscible with water.
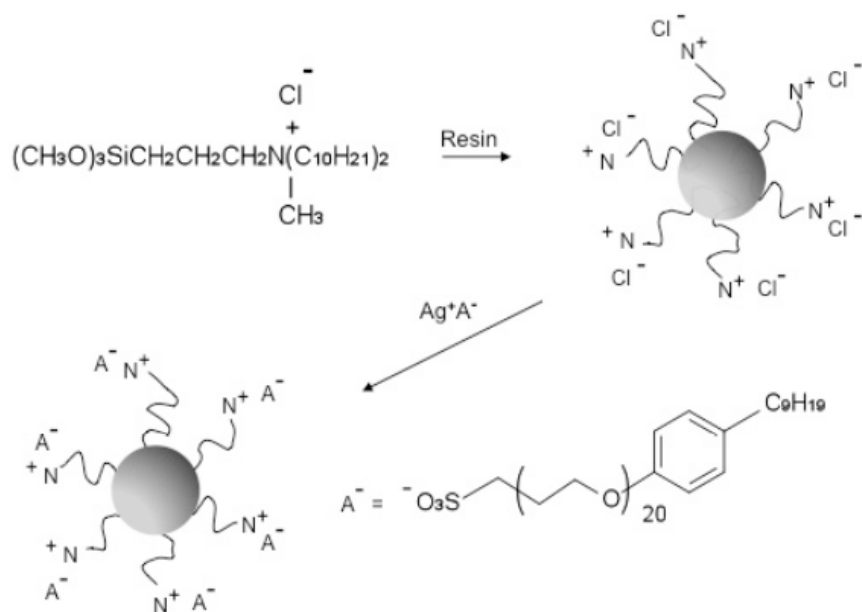
Figure 1. Synthetic scheme illustrating resin-assisted condensation of trimethoxysilane to produce chloride nanoparticulate salt, followed by anion exchange of the chloride to produce nanofluid.

We examined the reproducibility of the preparation and the sensitivity of the reproducibility to some preparative variations. The DSC (differential scanning calorimetry) of three batches (I, II, and III) of nanofluid at a relatively slow scan rate of 5°C/min is illustrated in Fig. 2. The melting endotherms over -10 to 25°C are superimposable over the main parts of the peaks, with some variability in the heat flow rate over the peak interval. We see similarly excellent reproducibility over the main part of the solidification exotherms over -25 to -35°C, with s me variability in the approach to the main part of the peak and some variation in the peak height. The glass transition at -61°C is not very noticeable in Fig. 2 because of the slow scan rate. However, the scan rate series illustrated in Fig. 3 shows that this Tg is "classical" in the sense that it is very well defined as a near step change in enthalpy flow rate and it essentially disappears from view in the limit of low scan rate.
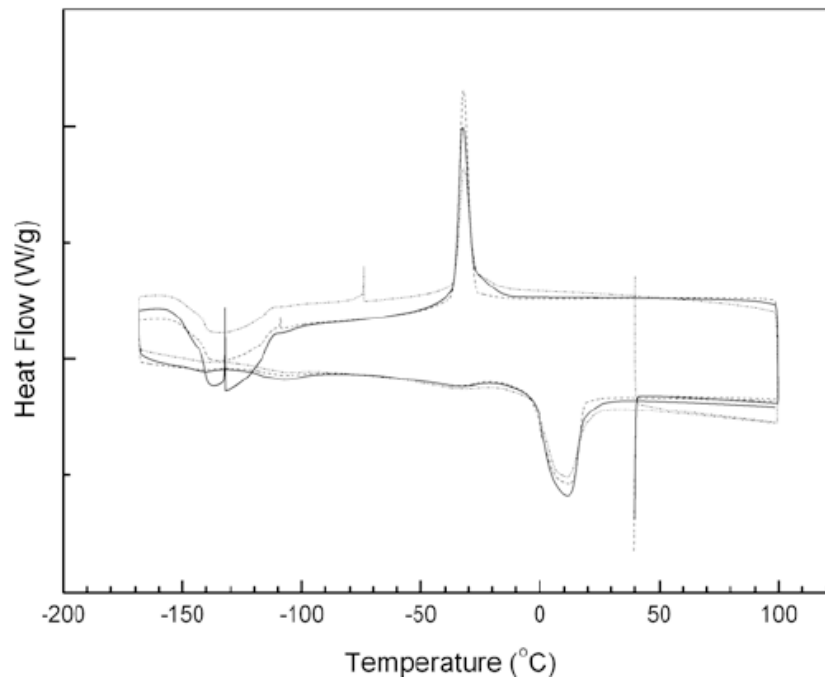
Figure 2. DSC scans of nanofluid preparations I (− −), II (......), and III (- - - -). Scans were done at 5°C/min, and initiated at about 40°C.

The same scan rate figure shows further classical behavior of a material subject to melting/solidification transitions and susceptible to glass formation. At a scan rate of the exotherms on cooling followed by the endotherms on heating appear a bit complicated, by an apparent exotherm between the glass transition on heating and the melting on further heating. This complication disappears on slowing the scan rate, and is explained by the fluid having insufficient time to equilibrate as it is cooled. At the scan rate of 15°C/min only a portion of the nanofluid can find its supra-Tg solid structure, with the remaining portion frozen as the material is super cooled further and locked into a glass structure. Upon heating up past the Tg, and yet below the melting regime, this portion of super cooled fluid continues to solidify, as evidenced by an exothermic component (the complication). Further heating produces the melting endotherm. At the higher scan rate of 20°C/min, the portion locked out of finding its supra-Tg equilibrium is increased, and the subsequent solidification upon warming past the Tg is again apparent. These are thermal phenomena well documented by many materials and are natural consequences of the hysteresis usually associated with first order melting-solidifying phase transitions and the effects of cooling rates on Boltzmann sampling of accessible super-cooled structures.
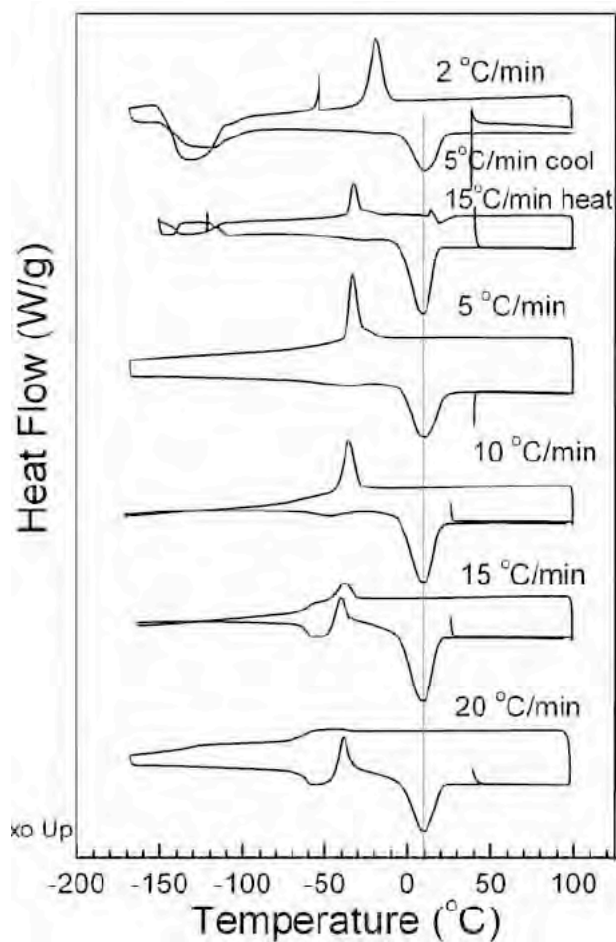
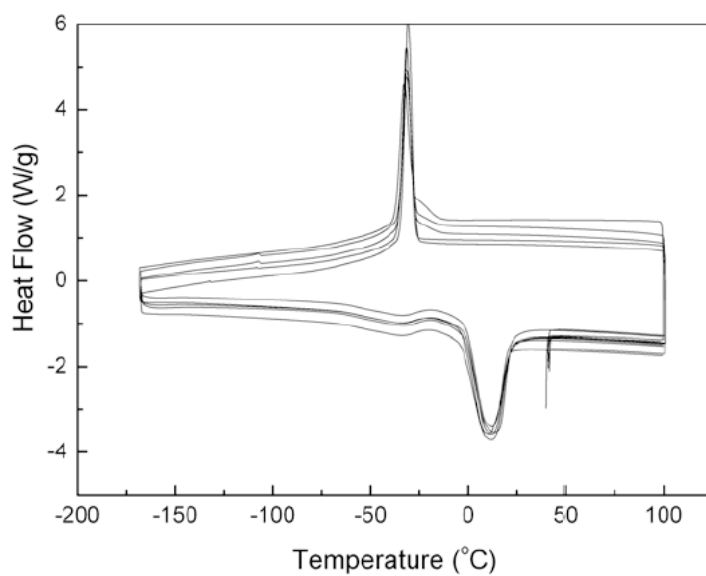**Figure 3. DSC of solvent-free nanofluid obtained at various scan rates.**

Figure 4. DSC of solvent-free nanofluid obtained by preparations illustrated in Fig 2 as well as two alternative purification procedures.

The nature of this nanofluid is further revealed by the TEM shown in Fig. 5. Firstly, the nanoparticles illustrated are not monodisperse, although they are vary small, with few examples appearing to have a visible dimension as large as 20 nm. Only a "conjoined droplet" mid-height on the left hand side of Fig. 5 appears almost 20 nm in length. The smallest particle size was probably set by dialysis tubing porosity. Particles as small as 2 nm or so appear to be present in Fig. 3. We stress that our view into particle shape through Fig. 3 is strictly two dimensional, and we impute nothing about the particle heights normal to the TEM grid support surface.

The two dimensional shapes evident in Fig. 5 vary from circular to square to oval to rectangular. Some regions exhibit very clear hexagonal packing and others exhibit rectangular lattice packing. This TEM sample was prepared from methylene chloride solution, so we cannot rationalize the patterns on the basis of thermal history alone. It is tempting to conclude that some of the particle "facets: result from close contacts with adjacent particles upon film formation, but we have no direct data yet on the properties of individual particles. All of our other data reflect collective properties. We cannot conclude that these smallest units of our nanofluid are droplets rather than "solid" particles. However, it is our belief that doublet-appearing particles are not in a state of coalescence, but rather are in a fixed state of sol-gel based fusion fixed in time.
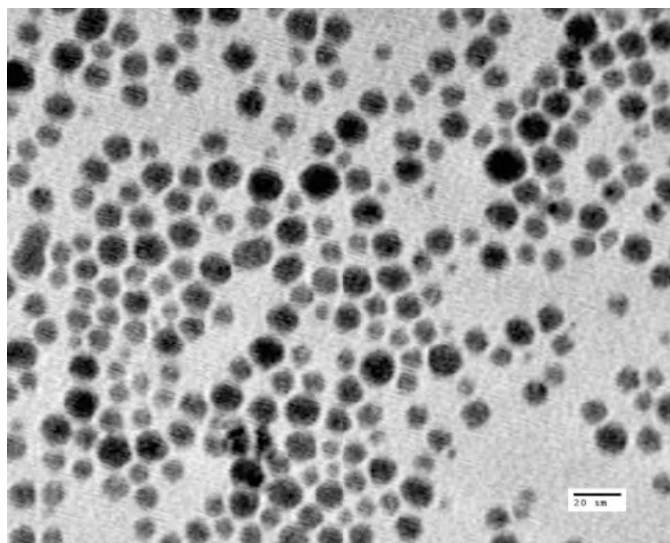

Figure 5. TEM of nanofluid prepared and examined at room temperature.

An exhaustive TEM image analysis of two separate sets of about 5,000 particles yielded number and volume frequency distributions illustrated in Fig. 6. The first moments of these distributions yielded a number average diameter of 9 nm and a volume average diameter of 12 nm. The distributions were tabulated under the assumption of effective particle sphericity, but this assumption was only for convenience and has not yet been proven.

A detailed rheology study basically mirrored the results obtained by DSC. The loss and storage moduli over (see SI) span almost ten orders of magnitude on heating and cooling between 100 and -100°C. The Tg is captured on cooling (only) as a jump discontinuity in the storage modulus at -63°C. More significant is the hysteresis on cooling and heating

through the melting11/ solidification range. At a scan rate of 3°C/min solidification occurs over -12 to -20°C. The DSC results at 2°C/min showed solidification occurring over -10 to -30°C. On heating the rheology shows melting over 3 to 23°C, and the DSC melting range traverses -1 to 22°C. The hysteresis supports the melting-solidification processes as a phase transitions. The moduli cross over one another during these melting-solidification transitions.
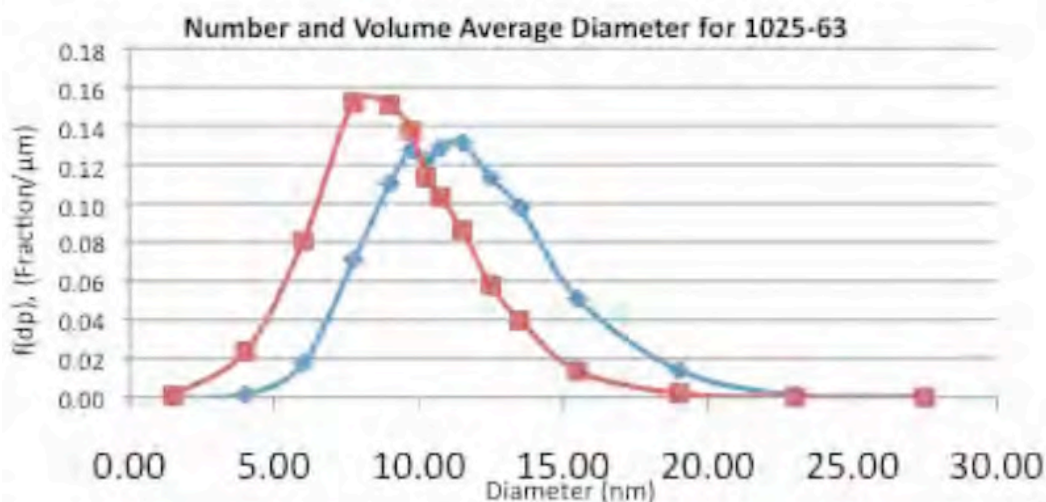

Figure 6. Number frequency and volume frequency particle size distributions obtained for nanofluid by TEM image analysis of about 10,000 particles.

Figure 7. Nanofluid rheology as a function of temperature for heating and cooling cycles. The insert shows that the Tg is revealed by a drop in the storage modulus on cooling.

The temperature dependence of the nanofluid viscosity for two nanofluid preparations is listed in Table 1 from 10°C to 150°C. The variation of from 2.4 Pa s at 30°C to 0.2 Pa s at 100°C to 0.11 Pa s at 150°C for the first listed 09-1025-73 sample are similar to those found for viscous fluids such as honey and olive oil. The range of the total variation is only a little more than one order of magnitude. The reproducibility of the results for the 09-1025-73 sample is good, while staying in the fluid temperature range. Below 30°C the fluid becomes metastable.

Viscosities were obtained for one of the runs in the super cooled state (at 20 and 10°C) but not in the other. A plot of ln(viscosity) vs 1/T yields an activation energy of about 3.9 kcal/mol. The high temperature regime has an apparent activation energy of about 1.2 kcal/mol.

An alternative approach to studying the Arrhenius behavior of the viscosities is to plot the ln(moduli magnitude) vs 1/T; this approach is illustrated in Fig. 8. Amorphous materials often exhibit high and low temperature activation energies, and this nanofluid does as well. A high temperature activation energy of 1.3 kcal/mol and a low temperature (30 to 60°C)

activation energy of 4 kcal/mol. Both of these approaches yield a Dormers fragility ratio of about 3 (3.9/1.2 = 3.3 and 4/1.3 = 3.1, respectively) qualifying this new material as a "fragile" material.

Table 1. Viscosities of two nanofluid samples up to 150°C.

T/°C	09-1025-63P Viscosity PaS	09-1025-73 Viscosity/PaS	09-1025-73 Jan 29 Viscosity/PaS
10	N/A	N/A	39.7
20	N/A	N/A	4.8
30	N/A	2.4	2.6
40	1.5	1.5	1.6
50	1	1.0	0.94
60	0.68	0.60	0.61
70	0.4	0.42	0.41
80	0.28	0.30	0.34
90	0.2	0.24	0.25
100	0.15	0.2	0.22
110	0.11	0.16	0.18
120	0.086	0.145	0.17
130	0.083	0.136	0.16
140	0.074	0.12	0.14
150	0.067	0.11	0.12
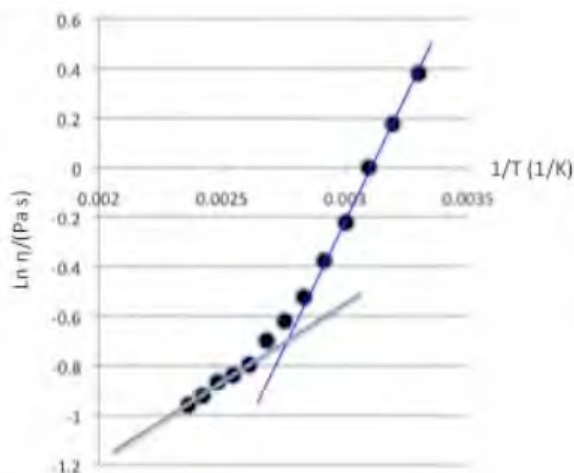
Figure 8. Nanofluid complex viscosity amplitude as a function of inverse temperature.

The melting-solidification interval can clearly be identified with hysteresis as demonstrated in fast and slow DSC scans as well as in rheological scans. Both methods, however, suggest a Tm of about -4°C, based on the average of the onset temperatures for heat flow and moduli, respectively, on cooling and on heating. However, the background heat capacity when extrapolated towards -4°C would appear to undergo a discontinuous jump there, save for the overlying lambda structure. The lambda structure suggests the

existence of a second order transition that overlies the melting-solidification interval or that melting-solidification is in fact a continuous or second order process.

Heat capacity measurements determined by a modulated (1°C/100 s) quasi-isothermal method are illustrated in Fig. 9. Surprisingly, lambda-like transitions appear to span both the glass transition and melting-solidification intervals. These features were found for three of the batches of nanofluid we prepared, as shown in Fig. 10.
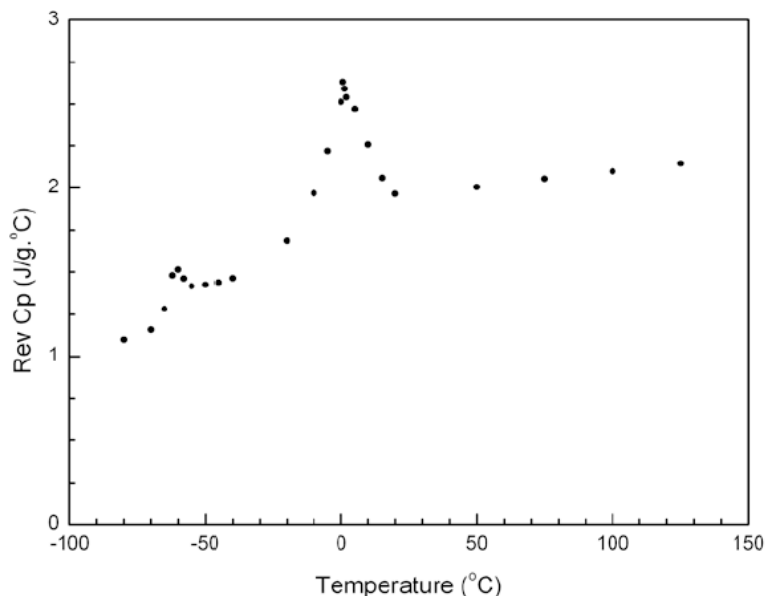

Figure 9. Heat capacity of nanofluid showing lambda-like transitions traversing the glass transition and melting-solidification regions.
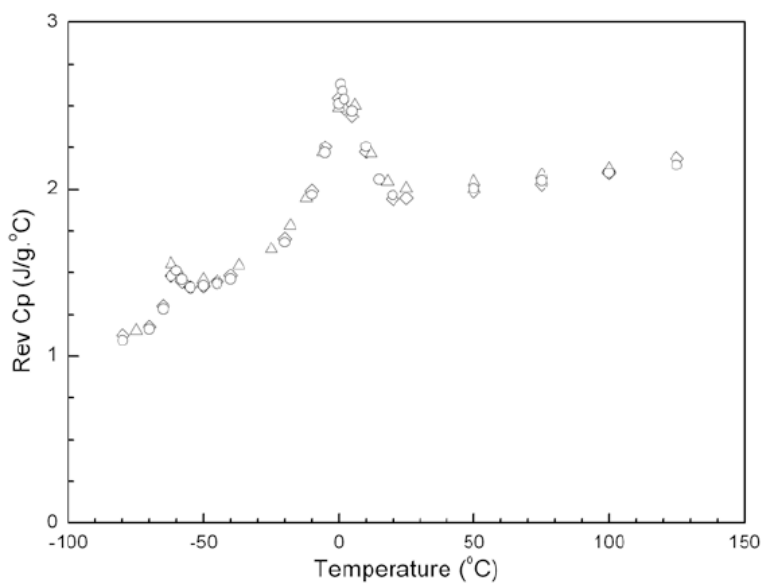
Figure 10. Heat capacity of nanofluid showing lambda-like transitions traversing the glass transition and melting-solidification regions for three different nanofluid batches.

Such an overlying second order transition may be due to cluster formation associated with sampling the energy density of states, similarly to jamming processes observed in monodisperse Of greater significance is the lambda-like transition observed over the glass transition interval. The enthalpy flow observed on cooling and heating in the DSC scan-rate data essentially vanishes on slowing the scan rate. This may be the first direct proof of a thermodynamic latent heat to be associated with a glass transition.
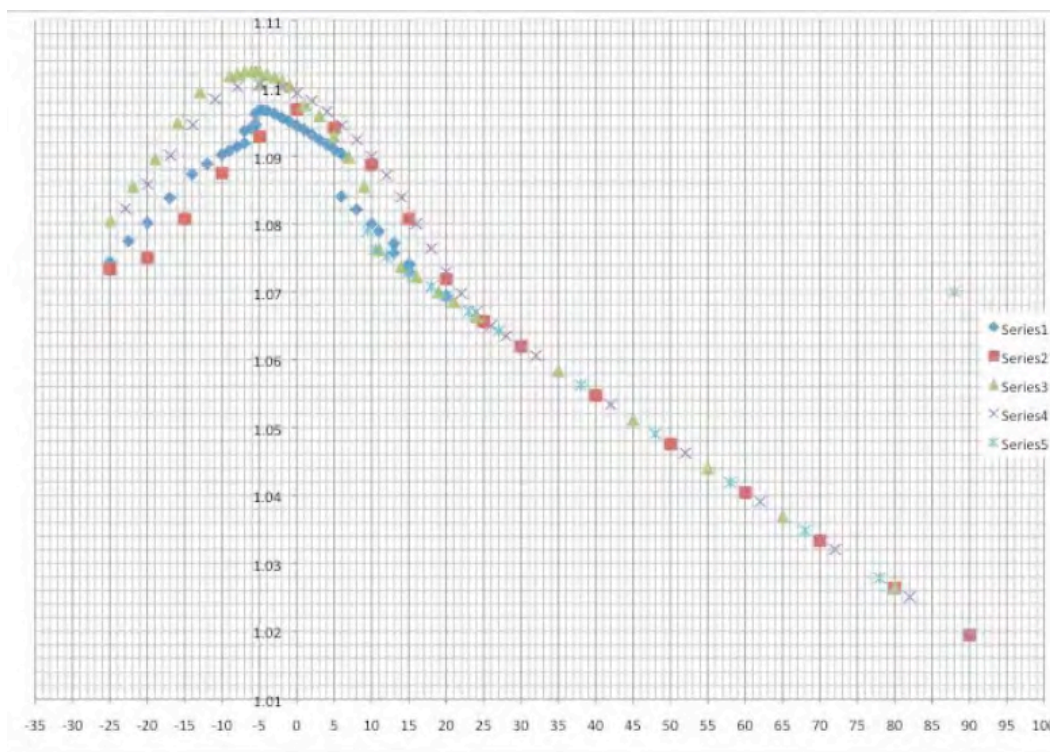
Figure 11. Nanofluid density measurements as a function of temperature (°C); each series of heating and cooling data is sequential.

A study of the density of this nanofluid is illustrated in Fig. 11. This on-going experiment, in its 4h month as of the drafting of this report, seems to show that the solidification-melting process is in fact a continuous or second order phenomenon, rather than a first-order phase transition.

While the onset of solid phase formation at about 10.5°C appears sharper than the melting process, the continuous nature of this process is unequivocal. The low temperature onset of melting appears at about 0°C, and we can therefore estimate the effective melting/freezing point as 4.5°C. This estimate is higher than that from the rheology, but the rheology could not be studied very effectively at the lower temperatures.

These density measurements were obtained using an Anton Paar DMA 4500M density meter. It's high temperature limit is 90°C. We had the low temperature limit expanded by customizing the insulation in the interior of the cell, and by passing dried air through the instrument continuously. We used an external chiller to circulate cold fluid through the instrument when working below 0°C. The instrument is based on the well known Coriollis coupling phenomenon in vibrating U-tubes and is known for the high accuracy of the method. However, the manufacturer does not condone the use of this instrument for

measuring solid densities, and we have not yet obtained a satisfactory method for calibrating its use for nominally solid samples.

While we cannot yet be certain about the accuracy of these measurements while the sample is in the solid state, the measurements do appear to be reproducible. Of particular interest is the pronounced expansion that occurs in the solid state below -5°C when the density decreases from 1.12 to 1.08 as the temperature decreases to -25°C. This anomalous expansion below -5°C is reminiscent of the expansion of ice upon freezing liquid water. It appears it may be twice as large as the relative expansion of ice compared to water as it appears to be a 20% effect.
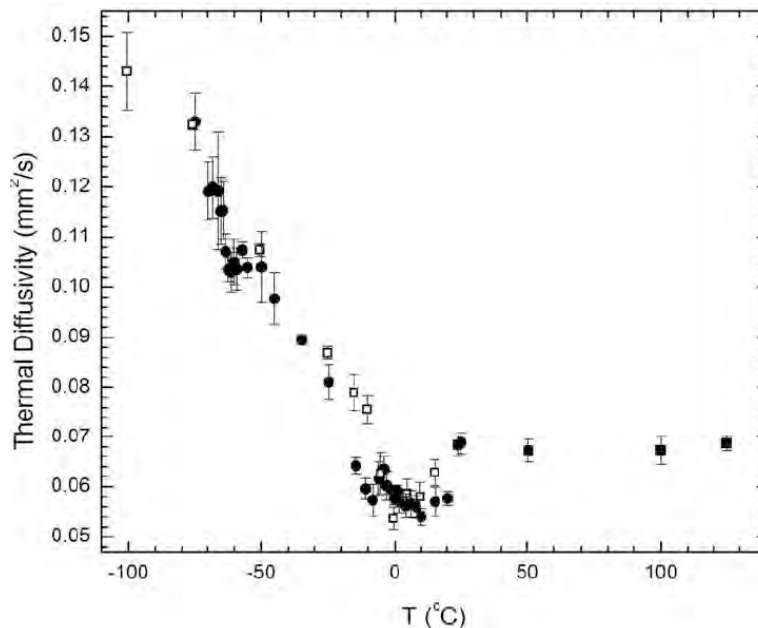
Figure 12. Thermal diffusivity of nanofluid over the range of -100 to 130°C. Open symbols – cooling; filled squares – heating.

A Netzsch LFA 457 laser flash thermal diffusivity instrument was used to examine one of the nanofluid samples. Results are shown in Fig. 12. A significant breakpoint in the data is seen at the Tg, at about -61°C, where the thermal diffusivity decreases with warming, as is conventional, but then stagnates over the -60 to -50°C interval, before resuming a decreasing trend. The behavior over the melting-solidification interval also appears anomalous. The diffusivity decreases with increasing temperature through -10°C, and then again stagnates as temperature increases to over 20°C. After this the diffusivity abruptly increases to 0.068-0.069 mm2/s, and stays in this range up to 130°C. The reversible heat capacity appears to oppositely compensate for this diffusivity dip over the melting-solidification interval, and the density appears to steadily decrease from its maximum at -5°C.

We also examined this nanofluid by broadband dielectric spectroscopy, using a Novocontrol Concept 80 system. A liquid sample cell was used, but the sample solidifies below 4°C. Measurements were commenced at 30°C over 0.1 to 107 Hz and at 10°C intervals down to -120°C and then back up to 30°C. All of the spectra (tan δ) displayed, except at -120°C, were obtained on warming. Broadly speaking the spectra overlay one

another on cooling and heating, except around the hysteretic melting-solidification transition, as might be expected.
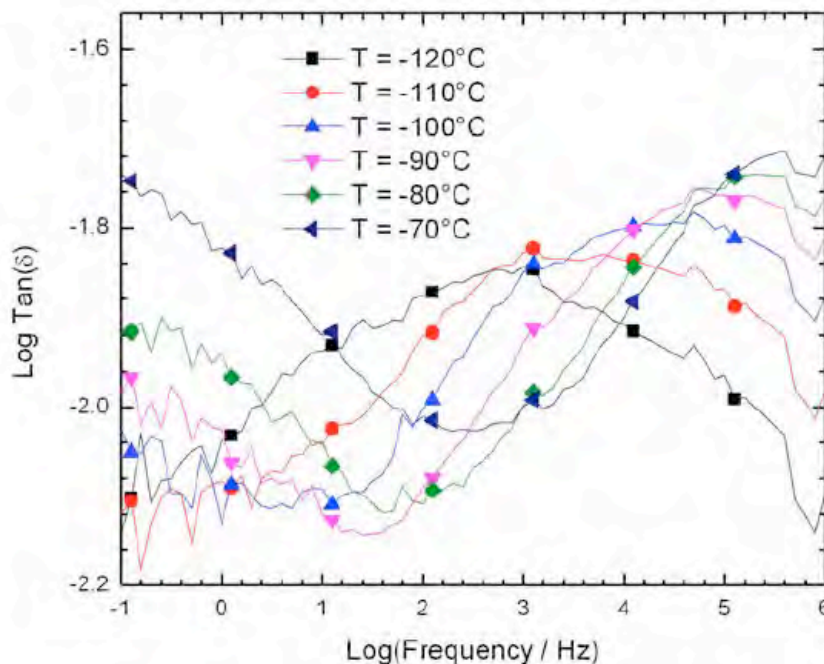

Figure 13. Log tan(δ) spectra over -120 to -70°C for nanofluid.

The data in Fig. 13 are all obtained below the Tg. A single loss peak at -120°C, centered at about 1 kHz, appears to shift to higher frequency with increasing temperature. The -70, -80, -90°C data show or suggest the existence an additional loss peak at lower frequencies. The inverse temperature dependence of the log peak frequencies in Fig. 13 is shown in Fig. 14.

The overall behavior appears Arrhenius, although the -90°C datum possibly defines a break point between two differing regimes. The slope of the left-most linear regression from -90 to -120°C is – 971. The overall fit to the dashed line is -1,633. Multiplying by the gas constant we have apparent activation energies of 1.9 kcal/mol and 3.2 kcal/mol, respectively. These values appear too small to relate to particle motion, and most likely relate internal degrees of freedom. There are many interior degrees of freedom in each particle, and many possible molecular motions and rotations possible that might exhibit such low activation.

Figure 15 illustrates the inverse temperature dependence of log tan(δ) values at 0.1, 1, and 100 Hz, respectively. We don't have a model for this behavior, although the data at 0.1 Hz appear to define some sort of Arrhenius process.

Figure 16 shows the much larger loss peaks observed at the high temperature end of our measurements, basically covering the liquid range of the nanofluid, up to 30°C. The log peak frequency vs. inverse temperature plot in Fig. 17 shows, in an approximate linear regression, that a slope of -10,600, or an activation of 21.2 kcal/mol is depicted. The typical activation energy for small molecule liquid diffusion is about 4 kcal/mol.
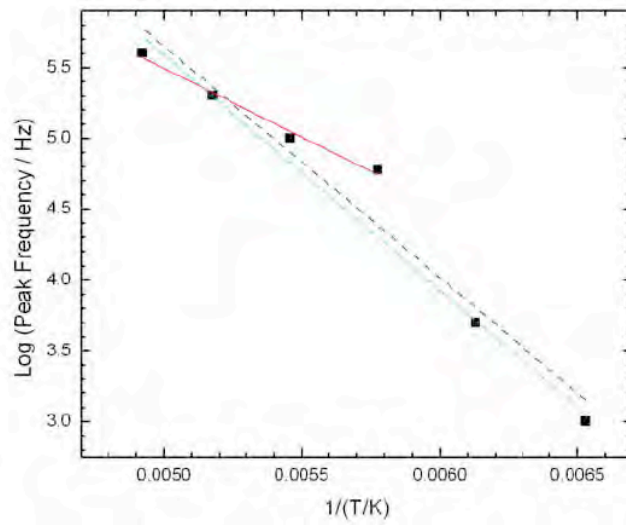
Figure 14. Inverse temperature dependence of loss peak frequencies on warming from -120°C to -70°C.
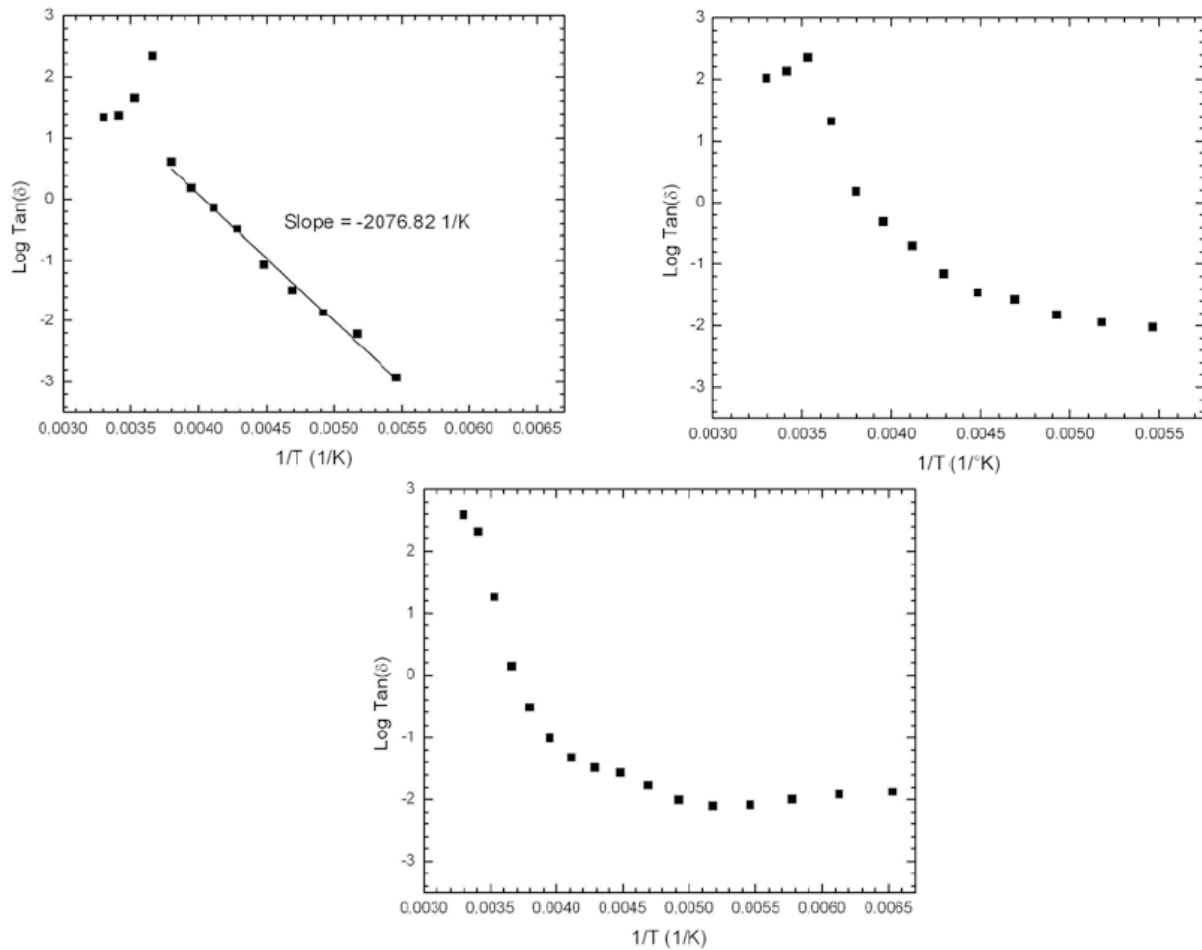

Figure 15. Log tan(δ) magnitude as a function of inverse temperature for spectra of nanofluid at (left) 0.1 Hz; (right) 1 Hz; (lower) 100 Hz. The temperature ranges (upper) from -120°C to 0°C in 10°C increments and (lower) from -120°C to 30°C.
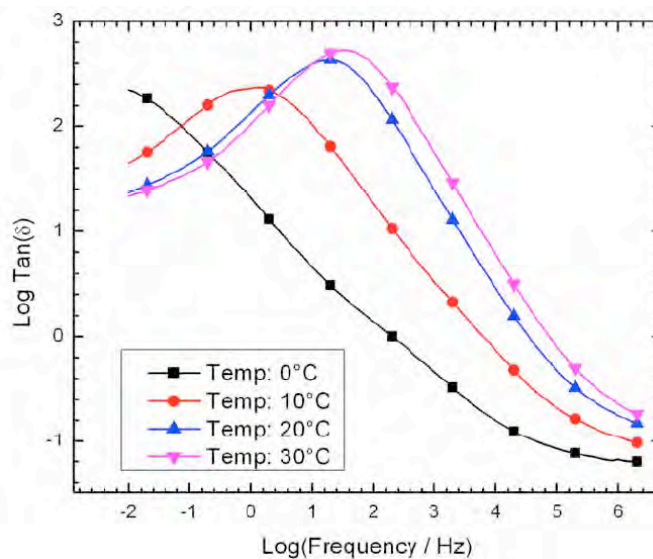
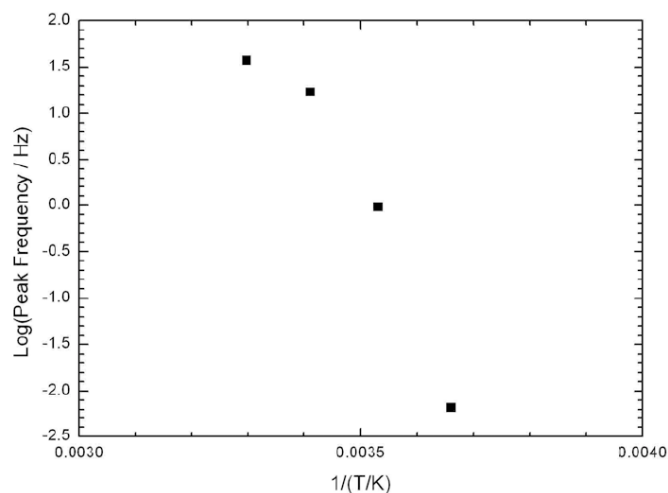**Figure 16. "High temperature" loss peaks of the nanofluid.**

Figure 17. Log peak frequency versus inverse temperature for the high temperature peaks depicted in Fig. 16.

The thermal stability of this nanofluid is illustrated in the thermogravimetric analysis illustrated in Fig. 18. The material basically appears thermally robust up to about 200°C. If the heat capacity of this nanaofluid could be substantially increased, it may serve as a new class of heat exchanging fluid over elevated temperature intervals. Future work should focus on including ion exchange groups within the sol-gel condensed article (as would results from doping with sulfo trimethoxysilane reagents) so that metals could be simply ion exchanged in and reduced to produce internal metallic phases.
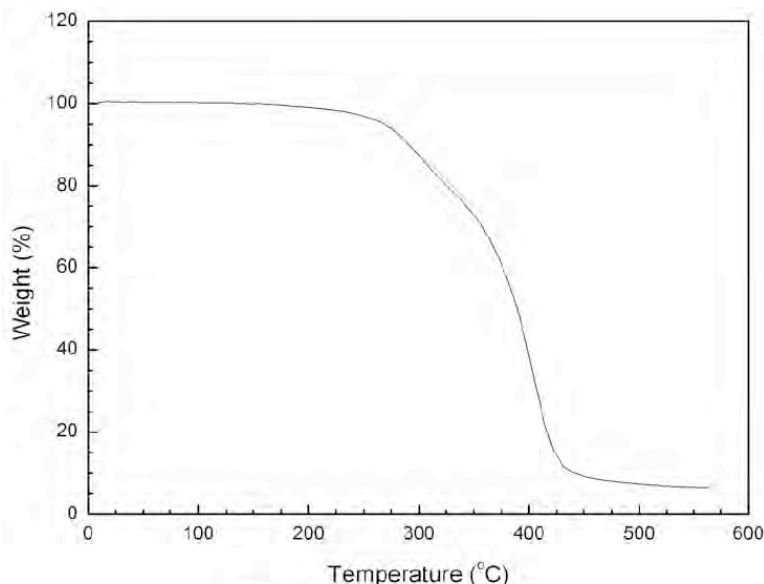
Figure 18. TGA of nanofluid.

Research Task 10

Hybrid electrical conductivity materials

Electrically conductive materials for electronics applications, for electrostatic charge dissipation, and for EMI shielding applications will be similarly derived by perfusing suitably porous polymers or random arrays of polymer beads with metal, carbon, and/or semiconducting nanoparticles.

WC nanoparticle/nanolatex films

This application showed how to stabilize and disperse WC nanoparticles in water wherein the particles are 1-3 nm in diameter. This work was published as archival publication No. 9, and the abstract is presented here:

Many inorganic nanoparticles are produced as powders, but their utilization is almost always in dispersion or suspension form. We present a novel nanolatex that is very effective at producing the first reported stable waterborne dispersions of nanoparticulate WC, starting with highly aggregated WC nanopowder. Transmission electron micrographs show that the nanopowder is highly dispersed in/on the hydrogel nanolatex particles. Thermal diffusivity, dielectric loss, optical, and mechanical properties of thin films derived from waternorne dispersions are presented. Such waterborne disperisons and nanocomposite films represent new materials for photothermal, hardening, and abrasive/polishing applications.

SWCNT/nanolatexes

This application showed convincingly that our nanolatexes could successfully stabilize SWCNT in water, betterthan any surfactant has been shown to do. This work was published as archival publication No. 3, and the abstract is presented here:

We report a nanolatex copolymer derived from an imidalozium bromide reactive acrylate surfactant. These nanolatexes and moderate sonication provide stable dispersions of single walled carbon nanotubes (SWCNTs) and electrically conducting coatings that adhere to plastics. The stable dispersions produced are the most concentrated in SWCNTs yet reported (1.4% w/w), and they form robust films. The electrically conducting networks formed upon film formation provide a new route to priming plastics for electrodeposition in addition to other applications. The efficacy of these nanolatexes is assigned to the imidazolium and bromide components shown in other studies to have an affinity for graphene surfaces.

The TOC graphic in Fig. 1 illustrates the mechanism of nanolatex stabilization hypothesized in this study. This cartoon illustrates that as exfoliation progresses, the number of surface bonds to exfoliated tubes with imidazolium bromide end groups can increase. The model also illustrates how nanolatexes bound to partially exfoliated tubes dramatically increase the effective inertia of the exfoliated segments. Such an inertial increase is expected to promote further exfoliation.
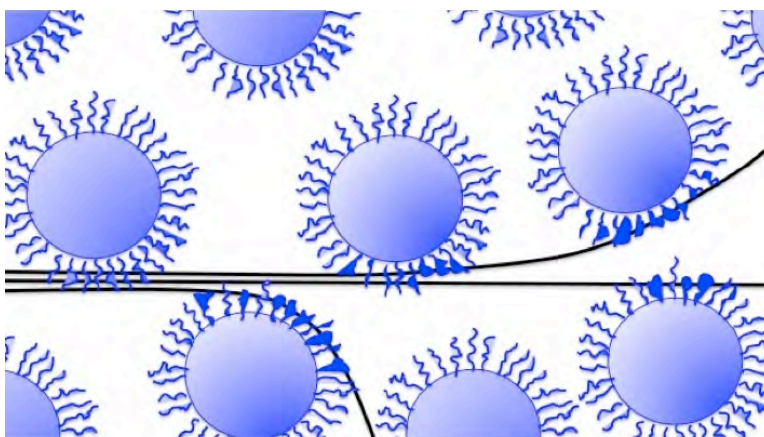

Figure 1. Two dimensional model illustrating mechanism of nanolatex stabilization of SWCNT during bundle exfoliation. The nanolatex diameter to SWCNT diameter is approximated at about 27nm:1nm in conformity with actual sizes. The mechanism of imidazolium bromide binding is illustrated as occurring through the outermost groups of the nanolatex that bind to the SWCNT partially before exfoliation and more so as the exfoliation progresses.

HTC/Nanolatexes

Our nanolatex-based waterborne dispersion work on hydrothermal carbons was continued with a view of comparing effects of various methods of N-doping, wherein the HTC is prepared by an autoclaving process. The sample HC-GA-750 was examined in a preliminary study and reported in last year's progress report. A recent publication summarizing this preliminary study of HCGA- 750 recently appeared in *Polymer*, and is included in the copies of publications appended to this report. The five samples reported on here and their formulation are described in the following:

Derived by autoclaving at 180°C overnight. The balance of all percentages is water.

HC-CH-750   10% Chitosan; after drying the powder, treated further at 750°C under nitrogen

HC-GA-750   10% Glucosamine; after drying the powder, treated further at 750°C under nitrogen

GMELA10N   10% Glucose; 10% Melamine; carbonized under nitrogen

K60G2N   10% Glucose, 2% K60 (BASF PVP); carbonized under nitrogen

72WF10N   10% Furfural; 10% 72W (BASF PVP/Polyvinylimidazole copolymer); carbonized under nitrogen

Luvitec® K 60 (BASF) is a 34-36% by weight solution of polyvinylpyrrolidone (PVP) in water with a pH of 7-9 and less than 0.03% nonvolatile residue. This polymer has a K value of 52-62 when dissolved at 1% in water.
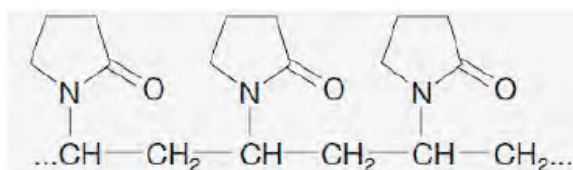
PVP

The K value is calculated from dilute solution viscosity measurements and is used to approximate the degree of polymerization:

$$\frac{\log(N_s/N_0)}{c} = \frac{75K^2}{1+1.5\,Kc} + K$$

where *Ns* is the solution viscosity, *No* is the solvent viscosity, and *c* in the polymer weight concentration in g/mL.

Luvitec® VPI 55 K72W (BASF) is a copolymer of vinyl pyrrolidone and vinyl imidazole.
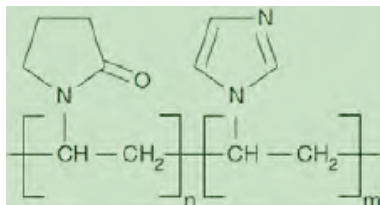
PVP-*co*-PVI

In this second phase of the study we made dispersions of 5 different biomass samples (HC-CH- 750, HC-GA-750, GMELA 10N, 72WF10N and K60G2N) in 16% w/w nanolatex. Each dispersion was prepared using approximately the same procedure:

1. Grind biomass sample in mortar and pestle;

2. Measure 2% w/w mixture of biomass sample and nanolatex;

3. Sonicate for 1 hour in ultra-sonic bath;

4. Check optical density of dispersion (the zero time optical density was that obtained for the dispersion after sonicating in a low power cleaning bath for one hour);

5. Sonicate directly at 50% power using the 1/8" probe, keeping the temperature below 50^0C, checking the optical density periodically, until the change in optical density with sonication time begins to approach zero. Optical density was determined at 500 nm by typically taking a 50 uL sample, adding it to a tared vial, and then adding deionized water (and again weighing) to dilute the sample so that an optical density between 0.1 and 1.0 was measured; the "equivalent" optical density was then computed by multiplying the experimental optical density by the dilution factor obtained gravimetrically.

6. Sonicate directly at 100% power using the 1/8" probe, keeping the temperature below 50^0C, checking the optical density periodically, again until the change in effective optical density with sonication time begins to approach zero.

7. Make castings of the resulting dispersions (2 round and 2 rectangular).

8. Centrifuge remaining dispersions at 3000RPM for 2 hours.

9. Separate supernatant from sediment.

Figure 1 shows that the ease and extent to which the five HTC samples disperse in aqueous nanolatex varies greatly, by over a factor of ten. Increasing optical density is taken as a measure of increasingly finely divided dispersion of the HTC, in analogy to similar studies of SWCNT and MWCNT, where complete exfoliation was shown to be achievable with an effective plateau in dispersion optical density. Some further insight into why some of the samples disperse more or less easily will come from further experiments discussed later. For now it suffices to note that the K60G2N disperses most extensively, and later it will appear that this sample is the most porous of the samples. The GMELA10N sample appears second most easily dispersed, reaching an optical density about 40% of that from K60G2N.
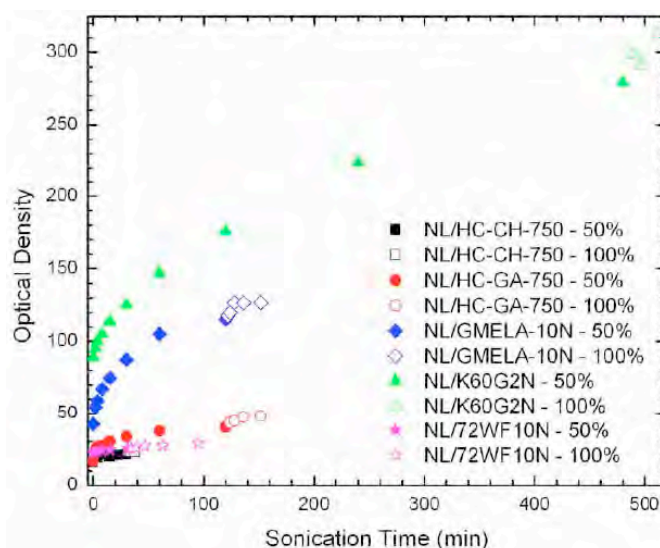
Figure 1. Equivalent optical density at 500 nm of HTC/NL (nanolatex) dispersions.

The remaining three samples are similar in poor dispersability by this sonication/nanolatex method, but they do differ in ultimate optical density with HC-GA-750 > 72WF10N > HC-CH-750.

We hypothesize that the relative ease of dispersion by sonication is related to the porosities of respective HTC samples. At present we do not have a quantitative measure of porosity for each material, but subsequent SEM images show that the K60G2N sample is very porous. If this hypothesis is borne out, the dispersion mechanism can be attributed to pore wall fracture.

Hydro-Thermal Carbon Nanolatex Dispersion Supernatant and Sediment Composition

The dispersions 2% w/w in nanolatex of the various hydro-thermal carbon samples that were prepared as described above were then used to make circular and rectangular wafers for further conductivity and morphology tests. A set of castings were made of the dispersions. Then the remaining amounts of dispersions were placed in a centrifuge for 2 hours at 3000 RPM. The supernatant was drawn out of the centrifuge tube using a Pasteur pipette. The boundary line between supernatant and sediment was determined by monitoring visually the optical density of the fluid being drawn up into the narrow part of the Pasteur pipette. When the fluid became darker (more optically dense), the removal was stopped, and what was left was determined to be sediment. In all cases the sediment was observed to have at least two layers, a slurry layer underneath a more fluid layer. The more fluid layer was a thin layer between the slurry and the supernatant, and was much more optically dense (blacker) than the slurry and the supernatant. Before anything further was done with the sediment, it was mixed together with a small steel spatula.

There were two notable exceptions to the above procedure. 1) After centrifuging and separating sample GMELA10N it was realized that castings of the pre-centrifuged dispersion sample had not been made. The sample was remixed, castings were made, then the sample was centrifuged and separated again. So there are two sets of measurements for this sample. 2) The centrifuge malfunctioned while spinning sample K60G2N. In order to

ensure a centrifuge dose consistent with the other samples, the sample was remixed and centrifuged again.

The distribution of samples by weight among supernatant and sediment is quantified in Table 1 with respect to actual weight and with respect to weight fraction. The GMELA10N dispersion

Table 1. Distribution of dispersion samples among supernatant and sediment after centrifugation.

Sample	Supernatant weight (g)	Weight fraction (w/w)	Sediment weight (g)	Weight fraction (w/w)
HC-CH-750	7.4594	0.957	0.3348	0.043
HC-GA-750	5.2434	0.949	0.2829	0.051
GMELA10N (1st)	8.0072	0.929	0.6072	0.071
GMELA10N (2nd)	5.2093	0.932	0.3827	0.068
K60G2N	5.5136	0.947	0.3075	0.053
72WF10N	5.6912	0.96	0.2355	0.040

provided the largest weight fraction sediment. The K60G2N and HC-GA-750 dispersions were
similar and next most highest, and the HC-CH-750 and 72WF10N samples were lowest in sediment fraction. The sediment weight fraction is composed of three contributions: (1) sedimented HTC particulates; (2) nanolatex particles adsorbed to the HTC particles and in suspension in the water present in the sediment; (3) water.

Table 2. Composition of samples based on TGA analysis

Sample	Wt% Water (%)	Wt% Latex (residue) (%)	Wt% HTC (%)	Wt% Residue (%)	Max Free Wt% Latex	Min Adsorbed Latex/HTC Wt Ratio
nanolatex 09-1045-57	82.00	18.00		0.27		
nanolatex 10-1079-68	85.02	14.98		0.22		
nanolatex 10-1089-9	87.58	12.42		0.19		
72WF10N-sediment	33.9	8.4 (0.1)	57.7	57.8	6.4	0.035
GMELA-sediment	49.7	13.9 (0.2)	36.4	36.6	9.4	0.124
HC-CH-750 sediment	23.1	8.9 (0.1)	68.0	68.1	4.4	0.066
HC-GA-750 sediment	44.8	12.4 (0.1)	42.8	42.9	8.5	0.091
K60G2N-sediment	40.6	12.2 (0.1)	47.2	47.3	7.7	0.095
HC-GA-750-supernatant	80.0	19.1 (0.3)	0.9	1.1	15.2	4.33
HC-CH-750 09-1045-58	80.51	15.5 (0.2)	2.0	2.23		

TGA analysis of three nanolatex samples shows in Table 2 that the remaining residue varies from 0.19 to 0.27% by weight. The relative amount of residue to original nanolatex solids is 1.5% in all three nanolatex samples. The residue at 575°C was taken as the remaining HTC in combination with the residue from nanolatex decomposition, about 1.5% of the nanolatex in the sample. The weight % nanolatex was taken as the double wave decomposition following water loss plus the small residue amount estimated to come from the total nanolatex (shown in parenthesis in the third column of Table 2). These absolute

amounts of nanolatex and HTC were then converted into relative amounts as illustrated in Table 3.

The last column in Table 2 represents an estimate of the minimum ratio of adsorbed latex to HTC solids, as a weight ratio. The supernatant was not analyzed for most of the samples, so we do not know very well how the different components were distributed between the supernatant and sediment. However, these minimum estimates suggest that the two samples that dispersed least easily (Fig. 1), HC-CH-70 and 72WF10N, have the lowest estimates of adsorbed latex per unit weight HTC, consistent with such samples having the lowest specific surface area of the sedimented particulates. Similarly, GMELA10N and K60G2N have the best dispersability, as shown in Fig. 1, and appear to have the highest estimates of adsorbed latex per gram HTC. However, the K60G2n sample disperses much more easily than the GMELA10N, while the GMELA10N sample has a much higher estimate of adsorbed latex per gram. The HC-HG-750 sample is a close third in poor dispersability (Fig.1), but very close to K60G2N in the value of its minimum ratio of adsorbed latex to HTC solids estimate.

A similar grouping of samples can be inferred from the gross latex to HTC solids ratio given in Table 3. The HC-CH-750 and 72WF10N samples, as the most poorly dispersing, exhibit the lowest ratios. The second best dispersing sample GMELA10N has the highest latex to HTC ratio for the sediment. However, the best dispersing sample, K60G2N, has a slightly lower ratio than does the HC-CH-750 sample. A more extensive adsorption analysis will be needed to more clearly associate ease of dispersibility with HTC specific surface area. However, see the subsequent section on SEM analysis of nanolatex adsorption for images of saturation irreversible nanolatex adsorption on the HC-CH-750 and K60G2N sediment samples.

Table 3. The relative amount of latex to hydro-thermal carbon for the various samples.

Sample	Wt% Latex (%)	Wt% HTC (%)	Latex/HTC Wt Ratio
72WF10N-sediment	12.7	87.3	0.145
GMELA10N-sediment	27.6	72.4	0.381
HC-CH-750_sediment	11.6	88.4	0.131
HC-GA-750_sediment	22.5	77.5	0.290
K60G2N-sediment	20.5	79.5	0.258
HC-GA-750-Supernatant	95.5	4.5	21.2
HC-CH-750_09-1045-58	88.6	11.4	7.77

10. Make castings of supernatant (2 round and 2 rectangular).

11. Make castings of sediment (1 round and 1 rectangular).

This procedure was followed with the following exceptions:

1. With the GMELA10N dispersion it was neglected to make castings before centrifugation. The dispersion was remixed and castings made. The remixed dispersion had an optical density close to the value before centrifugation (OD before centrifuge = 126.9, OD after remix = 132.5). The optical density of the supernatant after the first centrifugation was

14.2. It was 9.5 after remixing and centrifuging again.

2. With the K60G2N dispersion the centrifuge did not function properly, so the dispersion was remixed and centrifuged a second time after the centrifuge was made to function properly (OD before centrifuge = 312.5, OD after remix = 310.1).

TGA of Dispersion Sediment

Thermogravimetric analyses of the HC-GA-750 supernatant, five dispersion sediment samples and of the dispersion of HC-CH-750 are presented below in Figs. 2-8. Table 4 below illustrates effects of drying between the time that the sample pan with sample was suspended and when the automated measurements were commenced. These effects were negligible with most being less than 0.5% relative to total sample weight. The deviation for HC-GA-750 was, however, the largest.

Table 4. Initial Weights of Samples Analyzed by TGA

Sample	Initial Wt (mg)	First Measurement Wt (mg)	% Change
nanolatex_09-1045-57	7.798	7.763	0.45
72WF10N-sediment	7.080	7.046	0.48
GMELA10N-sediment	9.714	9.678	0.37
HC-CH-750-sediment	6.510	6.482	0.43
HC-GA-750-sediment	11.245	11.214	0.28
K60G2N-sediment	10.281	10.242	0.38
HC-GA-750-supernatant	6.158	6.123	0.57
HC-CH-750 09-1045-58	10.392	10.355	0.36
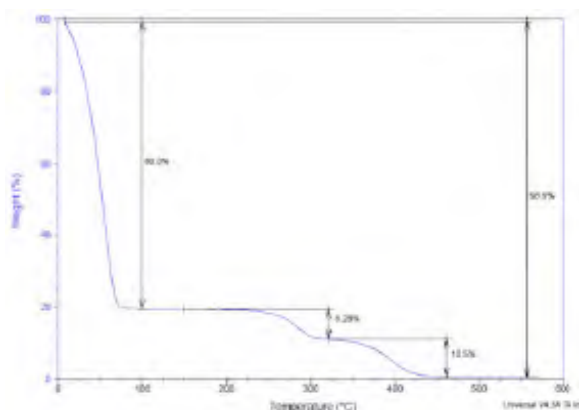
Figure 2. HC-GA-750 Supernatant TGA
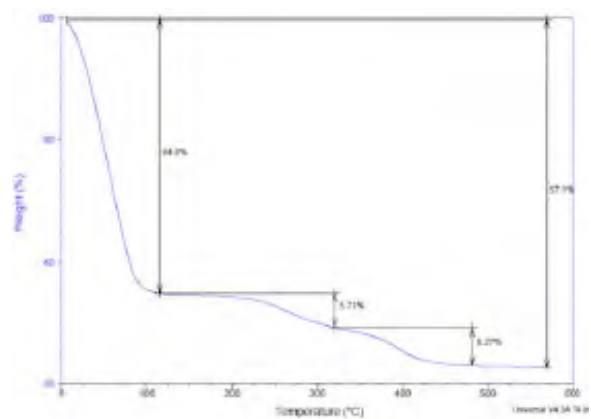
Figure 3. HC-GA-750 Sediment TGA
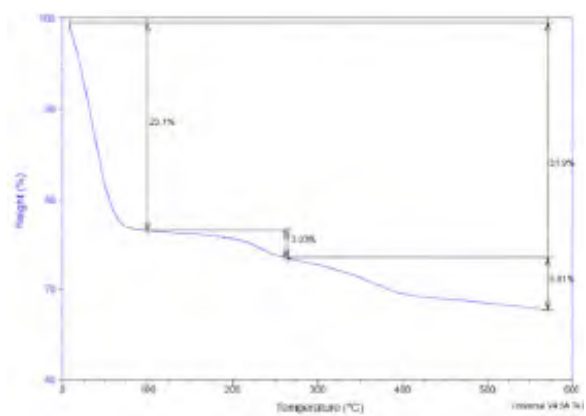
Figure 4. HC-CH-750 Sediment TGA
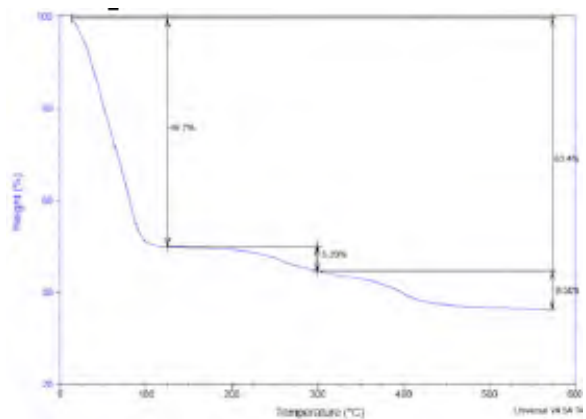
Figure 5. GMELA10N Sediment TGA
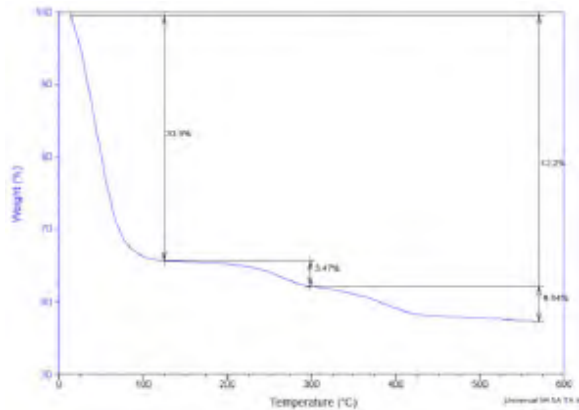
Figure 6. 72WF10N Sediment TGA
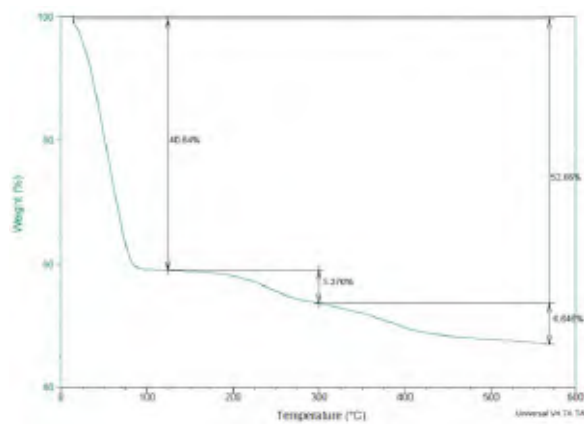
Figure 7. K60G2N Sediment TGA
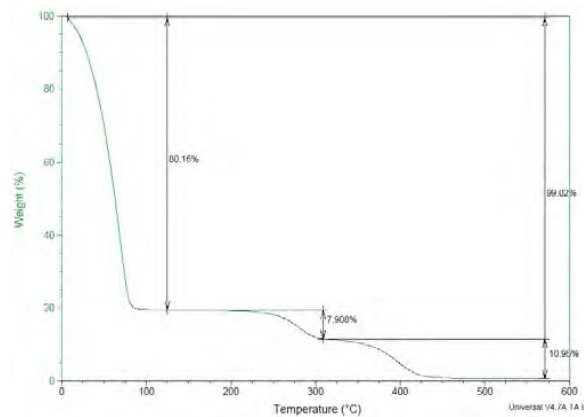
Figure 8. HC-CH-750 Dispersion TGA

SEM/EDAX Analyses of Dispersion Castings

The dispersions were used to make a series of castings of 25mm---diameter wafers and rectangular films about 25mm long and 8mm wide so that various conductivity and SEM analyses could be made. In Figs. 9---14 we illustrate SEMs of freeze fracture cross---sections of circular wafers and illustrate a rectangular grid system used to analyze for

weight percent C and Br. Figure 15 illustrates the numerical results of these EDAX-based C and Br analyses in a series of bar charts.

The nanolatex control film cross-section is shown in Fig. 14. This film has no HTC in it and the artifacts seen such as a mottled surface in the righthand half of Fig. 14 and an apparently surface porated structure along the top side (left hand side of the figure) of the film can be taken to be characteristic of HTC-free nanolatex.
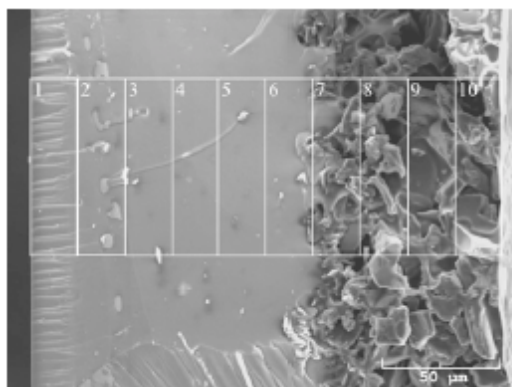
Figure 9. HC–CH–750
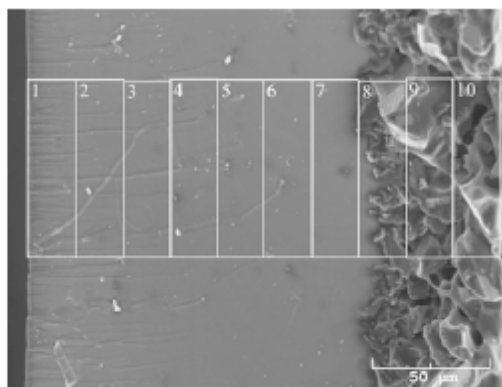
Figure 10. 72WF10N
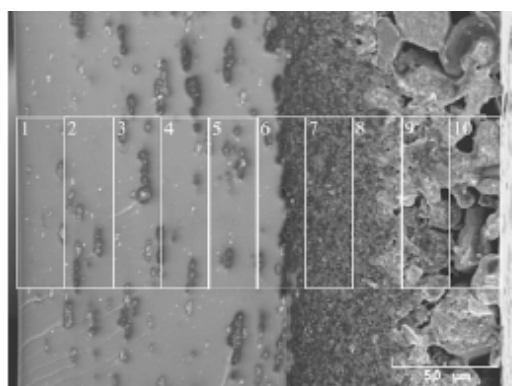
Figure 13. K60G2N
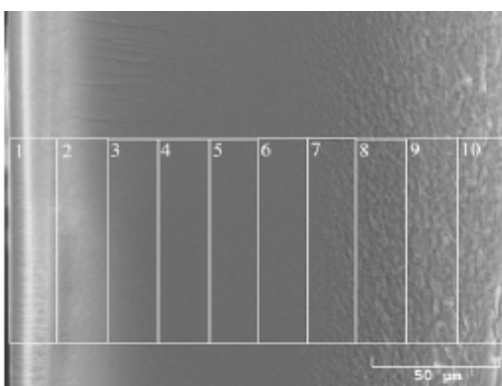
Figure 14. nanolatex
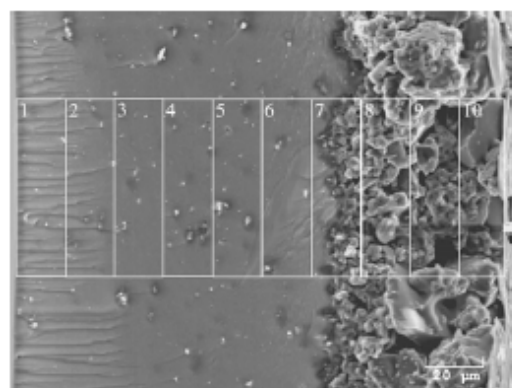
Figure 11. HC–GA–750
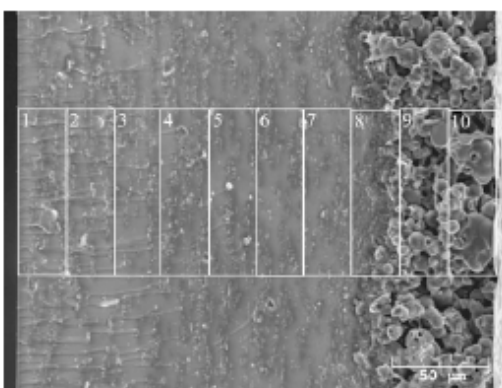
Figure 12. GMELA10N

The casting for dispersions of HC-CH-750 and 72W10N in Figs. 9 and 10, respectively, show that the bulk of the sediment is compacted at the bottom of the film (right hand side of figure). The presumably mostly nanolatex film to the left of the compacted sediment has a

few particulates visible, but otherwise does not appear to be grossly heterogeneous. The HC-GA-750 sample in Fig. 11 yielded a higher effective optical density, by about 60%, than did HC-CH-750 and 72W10N (Fig. 1), and the mostly nanolatex domain on the lefthand side in Fig. appears to have many more particulates suspended therein. This progression in increased particulates within the nanolatex upper part of the film continues with the GMELA10N sample in Fig. 12. K60G2N, the most highly dispersed sample, exhibits a very difference texture to the freeze fracture SEM in Fig. 13. The texture of the mostly nanolatex layer appears very different than in the other samples. In addition, a very thick layer of very fine sediment appears at the interface between the mostly nanolatex layer and the larger sediment at the bottom of the film. This progression in particulate changes seems very consistent with the limiting effective optical densities depicted in Fig. 1.

The rectangular grid system pictured in each of Figs. 9-15 illustrate domains over which we raster scanned EDAX elemental analyses, relying on the x-ray fluorescence generated by the scanning electrons. We focused on analyzing for Br, C, and O, and in plotting the relative weight
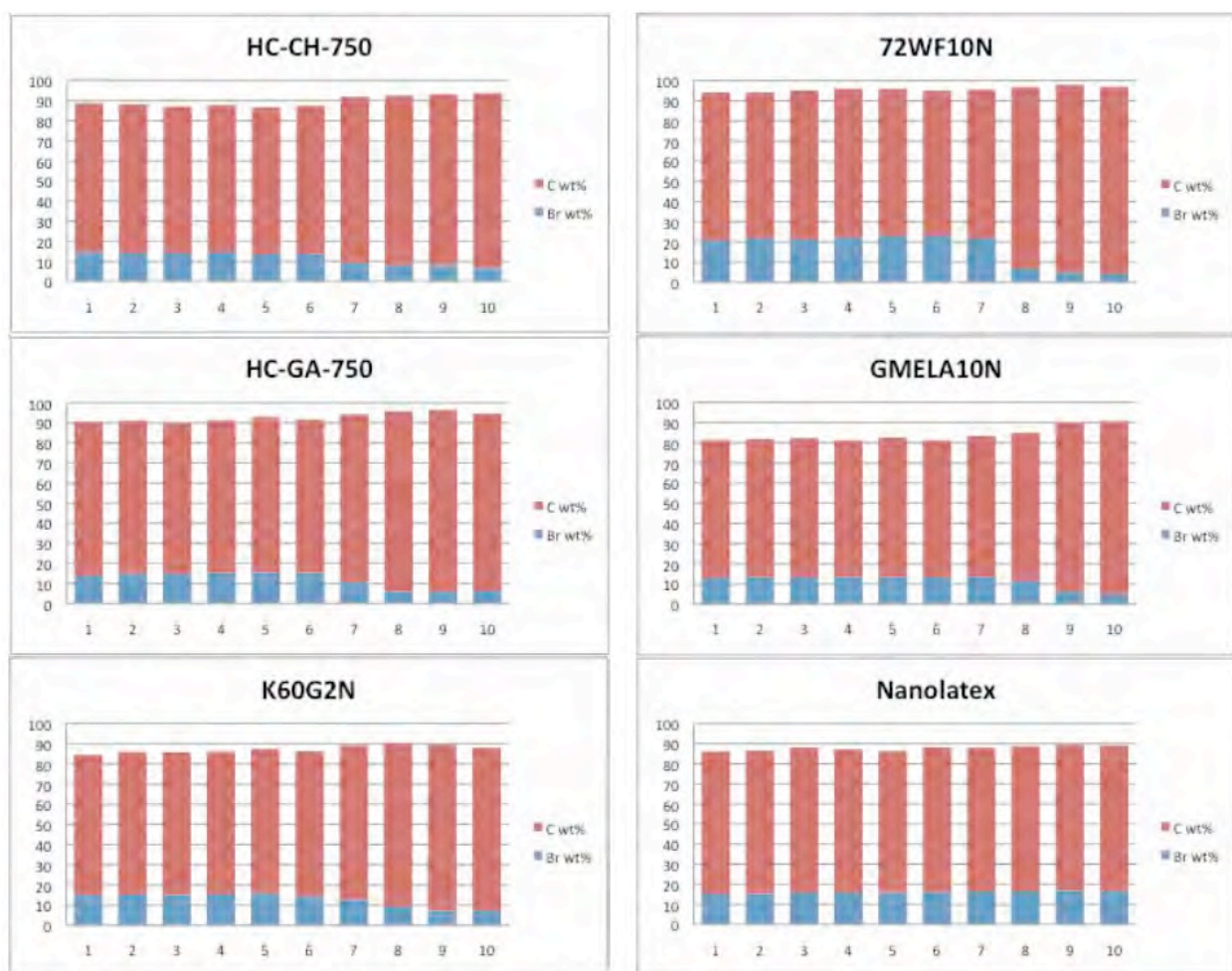
Figure 15.

percentage of Br and C in the various rectangular domains across the samples. For the nanolatex in the absence of water, the theoretical weight percentages of Br, C, and O are

14.1, 65.6, and 20.3 %, respectively. While EDAX analyses are not known for their outstanding accuracy, particularly for the very light elements like C and O, we see in Fig. 15 for Br in the
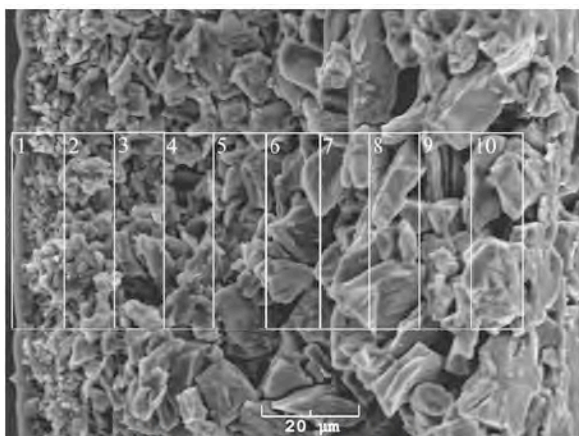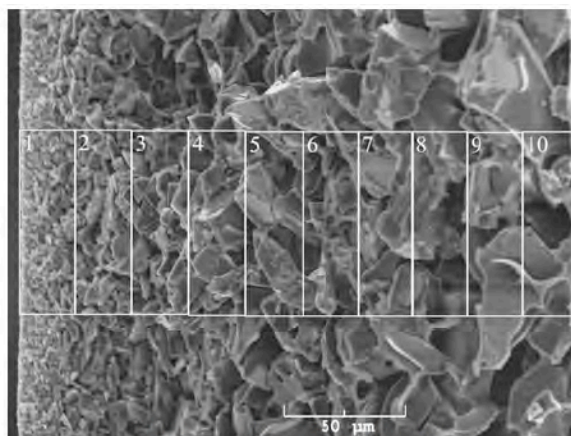

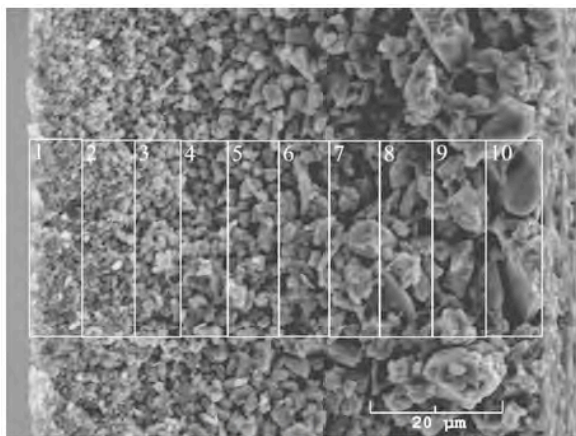Figure 16. HC-CH-750

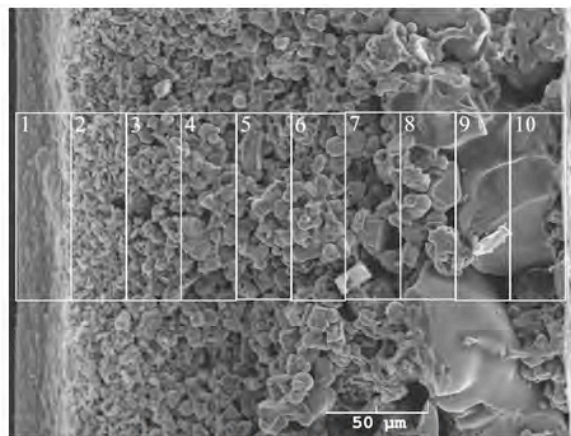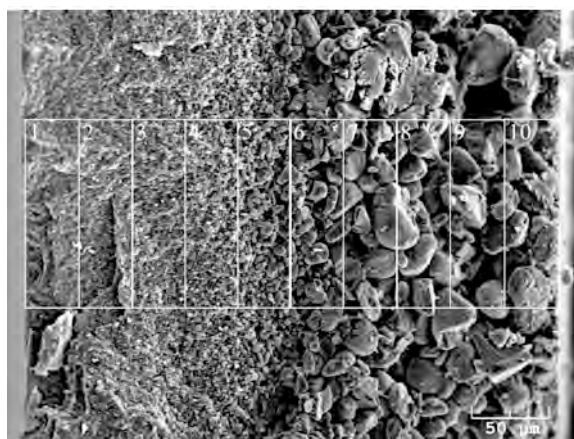Figure 17. 72WF10N

Figure 18. HC-GA-750

Figure 19. GMELA10N

Figure 20. K60G2N

nanolatex that the measured results, in this control sample, range from 18% at the "bottom" to 15% at the "top". The C appears overestimated by 6% (at 72%) uniformly across the sample (and O is proportionately underestimated). The depressed Br values in

the top two to four rectangular regions, overall, nicely correlate with the visual sediment images and the widths of these sediment layers in Figs. 2-9.

SEM/EDAX Analyses of Sediment Castings

Similar analyses were made of wafers and films made from the sediment produced by centrifugation of the various dispersions. SEMs of freeze fracture cross-sections are illustrated below in Figs. 16-20. The sediment slurries were vigorously stirred before the wafers and films were cast, and the illustrated gradation in particle size from gravitational sedimentation nicely illustrates the range in particle sizes produced in the dispersion/sonication process.

Sample HC-CH-750 and 72WF10N appear to have larger particles traversing the bottom (righthand sides) 60% and the finer particles appear to occupy a volume fraction less than 15- 20%. These observations are consistent with these samples being the least dispersed (Fig. 1). The sediment distribution for K60G2N in Fig. 20 appears to be composed of a fine sediment of about 50% of the layer width and larger particles in the bottom half of the film. This distribution
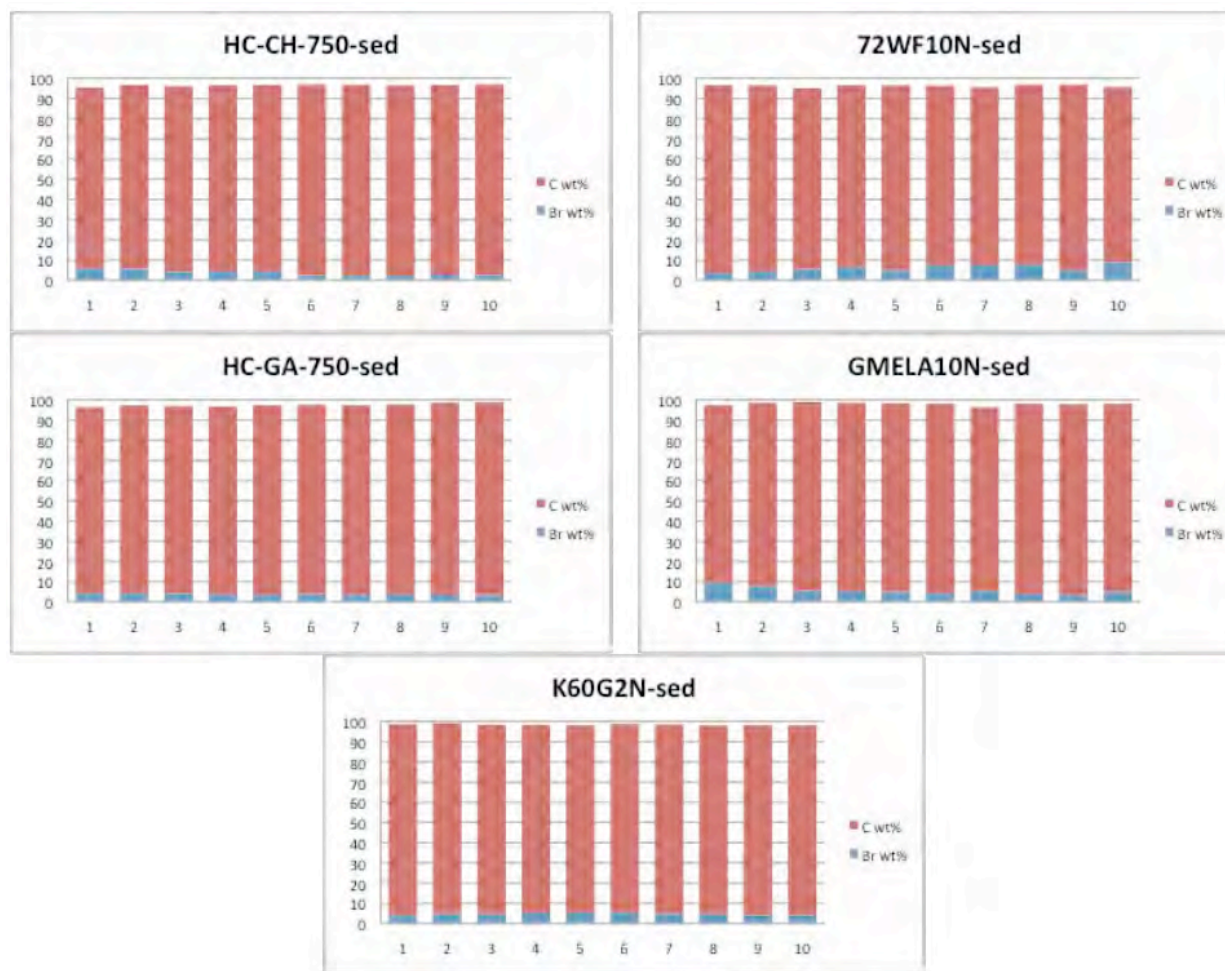

Figure 21. EDAX elemental analysis of C, O, and Br in sediment castings.

is consistent with this sample being the most highly dispersed (Fig. 1). It is not so obvious why the GMEAL10N (Fig. 19) sample disperses much more extensively than HC-GA-750 (Fig. 18). EDAX analyses for Br, C, and O in these sediment films showed essentially two phenomena. Firstly, the weight percent of Br was dramatically suppressed over the nanolatex level, consistent with the nanolatex content being greatly reduced. In addition, the C content was also significantly
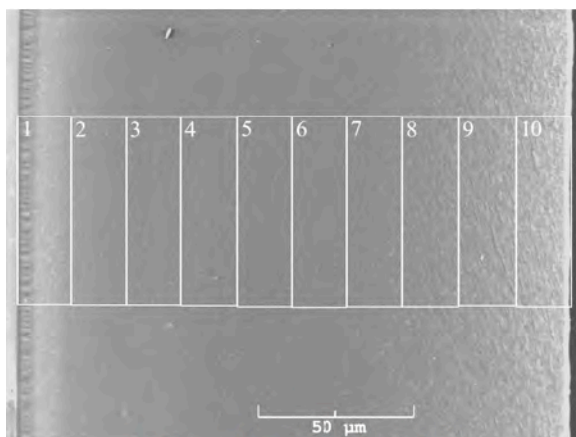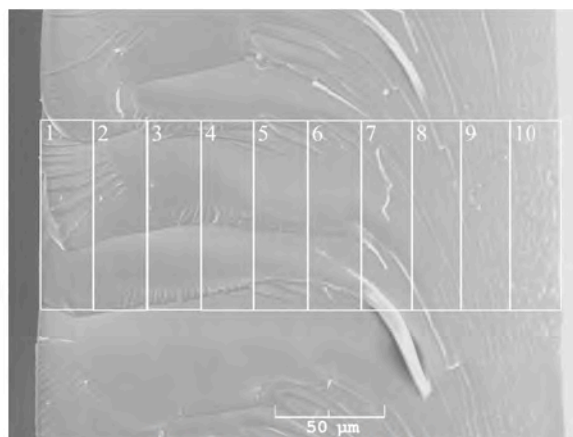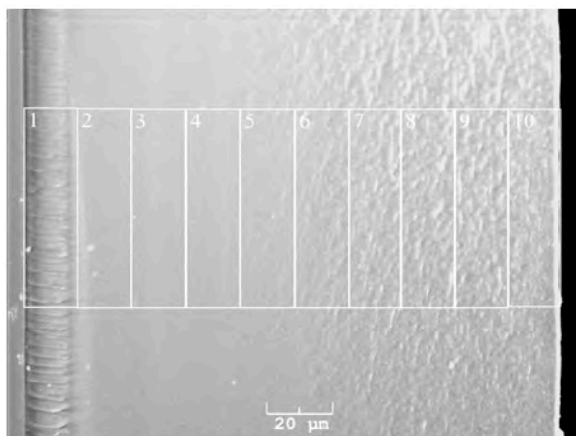

Figure 22. HC-CH-750

Figure 23. 72WF10N

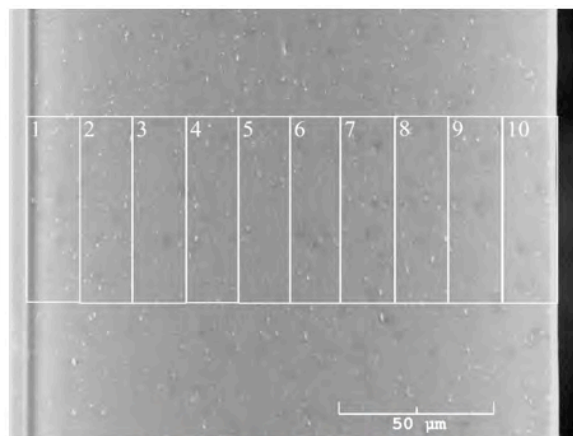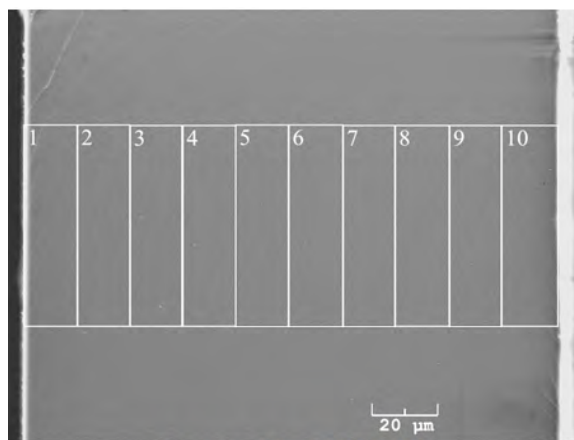**Figure 24. HC-GA-750**

Figure 25. GMELA10N

Figure 26. K60G2N

increased, consistent with the films being composed mostly of HTC C particulates. The TGA analyses of the sediment summarized in Table 3 suggests that Br should vary between 1.5 to 5% by weight, and this range is seen in the Br measurements of Fig. 21.

SEM/EDAX Analyses of Supernatant Castings

Similar film cross-sections made from castings of the supernatant are illustrated in Figs. 22-26. The three least dispersing samples, HC-CH-750, 72WF10N, and HC-GA-750 (Figs 22-24, respectively), appear very similar to the nanolatex control cross-section of Fig. 14. The GMEL10N cross-section with quite noticeable particulates distinguishes this supernatant sample. The K60G2N cross-section appears very uniform, except for a very thin layer of very fine sediment at the bottom (righthand side) of the film.

The EDAX analyses of these supernatant film cross-sections do not reveal any qualitative features, except that the Br and C contents appear too high in most of the samples.
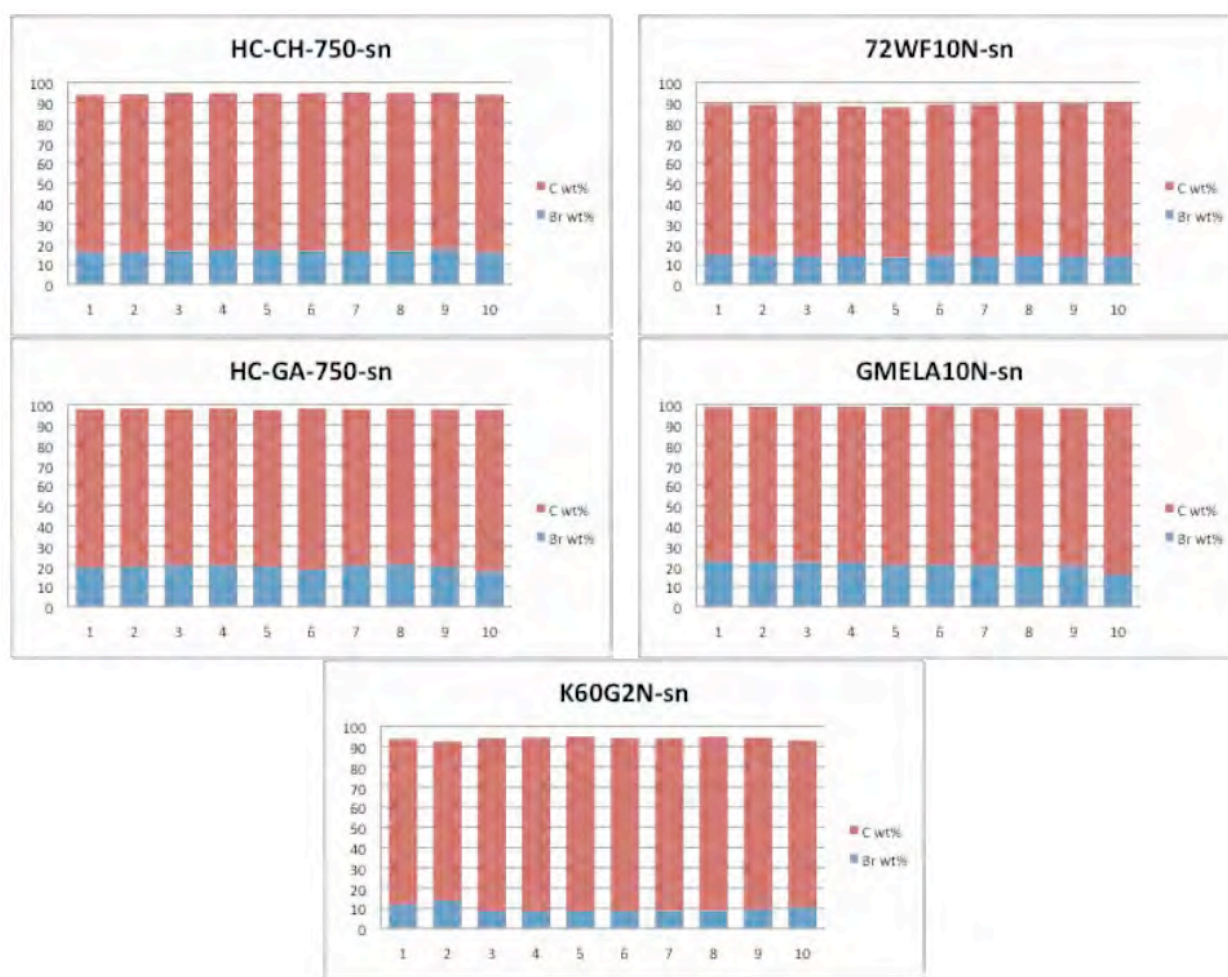

Figure 27. EDAX elemental analysis of C, O, and Br in supernatant castings.

Adsorption of nanolatex onto HTC surfaces (SEM analysis) While the mode of HTC dispersion for the smallest HTC particulates by the nanolatex is not certain, we have found that the mode of adsorption of the nanolatex onto HTC surfaces appears to be random and irreversible. We base this conclusion on SEM images of the worst and best dispersing HTC

samples, Hc-CH-750 and K60G2N, respectively. The images analyzed were found in the freeze fracture cross-sections illustrated in Figs. 28 and 29. The Hc-CH-750 sample offers a greater number of relatively large and flat surfaces to image, while the K60G2N sample offers fewer expansive flat surfaces and mostly porous and rounded surfaces.
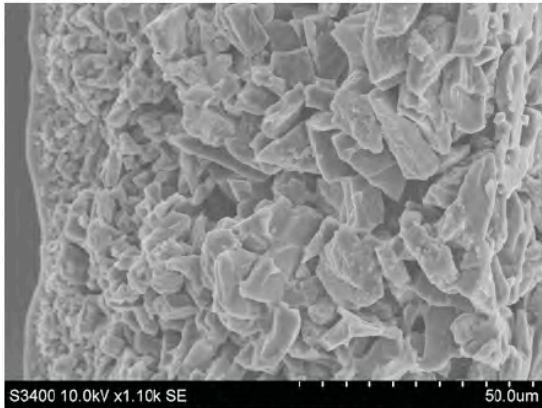

Figure 28. SEM of HC-CH-750 sediment cross-section fracture surface.
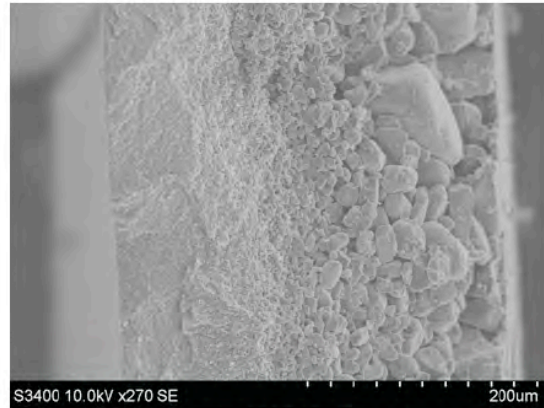

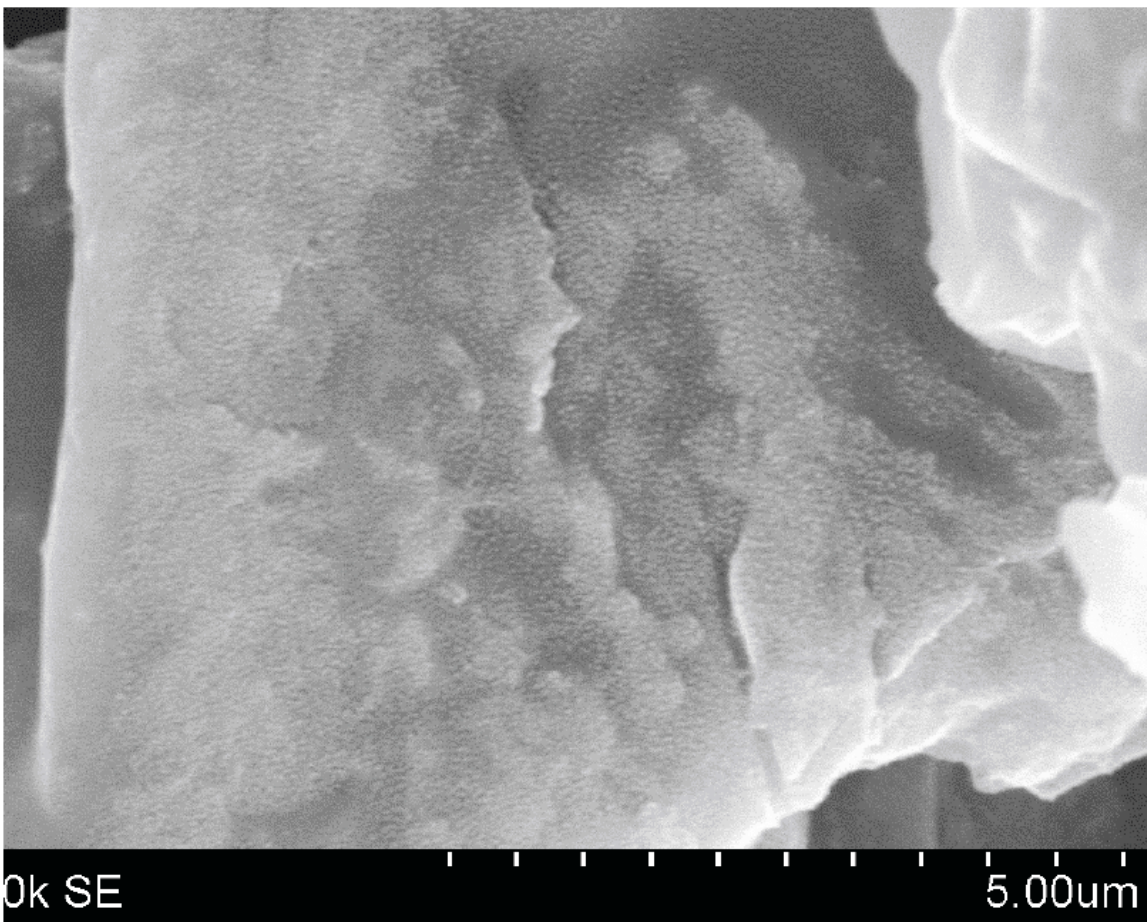**Figure 29. SEM of K60G2N sediment cross-section fracture surface.**

Figure 30. SEM of HC-CH-750 sediment illustrating adsorbed nanolatex particles.
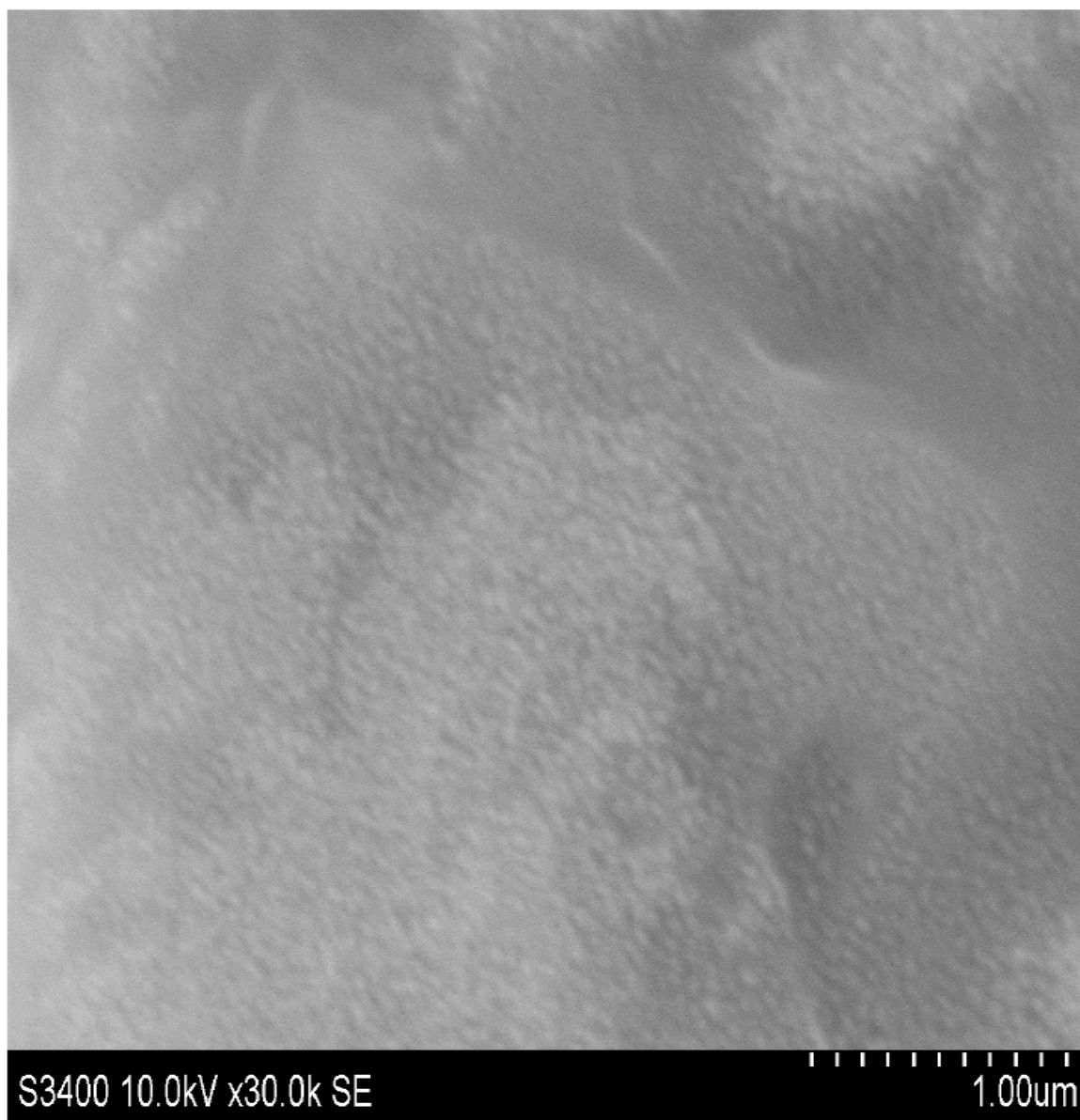
Figure 31. SEM of HC-CH-750 sediment illustrating adsorbed nanolatex particles.

Figures 30 and 31 illustrate saturation packing of the nanolatex on HC-CH-750, and Figures 32 and 33 illustrate saturation adsorption on K60G2N surfaces. The highest packing density would be a close-packed hexagonal packing pattern. Such a packing pattern might be obtained if adsorption of nanolatex particles were annealed and subject to an equilibration processes.

Distorted hexagonal assemblies can be found in parts of the images for each sample, but this mode of packing is not predominant. If we posit an adsorption mechanism based on imidazolium bromide groups binding to HTC sites, and that each nanolatex particle binds with multiple points of contact, the adsorption mechanism can become effectively irreversible.

In the near future we plan to quantitatively examine the packing density of nanolatex particles on the surface of these and other samples. Our SEM analyses indicate regions of adsorption that appear to be templated in parallel rows. We expect to soon have FE-SEM imaging that hopefully will provide greater detail on the packing density and apparent adsorption mechanisms.
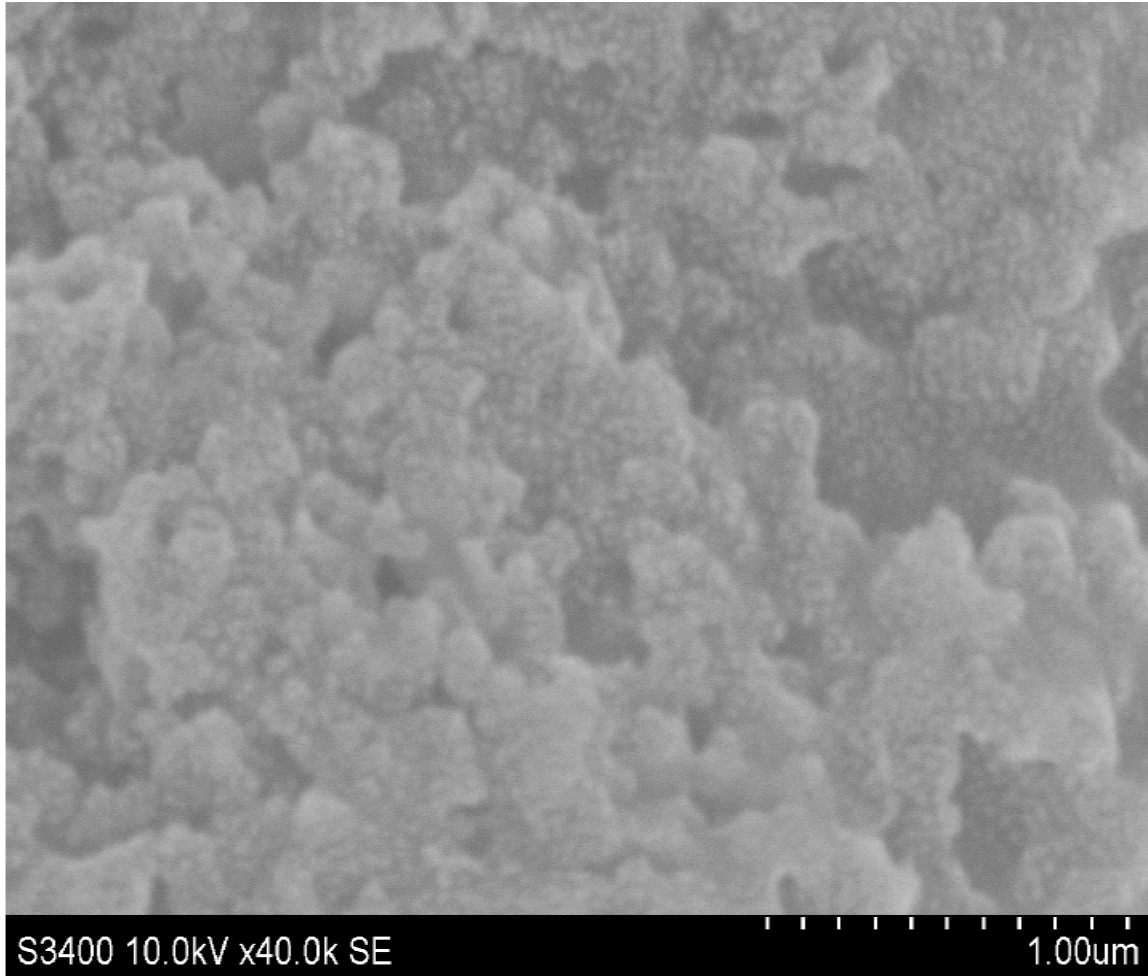

S3400 10.0kV x40.0k SE   1.00um

Figure 32. SEM of K60G2N sediment illustrating adsorbed nanolatex particles.
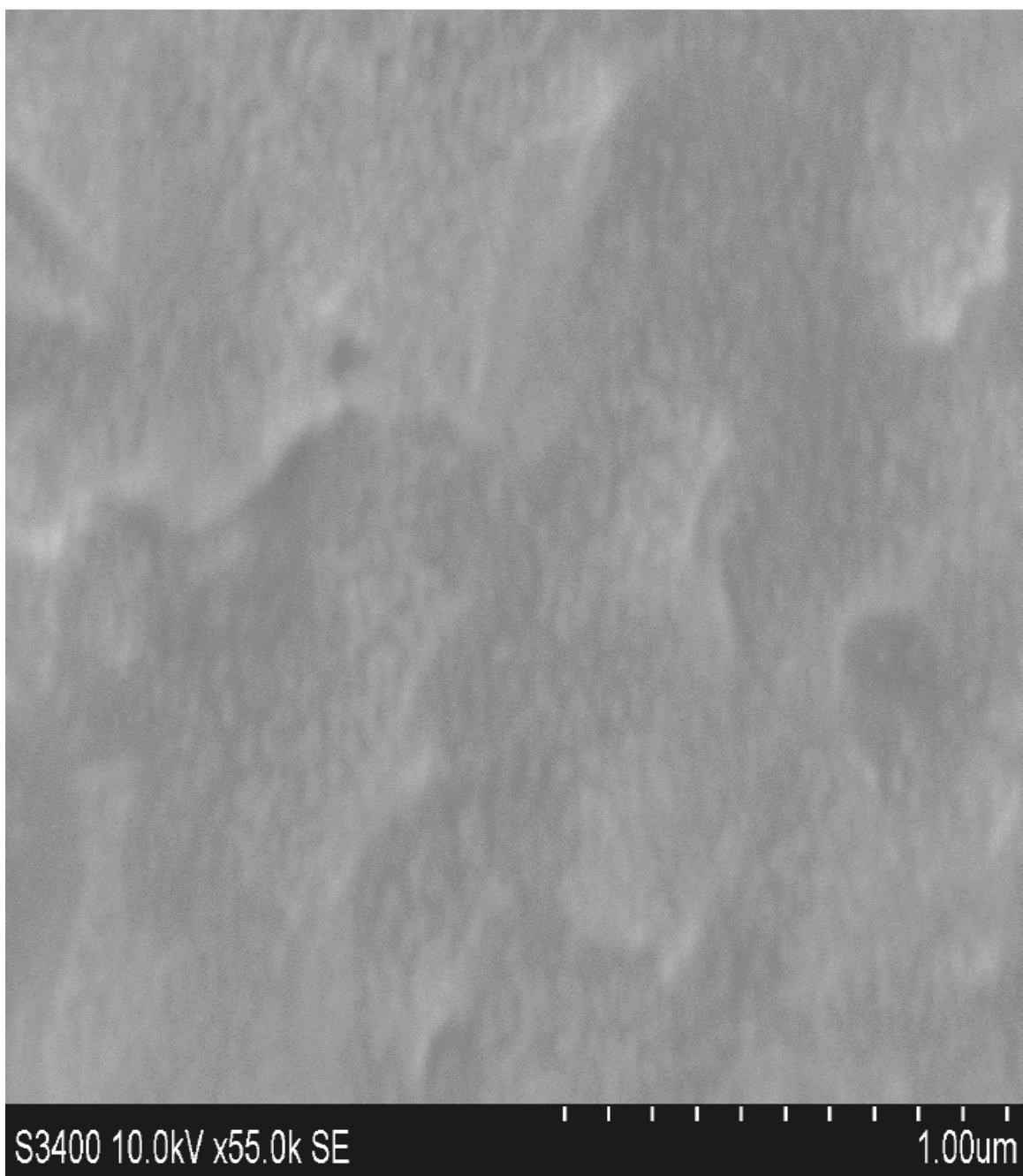
Figure 33. SEM of K60G2N sediment illustrating adsorbed nanolatex particles.

Porosity of K60G2N

The K60G2N sample as the most easily dispersing form of HTC prepared also appears to differ from the less dispersible samples in its intrinsic porosity. Some of the intrinsic porosity of K60G2N is illustrated in Figs. 34 and 35. The particle examined in Fig. 34 is a medium large sediment particle and Fig. 35 illustrates some of the largest sediment particles. These particles appear to have intrinsic porosity that is sub-micron in dimension. We hypothesize this porosity is important in the mechanism of dispersion.
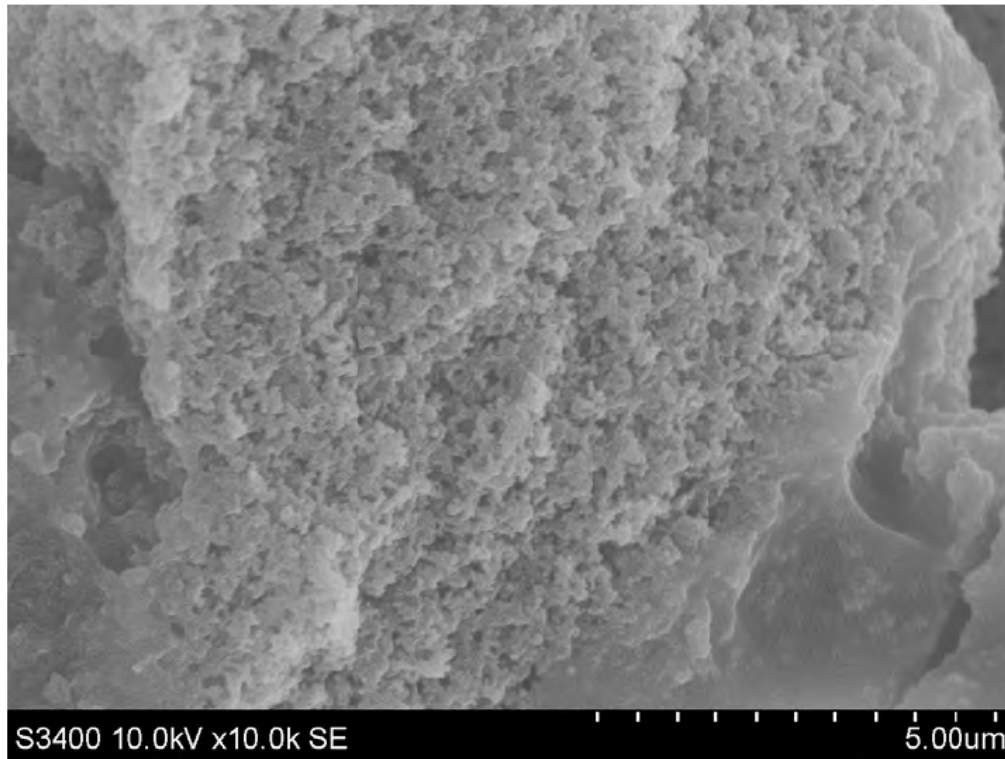
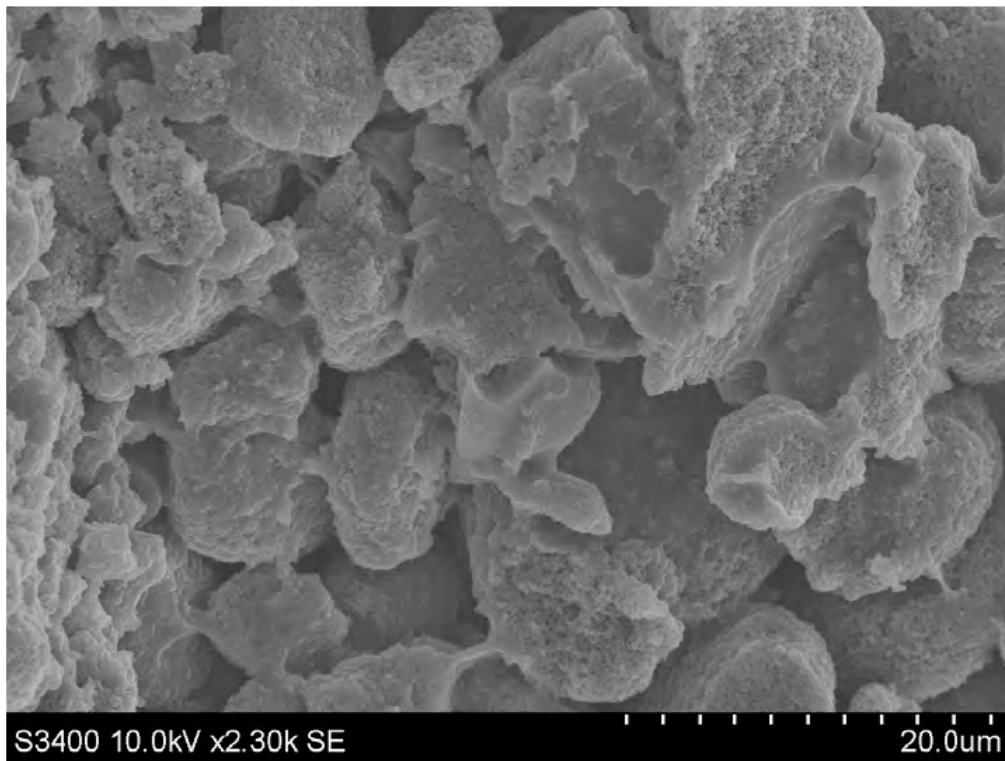**Figure 34. SEM of K60G2N sediment illustrating intrinsic porosity.**

Figure 35. SEM of K60G2N sediment illustrating intrinsic porosity.

Electrical Conductivity of HTC

Through---plane conductivities of dispersion, sediment, and supernatant castings described above were measured using a Novocontrol Dielectric spectrometer at 25^0C f\rom 0.1 to reduce contact resistance and equilibrated to 44% RH prior to measurement. Except for the   frequencies. For the other samples, a local minimum in the imaginary impedance in the lower frequency range (from a Nyquist plot) was identified, and the conductivity taken at the c orresponding frequency.

Table 5. Through-plane HTC film conductivities

Dispersion Castings

Sample	Conductivity (mS/cm)	Frequency (Hz)
NL/HC-CH-750	0.0945	15.8
NL/HC-GA-750	0.0442	6.31
NL/GMELA10N	0.0179	3.98
NL/K60G2N	0.0324	5.01
NL/72WF10N	0.0439	5.01

Supernatant Castings

Sample	Conductivity (mS/cm)	Frequency (Hz)
NL/HC-CH-750-SN	0.0819	15.8
NL/HC-GA-750-SN	0.0849	15.8
NL/GMELA10N-SN	0.0964	79.4
NL/K60G2N-SN	0.1024	19.95
NL/72WF10N-SN	0.0977	20

Sediment Castings

Sample	Conductivity (mS/cm)	Frequency (Hz)
NL/HC-CH-750-sed	26.7	
NL/HC-GA-750-sed	9.42	
NL/GMELA10N-sed	0.0151	0.1
NL/K60G2N-sed	7.63	
NL/72WF10N-sed	7.35	

The most notable result is the relatively low through-plane conductivity of the dispersion GMELA10N wafer, which at 0.018 mS/cm is only marginally higher than nanolatex control films at 25°C. The three most highly conducting dispersion sample wafers are the three that were the most difficult to disperse. The most highly dispersible K60G2N dispersion wafer has a conductivity of 0.032 mS/cm, and is second lowest to GMELA10N.

The supernatant results in Table 5 exhibit a different trend. We know from the previously discussed SEM cross-section analyses that the dispersion wafers and films exhibit a nominally two-layer structure with a bottom layer of HTC sediment (or most of the sediment) and a top layer of mostly nanolatex in which an unquantified amount of finer HTC sediment is suspended. The supernatant cross-sections all appear fairly homogeneous (Figs. 22-26). All of these samples exhibit through plane conductivities 8-10 fold that of the nanolatex control (0.01 mS/cm). This includes the GMELA10N sample.

The wafers derived from sediment exhibit the highest conductivities. As shown in Table 5, all of the samples except GMELA10N have relatively high through-plane conductivities at 7-27 mS/cm. Each of these samples exhibits an interesting gradation in sediment, as shown

Table 6. Surface conductivities of dispersion castings

Sample	side	current (uA)	conductivity (mS/cm)
HC-CH-750	matte	10	1.08
HC-CH-750	matte	1	1.02
HC-CH-750	shiny	10	7.5
HC-CH-750	shiny	1	8.55
HC-GA-750	matte	10	0.962
HC-GA-750	matte	1	0.961
HC-GA-750	shiny	10	2.1
HC-GA-750	shiny	1	2.17
GMELA10N	matte	10	0.396
GMELA10N	matte	1	0.444
GMELA10N	shiny	1	0.114
GMELA10N	shiny	0.5	0.098
K60G2N	matte	10	1.51
K60G2N	matte	1	1.46
K60G2N	shiny	10	1.96
K60G2N	shiny	1	1.9
72WF10N	matte	10	2.43
72WF10N	matte	1	2.21
72WF10N	shiny	10	6.6
72WF10N	shiny	1	6.81

in Figs. 16-20. The 26.7 mS/cm from the HC-CH-750 sample is the highest value observed and the GMELA10N samples is lowest at 0.015 S/cm. It appears that the incorporation of melamine yields a fairly low conductivity in comparison with the other formulations.

Surface conductivities were measured using a four-electrode (Pt wire) probe and a Gamry impedance spectroscopy system. The two inner parallel electrodes were used to measure voltage and phase shift and the two outer electrodes were used to measure current at frequencies varying form 1 Hz to 100 kHz. Current amplitudes of 0.5 to 10 μA were used. Because of the relatively high conductivities, Nyquist plots were discarded and values were

taken at 1 Hz. The films used for these surface measurements were rectangular films cast in Teflon molds. Conductivities were calculated from the measurements using the equation

$$\sigma = \frac{d}{RA}$$

where d is the separation distance of the inner two electrodes, A is the cross-sectional area of the film (width x thickness), and R is the measured resistance. The films cured by drying at some temperature, and the bottom sides always presented as matte and the top surfaces always appeared shiny.

Table 7. Surface conductivities of supernatant castings

Sample	side	current (uA)	conductivity (mS/cm)
HC-CH-750-sn	matte	1	0.273
HC-CH-750-sn	matte	0.5	0.267
HC-CH-750-sn	shiny	1	0.445
HC-CH-750-sn	shiny	0.5	0.409
HC-GA-750-sn	matte	1	0.308
HC-GA-750-sn	matte	0.5	0.287
HC-GA-750-sn	shiny	1	0.300
HC-GA-750-sn	shiny	0.5	0.306
GMELA10N-sn	matte	1	0.333
GMELA10N-sn	matte	0.5	0.305
GMELA10N-sn	shiny	1	0.422
GMELA10N-sn	shiny	0.5	0.413
K60G2N-sn	matte	1	0.257
K60G2N-sn	matte	0.5	0.244
K60G2N-sn	shiny	1	0.296
K60G2N-sn	shiny	0.5	0.276
72WF10N-sn	matte	1	0.263
72WF10N-sn	matte	0.5	0.241
72WF10N-sn	shiny	1	0.302
72WF10N-sn	shiny	0.5	0.279

Surface electrical conductivities of the dispersion castings are listed in Table 6. Surprisingly the shiny sides of most of the samples had higher conductivities than the matte sides. The samples follow the ranking 72WF2N > HC-CH-750 > HC-GA-750 ~ K60G2N > GMELA10N in order of decreasing conductivities.

Surface electrical conductivities of the supernatant castings are listed in Table 7. Again, the shiny sides of most of the samples appear to have slightly higher conductivities than the matt sides. In addition, the magnitude of these two values, shiny vs matte, are very similar for all of the samples. Many of these surface conductivities are in the 0.24-0.33 mS/cm range measured for nanolatex control films (see Table 9).

Table 8. Surface conductivities of sediment castings

Sample	side	current (uA)	conductivity (mS/cm)
HC-CH-750-sed	matte	10	9.06
HC-CH-750-sed	matte	1	9.17
HC-CH-750-sed	shiny	10	10.2
HC-CH-750-sed	shiny	1	10.3
HC-GA-750-sed	matte	50	3.1
HC-GA-750-sed	matte	10	3.31
HC-GA-750-sed	shiny	50	4.74
HC-GA-750-sed	shiny	10	4.64
GMELA10N-sed	matte	10	0.0492
GMELA10N-sed	matte	1	0.0439
GMELA10N-sed	shiny	1	0.0339
GMELA10N-sed	shiny	0.5	0.0379
K60G2N-sed	matte	10	6.77
K60G2N-sed	matte	1	6.74
K60G2N-sed	shiny	10	7.75
K60G2N-sed	shiny	1	7.67
72WF10N-sed	matte	50	3.25
72WF10N-sed	matte	10	3.66
72WF10N-sed	shiny	50	4.39
72WF10N-sed	shiny	10	5.07

Surface electrical conductivities of the sediment castings are listed in Table 8. Again, the shiny sides of most of the samples appear to have slightly higher conductivities than the matte sides. The samples follow the ranking HC-CH-750 > K60G2N > 72WF2N > HC-GA-750 >GMELA10N in order of decreasing conductivities. While the GMELA10N sample again is the least conductive, in this case the K60G2N sample appears second most conductive to HC-CH- 750. It is difficult to assign cause for this exception, but it may be that the fine sediment illustrated in Fig. 13 as a middle layer may be in a form that is particularly conductive with low interparticle resistance, and that this fine sediment pervades the surfaces for the sediment sample (Fig. 20).

Figure 36 illustrates the correlation between average surface or in-plane and through-plane electrical conductivities. Overall, it appears that the most difficult to disperse material, HC-CH- 750 has the highest electrical conductivity and the most easily dispersed material, K60G2N has variable conductivity, depending on the layer structure. The second most easily dispersed material, GMELA10N, has the lowest electrical conductivity. These materials exhibit the following rank ordering in their electrical conductivities: HC-CH-750 > K60G2N ≈ 72WF10N ≈ HC-GA-750 > GMELA10N.
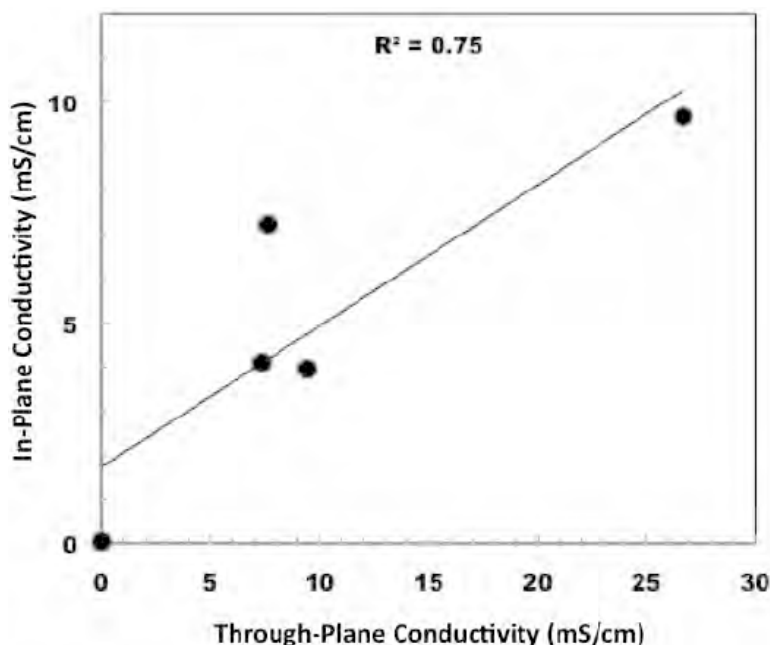
Figure 36. In-plane or surface conductivity as a function of through plane conductivity for the sediment casting samples.

Table 9. Surface conductivities of nanolatex control casting

Sample	side	current (uA)	conductivity (mS/cm)
NL-10-1073-84	matte	1	0.332
NL-10-1073-84	matte	0.5	0.335
NL-10-1073-84	shiny	1	0.232
NL-10-1073-84	shiny	0.5	0.259

Dielectric Spectroscopy of HTC Films

Tan (δ) spectra of the dispersion, supernatant, and sediment castings and films are illustrated in Figs. 37, 38, and 39, respectively. Prominent loss peaks appear for each of the samples that are much greater than the nanolatex control peak, except in the case of GMELA10N, two loss peaks of about equal height are observed, and one of these is most likely due to the nanolatex component and the other due to the dispersed HTC component. Further work on assignment is needed to be sure, however.

A similar set of spectra are seen for the supernatant films as shown in Fig. 38, except that only a single peak is observed for the GMELA10N sample. We cannot preclude that these single peaks as well as those of Fig. 37 are due to a major peak close to the illustrated peak frequencies as well as a lower intensity "free nanolatex" component. We tentatively assign the larger peaks to segmental motions and polarization due to nanolatex components adsorbed onto HTC. The very high tan(δ) values for the sediment samples and illustrated in Fig. 39 come from the relatively high conductivities of these samples. The GEMLA10N sediment again exhibits behavior similar to that of the free nanolatex, so we can conclude

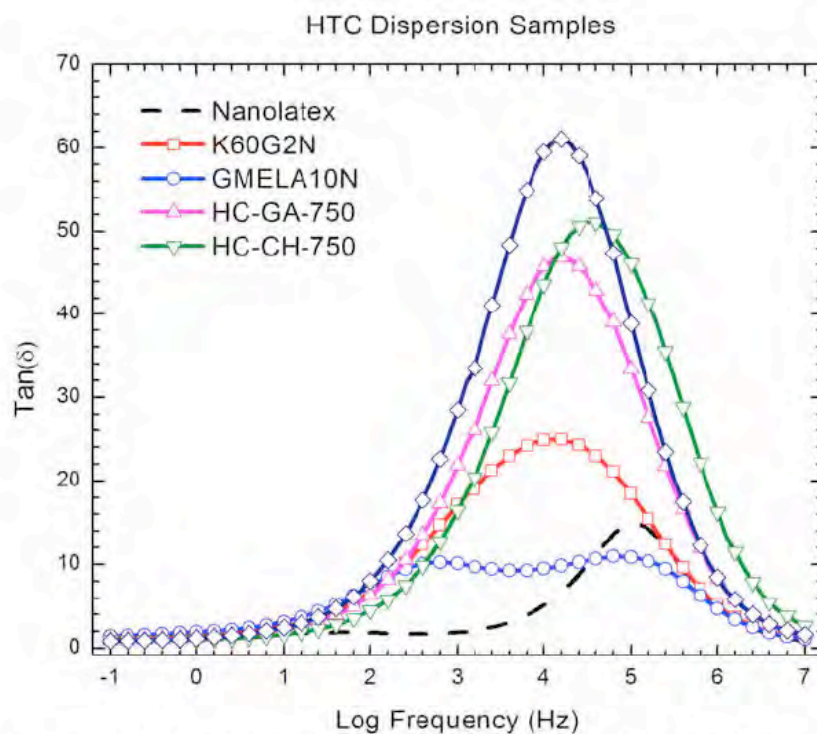that this HTC material is of distinctly lower electrical conductivity than the other HTC materials.

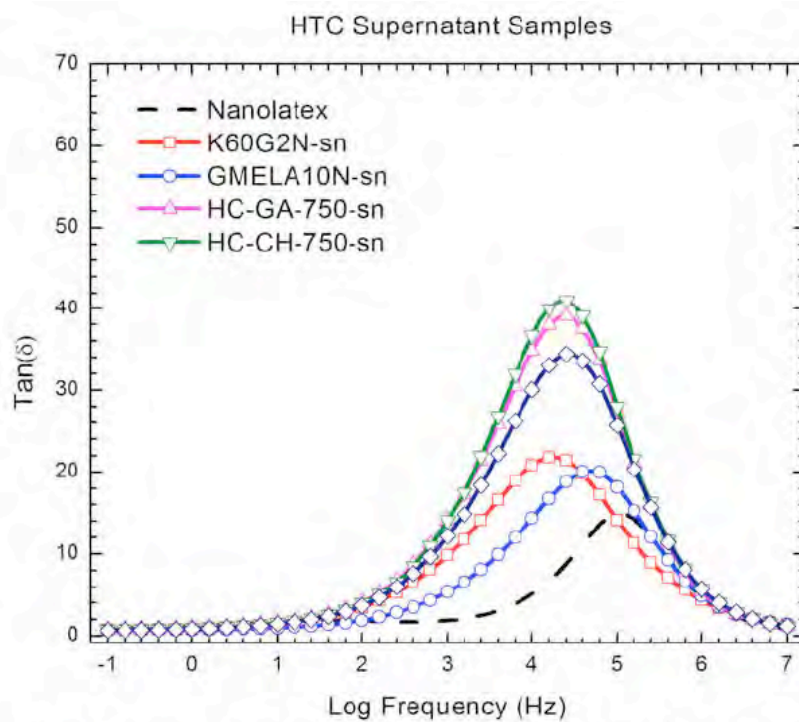Figure 37. Tan(δ) dielectric spectra of dispersion castings at 25°C.

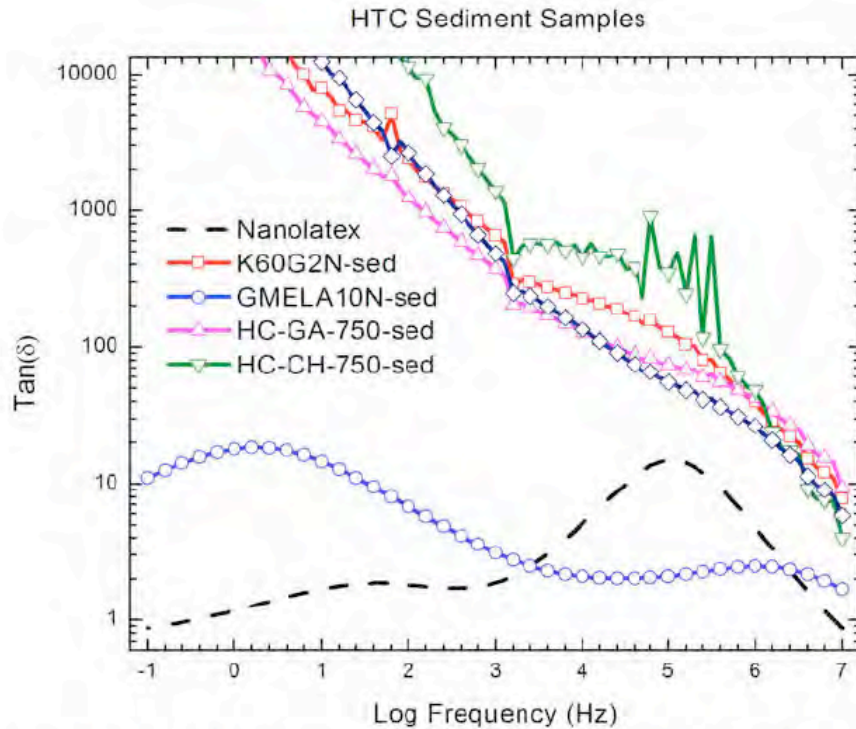Figure 38. Tan(δ) dielectric spectra of supernatant castings at 25°C.

Figure 39. Tan(δ) dielectric spectra of sediment castings at 25°C.

In-plane Thermal Diffusivity

When we started trying to measure in-plane thermal diffusivities we were somewhat confused as to how to fit the curves. We encountered in some cases a very steep rise time sometimes followed by a further slowly increasing curve that then slowly decayed. An example is the reddish brown (top) curve in Fig. 40. If we fit the data over a 30s interval, so that the peak and the slow decay were included, we would get a thermal diffusivity of the order of 1 mm2/s. If we only measured a response over the first 500 ms and fit that curve, we might obtain a value of 20 mm2/s. The software provided assumes the sample is homogenous and uniform, and of course our samples are not.

The same circular castings we examined in earlier discussed tests were used for thermal diffusivity measurements; both In-plane (||) and through-plane (⊥) measurements were done and compared with nanolatex controls. Measurements were done with a Netzsch L447 xenon flash thermal diffusivity instrument. Getting little assistance from the vendor, we executed various series of experiments to find the source of the peak we were observing (such as in the top curve of Fig. 40) at longer times in in-plane experiments. We proceeded by blacking various apertures with aluminum foil to see if the xenon flash unit was providing an additional source of sample heating, additional to the initial short flash. When we covered the aperture below the sample with such a foil, so that the sample was not directly irradiated, we obtained the middle curve (green) of Fig. 40, which exhibits a much slower rise, a peak at about the same place as the reddish brown curve, and a similarly long decay portion. When we subtract the middle from the top curve, we get the lower (blue) curve. This difference curve has the steep rise character of the top curve as well as the slow cooling character of both the top and middle curves.
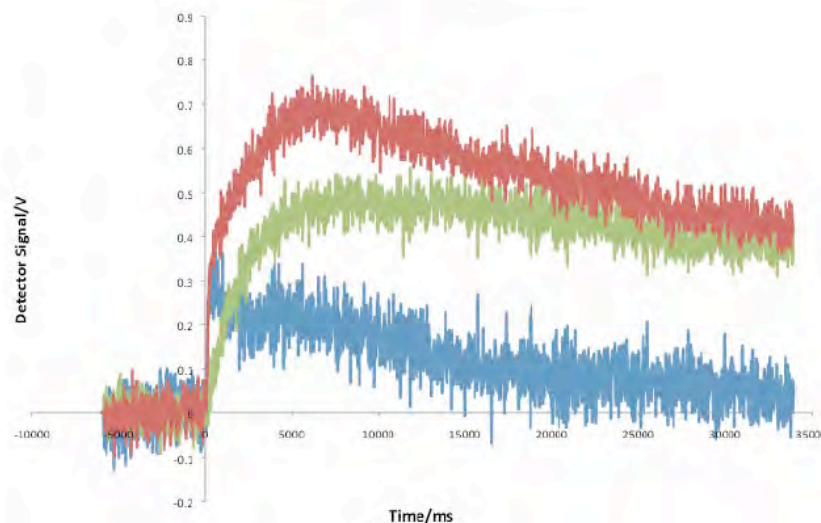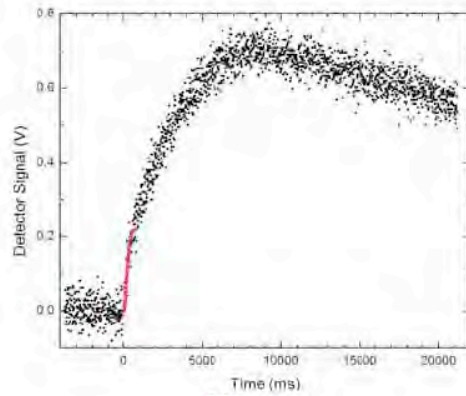
Figure 40. Temperature (detector signal) versus time after xenon flash of an HTC sediment film (top; reddish brown), after closing aperture between sample and flash unit (middle, green), and arithmetic difference (lower, blue) for in-plane thermal diffusivity (xenon flash) measurements on GMEL10N/nanolatex sediment film.

This simple series of experiments shows an inherent limitation of our xenon flash thermal diffusivity instrument for samples that conduct heat radially at slow to intermediate rates. The initial temperature rise is due to the sample, but the longer time rise and fall are due to the thermal inertia of sample cell heating by the flash unit and the relatively slow cooling rate provided by the sample cell cooling system.

In Fig. 41 we show two experimental data sets, one for HC-CH-750 and one for GMELA10N, where both are sediment sample films. In each column we illustrate fits of the homogenous single layer model to the respective samples over time intervals ranging from 800 ms to 30s. The data sets are composed of the black dots, each dot being an individual datum. The red (solid line) curves beginning at time zero are the respective fits over various time intervals and over various portions of the respective data sets. We see that the rising portion of the fits results in an improved fit (over the rising portion) as the fitting interval is decreased to 800 ms. We therefore are convinced that these fits are the most reliable, and therefore are the values reported herein. More work is needed to prove that these values are entirely reliable, and we are working on improving the modeling of the obtained data sets to handle layer structured samples as well as the inertial heating components of these data sets.
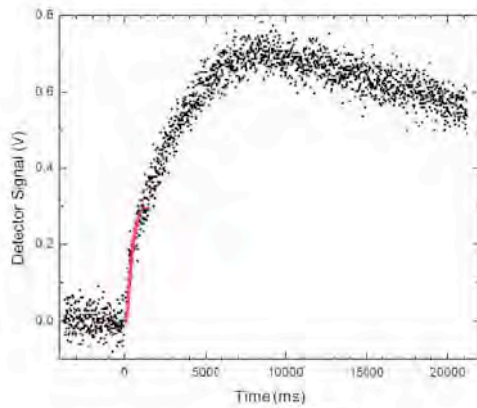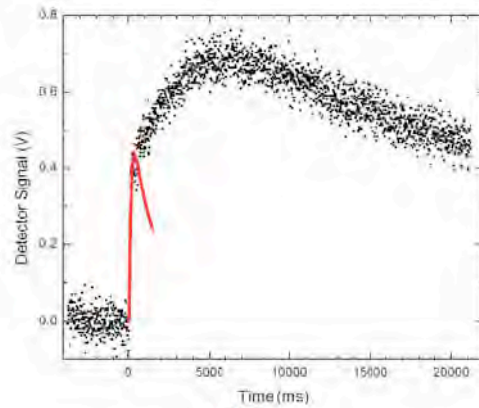
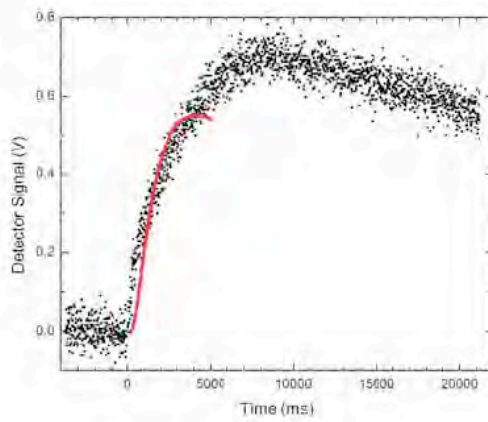**HC-CH-750 shiny**

GMELA10N sed matte
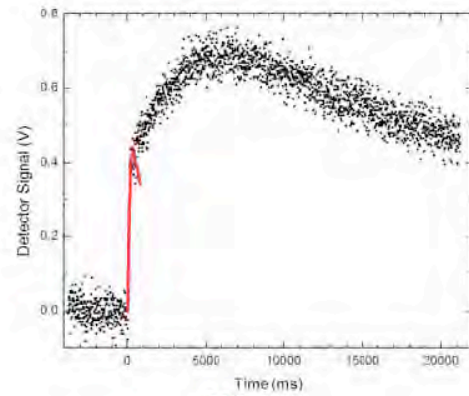
800ms

800 ms

1500ms

1500ms

5s

5s

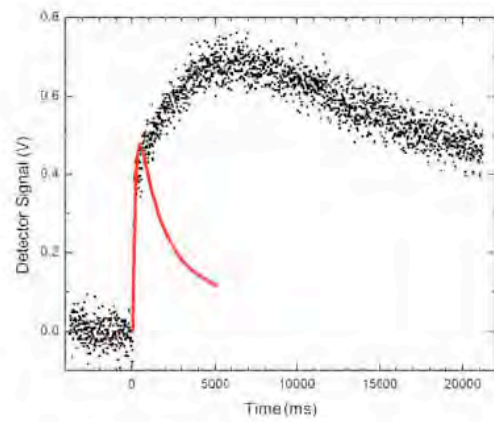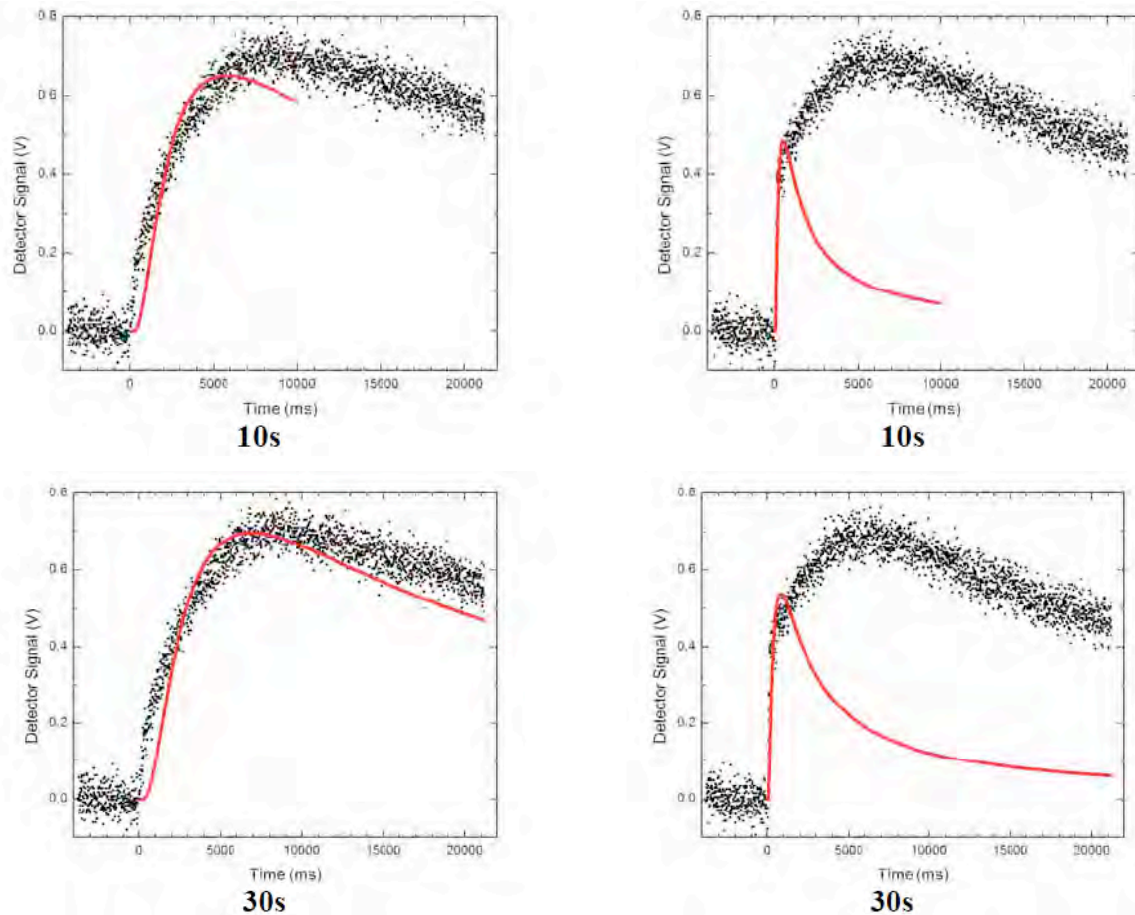**Figure 41. Temperature (detector signal) versus time after xenon flash of HC-CH-750 (left column) and GMELA10n (right column) sediment films and homogeneous model fitting results for various fitting times from 800ms (top row) to 30s (bottom row).**

Thermal Diffusivities of HTC

The through-plane ($\perp$) thermal diffusivities of the HTC films listed in Table 10 appear nearly the same whether the shiny (top) or the matte (bottom) side is experimentally presented to the xenon flash. The values for the different samples are also close to one another, with HC-GA-750 being the highest and K60G2N being the lowest. For the in-plane ($\parallel$) measurements there was a general effect of whether the shiny or matte side was presented to the xenon flash. Higher values were obtained when the matte side received the flash, except in the case of HC-CH-750. Matte in-plane values decreased in the order 72WF10N > GMELA10N > K60G2N > HC-CH-750 > HC-GA-750.

The corresponding anisotropies are listed in the last column of Table 10. Overall, values range from 4.2 to 8.2, but there is a big effect of whether the incident flash is upon the matte side or shiny side, with the matte side producing the larger anisotropies, except for HC-CH-750. It is interesting that such anisotropy can be simply manufactured by sedimentation, to produce the two-layer (three in the case of K60G2N) structures illustrated in Figs. 9-13. The granular sediment layers appear much more thermally

11:42 PM

93

diffusive than the more uniform and mostly nanolatex layers. The typical thermal diffusivity found for the nanolatex itself is about 0.06-0.08 mm2/s.
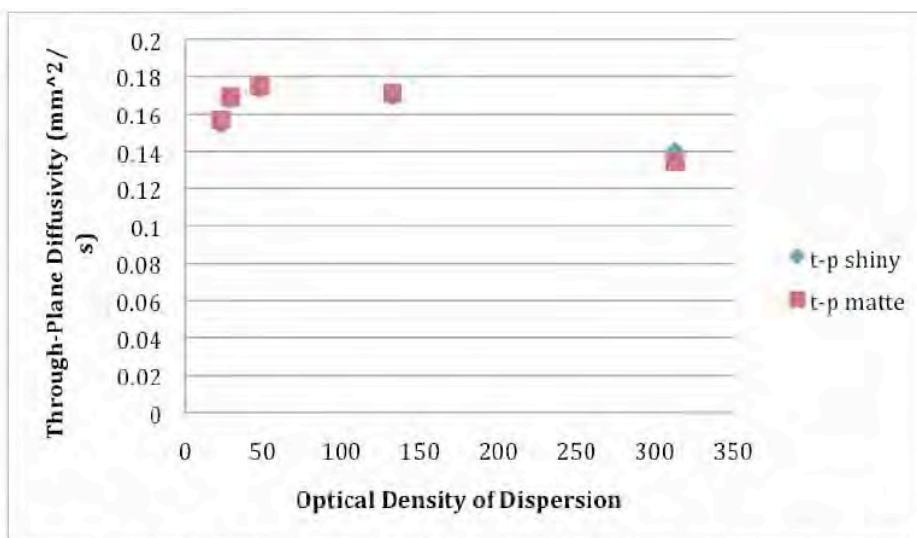

Figure 42. Through-plane thermal diffusivity of thin films as a function of effective dispersion optical density.
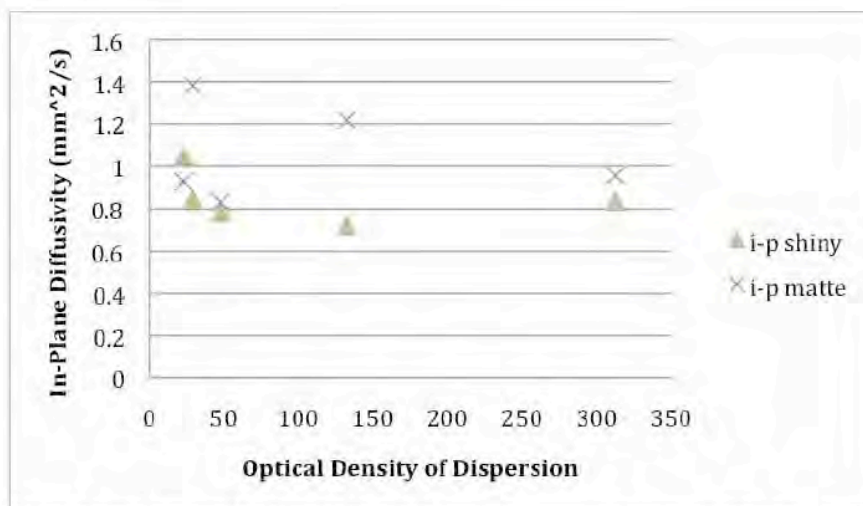

Figure 43. In-plane thermal diffusivity of thin films as a function of effective dispersion optical density.

These dispersion film through-plane thermal diffusivities are plotted in Fig. 42 as a function of the effective optical density of the starting dispersion. In-plane results are similarly plotted in Fig. 43 The GMELA10N sample exhibits the greatest "polarity" effect, where the measured inplane diffusivity depends on which side receives the incident xenon flash. The 72WF10N sample exhibits the second greatest polarity effect.

Table 11. Through-plane (⊥) and in-plane (∥) thermal diffusivities of HTC films of supernatant castings

Sample	OD	⊥ shiny mm²/s	⊥ matte mm²/s	∥ shiny mm²/s	∥ matte mm²/s
HC-CH-750-SN	22.9	0.195	0.201	0.815	13.1
HC-GA-750-SN	48	0.163	0.156	5.875	0.938
GMELA10N-SN	132.5	0.146	0.151	0.848	8.16
K60G2N-SN	312.5	0.152	0.157	1.01	6.90
72WF10N-SN	28.9	0.181	0.185	5.94	7.02

Table 12. Through-plane (⊥) and in-plane (∥) thermal diffusivities of HTC films of sediment castings

Sample	OD	⊥ shiny mm²/s	⊥ matte mm²/s	∥ fitting interval ms	∥ shiny mm²/s	∥ matte mm²/s
HC-CH-750	22.9	0.2636	0.2734	2100	3.81 ± 0.13	5.79 ± 0.25
				1500	5.23 ± 0.25	20 ± 2
				800	11.3 ± 1.0	26 ± 4
HC-GA-750	48	0.3278	0.3456	2100	2.52 ± 0.16	5.46 ± 0.27
				1500	3.33 ± 0.35	13.5 ± 1.7
				800	3.6 ± 1.1	13.0 ± 1.5
GMELA10N	132.5	0.2116	0.2218	2100	3.19 ± 0.13	20 ± 1
				1500	4.54 ± 0.28	24 ± 3
				800	8.7 ± 1.2	23 ± 2
K60G2N	312.5	0.2598	0.2606	2100	1.51 ± 0.05	5.0 ± 0.2
				1500	2.14 ± 0.10	6.2 ± 0.3
				800	4.30 ± 0.40	6.1 ± 0.3
72WF10N	28.9	0.323	0.3228	2100	2.71 ± 0.1	7.44 ± 0.37
				1500	3.57 ± 0.22	25 ± 5
				800	9.3 ± 1.4	26 ± 5

Taking an average of in-plane results, the HTC samples' thermal diffusivity decreases in the order: HC-CH-750 ≈ 72WF10N > GMELA10N > HC-GA-750 > K60G2N. The through plane results provide a different ranking: HC-GA-750 > 72WF10N > HC-CH-750 > K60G2N > GMELA10N. It must be stressed that the fitting of these films was done using vendor supplied software that was different for the through plane and in-plane fits. In addition, both programs assumed the samples were homogeneous, and of course even the sediment samples are very inhomogeneous. We have initiated a modeling program to try to develop a more systematic approach to fitting such data that also takes account of instrumental heating anomalies, such as that illustrated in Fig. 40.

HTC Dispersions

Experimental

Materials

Chitosan (medium molecular weight), D(+)-glucose, melamine, furfural and D(+)-glucosamine hydrochloride (>99.0%, HPLC) were purchased from Sigma–Aldrich and used without further purification. Luvitec K60 (obtained from BASF) is a 34-36% by weight solution of poly(vinyl pyrrolidone) (PVP) in water with a pH of 7-9 and less than 0.03% nonvolatile residue. Luvitec VPI 55 K72W (obtained from BASF) is a copolymer of vinyl pyrrolidone and vinyl imidazole.

Methods

HTC Synthesis
Carbon, optionally nitrogen dopant (amine or N-containing polymer), and water were mixed and sealed into glass vials and then autoclaved at 180 °C overnight. After the reaction, the autoclaved vials were cooled in a cold water bath. The resulting black solid powder was filtered and washed with distilled water several times followed by drying in a vacuum oven at 80°C overnight. Afterwards, in order to improve the level of structural order in the carbon, further high temperature (750 °C) calcination was performed in an oven under N_2 flow.

Hydrothermal Carbon Compositions

HC-CH-750	10% Chitosan; after drying the powder
HC-GA-750	10% Glucosamine; after drying the powder
GMELA10N	10% Glucose; 10% Melamine
K60G2N	10% Glucose, 2% K60 (BASF PVP)
72WF10N	10% Furfural; 10% 72W (BASF PVP/Polyvinylimidazole copolymer)

Compositions autoclaved 24 h at 180°C and then carbonized further at 750°C under nitrogen.

Nanolatex Synthesis
A nanolatex of ILBr (1-[11-acryloylylundecyl]-3-methyl imidazolium bromide) and MMA (methylmethacrylate) was prepared by microemulsion (dispersion) polymerization at 60C overnight using a microemulsion formulation comprising 6% (w/w) ILBr, 4% (w/w) MMA, and 90% (w/w) water, with AIBN added at 0.5% (w/w) relative to total monomer. The resulting 20-30 nm diameter (determined by photon correlation spectroscopy with a D90xx PCS instrument; Brookhavem Instruments, Hoboken, NY, USA) nanolatex particles were concentrated to 15-20% (w/w) by ultrafiltration, using an Amicon (Millipore, USA) ultrafiltration cell pressurized to about 30 psi using N_2 gas.

Instrumental Measurements
SEM (scanning electron microscopy) was done with a JEOL SEM (JEOL, Berlin, Germany) and with a Hitachi V3400N (Hitachi Instruments, Pleasantville, CA, USA). Porosity and specific surface area were determined by BET N_2 adsorption using a Quantachrome

instrument (Quantachrome, Germany). C, H, and N compositions were determined by combustion analysis. Dielectric spectroscopy was done using a Novacontrol System B80 broadband dielectric spectrometer (Novocontrol. Mulheim, Germany). TGA (thermogravimetric analysis) was done using a QA Instruments Q200 thermogravimetric analyzer (New Castle, DE, USA). Optical absorption measurements were done using a Jasco UV/Vis double beam spectrophotometer (Jasco).

Dispersion Processing

Waterborne dispersions were prepared by combining 2 g carbon, sufficient nanolatex dispersion to produce a 10:1 nanolatex/HTC weight ratio, and enough additional water to produce a total dispersion weight of 10 g. The resulting crude dispersion was sonicated for 10-30 minutes in a Branson ultrasonic cleaning bath, followed by sonication at 0C using a Dultron Sonifier outfitted with a microchip ultrasonic horn. Aliquots (30-70 µL) of dispersion were withdrawn periodically and diluted 50 to 600-fold to yield a diluted dispersion having an optical density at 500 nm of 0.1-1.5. This optical density and the associated dilution factor was then used to determine the effective dispersion optical density at 500 nm.

HTC preground in mortar and pestle

2% w/w dispersion in 20% nanolatex prepared

Sonicated in ultasonic cleaning bath for 60 min

Sonicated at 50%/100% amplitude using 3-4 mm diameter microtip sonic horn

Optical density at 500 nm checked periodically to monitor "state" of dispersion

Dispersion Casting and Thin Film Formation

Thin film freestanding wafers were prepared by casting approximately 1 g of dispersion into the annular cup inside 50 mL centrifuge tube caps and allowing the dispersion to dry overnight. After drying at ambient conditions, an Exacto knife was used to cut around the annular cup. The resulting mechanical treatment then generally caused the cast film to release.

Results and Discussion

HTC Preparation

Nitrogen-doped carbons

Chitosan or D(+)-glucosamine hydrochloride (2 g) and 18 g of deionized water were mixed together and labeled as s-CH and s-GA, respectively. Glucose (2 g) and 0.4 g of the polymer K60 and 17.6 g of deionized water were mixed together and labeled as s-K60G2. s-GMELA10 is composed of 2g of glucose, 2g of melamine and 16g of deionized water and sample s-72WF10 contains 2g of furfural, 2g of polymer 72W and 16g of deionized water.

The mixtures were sealed into glass vials inside PTFE inlets autoclaves followed by hydrothermal treatment at 180 °C overnight. After the reaction, the autoclaves were cooled down in a cold water bath, then the obtained black solid powder were filtered and washed with distilled water several times followed by drying in vacuum oven at 80 °C overnight leading to HC-CH, HC-GA, K60G2, GMELA10 and 72WF10. Afterwards, in order to improve the level of structural order, further high temperature (750 °C) treatment was performed in an oven under N_2 flow. The calcined samples were referred to HC-CH-750, HC-GA-750, HC-K60G2N, GMELA10N and 72WF10N.

HTC Physical Characterization

Material morphology of the nitrogen-doped carbons was initially investigated by SEM, as shown in Figure 1. Samples HC-CH-750, HC-GA-750 and GMELA10N show agglomeration of very small nanoparticles without any structural order at high magnification, whereas the sample K60G2N shows a well defined monolithic structure with interconnected macropores. On the other hand, sample 72WF10N consists of a flat surface with no appreciated porosity.
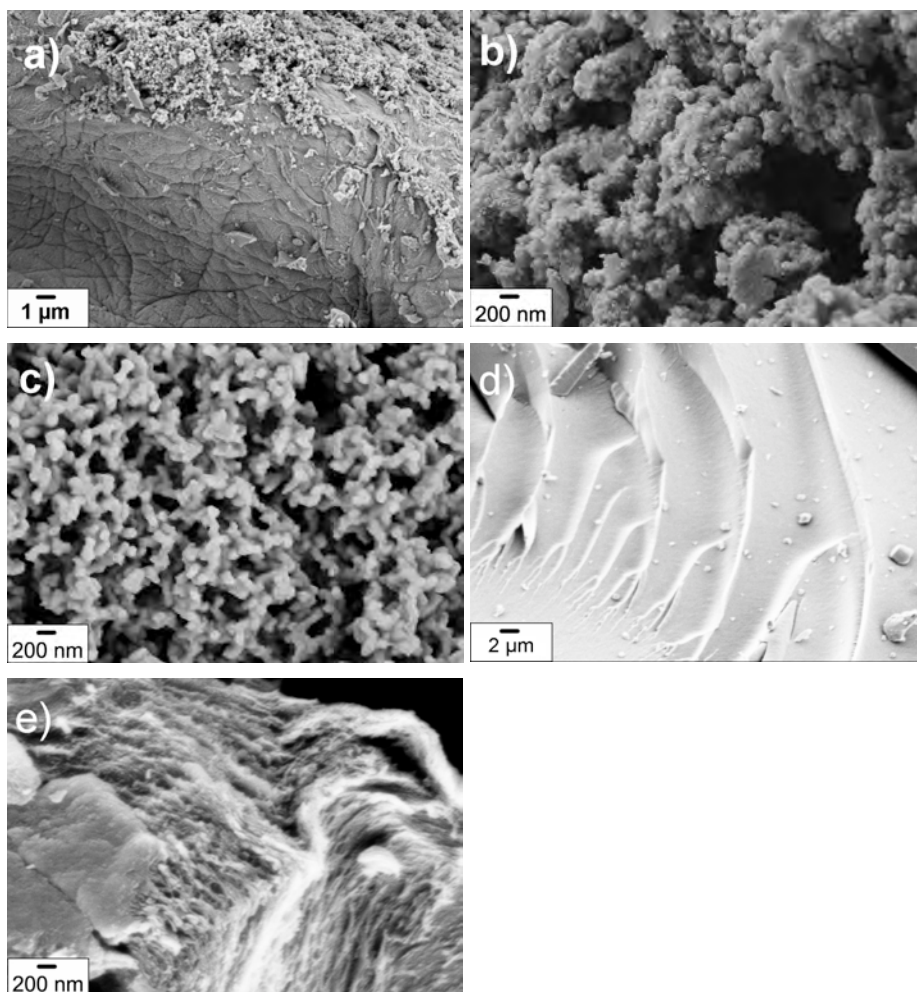
Figure 1. SEM images of a) HC-CH-750, b) HC-GA-750, c) K60G2N, d) 72WF10N and e) GMELA10N

The nitrogen amount of the carbons is relatively high, as shown in Table 1. This indicates the successful and stable incorporation of nitrogen into the carbon matrix via hydrothermal carbonization, being stable enough to actually incorporate into the growing aromatic/ pseudo-graphitic carbon structure upon processing at elevated temperatures (e.g. 750 ºC).

Table 1. Elemental percentage and porosity characters of the nitrogen-doped carbon materials.

HTC Sample	%C	%N	%H	C/N	S_{BET} (m²/g)	Pore Volume (cm³/g)
HC-CH-750	79.2	9.1	1.51	8.8	1.49	0.01
HC-GA-750	81.6	6.6	1.43	12.4	15.7	0.04
K60G2N	92.7	2.8	1.15	33.1	320	0.17
GMELA10N	67.7	21.8	1.61	3.1	57.2	0.11
72WF10N	83.9	8.8	1.35	9.5	2.51	0.01

Waterborne Dispersion
OD vs sonication
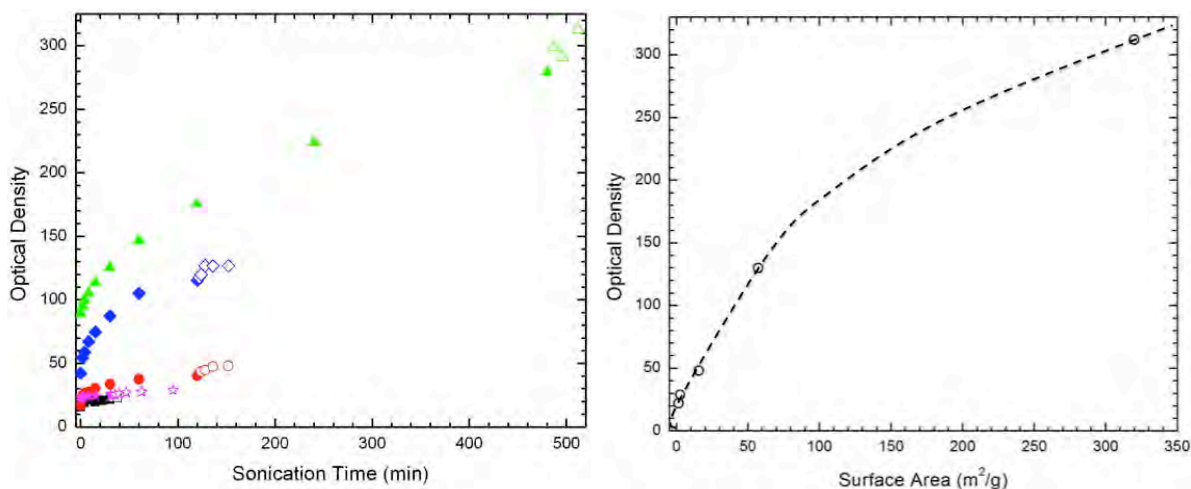
Figure 2. (left) Effective dispersion optical density at 500 nm of HTC dispersions as a function of sonication time; HC-CH-750 (★,☆); HC-GA-750 (●,○); K60G2N (▲,△); 72WF10N (■,□); GMELA10N (◆,◇); full symbols sonicated at 50% amplitude; open symbols sonicated at 100% amplitude. (right) Correlation of asymptotic optical density achieved for each of the five HTCs studied after exhaustive sonication in our waterborne dispersion process as a function of the measured pore surface area. The high optical density achieved in excess of 300, suggests an average extinction coefficient at the 500 nm test wavelength, that is competitive with SWCNT and MWCNT.

Porosity

The BET surface areas of HC-CH-750 and 72WF10N (Table 1) are very low, indicating that there is no defined porosity as shown in the isotherm in Figure 2 and as predicted by SEM images. Sample HC-GA-750 has a surface area of 15.67 m^2 g^{-1}, which indicates the presence of a small amount of macropores without any order as well as in sample GMELA10N (57.2 m^2 g^{-1}). Finally, the isotherm of the sample K60G2N show a high adsorbate adsorption and a relatively high surface area (> 300 m^2 g^{-1}) formed of micropores and mesopores.

Coatings

Our work on hydrothermal carbon (HTC) showed that we could very effectively disperse some of the HTC samples using our nanolatex/sonication waterborne processing. We showed that nanolatex areal adsorption appeared to be random and irreversible, with sight additional nanolatex wetting of the HT after adsorption (similarly as on MWCNT). The five different HTC samples investigated, based on some SEM observations, appeared as though they varied in porosity. We very recently have finished having each of these HTC samples analyzed for porosity, and the results are illustrated in Fig. 3. There we wee that the specific surface area (also porosity) increases as the ease of aqueous dispersion increases. The ease of aqueous dispersion is indicated by the effective optical densities recorded with exhaustive sonication.
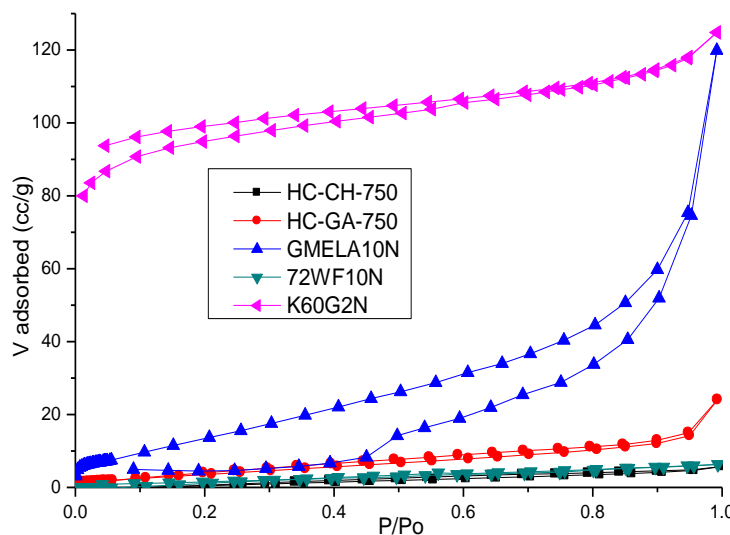
Figure 3. N$_2$ sorption isotherms of HC-CH-750 (■), HC-GA-750 (●), GMELA10N (▲), 72WF10N (▼), and K60G2N (◄).

It appears, therefore, that the correlation of Fig. 3 provides a design criterion for forming sustainable HTCs that can be transformed into waterborne dispersions. Such dispersions are useful for delivering micron to nanosize carbon particles for various applications, including printing, photothermal heating, inkjet writing of wiring (circuits and RFID), conventional composites, and as fuels for carbon fuel cells. This design criterion relates to formulating for high porosity. The porous cells presumably are more susceptible to sonication induced fracture.
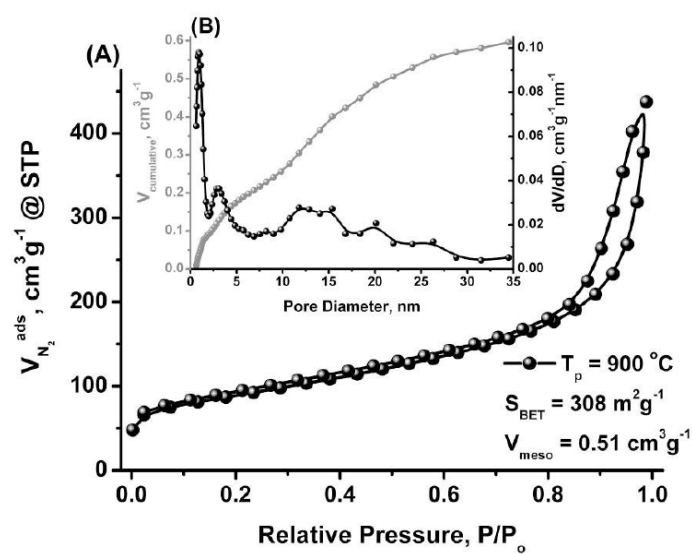
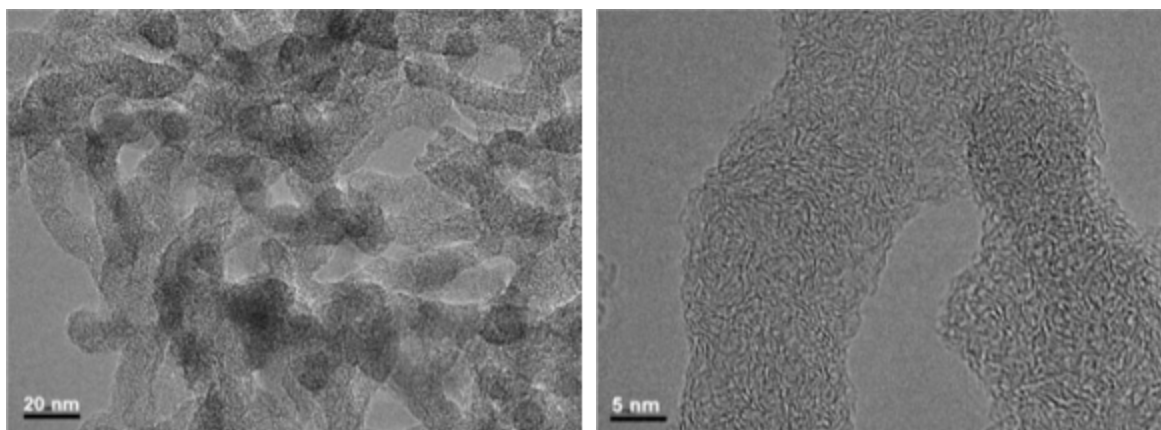**Figure 4. High porosity HTC from D-glucose and albumin**

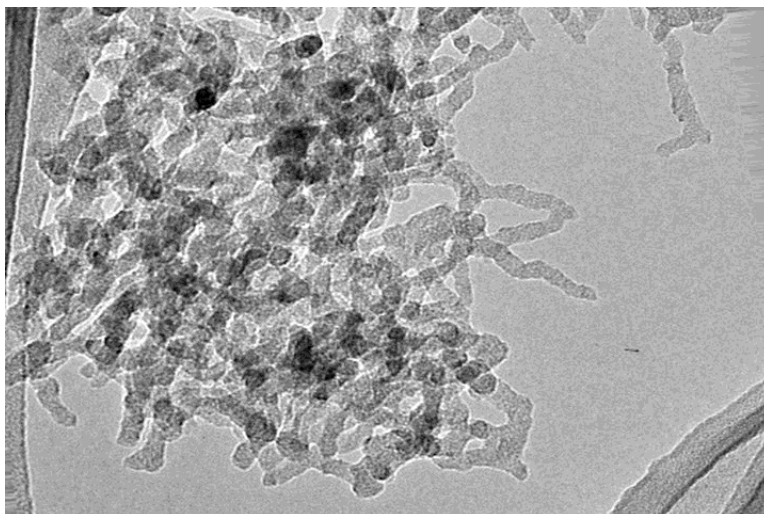**Figure 5. HRTEM of highly porous HTC**

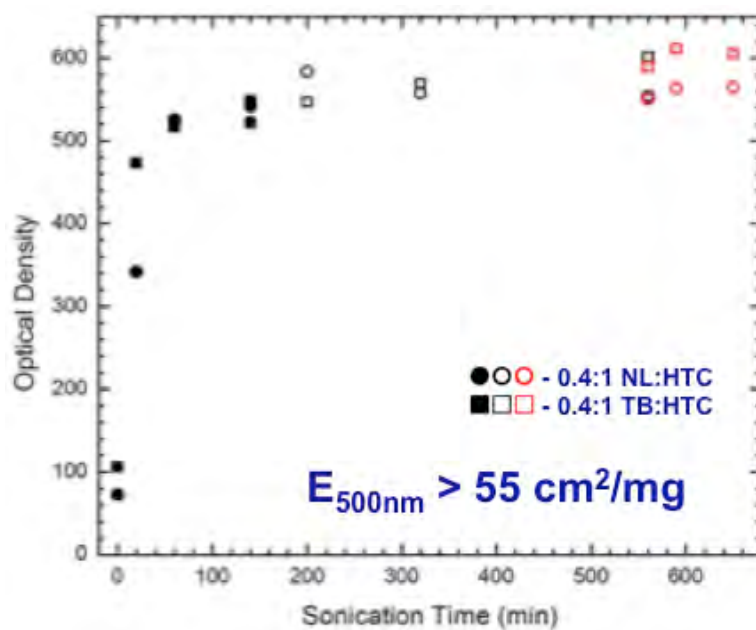**Figure 6. 3D HRTEM of high porosity HTC**

Figure 7. OD$_{500nm}$ vs sonication time showing data sets obtained using nanolatex (NL) and using triblock copolymer (TB).
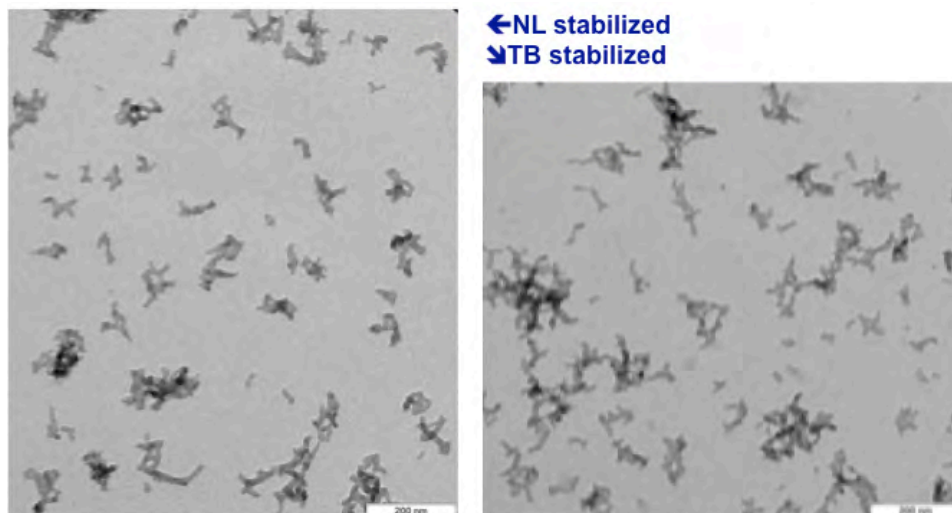
Figure 8. TEM of HTC dispersions

MWCNT/Nanolatexes

11/9/11The earlier reported work on dispersing SWCNT with nanolatex was continued with MWCNT with even greater success and understanding. Multiwall carbon nanotubes, Baytubes, were obtained from Bayer Advanced Materials. We expect MWCNT nanolatexes to establish a new class of electrically and thermally conductive paints and to facilitate the formation of diverse membrane materials for fuel cell, battery, and other applications. The nanolatex we refer to is the same composition as earlier described, ILBr:MMA, about 4:2.67 by weight (about 1 MMA momomer per 3 ILBr monomers.

In Fig. 1 we illustrate the dispersion equivalent optical density at about 500 nm obtained for a dispersion of MWCNT in nanolatex. The concentration of MWCNT was 1% (w/w) and the solids concentration of the nanolatex was about 18% (w/w). We see that the effective
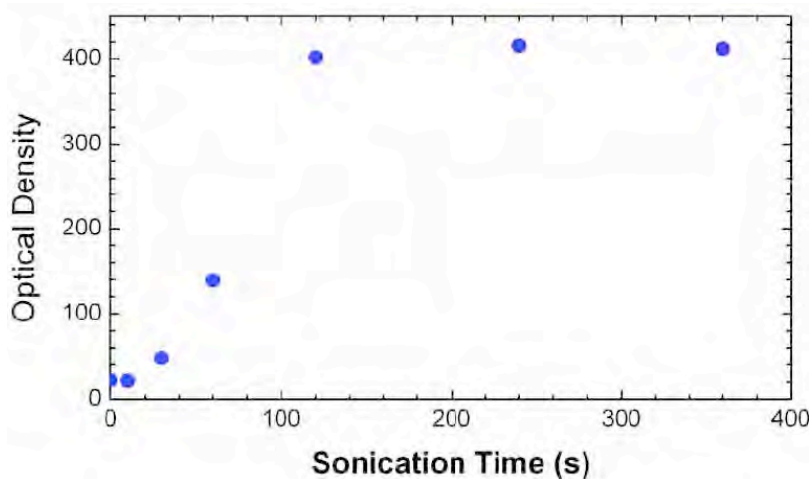

Figure 1. Effective dispersion optical density as a function of sonication time for nanolatex/MWCNT dispersion 1% in MWCNT and 18% in nanolatex solids.

optical density rises steeply, after an induction period, to an effective optical density in excess of 400. This 1% weight concentration corresponds to 10 mg/mL the 418 effective optical density means the MWCNT in this dispersion exhibit an extinction coefficient of 41.8 cm^2/mg. This is substantially greater than the 28.6 cm^2/mg value reported for SWCNT.

Similar dispersions were prepared with MWCNT contents of 0.399, 0.801, and 2.20 % (w/w). These and the 1% dispersion were used to make thin film castings as originally described in our SWCNT/nanolatex work. We used the inner annular seal of 50 mL centrifuge tube caps as polypropylene molds to make air dried wafers. Each annular ring holds about 850-950 mg of dispersion.

Figure 2 illustrates various of these castings prepared for dispersions wherein the nanolatex solids were 18% and the MWCNT levels were 0.399% (MA), 0.801% (MB), and 2.20% (MC). After removal, the thin films or wafers are about 150-300 um in thickness. This series was initially prepared to see if an optimal level of MWCNT would be evident from effective dispersion optical density or other physical property measurements.

Figure 2. Polypropylene centrifuge cap castings of MWCNT/nanolatex dispersions at 0.399 (MA), 0.801 (MB), and 2.20% (MC) MWCNT (w/w).
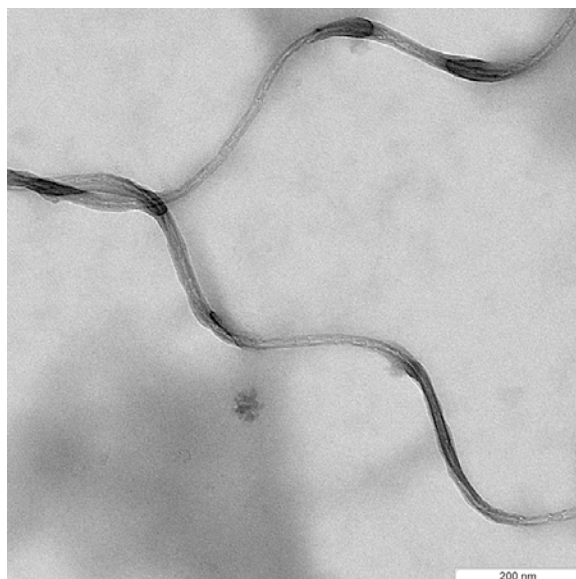

Figure 3. TEM of MWCNT in the process of exfoliating. This sample was taken from a sampling of the 1% MWCNT dispersion after 360 s sonication and was highly diluted for effective optical density measurement (Fig. 1).

Figure 3 illustrates the exfoliation or detwisting of two MWCNT. This sample was taken from the dilution used to measure the effective optical density of the 1% MWCNT dispersion sonicated for 360 s (Fig. 1). Individual nanolatexes are not particularly visible in this TEM, although some background blotches are attributable to nanolatexes, and some areas of excess density on the MWCNT may be due to adsorbed nanolatexes, but these features are simply not very visible under these transmission electron microscopy conditions. Very recent FE SEM work, to be reported in the final report, and similar to the FE SEM data reported earlier in this report for nanolatex adsorption onto HTC surfaces, show that these nanolatexes appear to bind to the MWCNT surfaces in a random and irreversible manner, leaving gaps on the surface too small to accommodate adsorption of another nanolatex particle.
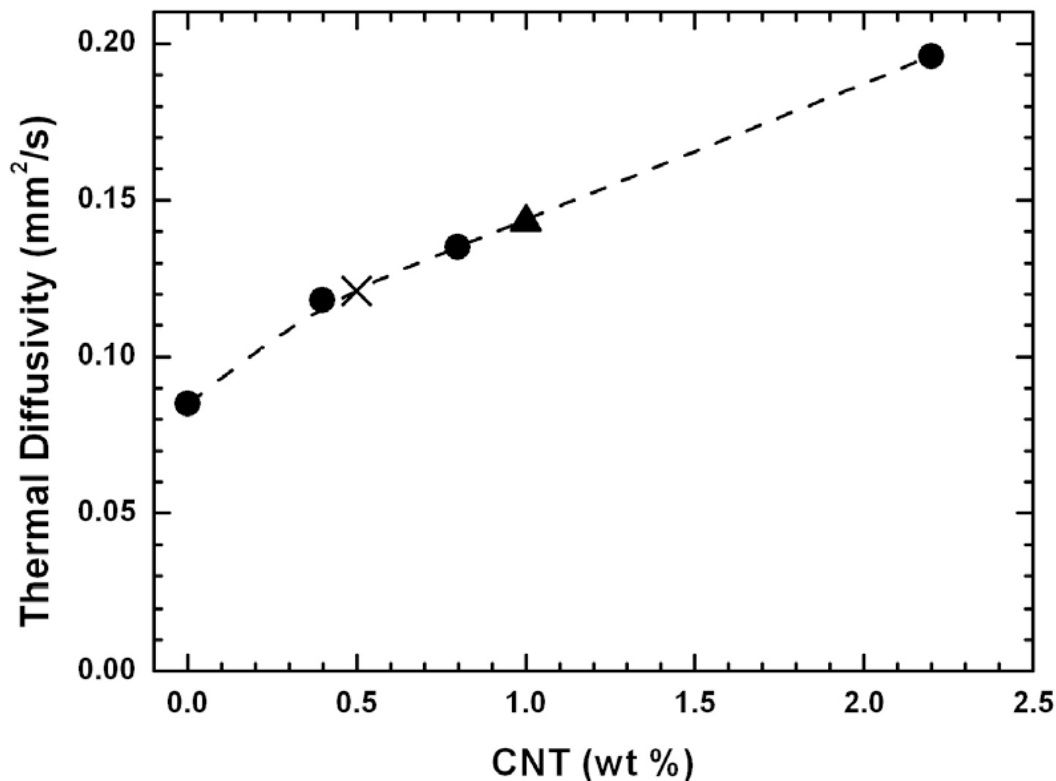

Figure 4. Thermal diffusivity measured by a xenon flash instrument (Netzsch LFA 447) for MWCNT/nanolatex films fabricated from dispersions 0.399, 0.801, 1.0, and 2.20 % (w/w) MWCNT and 18% (w/w) aqueous nanolatex. The datum at 0% CNT is from a CNT-free control nanolatex film, and the datum at 0.51% is from a comparable wafer fabricated from a SWCNT dispersion.

Thermal diffusivity in through-plane geometry is illustrated in Fig. 4 for thin wafers formed from nanolatex/MWCNT dispersions at various weight% values of MWCNT. The 0% control was derived directly from the nanolatex dispersion. The values fit a smooth curve and steadily increase with increasing MWCNT loading. The datum indicated by the "Î" is from a similar thin wafer derived from a nanolatex/SWCNT dispersion. The MZ wafer at 1.00% w/w MWCNT also exhibited an in-plane thermal diffusivity of 1.10 mm2/s, indicating an anisotropy for thermal diffusion and conductivity of about 8. This anisotropy

indicates a significant alignment of the MWCNT parallel to the in-plane direction resulting during the drying/curing process.

Through plane electrical conductivity measurements as a function of frequency for this same weight series of thin wafers are illustrated in Figs. 5-8 from 0.1 Hz to 10MHz and from -50°C to 25°C. The data in Fig. 5 show that the intrinsic ionic conductivity from the nanolatex dominates over MWCNT-based electrical conductivity. As the loading of MWCNT increases, we see in Fig. 6 that electrical conductivity predominates at -50°C to 25°C, but that ionic conductivity dominates at higher temperatures.
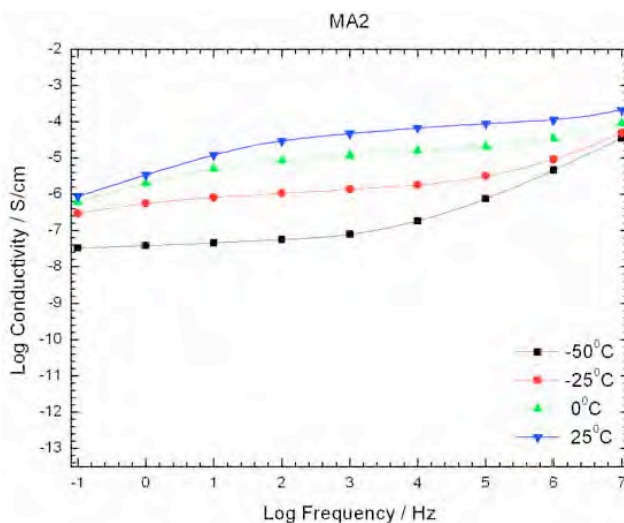
Figure 5. Electrical conductivity (through plane) as a function of frequency for nanolatex/MWCNT nanocomposite derived from the 0.399% (w/w) nanolatex/MWCNT dispersion MA.
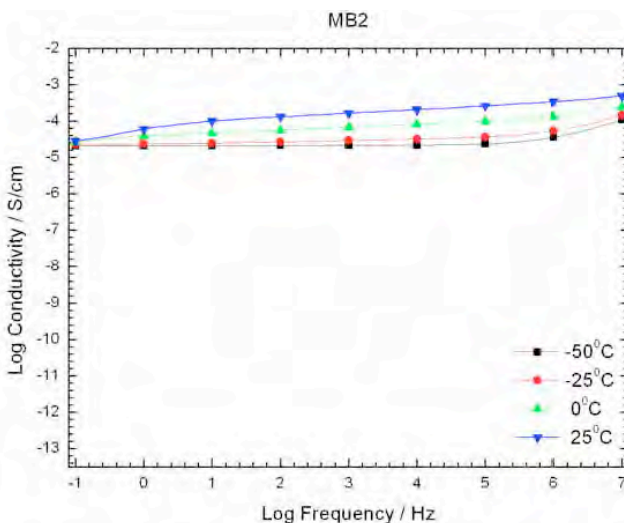

Figure 6. Electrical conductivity (through plane) as a function of frequency for nanolatex/MWCNT nanocomposite derived from the 0.801% (w/w) nanolatex/MWCNT dispersion MB.

Figure 7 illustrates the conductivity for the wafers derived from 1.0% (w/w) MWCNT dispersion. The slightly higher loading shows essentially metallic (frequency independent) conductivity over most of the frequency range, with a slight ionic conductivity deviation at room temperature and higher frequencies.
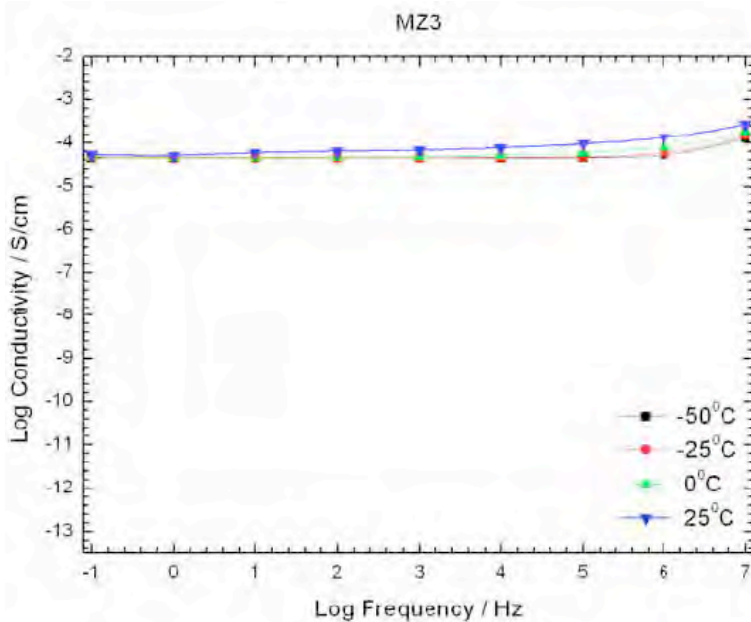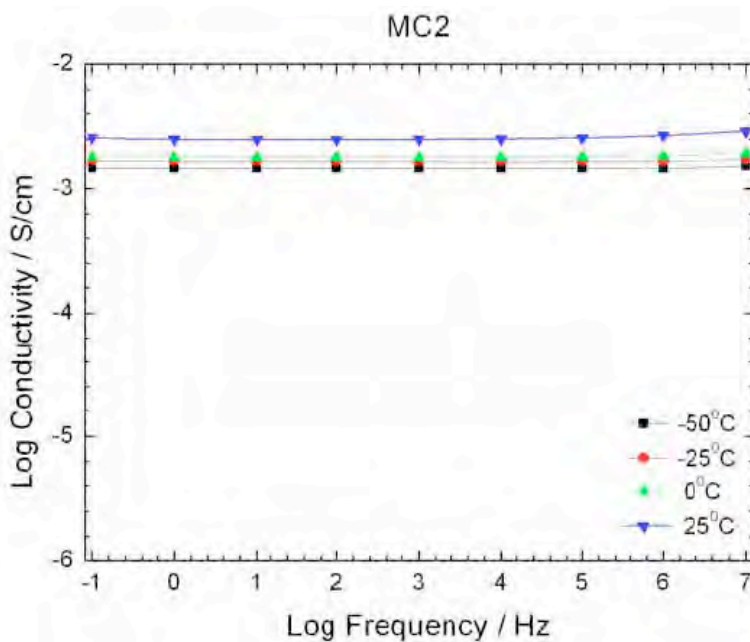

Figure 7. Electrical conductivity (through plane) as a function of frequency for nanolatex/MWCNT nanocomposite derived from the 1.00% (w/w) nanolatex/MWCNT dispersion MZ.

Figure 8. Electrical conductivity (through plane) as a function of frequency for nanolatex/MWCNT nanocomposite derived from the 2.2% (w/w) nanolatex/MWCNT dispersion MC.

Figure 8 illustrates the through plane conductivity spectra for the most highly loaded wafers, and here the conductivity has increased by over an order of magnitude, ranging from about 1.5 to 2 mS/cm over the -50 to 25°C temperature range.
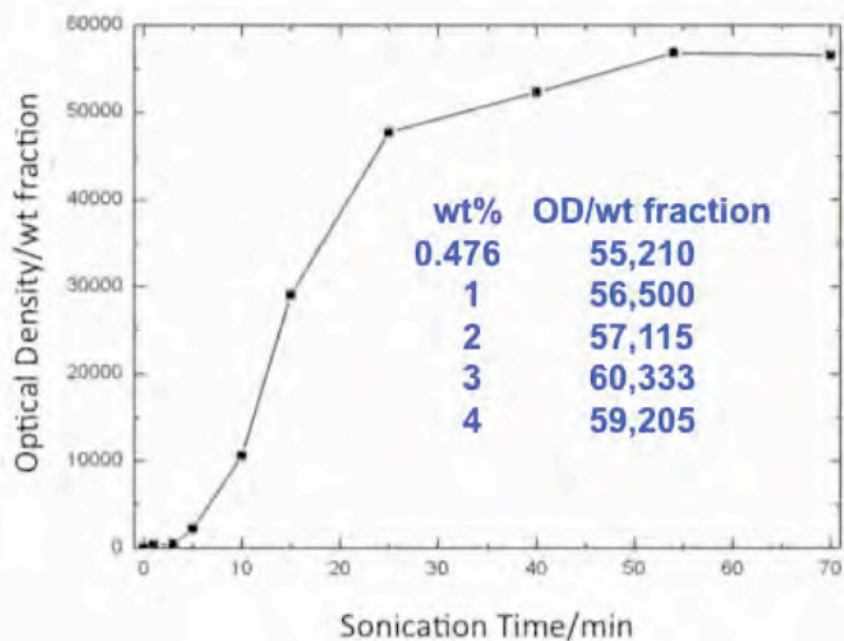

Figure 9. Effective optical density of waterborne nanolatex/MWCNT dispersions as a function of the sonication time where the MWCNT content was kept constant at 1% (w/w) and the nanolatex content was varied from 0.595 to 20.0 % (w/w).
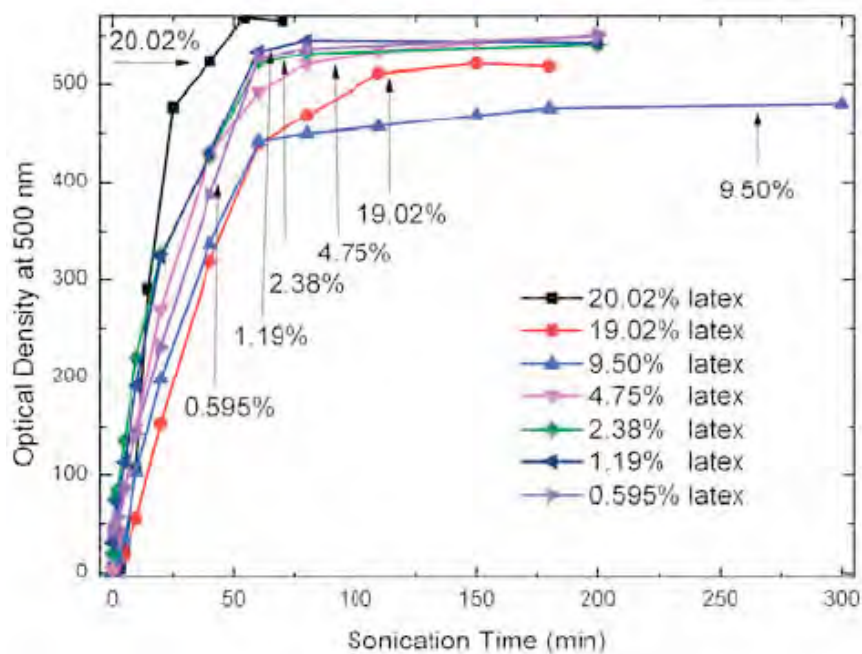

Figure 10. Effective optical density of waterborne nanolatex/MWCNT dispersions as a function of the sonication time where the MWCNT content was kept constant at 1% (w/w) and the nanolatex content was varied from 0.595 to 20.0 % (w/w).

Figure 9 illustrates effective MWCNT/nanolatex dispersion optical density normalized to the MWCNT weight fraction for a 4% (w/w) dispersion about 20% in nanolatex as a function of sonication time. Limiting similarly normalized optical densities for dispersions of other MWCNT weight fraction are also listed in this figure, and show that over the 0.5 to 4% (w/w) interval the effective normalized optical density (at 500 nm) is essentially the same. We interpret this "sameness" as indicative that the MWCNT samples are completely exfoliated by the time this asymptotic optical density is reached.

In Fig. 10 we illustrate effective dispersion optical densities for dispersions 1% (w/w) in MWCNT at varying nanolatex loadings. The nanolatex loading is varied from 0.595 to 20%, and we see that almost all of the dispersions reach a fully exfoliated effective optical density of 550.
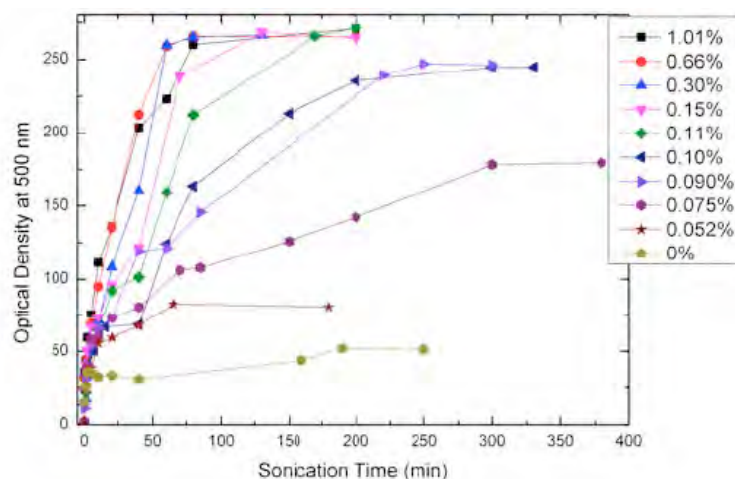

Figure 11. Effective optical density of waterborne nanolatex/MWCNT dispersions as a function of the sonication time where the MWCNT content was kept constant at 0.5% (w/w) and the nanolatex content was varied from 0 to 1.0 % (w/w).
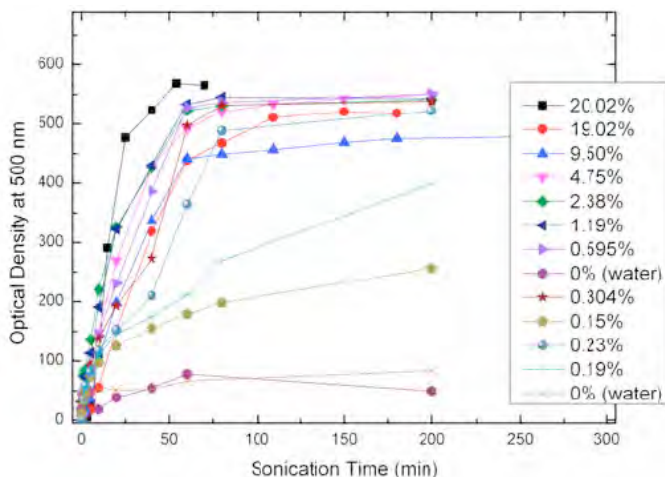

Figure 12. Effective optical density of waterborne nanolatex/MWCNT dispersions as a function of the sonication time where the MWCNT content was kept constant at 1% (w/w) and the nanolatex content was varied from 0 to 20.0 % (w/w).

In Fig. 11 we illustrate effective dispersion optical densities for dispersions 0.5% (w/w) in MWCNT at varying nanolatex loadings. The nanolatex loading is varied from 0 to 1.01%, and we see that most of the variation of the high dose effective densities occurs over a very low interval in nanolatex to MWCNT weight ratio, 0 to 0.1%. Figs. 12, 13, and 14 similarly show variations in effective dispersion optical density vs. sonication time for 1, 2, and 4% (w/w) for varying levels of nanolatexes.
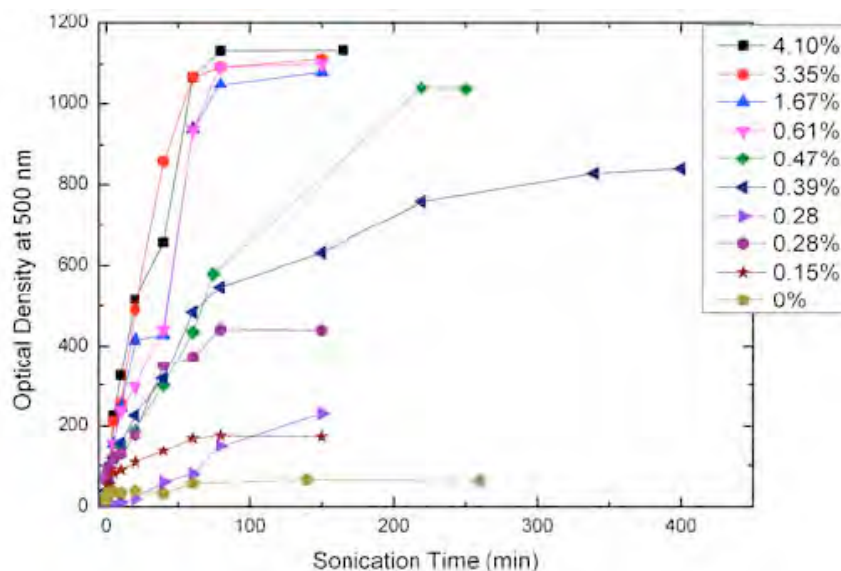

Figure 13. Effective optical density of waterborne nanolatex/MWCNT dispersions as a function of the sonication time where the MWCNT content was kept constant at 2% (w/w) and the nanolatex content was varied from 0 to 4.2 % (w/w).
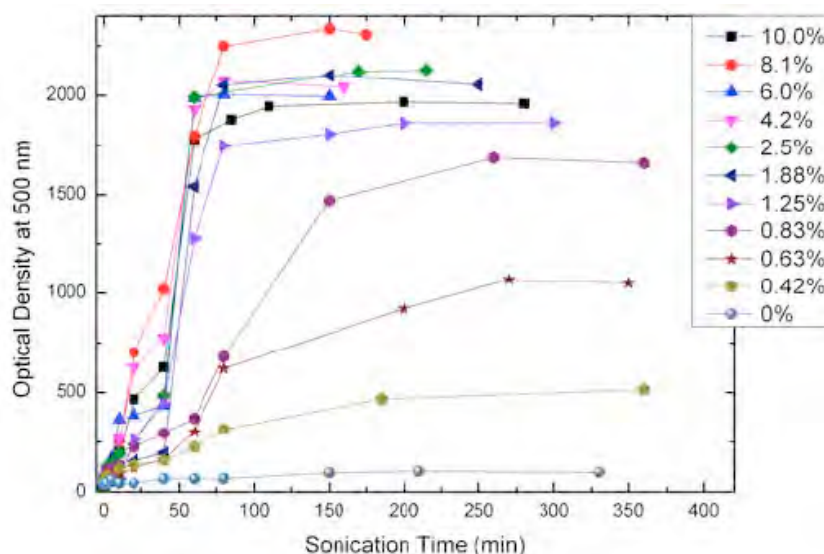

Figure 14. Effective optical density of waterborne nanolatex/MWCNT dispersions as a function of the sonication time where the MWCNT content was kept constant at 4% (w/w) and the nanolatex content was varied from 0 to 4.2 % (w/w).

The asymptotic optical density data of Figs. 10-14 are replotted in Figs. 15 and 16 as a function of nanolatex/MWCNT weight ratio. For each level of MWCNT the data show a steadily increasing linear behavior interesting an asymptotic surface saturation limit. The intersection of these behaviors, the break point, corresponds to the surface saturation ratio of nanolatex to MWCNT. This amount corresponds approximately to weight ratios of 0.23 to 0.30 as the total weight concentration of MWCNT increases from 0.5 to 4%. These data show that completely exfoliated MWCNT dispersions can be obtained by using about 30% nanolatex relative to MWCNT. This amount increases slowly (0.23 to 0.30) as the MWCNT concentration increases 8 fold. This relative level of adsorbed nanolatex represents the amount of adsorbed nanolatex require in order to suppress MWCNT aggregation. It appears to be a weak function of absolute MWCNT concentration.
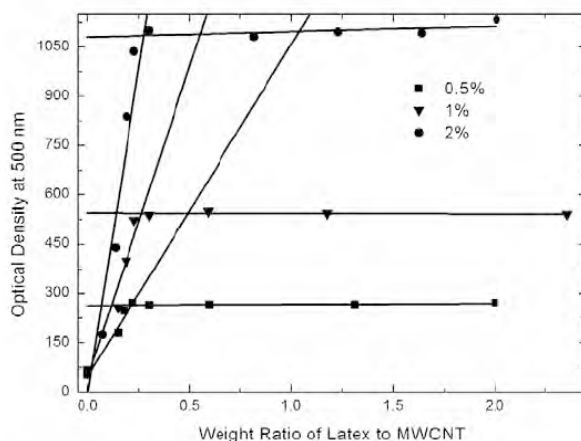

Figure 15. Effective optical density of waterborne nanolatex/MWCNT dispersions as a function of the weight ratio of nanolatex to MWCNT for dispersions 0.5, 1.0, and 2.0 % (w/w) in MWCNT.
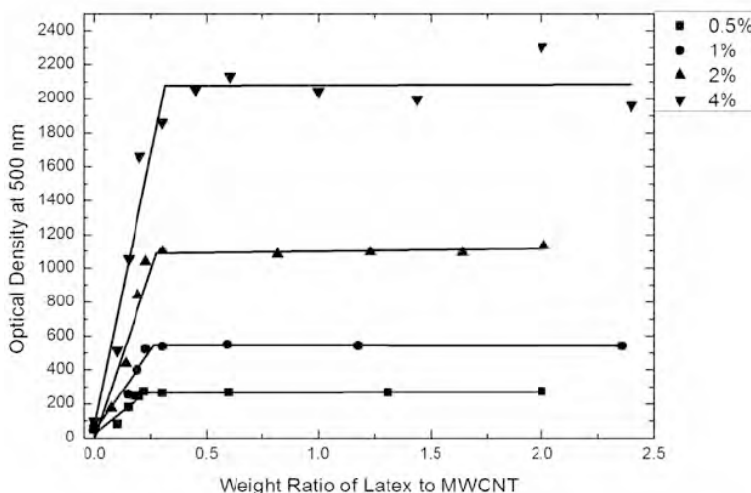

Figure 16. Effective optical density of waterborne nanolatex/MWCNT dispersions as a function of the weight ratio of nanolatex to MWCNT for dispersions 0.5, 1.0, and 2.0 % (w/w) in MWCNT. Same as Figure z except data for 4% (w/w) MWCNT dispersion have been added.

These waterborne MWCNT dispersions are the most concentrated, by far, to be reported. Our ionic liquid based nanolatex appears to be the most effective dispersant yet reported, and we believe this efficacy is due to the high affinity of the imidazolium group for nanocarbon surfaces. The mechanism of stabilization has been shown to be due to a consistent saturation level, 0.22-0.30 on a weight ratio basis, of nanolatex on MWCNT.
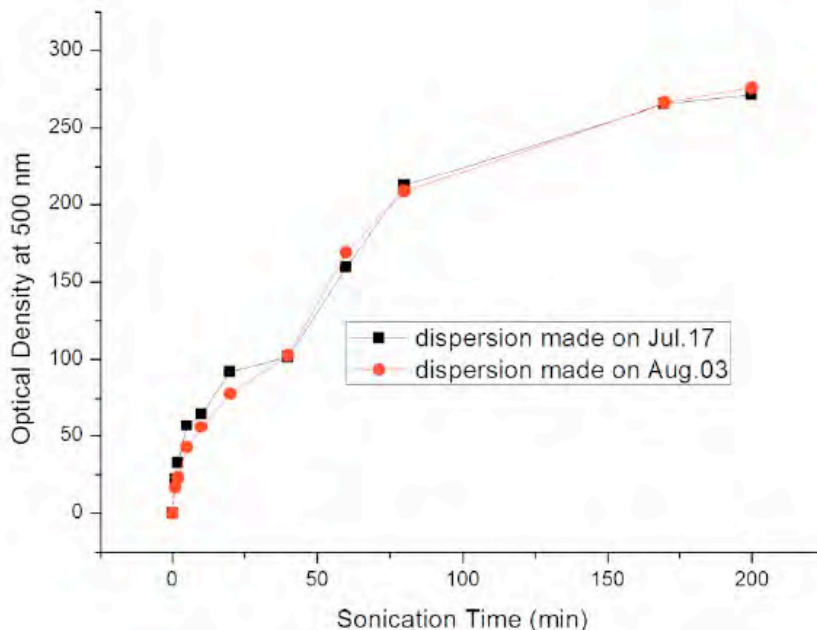

Figure 17 Effective optical density of waterborne nanolatex/MWCNT dispersion, 0.5% (w/w) in MWCNT as a function of sonication time for experiments done 3 weeks apart.

Figure 17 illustrates the reproducibility of the dispersion process for 0.5% (w/w) MWCNT dispersions with a 0.22 nanolatex/MWCNT weight ratio, showing that this high level of effective optical density, corresponding to complete exfoliation, is repeatedly obtainable.

In order to examine the nanolatex adsorption and stabilization mechanism in more detail, nanolatex stabilized MWCNT dispersions and control nanolatex dispersions were examined at 25°C using an Anton Paar density meter. From these measurements we found that the MWCNT have a density of 2.11 g/cm^3 and the nanolatex particles have a density of 1.21 g/cm^3.

The specific surface area of the MWCNT, treated as a cylinder of diameter d, is $4/(\rho_{CNT}d)$, where ρCNT is the MWCNT density. For a diameter of 40 nm (40 x 10^{-7} cm), a specific surface area of 4.74 x 105 cm^2/g or 474 m^2/g.

The specific surface area of a nanolatex particle, treated as a sphere of diameter d, is $6/(\rho_L d)$, where ρ_L is the nanolatex density. For a diameter of 25 nm (25 x 10^{-7} cm), a specific surface area of 1.98 x 10^6 cm^2/g or 1980 m^2/g. For a 30 nm diameter nanolatex, a specific surface area of 1650 m^2/g is obtained. If we assume that half of each adsorbed nanolatex particle is in contact with the MWCNT surface, an "adsorbed specific surface area" of 825-940 m^2/g or 882 m^2/g is obtained.

The ratio 474 m^2/g_{CNT}/882 m^2/gL = 0.54 gL/g_{CNT} describes the weight ratio of nanolatex to MWCNT when the MWCNT surface is completely covered by adsorbed nanolatex. The experimental values of 0.22-0.30 gL/g_{CNT} suggests that the actual saturation adsorption covers 41-55% of the MWCNT surface. A value of 0.55 (RSA) is the well known jamming limit for irreversible and random saturation adsorption of uniform spheres on a surface. Smaller saturation limits are obtained when the adsorbed particle spreads partially after adsorption. Our saturation limits, therefore, support a random and irreversible adsorption model admitting post adsorption spreading for some of the particles. Recent FE SEM data provide evidence that this is indeed the mechanism followed, and show that many adsorbed nanolatex particles adsorb conformally to the MWCNT, flattening to disk shaped particles.

MWCNT Monoliths

Nanolatex/MWCNT films

Wafers of MWCNT/nanolatexes produced as described in the previous section, about 200-300 μm in thickness, were used to examine the production of monoliths via pyrolysis of the nanolatex. An SEM image of powdered MWCNT is shown in Fig. 1(a). A rectangular section of a wafer derived from a 4% MWCNT dispersion in 20% nanolatex was heated to 800°C under nitrogen. The monolith did not maintain its original dimension on pyrolysis of the nanolatex and
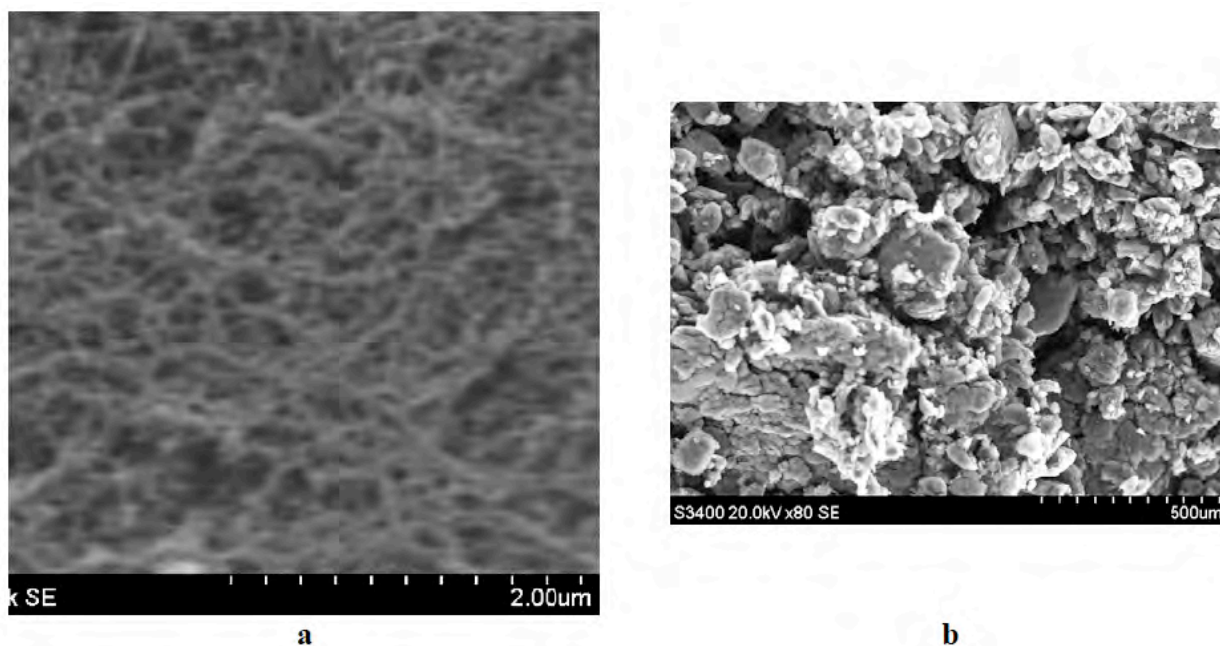

Figure 1, (a) Top view SEM of MWCNT/nanolatex composite derived from 4% (w/w) MWCNT dispersion 20% in nanolatex after anaerobic pyrolysis of nanolatex in N2 stream; (b) SEM of MWCNT powder prior to sonication.
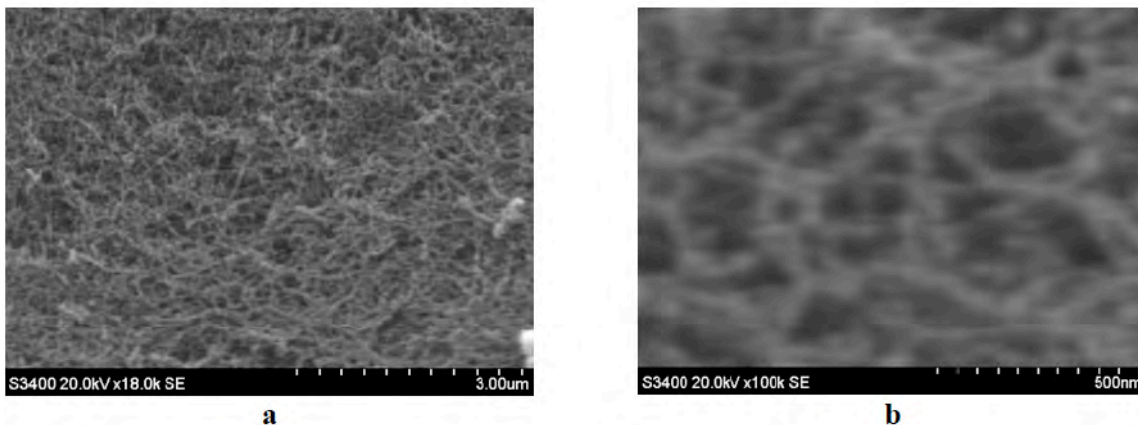
Figure 2. (a), (b) Two additional views of the pyrolyzed monolith illustrated in Fig. 1(a).

reduced each of its dimension about 15% while keeping its parallelepiped shape. Fig 1(b) illustrates the porosity evident after pyrolysis of the nanolatex. Two additional views of the pyrolyzed MWCNT monolith are shown in Fig. 2.

Figure 3 shows the TGA of a control nanolatex film and Fig. 4 shows the TGA of the film sample used to produce the monolith of Figs 1(a) and 2. The nanolatex decomposes in two waves, first the ILBr-based part, followed by the MMA component. These separate waves corroborate the tendency of the ILBr and MMA monomers to polymerize in a de facto block form, most probably because of the differences in their respective propagation rate constants. By 600°C the nanolatex is reduced to less than 2% ash. The TGA of the monolith precursor film in Fig. 4 shows an essentially theoretical amount of residue, due to the unpyrolyzed MWCNT.
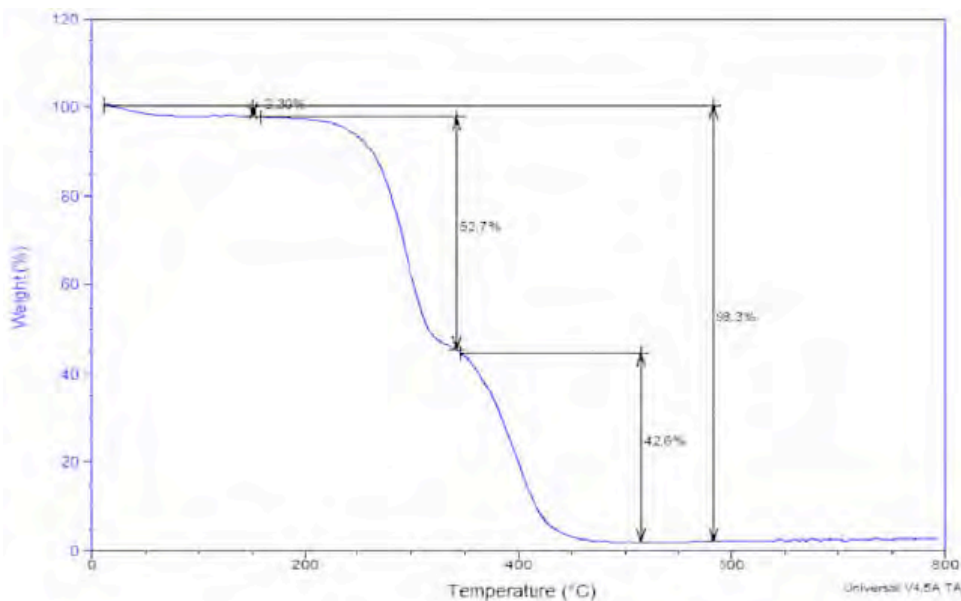

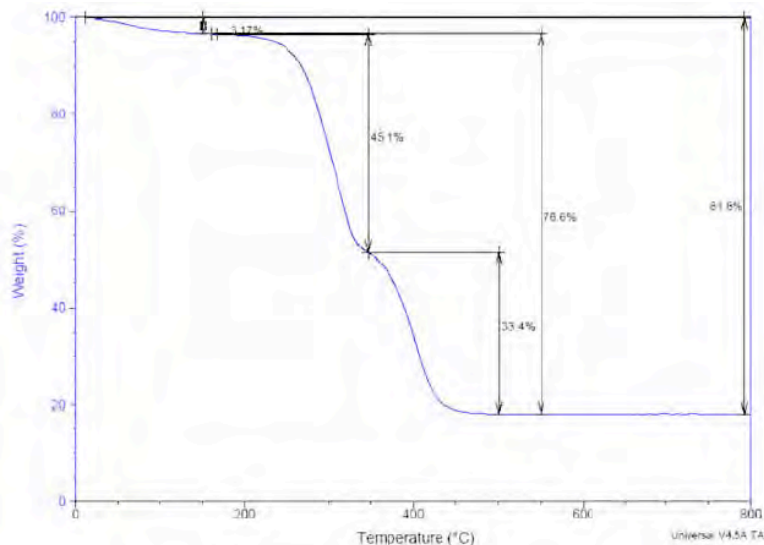**Figure 3. TGA of control latex film.**

Figure 4. TGA of monolith precursor film.

Figure 5 shows an SEM of the monolith precursor top surface prior to pyrolysis. The high content of coalesced nanolatex film presents a more or less smooth surface. At higher magnification it is still not possible to see structures due to the MWCNT.
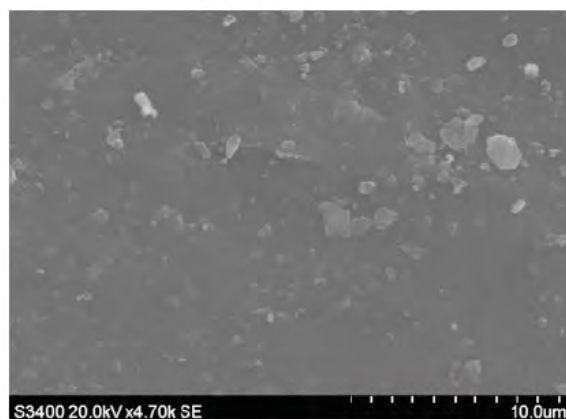

Figure 5. SEM of monolith precursor film (top view).

Coatings on flash paper

It was decided to try to use paper as a template on which to cast and coat MWCNT dispersions, since the cellulose in paper likely will pyrolyze at an even lower temperature than the nanolatex. The TGA in Fig. 6(a) is for a sample of ordinary office copier paper. We see it leaves a residue of about 20%. While most of the decomposition occurs over the 250-350°C interval, and additional component does not decompose until almost 600°C. We then decided to try magician's flash paper. This paper typically is heavily nitrated in a nitric acid/sulfuric acid bath, in order to promote extremely rapid combustion with minimal ash. A TGA of such a paper is illustrated in Fig. 6(b), where we see essentially complete pyrolysis over a very narrow 180-200°C interval.
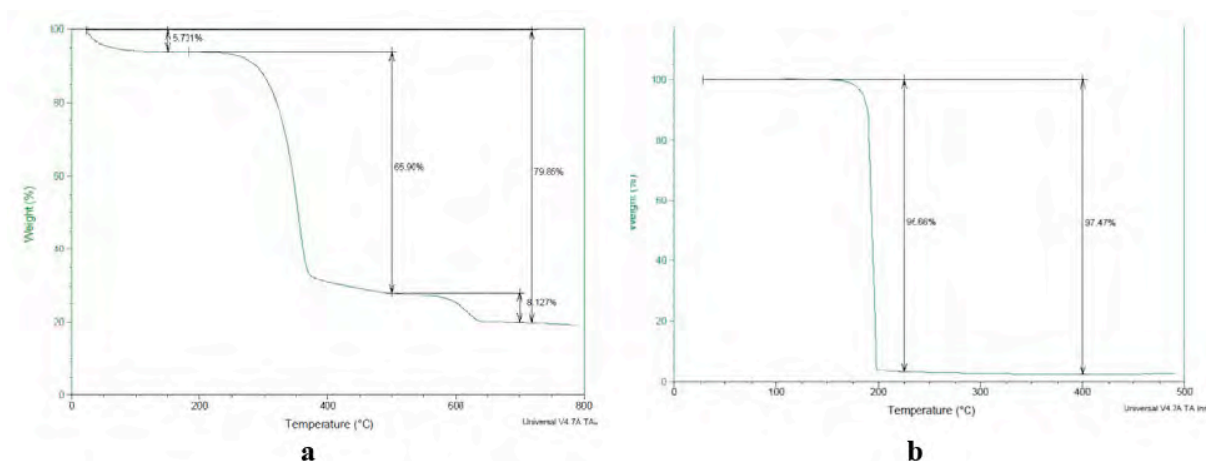
Figure 6. TGA of (a) office copy paper and (b) flash paper showing rather modest decomposition temperature under a nitrogen carrier gas flow.
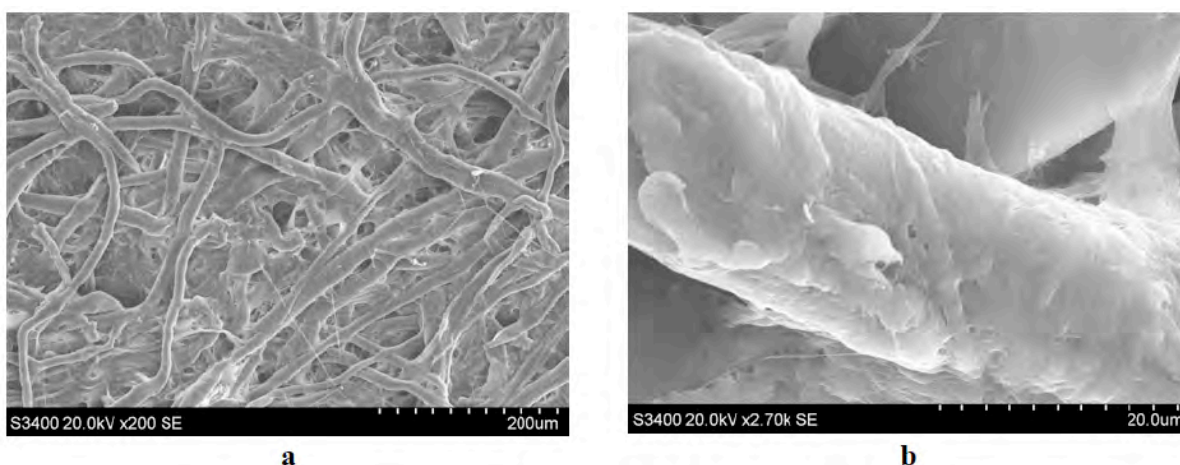

Figure 7. SEM of magician's flash paper; this paper is designed to combust in a flash and to leave no perceptible ash (visible to an audience); it is basically a highly nitrated paper. (a) Low magnification image showing fiber and pore structures; (b) magnified view of a single fiber.

SEM of this flash paper are illustrated in Figs. 7(a) and 7(b). We see the paper has a diffuse network of large pores, 20-100 μm. We see in Fig. 7(b) an individual paper fiber about 20 μm in diameter. We therefore began a series of experiments using this flash paper as a template upon which to coat our MWCNT/nanolatex dispersions.

Figure 8 illustrates how the flash paper can be easily coated. A piece of flash paper is first appended to a smooth support by tape. In this case we used an aluminum coupon as support. A draw down bar is then placed over the paper and a given amount of dispersion is poured along the back edge of the bar. The bar is then moved along the coupon, spreading the dispersion uniformly over the paper. The excess dispersion is wicked down into the paper, and the coating is air-dried. The final result is shown in Fig. 8(right).
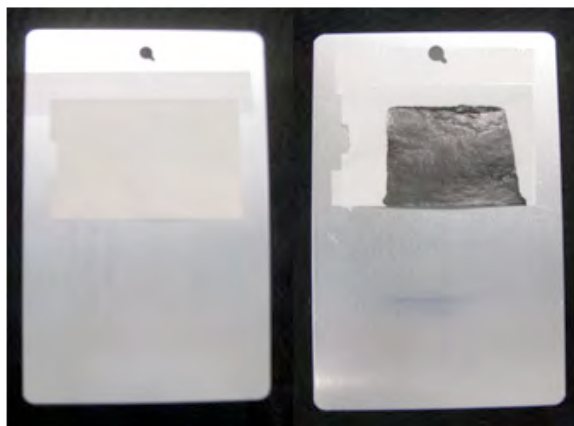
Figure 8. Photographs of (left) flash paper appended to aluminum coupon with tape prior to coating and (right) coated flash paper after coating with 4%/1.25% MWCNT/nanolatex dispersion.

The coated paper is then cut into two sections, and one of them was placed in a muffle furnace and heated to 250°C, to pyrolyze the paper template. The resulting MWCNT monolith, along with the unpyrolyzed half of the coating are illustrated in Fig. 9.
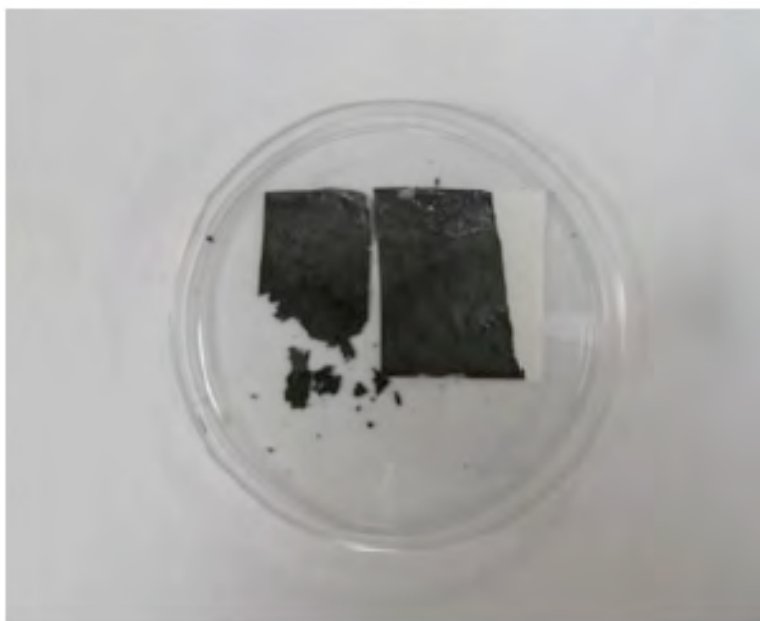

Figure 9. Photograph of (left) large MWCNT monolith after pyrolysis of flash paper template and (right) companion section of unpyrolyzed and coated flash paper illustrated in Fig. 8(right).

One of the mechanical difficulties facing one after pyrolysis is the mechanical integrity of the resulting MWCNT monoliths. They tend to crumble easily when subjected to compression or shear. In order to overcome this handling problem, we decided to try coating such monoliths with an adhesive polymer. Our first attempt is illustrated in Fig. 10, where we coated a pyrolyzed MWCNT monolith with a solution of cyanoacrylate in methylene chloride. The air drying monomer very nicely cured to give the desired effect.

More work in this area is needed, as the porosity must be controlled for many anticipated applications.

Figure 10. Photographs of (left) monolith of MWCNT after pyrolysis of flash paper template and (right) monolith after wetting with methylene chloride solution of cyanoacrylate (superglue).

Adsorption of nanolatex on MWCNT

While earlier work clearly resolved the amount of nanolatex needed to stabilize a given weight percent MWCNT dispersion in water, direct evidence of how the nanolatex adsorbs on the MWCNT surfaces was lacking. SEM was previously used to image such nanoparticles on surfaces of hydrothermal carbon, as discussed and illustrated in a prior section of this report. We therefore used FE SEM to try to image nanolatex particles adsorbed upon MWCNT. Such imaging is not possible when thin films are cured in the presence of excess nanolatex. We found, however, that coating a 1.0%/0.3% MWCNT/nanolatex dispersion on flashpaper resulted in the excess dispersion being wicked down into the flash paper support, allowing the MWCNT coating to dry without the pores being obstructed by excess aqueous nanolatex. The resulting FE SEM are illustrated in Figs. 11 and 12 below, where it can be seen that the nanolatex particles (1) appear to adsorb in a random and irreversible
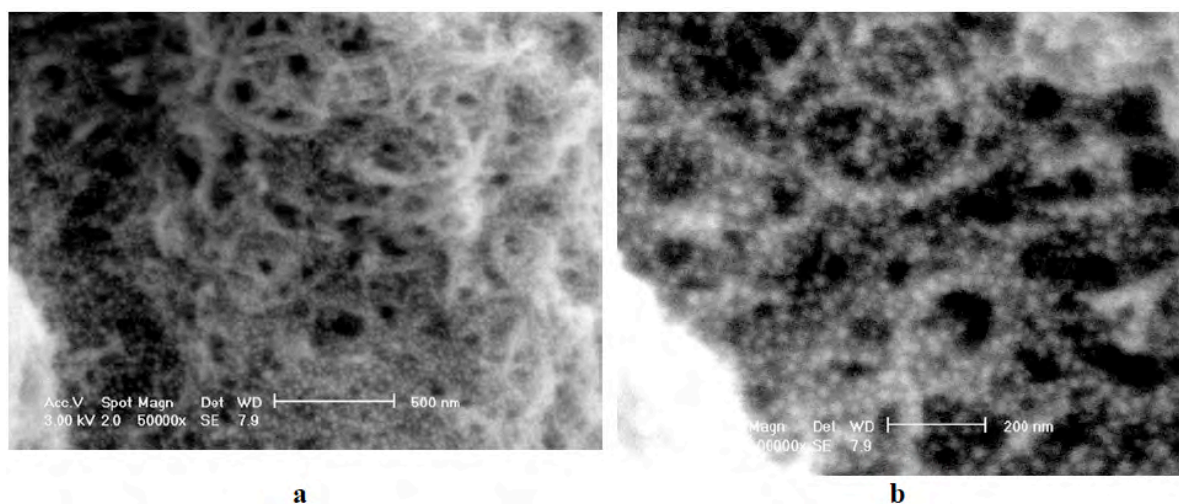

Figure 11. SEM of MWCNT/nanolatex dispersion, 1.0%/0.30%, after being coated on flash paper.
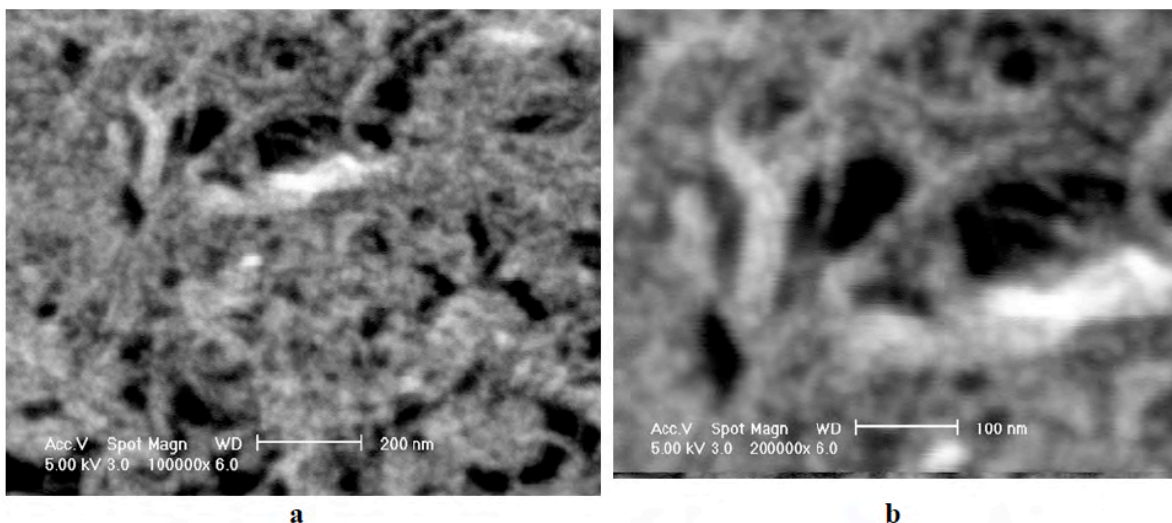
Figure 12. SEM of MWCNT/nanolatex dispersion, 1.0%/0.30%, after being coated on flash paper.

manner and (2) the nanolatex particles appear to adsorb somewhat conformally to the curved MWCNT surfaces. This type of adsorption can be characterized as adsorption followed by wetting or spreading.

MWCNT Coatings

We have made very significant advances in formulating carbon nanotube aqueous dispersions and in developing coating processes for these dispersions. We also have produced outstanding results in thin film thermal transfer. Our recent MWCNT coatings exhibit a thermal diffusivity of about 1,600 mm^2/s in the coating plane, with a thermal anisotropy of about 1,500-2,000. This is about 15-fold faster than copper, and after taking account of density and specific heat, our MWCNT coatings have an in-plane thermal conductivity about 40-50% greater than copper, and an extremely high anisotropy that copper does not have! This MWCNT result also out performs pyrolytic graphite by 30%. Our processes are highly scalable using high volume dispersion and coating tools, and are totally waterborne (no organic solvents needed).

Electrical conductivities of our very recently templated MWCNT coatings, in-plane (||) and through-plane ($\perp$), are illustrated in Fig. 1. Here we are templating by coating on mulberry paper support with an under layer of flash paper that quickly wicks away the water. The dispersion coated had essentially the minimum required nanolatex (0.31 nanolatex to MWCNT weight ratio) needed for complete exfoliation. The MWCNT envelope the templating fibers, and the conductivity increases with each coating pass. The anisotropy in electrical conductivity is about 100-200 for these coatings. It is clear that higher surface conductivities are achievable.

More profoundly, we illustrate thermal diffusivity measurements in Figs. 2-4. We compare one of our templated MWCNT coatings (3 mg MWCNT/cm^2) with some commercial carbon
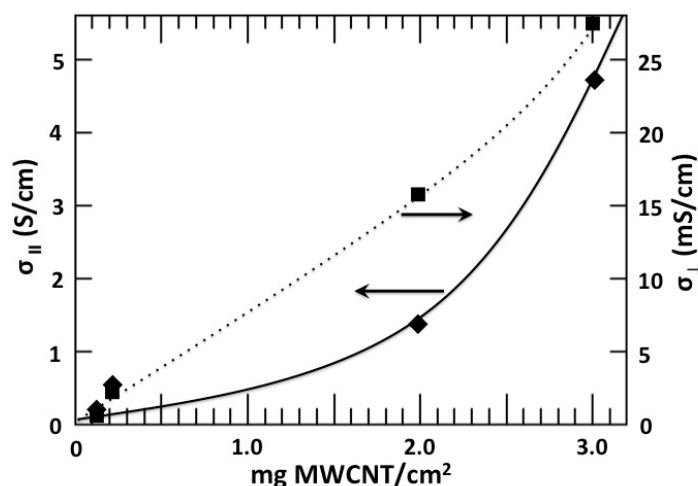
Figure 1. Electrical conductivity at room temperature of templated MWCNT coatings as a function of MWCNT areal coverage. Electrical conductivity is illustrated in-plane (u; left ordinate) and through-plane (n; right ordinate).

fiber paper. The carbon fiber paper has an in-plane electrical conductivity of 100 S/cm and a through plane electrical conductivity of 23 mS/cm. It also has reasonably high in-plane and through-plane thermal diffusivities, about 46 and 5 mm^2/s (anisotropy of 9), respectively, in comparison to polymers (0.06-0.1 mm^2/s), but still lower than copper (112 mm^2/s) and gold 127 (mm^2/s). Our MWCNT coating, on the other hand, exhibits a through-plane thermal diffusivity of about 0.7-1.0 mm^2/s (typical of polymers) and an in- plane
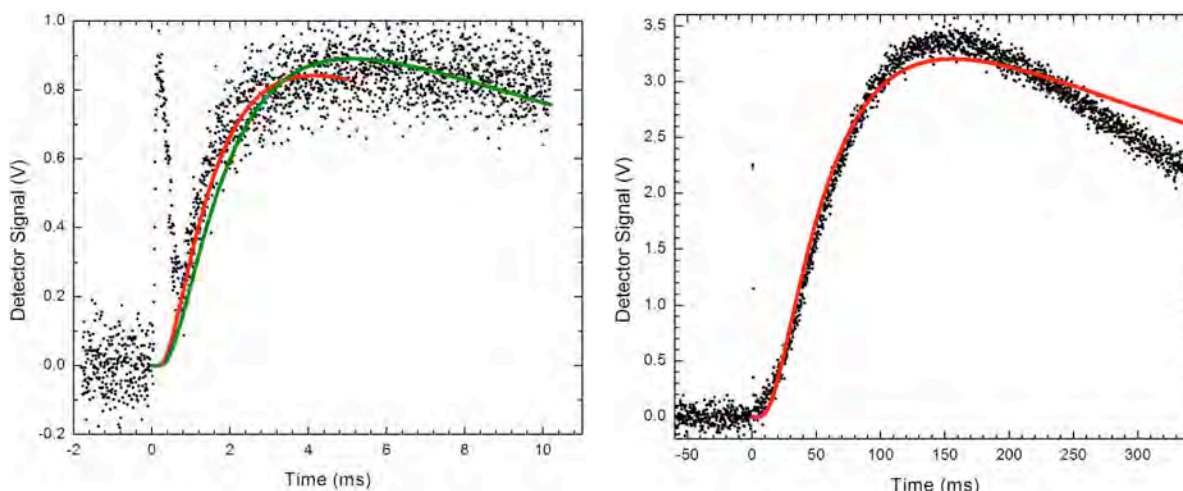
Figure 2. In-plane thermal diffusivity measurements illustrating IR detector voltage response as a function of time for (left) our MWCNT coating at 3 mg MWCNT per cm^2 and (right) a sample of carbon fiber paper. The "flash through" illustrated beginning at 0 ms is due to IR "flash through" (only a few values are sampled on the right due to the lower density of data sampling over a much longer time interval); this "flash through is simply IR radiation penetrating the sample and scattering to the detector".

thermal diffusivity of about 1,600 m²/s, 12-fold greater than gold and 30% higher than pyrolytic graphite (and 25-50% of theoretical for single CNTs)! While the carbon fiber paper is (much thicker) a more highly electrically conducting material, our templated MWCNT coating transmits heat at about 130% the rate of pyrolytic graphite, in-plane, and with a larger anisotropy, about 1,500-2,000 than pyrolytic graphite (about 330)! Such materials are unique and superior to metals in being able to directionally direct heat flow in one or two dimensions, rather than isotropically.
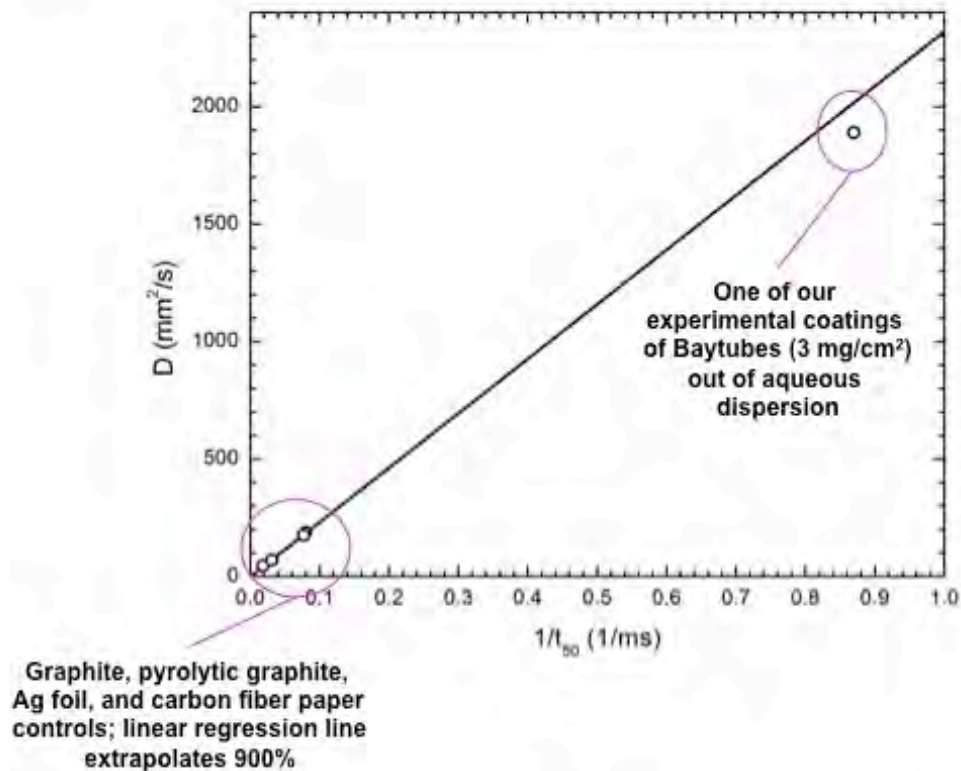

Figure 3. Measured thermal diffusivity, D, vs inverse rise time, t_{50}^{-1} for four control standards and for one of our templated coatings on mulberry paper.
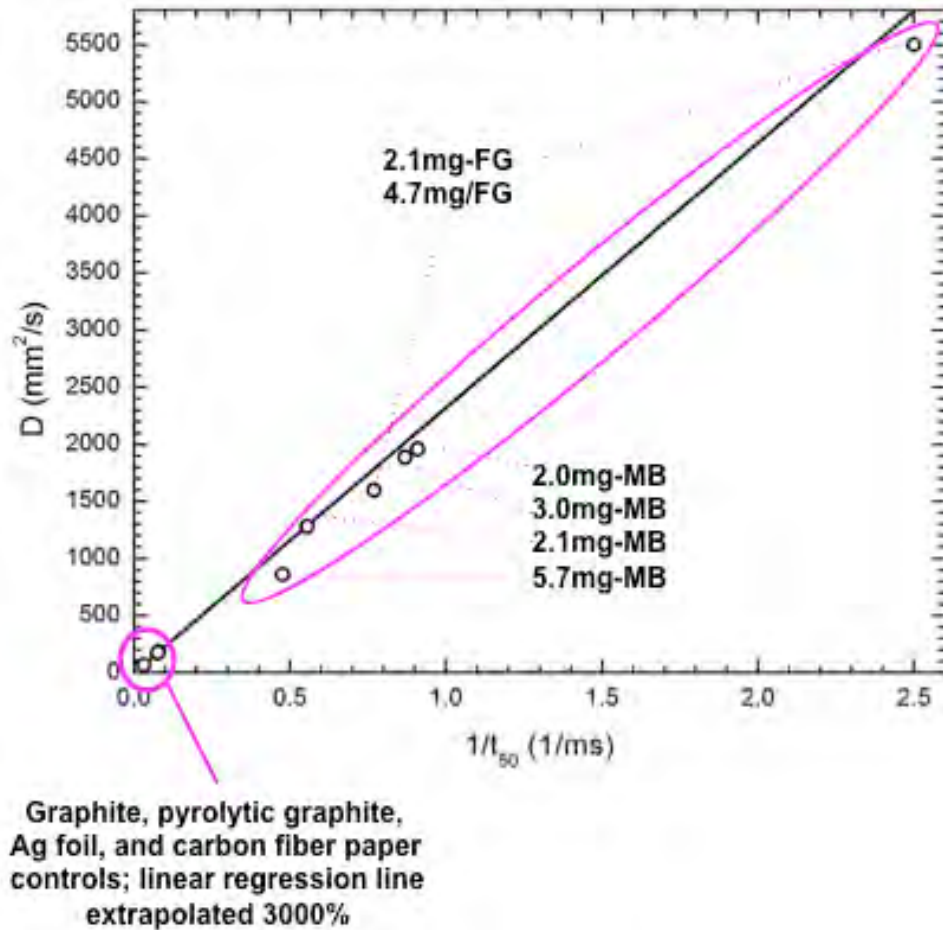
Figure 4. Measured thermal diffusivity, D, vs inverse rise time, t_{50}^{-1} for four control standards and for six of our templated coatings of MWCNT, four on mullberry paper and two on fiberglass tissue.

Our templated MWCNT dispersion coatings, using measured densities and heat capacities, result in thermal conductivities ranging from about 0.5 to 3 kW/m/K with anisotropies of about 1,000. These are the most thermally conductive materials ever made outside of a vacuum chamber and appear competitive with the low to mid diamond range.

Important issues of understanding remain. For example, simply coating higher amounts of MWCNT dispersion per unit area usually results in a lowering of the net diffusivity and thermal conductivity. The templates provide anisotropy, and initial coverages naturally will be spatially directed by the paper and fiberglass fibers. As loading increases the amount or fraction of isotropically oriented MWCNT is expected to be increased. Closer examination of these issues and studies using other types of templates are needed.

Graphene Dispersions and Coatings

To understand why graphene was claimed to exhibit significantly lower optical absorption in the visible than carbon nanotubes and even hydrothermal carbon, we purchased graphene and prepared dispersions using our nanolatex. These dispersions were initially formulated to be about 1.1% by weight graphene with a nanolatex to graphene weight ration of 0.3. The first experiments are illustrated in Fig. 1 depicted by the black and red circles. The formulation was first sonicated at 50% amplitude (black filled circles). It was next sonicated at 100% amplitude (open black circles). The amount of added nanolatex was then increased to a weight ratio of 0.4:1 and sonication was continued at 100% amplitude (red open circles). We next prepared a 1.1% dispersion and added a 0.4:2 weight ratio of nanolatex to graphene and sonicated at 1005 amplitude. These data point are royal blue hexagons in Fig 1, and we see an initially much higher increase of optical density with
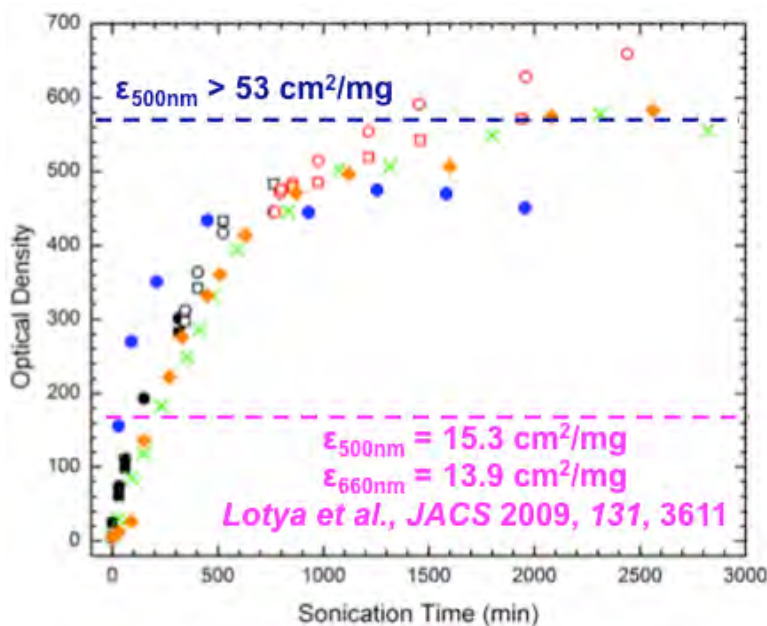
Figure 1. Optical density of graphene dispersions stabilized by nanolatex as a function of sonication time.

sonication time, but then we see a leveling at about 450 OD units. We then twice repeated the regimen used for the first two runs, and these two runs, indicated by the green crosses and the orange diamonds, reproduced fairly well. From these results we can conclude the optical absorption coefficient for exfoliated graphene is at least 53 cm^2/mg.
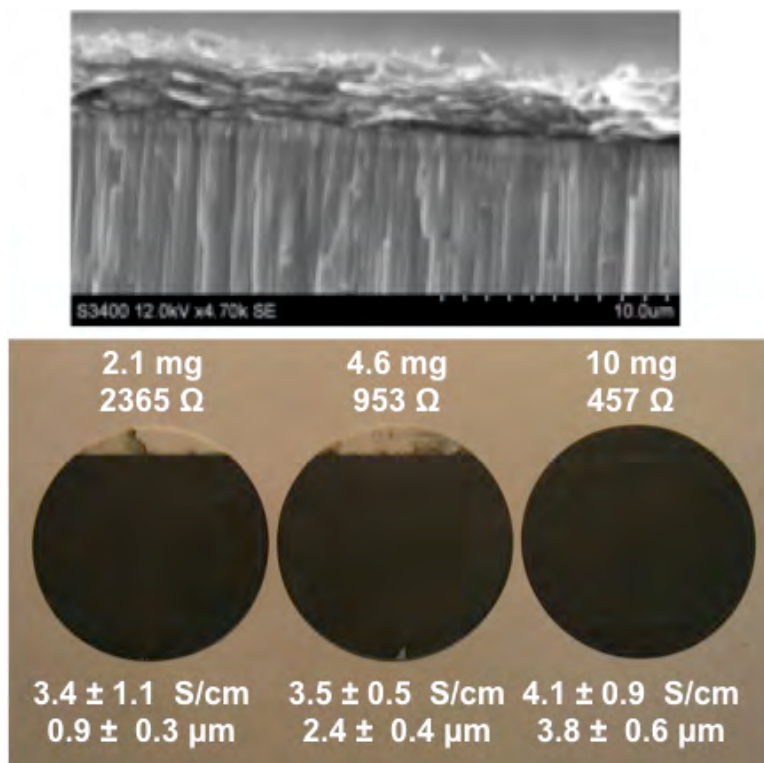
Figure 2. (upper) SEM of graphene on alumina membrane coating cross-section; (lower) photographs of three graphene on alumina membrane coatings with indicated amounts of stabilized graphene coated on each 47-mm diameter membrane, the average and standard deviation thicknesses measured for the membrane sections examined for in-plane electrical conductivity, the measured resistance coming from NY Quist plots of our conductivity measurements, and the resulting in-plane conductivities.

We next made a series of coatings of our graphene dispersions on Anapore® alumina membranes. After drying the coated membranes were weighed to determine the net weight of graphene coated. We slit the coated membranes to produce 4-5mm thick rectangular coating sections that were then examined for electrical conductivity using a four electrode measurement cell, where each electrode was a short section of Pt wire. We then obtained resistance values by taking the low frequency limit, and computed the electrical conductivities (σ)by using the equation:

$$\sigma = \frac{d}{RA}$$

where d is the distance between the closest two electrodes in the middle, R is the measured resistance, and A is the cross-sectional area of the electrode. Uncertainties in thickness measurement were computed from typically 30-40 measurements made along the sample by using the SEM and its stage motion controls.

The cross-section shown in Fig. 2(upper) illustrates some of the variability in coating thickness obtained in the coatings shown in the (lower) frame. The degree of exfoliation cannot be resolved at the magnification used in Fig. 2(upper).
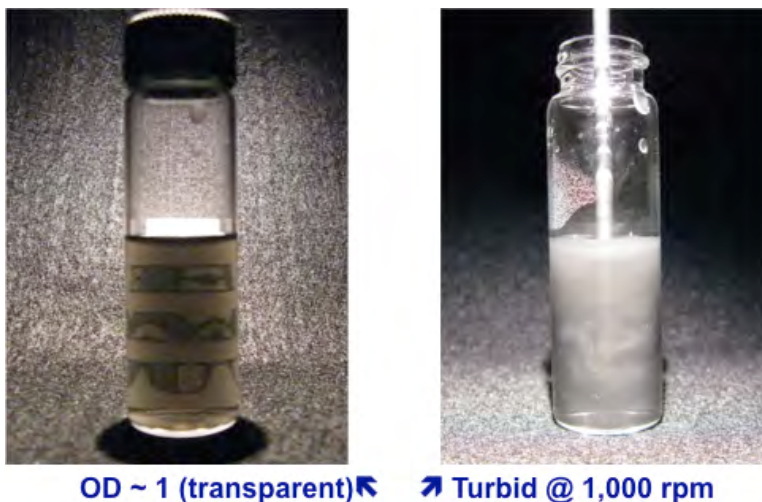

Figure 3. Graphene waterborne dispersions as opt-rheological fluids

An unexpected result is illustrated in Fig. 3. The diluted dispersion illustrated in Fig. 3(left) was an approximately 600-fold dilution of the concentrated (1.1% by weight graphene) dispersion sonicated for over 2400 minutes in the first experiment illustrated in Fig. 1 (red circles). We see in the photograph in the left frame that this dilution (made so as to be able to easily measure the effective optical density by visible absorption spectrometry) is transparent and a green "EMU" printed in green on white stock can be seen by looking through the vial. The lighting used in this photo was from above. In the righthand frame we see the same vial illuminated from the front, and the vial as a 4-mm metal rod inserted and connected to an adjustable stirrer. In this photo the contents no longer appear transparent due to refraction of the light at the inner and outer glass water and glass-air interfaces. However, in this view the stirrer is being driven at about 1,000 rpm, and also visible is turbidity being generated by light scattering from graphene platelets that are orienting parallel to the coquette flow filed. Thus this dilution (and the original concentrate) are opto-rheological fluids. In the suspension at rest the graphene platelets orient randomly and do not scatter an appreciable amount of light. When subjected to a coquette flow field the scattering of light normal to the vial surface is increased substantially.

Research Tasks 11 & 12

Filling membrane and films pores with templated polyaniline or with phenolic resins was abandoned in favor of further developing results under Research Task 10.

Bottom-up self-assembly of surface-modified nanorods/nanowires for conducting composites (Texter)

Research Task 13

Produce uniform nanorods at three different lengths (constant diameter) with end cap surface functionalization as described above (amine and isocyanate). Study morphology and "polymerization" statistics as a function of mole ratio of differently functionalized nanorods in solvent suspension.

This initial objective was abandoned when difficulties were encountered in producing suitable conducting electrodes on the alumina membranes. Effort was redirected at producing polymer brushes in such membranes using reactive nanofluids.

Nanofluid fibers cast in alumina membranes

The objective of creating metallic nanorods was supplanted by the objective of developing polymeric nanorods that could be used as anisotropic composite fillers and as templates to deposit metallic thin films for use in creating a new class of electrically conducting nanocomposites.

Anodic alumina membranes were used as substrate and a new class of hybrid resin precursors based on high viscosity nanofluids was used to create the hybrid polymer (nanocomposite) filaments. The hybrid resin precursor is based on the nonreactive nanofluids reported by Giannelis and co-workers, where inorganic nanoparticles are extensively surface decorated with ionic liquid kinds of organic salts. The reactive resin precursor we have initially used was synthesized by the scheme illustrated in Fig. 47. Ludox-SM is a commercially available nanosilica suspension with silica particles approximately 8-9 nm in diameter. These particles were decorated with the two trimethoxysilanes illustrated, one to provide nanofluidity (liquidity
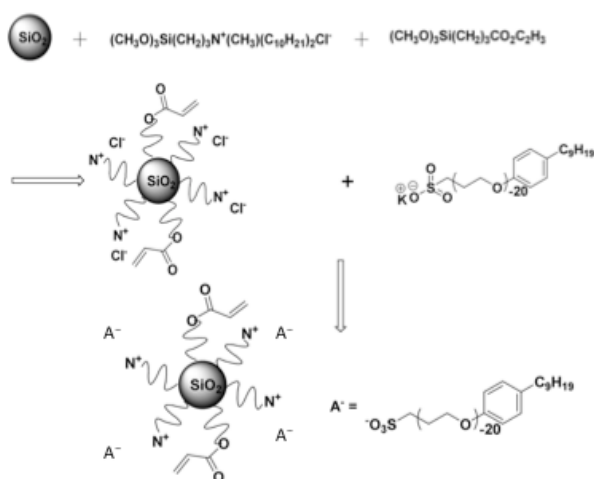

Figure 47. Synthesis of vinyl-functionalized nanofluid: Acryl sulfonate.

in the absence of solvent), the ammonium chloride, and one to provide interparticle reactivity, by providing surface acrylate groups. After these reagents are condensed on the particle surfaces the chloride is replaced by a very soft sulfonate, and the resulting product is a viscous liquid. The acrylate is a useful group whether using thermal initiation or, as used here, direct UV irradiation. To make introductory resin, this nanofluid was combined with a tetraacrylate obtained from Sartomer, SR494.
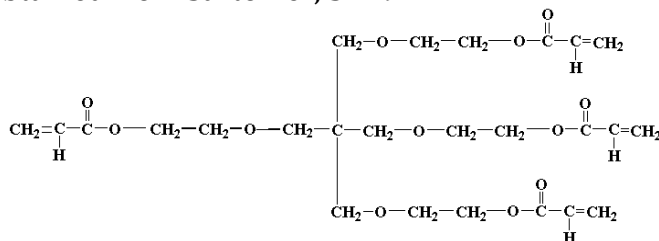
SR494

The alumina membranes were loaded by putting a drop of acryl sulfonate + SR494 mixture on the membrane using a syringe. The drop was gently spread on the membrane (this surface is the "top" surface). Then the membrane was placed in an oven at 90°C for 45 min. After removing from the oven, the membrane was turned upside down and the "bottom" surface was wiped gently with a Kim wipe. Then the loaded membrane was cured under UV (4 passes under a Fusion processing lamp), only exposing the bottom surface. The sample was then immersed in 1 M NaOH for 1 hr, rinsed, dried, and imaged by SEM
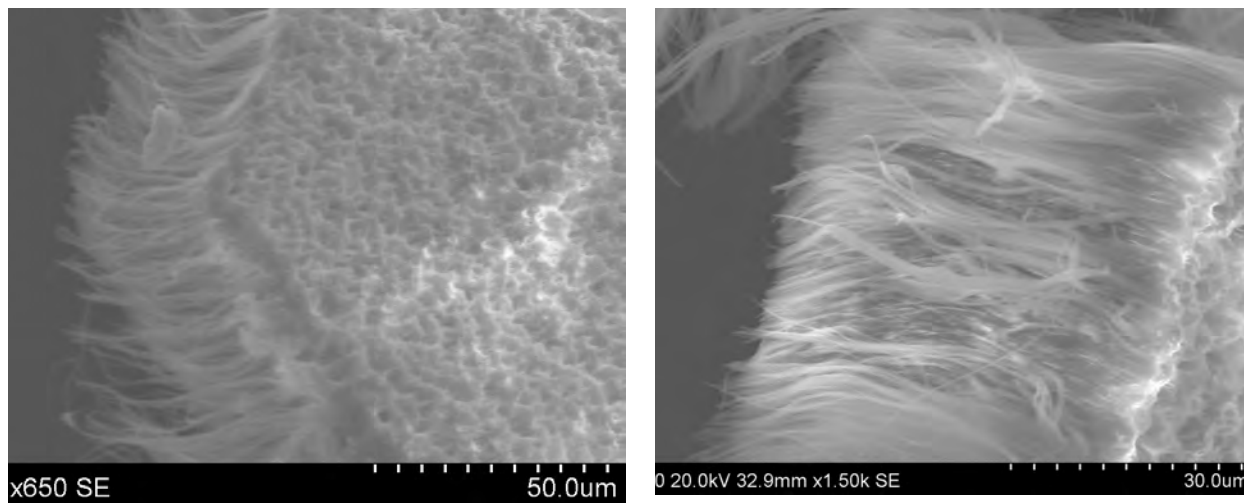
Figure 48. Nanofluid/SR494 fibers templated in 200nm pore alumina membranes and cured using direct UV irradiation after substantial dissolution of the membrane by hydrolysis in aqueous 1 M NaOH.

SEM of this new class of resin brushes are shown in Fig. 48. It appears that the aqueous dissolution of the membrane is substantial after one hour. Since the bottom surface appears to have free and unfettered fibers, it appears separable fibers can be obtained once

the excess monomer is eliminated form the top or a method is devised to removed this excess resin prior to the dissolution of the membrane. Careful removal of the excess bulk polymer on the top side must be developed in order to make the individual fibers separable.

We expect unreacted vinyl groups on the ends and surfaces of the fibers will be useful for linking the fibers together and for nucleating thing metallic films on their surfaces.

Research Task 14

The objective of preparing gels of nanorods was abandoned following abandoning metal rod synthesis in Research Task 13.

Synthesis, Characterization and Application of High Temperature Organic-Inorganic Hybrid Polymer Coatings (Baghdachi)

Research Tasks 15 and 16

Chemically modify the inorganic polysilazanes and develop convenient to process high temperature resistant coatings while providing excellent thermomechanical, toughness, and barrier properties.

Resins will be formulated to produce prototype spray applied coatings. For high temperature resistance and to provide outstanding surface and barrier properties the polymers will be combined with nano zirconium oxide, aluminum hydride, micron-sized hollow zirconium silicate or other nano-sized ceramic particles.

Synthesis of thermally resilient resins

We have synthesized inorganic/organic hybrid polymers using polysilazane, a ceramic particle precursor, and a variety of functionalized silsesquioxane and polydimethylsiloxane oligomers and polymers. Based on theoretical calculations the approximate MW of these film formers are about 21,000 Da. We have been unable to produce molecular ions from these high temperature resistant polymers. In addition, these polymers are not readily soluble in common organic solvents.

In this phase of research we concentrated on selecting ceramic precursor-polysilazanes- and investigated their film formation and their use as an inorganic polymer in high temperature resistant hybrid films. Two

commercially available materials HTT-1800 and HTA-1500 (Kion Defense Technologies Inc.) were selected. The chemical structures of HTT-1800 and HTA-1500 are shown in Fig. 49.
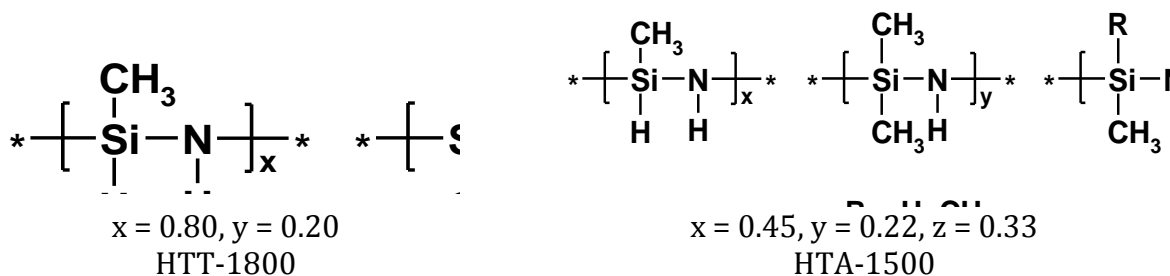

x = 0.80, y = 0.20
HTT-1800

x = 0.45, y = 0.22, z = 0.33
HTA-1500

Figure 49: Representative chemical structures of polysilazane ceramic cursers

HTT-1800 when applied and processed as neat polymer cures at 200·C and forms brittle films. HTA-1500 is a room temperature curing polymer that forms brittle films in 24-48 hours. These films when heated to 450°C in the presence of oxygen do not show any color change and return to their original state (as brittle films) without wrinkling, adhesion loss, or appreciable change in their general appearance. Figure 50 illustrates the temperature resistance of polysilazane films by TGA.
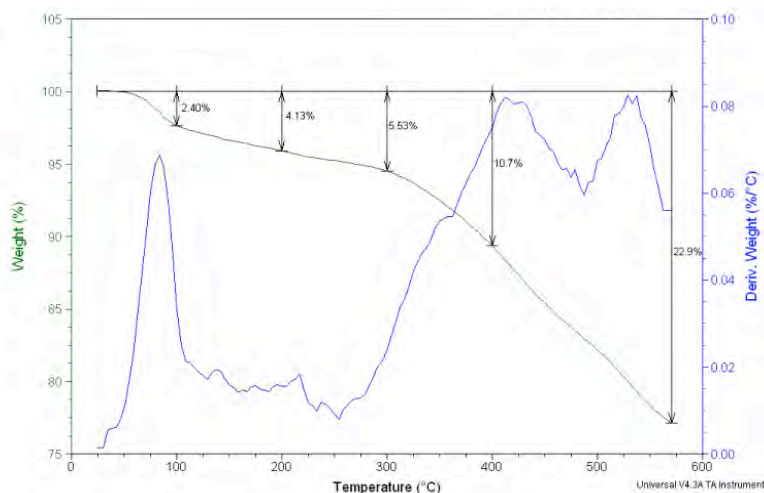

Figure 50. Temperature resistance profile of HTA-1500 film cured at RT

While polysilazane films possess outstanding high temperature resistance properties, they must be further modified to yield films that can be readily applied. Thus, treating polysilanes with functionalized PDMS (Fig. 51) may result in increase in elasticity without compromising high temperature resistance.
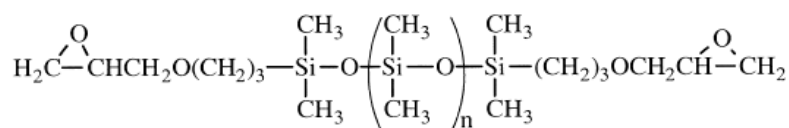

Figure 51. Representative chemical structure of DMS-E11

The reaction of polysilazane HTA with DMS-E11 at 1:1 w/w ratio produces a slightly more flexible coating film. Similar approaches followed using hydroxyl terminated oligomeric PDMS that resulted in minimal gain in film flexibility. All attempts to gain film flexibility and high temperature resistance balance failed.

In a series of experiments a commercial polysiloxane resin 840 (Dow Corning) was reacted with both grades of the above polysilazane polymers. The rational for selection of this resin was two folds: 1) In Dow Corning 840 resin about 30% of the methyl groups have been replaced by phenyl moiety which should help increase the high temperature resistance of the product; 2) the high molecular weight (~ 4500 g/mol) most likely would increase the flexibility. In the above experiments we varied the amount of 840 resins within 10-75% range using either one of the polysilazane resins. Again, the aim was to reach a balance between the film flexibility and further gain in high temperature resistance. As can be seen in Fig. 52 the reaction product of polysilazane 1500/polysiloxane at 1:1 ratio produces films that show further gain in high temperature resistance (10.7% loss at 400°C vs 7.2% loss at 400°C).

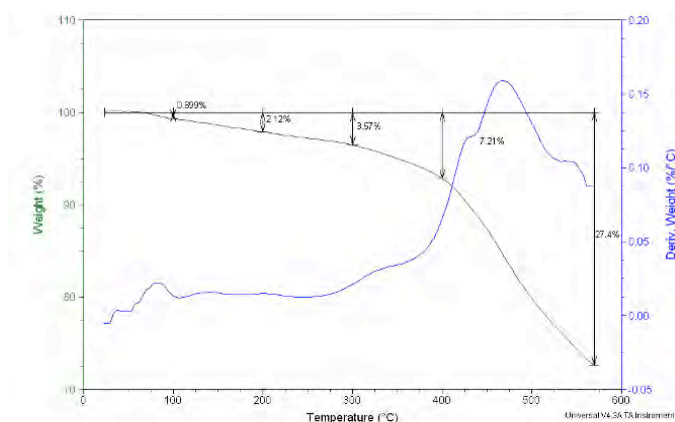**Figure 52. Temperature resistance profile of reaction product of HTA1500/840 at 1:1 ratio.**

The reaction of polysiloxane 840 with polysilazane HTT 1800 at 1:1 ratio produced thin films that demonstrate excellent gains in high temperature resistance. This reaction product also showed residual improvement over the polysilazane alone. Figure 53 illustrates the temperature profile of this reaction product.
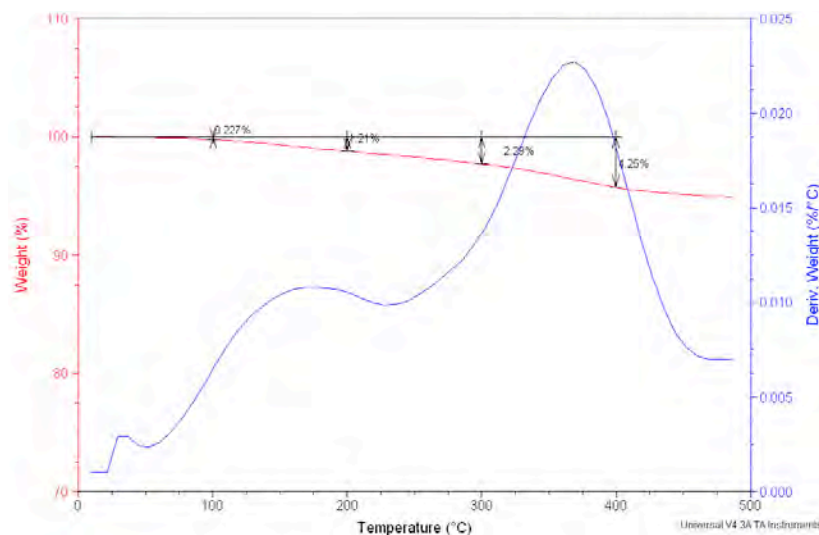
Figure 53. Temperature resistance profile of reaction product of HTT1800/840 at 1:1 ratio.

Table 1. Key properties of selected organic/inorganic hybrid films

Material	% Degradation @ 400°C	Flexibility as thin film	Appearance
Polysilazane HTA-1500	10.71	Very poor	Cracked
Polysilazane HTT-1800	7.52	Very poor	Cracked
HTA-1500/840 resin 1:1	7.21	Poor	Wrinkled
HTT-1800/840 resin 1:1	4.25	Poor	Wrinkled

As can be seen from Table 1, both the temperature resistance and flexibility of the hybrid films improve when reacted with flexible polydimethylphenylsilicone resin 840. However, all attempts to produce uniform films without flow modifying materials failed.

Since using polysilazane as demonstrated above provides rather rigid films, certain polymer backbone modification is necessary. Polyamides and polyimides are known for their high heat resistant properties. Thus, we envisioned synthesizing aromatic polyamic acid polymers and further extend the chain with either 840 resin and ceramic procures. The polyamic acid (Fig. 54) can be synthesized to contain primary amine functional groups that can be used for chain extension using various epoxy functional polysiloxane, and polysilsesquioxanes.

The synthetic pathway of aromatic polyamic acid oligomer using pyromellitic dianhydride (PMDA) and 4,4'-oxydianiline (ODA) is shown in Fig. 54, and the product FTIR in Fig. 55.
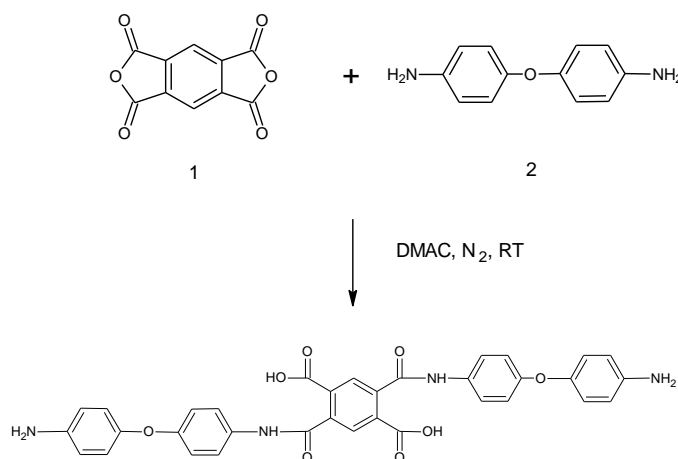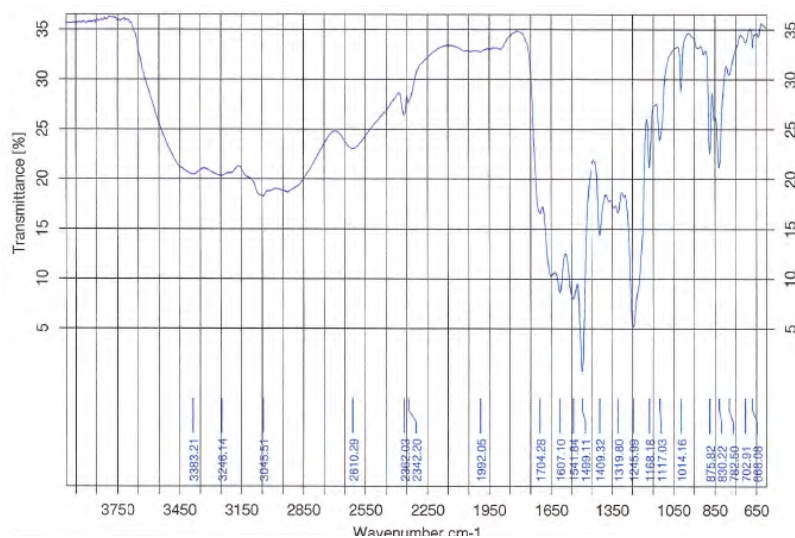
Figure 54. Polyamic acid synthetic pathway.

Figure 55. FTIR spectrum of amine terminated PPA.

In the next step the polyamic acid was treated with epoxy functional polysiloxane DMS-E11 and cured at temperatures ranging from 50-200°C. As can be seen from the Table 2 below, the reaction of polyamic acid with di-epoxy polysiloxane yields a new film forming material that when cured at 200 °C yields PDMS modified PBI composite film.

Table 2. Crosslinking and PBI formation between PPA and DMS-E11

Curing T/°C	Curing time (h)	Result
50	4	Tacky film
100	2	Dry film
150	2	Cured film
200	2	Cured film

As can bee seen from Fig. 56 and Table 3, the reaction product affords films with very good thermal profile. In comparison, the standard amine cured bisphenol A epoxy (Fig. 57) loses more than half of its original weight upon exposure to high temperature.
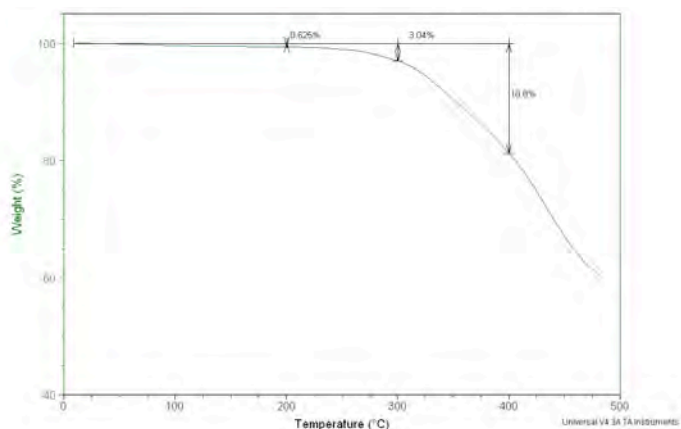
Figure 56. TGA of reaction product of PPA and DMS-E11.

Table 3. %Degradation of organic/inorganic hybrid thin film as a function of temperature.

T/°C	% Degradation		
	Cured at 100°C	Cured at 150°C	Cured at 200°C
200	4.23	0.88	0.63
300	8.63	4.81	3.04
400	23.10	20.50	18.80

Figure 57. Temperature resistance profile of amine-cured bisphenol-A epoxy resin.

Hybrid Materials for Thermal Management in Thin Films and Bulk Composites

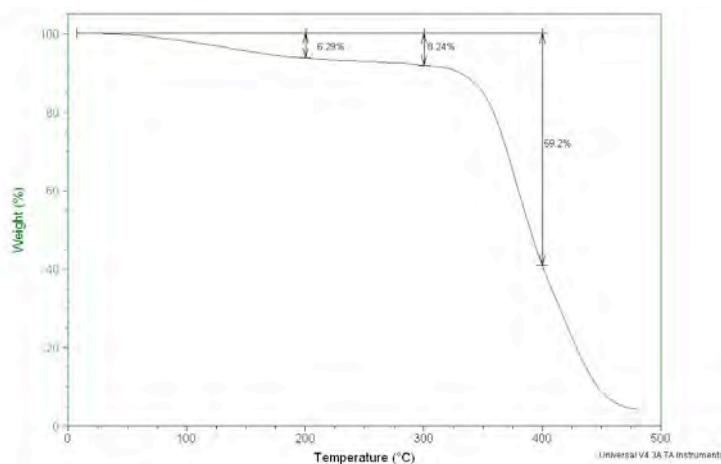Polymeric aromatic polyimides are characterized by their high temperature resistance, electrical conductivity and structural integrity but rather poor flexibility and film forming properties. Such polymers have found applications as a high-temperature adhesive in a number of aerospace and electronic end-uses. [1,2]. Phenyl and some alkyl substituted silsesquioxanes are also known for their high temperature resistance but are not good film formers.
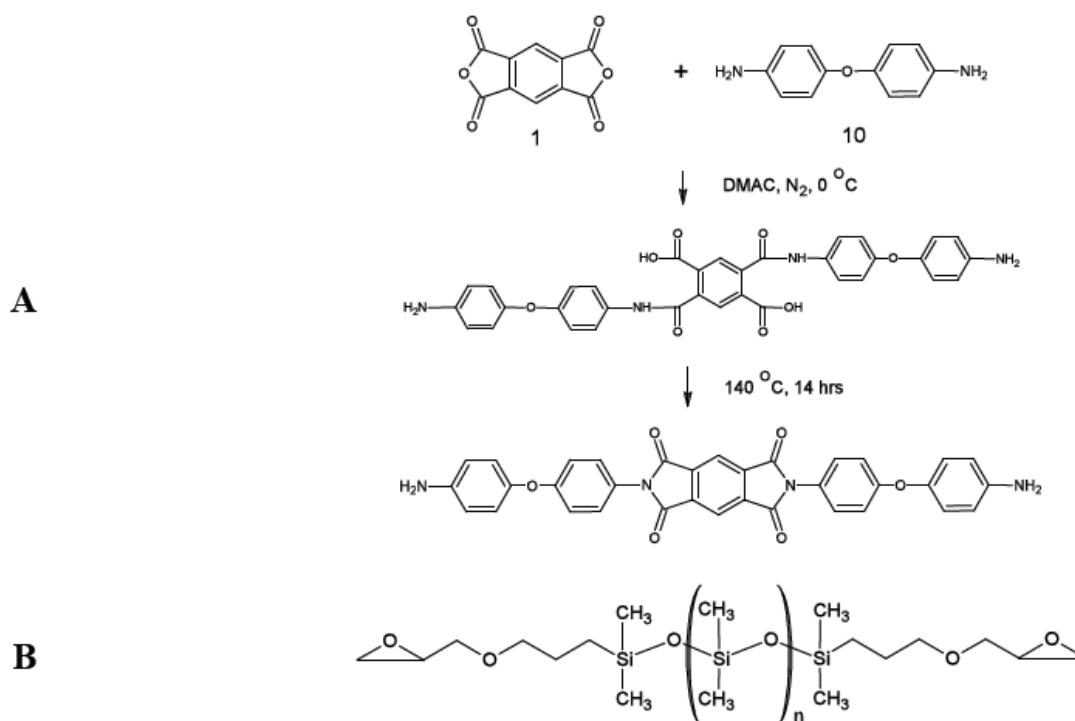

Figure 1. Schematic representation of A; amine-terminated aromatic polyimide and B; di-epoxy polysiloxane resins.

The objective in this phase of the research work was to prepare hybrid organic-inorganic polyimide resins that can be formulated into high temperature coatings for thermal management in thin films and composites.

Previously we reported the successful modification of an amine-terminated polyimide with commercially available linear di-epoxy polydimethylsiloxane (Fig. 1), which resulted in film forming polymer.

The thermosetting product when cured at 200°C afforded a film that showed improved thermal resistance and flexibility. The thermal profiles of polysiloxane modified polyimide and the standard epoxy coating are shown in Figure 2.
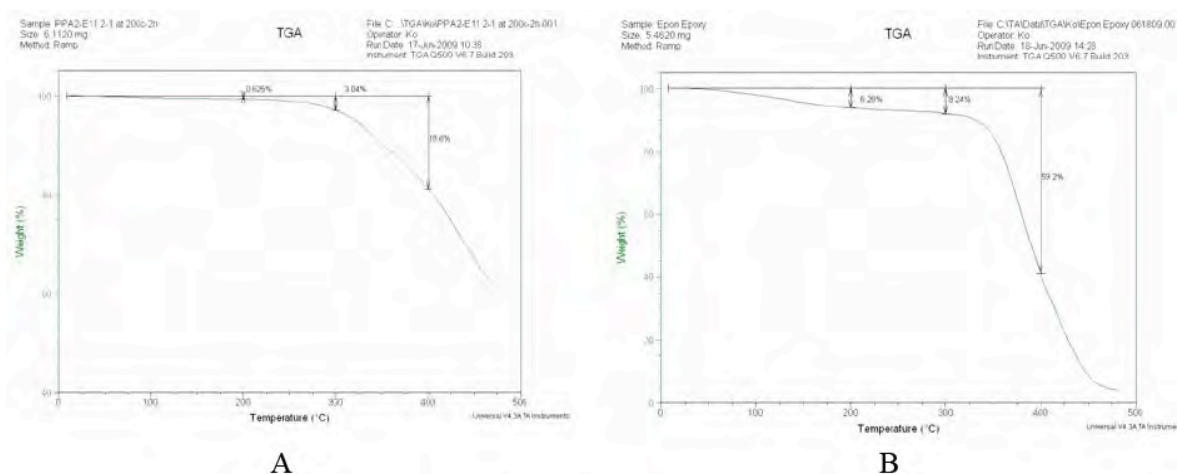
Figure 2. TGA thermal profile of A; polyimide/siloxane adduct and B, control amine-cured bisphenol-A epoxy resin.

As can be seen from Figure 2, the polyimide film only show about 18.8% degradation at 400 oC while the control epoxy loses about 59.2% of its original weight at the same temperature. In order to improve the thermal resistance beyond 400oC it may be possible to treat the amine functional polyimide with epoxy functional silsesquioxane and liner polysiloxane resins (Fig. 3 A and B). Octa(propylglycidyl ether)polyhedral oligomeric silsesquioxane (epoxy POSS)
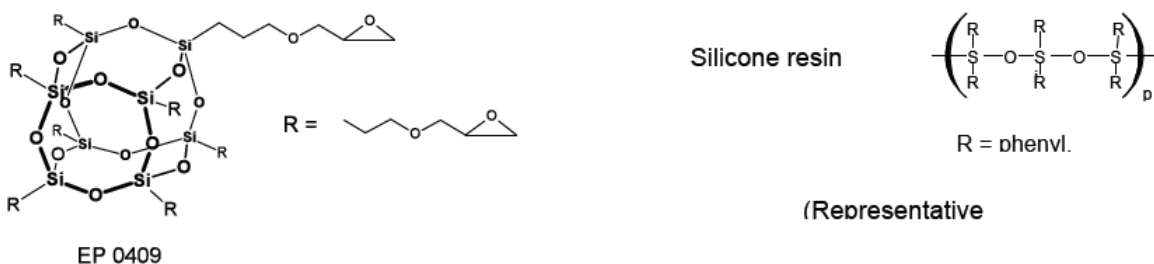
Figure 3. Representative chemical structures of A, epoxy silsesquioxane; B, linear high temperature silanol functional siloxane resin.

Consists of eight oxirane groups. It can be used with many solvents, such as tetrahydrofuran, chloroform, toluene [3,4,5]. The Dow 840 and 805 are silicon resins containing silanol functionality. They are used to improve heat and corrosion resistance. Polysiloxane 840 resin provides higher hardness than 805 resin [6,7].

Treatment of polyimide with octa-epoxy silsesquioxane at a molar ratio of 1:2 at room temperature followed by reaction at 100oC produced a brown liquid (Fig. 4). After removal of the toluene soluble excess silsequioxane, the product was further purified through fractionation and vacuum treatment.

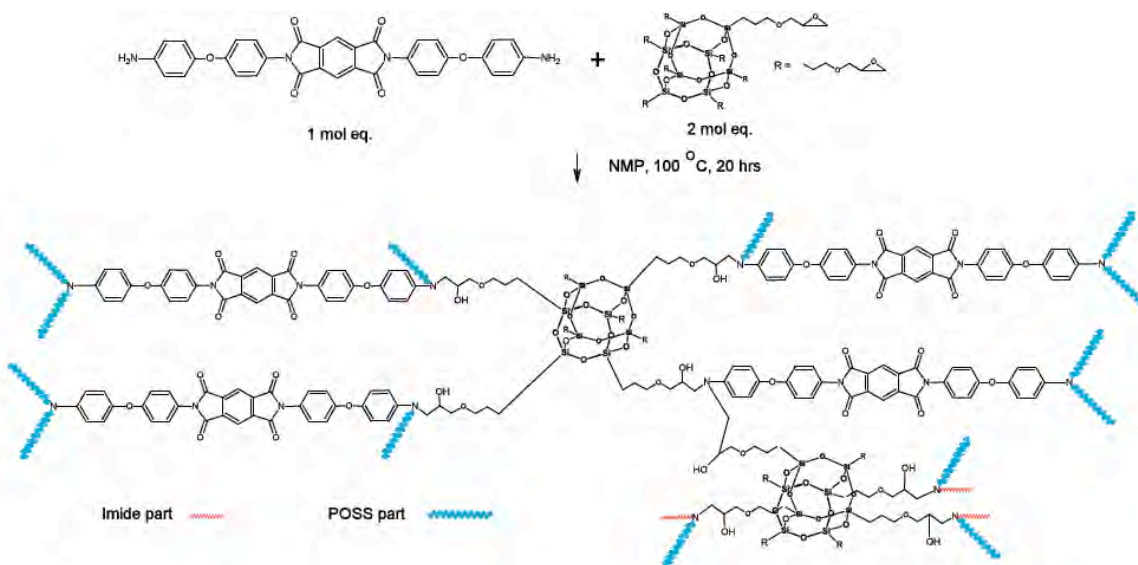**Figure 4. Schematic representation of the reaction of EP-0409 and Polyimide (E-I) at (2:1)molar ratio.**

The FTIR spectrum of the product (Fig. 5) clearly show a broad hydroxyl stretching peak at 3423 cm-1 which can be taken as evidence of oxirane ring opening through the reaction with primary amine groups on the polyimide chain.
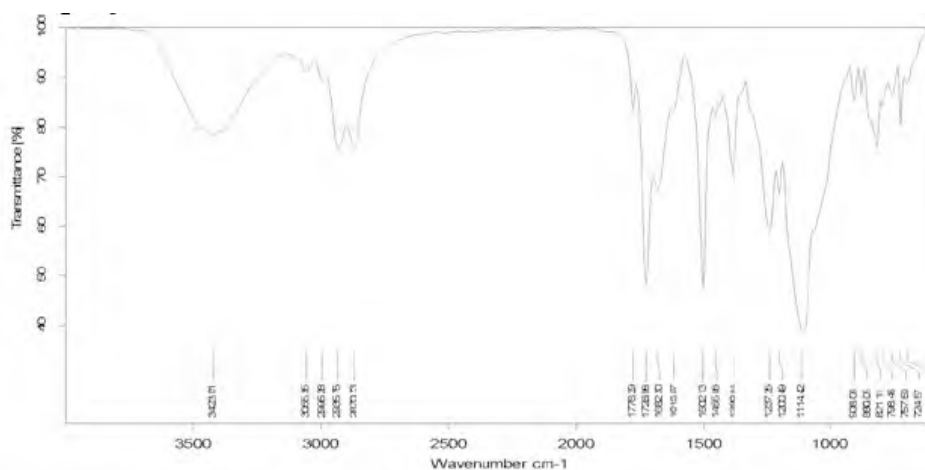
Figure 5. FT-IR of the reaction of EP-0409 and polyimide at (2:1) molar ratio

The solution of silsequioxane treated polyimide (E-I) in a 1:1 mixture of 2-NMP and acetonitrile is a brown viscous liquid that forms pale-yellow brown films when processed at 200°C. As can be seen from the TGA profile in Fig. 6 treatment with silsesquioxane appears to have increased the thermal resistance and reduced the percent degradation at 400°C from 18.8% for untreated to 12.9% for treated product. It is also important to note that the degradation profile appears to reach a plateau past the 600°C.
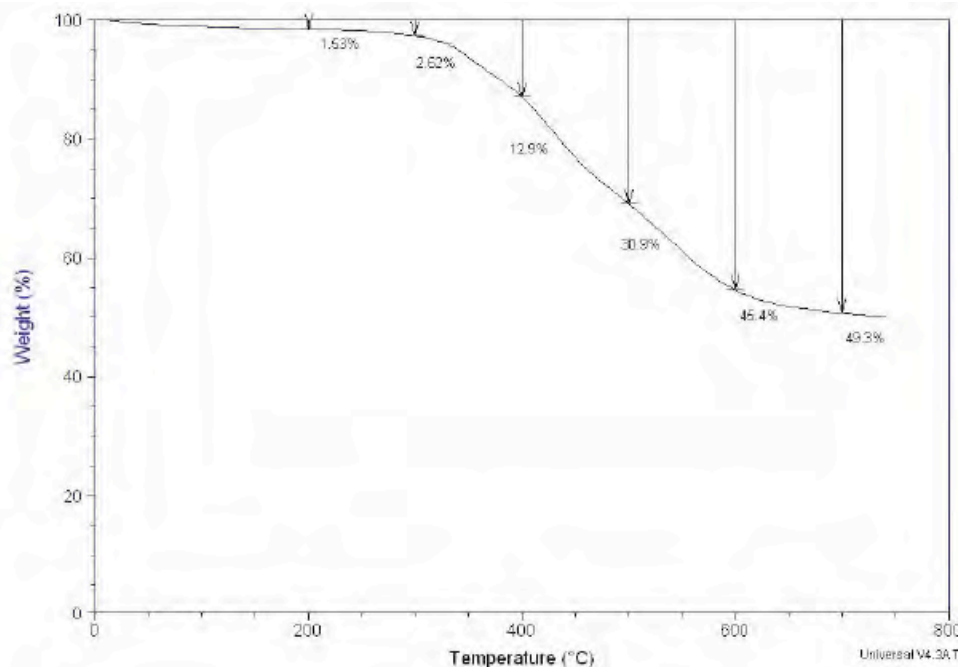
Figure 6. TGA profile of the reaction product of EP-0409 and polyimide at 2:1 molar ratio.
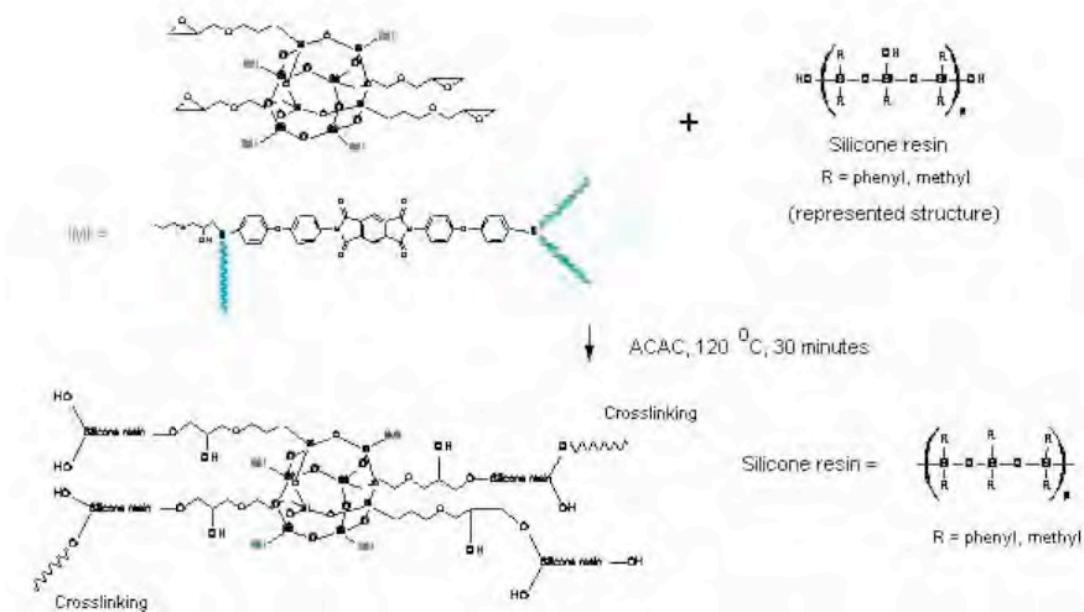
Figure 7: Reaction of EP-0409 modified polyimide with silanol containing polysiloxane.

While the thermal degradation of the product is at least four fold better than that of the standard bisphenol-A epoxy films, it still is rather brittle and needs to be toughened. Since the reaction product contains un-reacted epoxy functional groups it can be reacted with a high molecular weight elastomer forming silanol terminated polysiloxane resin such as

commercially available Dow 840 or 805 resins. The treatment of the above adduct separately with 840 and 805 resins in presence of aluminum triacetylacetonate (ACAC), and at 120 oC afforded products that appeared to have good solubility in acetonitrile. It is conceivable that at high temperatures and in the presence of the aluminum triacetylacetonate catalyst epoxy moieties and OH groups from Si-OH to react [8]. It is also possible that OH groups from C-OH in the backbone react with epoxy from octa-epoxy POSS. The general reaction scheme is shown in Fig. 7.

Different types of silanol-silicone resins and varying mole equivalent of the silicone resins were evaluated and compared by means of film appearance (visual) (Figs. 8, 9), film flexibility (bending test), solvent resistance (Toluene rub test), functionality (FT-IR), glass transition temperature (DSC), thermal degradation (TGA), and toughness of film (DMA) (Fig. 10).

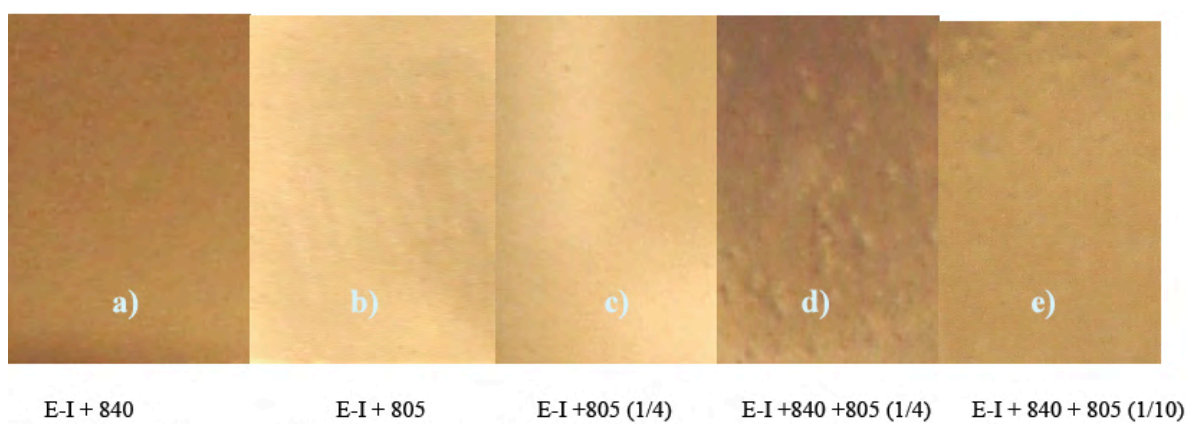| a) | b) | c) | d) | e) |
| E-I + 840 | E-I + 805 | E-I +805 (1/4) | E-I +840 +805 (1/4) | E-I + 840 + 805 (1/10) |

Figure 8. Films applied and baked on stainless steel panels; ( ), added fraction.

Figure 9. Films applied and cured on Teflon substrate.

Some physical properties and general appearances of the thin films are shown in Table I and II.

Table I: Appearance and physical properties of silicone modified polyimide films

Material	Film appearance on stainless steel	Flexibility	Cured free film
a) E-I(2:1) + 840	Good film, no crater	Fail, film is cracked	Brittle, brown color
b) E-I(2:1) + 805	Good film, no crater	Pass	Flexible, a bit tacky, light brown color
c) E-I(2:1) + 805(1/4)	Good film, no crater	Pass	Flexible, a bit tacky, brown color
d) E-I(2:1) + 840 + 805(1/4)	Non- uniform film	Pass	Flexible, brown color
e) E-I(2:1) + 840 + 805(1/10)	Non-uniform film	Pass	Flexible, brown color

Table II: Thermal degradation of various modifications from TGA profile

Products	Thermal degradation (%)					
	200^oC	300^oC	400^oC	500^oC	600^oC	700^oC
a) E-I(2:1) + 840	0.04	1.45	6.42	12.8	23.4	27.1
b) E-I(2:1) + 805	0.24	2.78	7.95	14.6	27.9	29.7
c) E-I(2:1) + 805(1/4)	0.05	2.39	7.34	14.9	31.4	33.3
d) E-I(2:1) + 840 + 805(1/4)	0.07	2.49	7.67	15.1	30.8	32.8
e) E-I(2:1) + 840 + 805(1/10)	0.16	2.60	7.94	15.1	30.1	32.1

As can be seen from Figs. 8 and 9 the polyimide modified with 840 resin alone while processes the lowest film degradation properties it is rather brittle. Other combinations: b), c), d), and e) were flexible enough to be loaded onto the Dynamic Mechanical Analyzer.
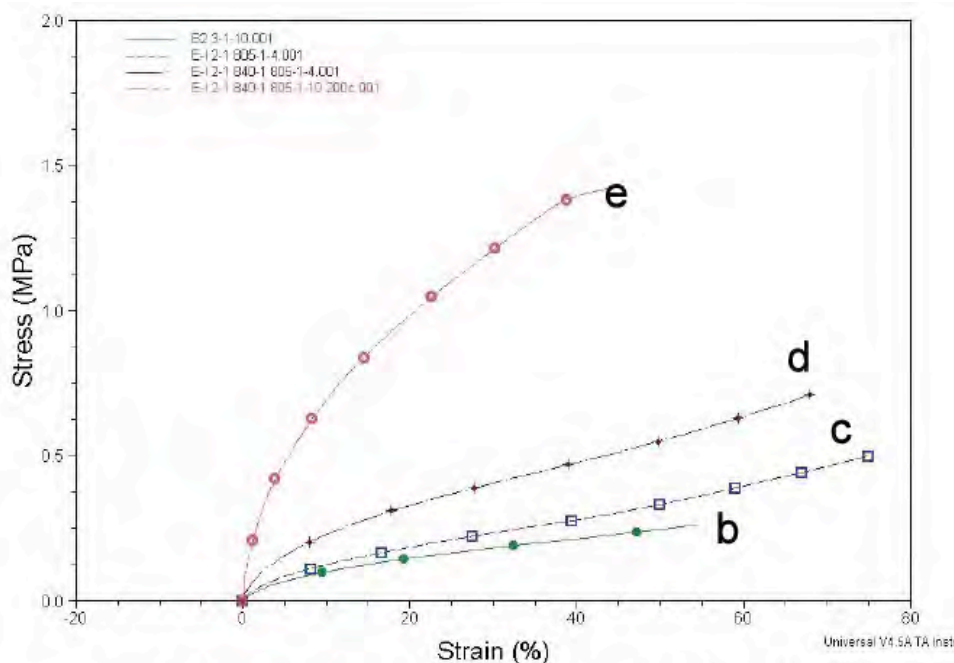
Figure 10. Stress/strain values of modified products

Table III. Comparison of Young's moduli of various modified products

Products	Young's modulus
a) E-I(2:1) + 840	-
b) E-I(2:1) + 805	1.52
c) E-I(2:1) + 805(1/4)	1.08
d) E-I(2:1) + 840 + 805(1/4)	4.37
e) E-I(2:1) + 840 + 805(1/10)	20.71

Table IV: Comparison of thermal degradation and Young's modulus of the various formulations

	Thermal degradation (%)						DMA
	200°C	300°C	400°C	500°C	600°C	700°C	Young's modulus
a) E-I(2:1) + 840	0.04	1.45	6.42	12.8	23.4	27.1	-
b) E-I(2:1) + 805	0.24	2.78	7.95	14.6	27.9	29.7	1.52
c) E-I(2:1) + 805(1/4)	0.05	2.39	7.34	14.9	31.4	33.3	1.08
d) E-I(2:1) + 840 + 805(1/4)	0.07	2.49	7.67	15.1	30.8	32.8	4.37
e) E-I(2:1) + 840 + 805(1/10)	0.16	2.60	7.94	15.1	30.1	32.1	20.71

In conclusion, the modification of the aromatic polyimide with linear epoxy functional silsesquioxane and its treatment with various mixed phenyl/methyl polysiloxane afforded flexible films with lower thermal degradation at considerably higher temperatures (Table IV).

References

1 Hergenrother, P.M., Watson, K.A., Smith, J.G., Connell, J.W., & Yokota, R. (2004). Copolyimides from 2,3,3',4'-biphenyltetracarboxylic dianhydride and pyromellitic dianhydride with 4,4-oxydianiline. *Polymer, 45,* 5441-5449.

2 Yang, C., & Su, Y. (2005). Colorless polyimides from 2,3,3',4'-biphenyltetracarboxylic dianhydride (BPDA) and various aromatic bis(ether amine)s bearing pendent trifluoromethyl groups. *Polymer, 46,* 5797-5807.

3 Lee, L., & Chen, W. (2005). Organic–inorganic hybrid materials from a new octa(2,3-epoxypropyl)silsesquioxane with diamines. *Polymer, 46,* 2163-2174.

4 Liu, Y., Chang, G., Hsu, K., & Chang, F. (2006). Epoxy/Polyhedral Oligomeric Silsesquioxane Nanocomposites from Octakis (glycidyldimethylsiloxy) octasilsesquioxane and Small-Molecule Curing Agents, *Journal of Polymer Science: Part A: Polymer Chemistry, 44*, 3825–3835.

5 Hybrid Plastics, POSS Chemical Catalog 2009, V.1.01.

6 Dow Corning, Paints & Inks Solutions3 Performance.Innovation.Expertise: Resins and Intermediates Selection Guide.

7 Dow Corning, Process Industry: What are silicone?

8 Liu, H., Zheng, S., & Nie, K. (2005). Morphology and Thermomechanical Properties of Organic-Inorganic Hybrid Composites Involving Epoxy Resin and an Incompletely Condensed Polyhedral Oligomeric Silsesquioxane. *Macromolecules, 38,* 5088-5097.

Deviations from Budget

The Award budget term was 15 August 2008 through 14 January 2011; a no cost extension was granted in December 2010, extending the grant term through 31 August 2011. The originally submitted budget anticipated a 36 month term. The award anticipated a 29 month term, and a reasonable attempt to spend out during this term was made.

Deviations for Senior Personnel (salary and fringe)

In Year 1 co-PI Prof. Baghdachi drew no salary and fringe although budgeted for two months. He was paid at a rate of 100% for the academic base year and additionally for the May through August 2009 period from other funds. Two months senior personnel salary and fringe were unexpended at the end of Year 1.

In Year 2 PI Prof. Texter was budgeted for three months, but expended an extra 1.5 months. Prof. Lindsay did not expend the month budgeted for her. Prof. Baghdachi was budgeted for two months and expended four months. About 2.5 months of senior personnel salary and fringe were expended over the budget for Year 2. A net 0.5 month salary and fringe over budget was expended for Years 1 and 2 combined.

In Year 3 Prof. Texter was budgeted for three months, Prof. Baghdachi for two months, and Prof. Lindsay for one month. Prof. Baghdachi made no reportable effort on the project after April of Year 2 and drew no salary in Year 3. Prof. Lindsay continued on her

alternative assignment and drew no salary in Year 3. Professor Texter drew three months salary and fringe, leaving about the senior personnel under budget for Year 3 by about 3 months salary and fringe and under budget for the total grant term by about 1.5 months salary and fringe (~$25k).

Deviations for Junior Personnel (Salary and Fringe)

Mr. Rene Crombez was hired to assist in the dispersion and coatings tasks; his assistance was not anticipated in the budget. His employment approximately balanced the amount saved by returning the quartz microbalance system. His salary and fringe amounted to about $115k.

Deviations for Equipment

The acquisition of a $135,000 quartz microbalance system with dynamic relaxation was cancelled because it could not measure processes important to the coating and materials thicknesses of import to this project. A spin coater and ultrasonic cleaner were retained and payment was made for expendables used in our testing. This instrument return yielded about $115k unspent in the capital equipment budget.

Total Deviations for Wages and Fringe: ~ $60k (about 10% of budgeted amount)

Total Deviations for Tuition: (~ $65k) (about half of budget amount)

Total Deviations for Equipment: (~ $79k) (about 21% below budget amount)

Total Deviations for Other Direct Costs: ~ $46k (about 34% over budget amount)

Total Deviations for Indirect Costs: ~ $38k (about 12% over budget amount)

Net Deviations: 0